

# Contents

|   |            |
|---|------------|
| <b>I New Physics</b>  | <b>1</b>   |
| <b>Dilepton Resonances at High Mass</b>   | <b>2</b>   |
| <b>Lepton plus Missing Transverse Energy Signals at High Mass</b>   | <b>34</b>  |
| <b>Search for Scalar Leptoquarks and Right-handed <math>W</math> Bosons and Neutrinos in Dilepton-Jets Final States</b> | <b>59</b>  |
| <b>Vector Boson Scattering at High Mass</b>   | <b>77</b>  |
| <b>Discovery Reach for Black Hole Production</b>  | <b>114</b> |



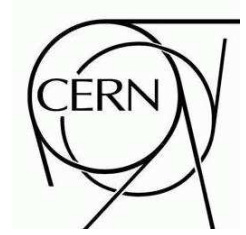
**Part I**

**New Physics**



# ATLAS NOTE

July 18, 2008



## Dilepton Resonances at High Mass

The ATLAS Collaboration

### Abstract

We present the discovery potential of a heavy new resonance decaying into a pair of leptons with early LHC data with the ATLAS detector. The dilepton final states are robust channels to analyze because of the simplicity of the event topology. The unprecedented available center-of-mass energy will allow one to probe regions that are inaccessible at previous experiments even with modest amounts of data. After studying the Standard Model predictions and the associated uncertainties one can then look for significant deviations as indication of beyond the Standard Model physics (BSM). The focus of the note is to study the prospects for discovering BSM physics in the dilepton final states with an integrated luminosity ranging from  $100 \text{ pb}^{-1}$  to  $10 \text{ fb}^{-1}$ .

# 1 Introduction

New heavy states forming a narrow resonance decaying into opposite sign dileptons are predicted in many extensions of the Standard Model: grand unified theories, Technicolor, little Higgs models, and models including extra dimensions [1–4]. The discovery of a new heavy resonance would open a new era in our understanding of elementary particles and their interactions. Because of the historic importance of the dilepton channel as a discovery channel and the simplicity of the final state, these channels will be very important to study with early ATLAS data. The strictest direct limits on the existence of heavy neutral particles are from direct searches at the Tevatron [5, 6]. The direct searches are limited by the available center-of-mass energy and are expected to ultimately be limited to about 1 TeV at the Tevatron [7].

The LHC will have a center-of-mass energy of 14 TeV which should ultimately increase the search reach for new heavy particles to the 5 - 6 TeV range. There are lot of exotic models which can be tested at the LHC and analyzing all the existing models is impossible. Instead we choose to take a different approach, grouping the early-data analysis by their final state topologies. There have been several other ATLAS studies evaluating the potential for discovery of a heavy resonance [8]. However, this is the first study to include full trigger simulation, misalignments, and data driven methods. Including these experimental issues is important to realistically estimate the analysis potential. We limit ourselves to the ‘early data phase’ of the experiment, defined roughly to include the accumulation of up to  $10 \text{ fb}^{-1}$  of ATLAS data.

In the remaining of this introduction, the investigated models are reviewed. In sections 2 and 3, we explore the detector performance concerning the electron, muon and tau reconstruction abilities at high energies and the corresponding trigger efficiencies. In section 4 we investigate the Standard Model predictions and associated uncertainties. After understanding the background sources and the Standard Model limits and its uncertainties, we proceed to search for Exotic resonances in section 5.

## 1.1 Models Predicting a $Z'$

Several models [1, 3] predict the existence of additional neutral gauge bosons. Grand unified theories as well as “little Higgs” models predict their existence as a manifestation of an extended symmetry group. Strongly interacting theories such as “Top Color” models predict these to help explain the heavy mass of the top quark. Generically, however, there are no predictions for the mass of these particles. Since the experimental consequences of these is very similar in the dilepton final state we examine only some representative models: the Sequential Standard Model (SSM)<sup>1)</sup>, the  $E_6$  and the Left-Right Symmetric models [9]. The width of the  $Z'$  boson is given by  $\Gamma(Z' \rightarrow \ell^+ \ell^-) \approx [(g_\ell^R)^2 + (g_\ell^L)^2] \frac{m_{Z'}}{24\pi}$  where  $g_\ell^R$  and  $g_\ell^L$  are the right and left handed couplings of the charged leptons to the  $Z'$  boson and  $m_{Z'}$  is the mass the  $Z'$  boson. For the masses and couplings considered here the natural width is typically around 1% of the mass of the resonance.

The strictest limits from direct searches come from the D0 and CDF experiments at the Tevatron [6]. Indirect searches have also been undertaken by the LEP experiments [10]. The direct limits range from several hundred GeV to approximately 1 TeV and are shown in Table 1.

These limits are not expected to improve much beyond 1 TeV [7]. It should be noted that for models where the  $Z'$  couples preferentially to the third generation the limits are lower, therefore we consider it important to look at a lower invariant mass region in this channel.

---

<sup>1)</sup>The Sequential Standard Model includes a new heavy gauge boson with exactly the same couplings to the quarks and leptons as the Standard Model  $Z$  boson.

| $Z'$ Model  | Indirect Searches (GeV) | Direct Searches (GeV) |                    |
|-------------|-------------------------|-----------------------|--------------------|
|             |                         | $e^+e^-$ Colliders    | $p^+p^-$ Colliders |
| $Z'_\chi$   | 680                     | 781                   | 822                |
| $Z'_\psi$   | 481                     | 366                   | 822                |
| $Z'_\eta$   | 619                     | 515                   | 891                |
| $Z'_{LRSM}$ | 804                     | 518                   | –                  |
| $Z'_{SSM}$  | 1787                    | 1018                  | 923                |

Table 1: 95% C.L. limits on various  $Z'$  models.

## 1.2 Randall-Sundrum Graviton

The Randall-Sundrum [4] model addresses the hierarchy problem by adding one extra-dimension linking two branes, the Standard Model brane and the Planck brane. The hierarchy is solved by assuming a warped geometry in the fifth dimension which decreases exponentially from the Planck scale to the TeV scale. The Randall-Sundrum model predicts the existence of a tower of Kaluza-Klein excitations of the graviton. These should be observable as resonances which decay into lepton pairs at the LHC. The current limits depend on the parameters of the model but range from several hundred GeV to a TeV [5]. We consider the observability of a Randall-Sundrum graviton decaying into electron pairs. The width of the graviton resonance would be very narrow. For the parameters considered here it ranges from  $10^{-4}$  to a few  $10^{-3}$  times the mass.

## 1.3 Technicolor

Strongly interacting theories like Technicolor and Extended Technicolor provide a dynamical solution to the problem of Electroweak Symmetry Breaking. Many new technifermions which are bound together by a QCD-like force are predicted by such theories. One of the most promising search channels is the dilepton decay of the  $\rho_{TC}$  and  $\omega_{TC}$ . Limits on the masses of these particles depend on the exact parameters assumed for the model but range in the several hundreds of GeV. We study the “Technicolor Strawman Model” or TCSM [11, 12] as a benchmark model for generic strongly interacting theories. The width of the techni-mesons is dependent on the number of technicolors but is generally assumed to be small, of the order of a few percent of their mass. More details on the exact values of the parameters considered are discussed in a later section.

# 2 Object Identification and Performance

This section describes the requirements used to select objects for the analyses and summarizes findings on the performance on the Exotic Monte Carlo samples.

## 2.1 Electron Identification

The electron identification and performance is described in detail elsewhere [13]; here we summarize the results concerning very high transverse momentum ( $p_T$ ) electron identification and reconstruction. The background to very high  $p_T$  electron pairs is expected to be low, therefore only minimal selection criteria need to be applied, in order to maximize the efficiency. These minimal criteria are called *loose*. On the other hand, when trying to select very high  $p_T$   $\tau$  lepton pairs where one  $\tau$  decays hadronically, a tighter selection on the electron from the other  $\tau$  decay is needed.

On top of the minimal requirements that the reconstructed clusters should have an absolute pseudo-rapidity ( $\eta$ ) less than 2.5 and should be associated with a track reconstructed in the inner detector, two electron selections were studied (both described in detail in [13]):

- A *loose* selection which is used to achieve very high efficiency while maintaining rejection against highly energetic pions with wide showers.
- A *medium* selection, which makes further requirements to obtain better rejection against single neutral pions by exploiting the very fine granularity of the first compartment of the electromagnetic calorimeter, and tighter requirements on the associated track.

Figure 1 shows the efficiency of the two selections in a sample of 1 TeV  $Z' \rightarrow e^+e^-$  events as a function of transverse momentum and pseudo-rapidity for clusters with  $p_T$  greater than 50 GeV and  $|\eta|$  smaller than 2.5. The inefficiency of the *loose* selection is dominated by the cluster to track association. It must be noted that this efficiency will be improved in future software versions.

The energy resolution for electrons at high  $p_T$  is about 1% except in the crack region between the forward and central calorimeters where the resolution is about 5%. The probability to assign the wrong charge to an electron ranges from 1% to at most 5% as the transverse momentum goes from 100 GeV to 1 TeV [14]. For a 1 TeV  $Z'$  a dielectron mass resolution of  $(0.80 \pm 0.02)\%$  is obtained.

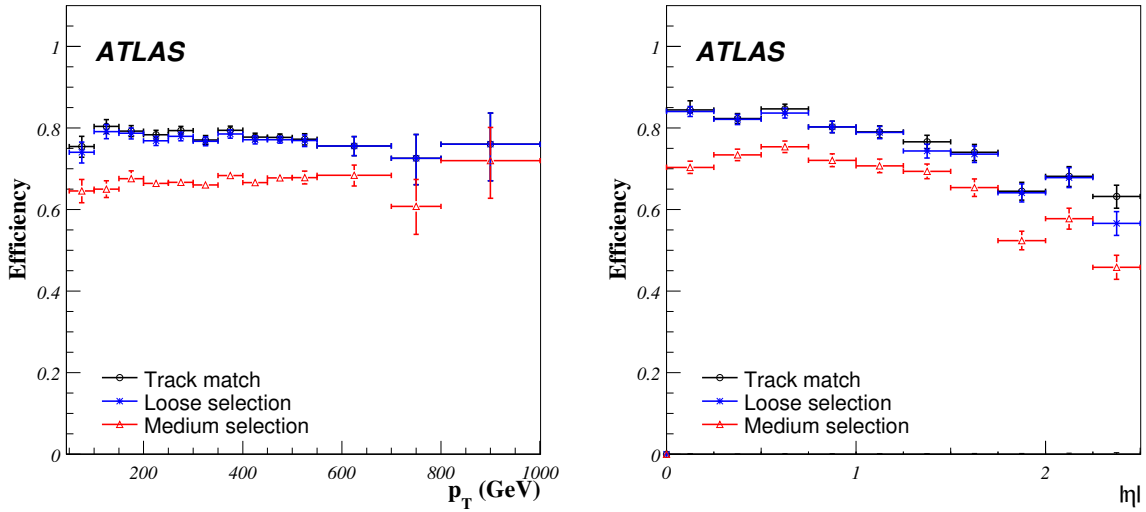


Figure 1: Efficiency of the *loose* and *medium* selection criteria in 1 TeV  $Z' \rightarrow e^+e^-$  events as a function of  $p_T$  (left) and  $\eta$  (right).

## 2.2 Muon Identification

Here we discuss the requirements used to select muons as well as a method to extract the identification efficiency from data. The ATLAS detector has an excellent standalone muon spectrometer: muon tracks can be found both in the inner detector and the muon spectrometer. A “combined” muon track consists in matched track segments from both the muon spectrometer and inner detector. We require that a muon, with  $p_T \geq 30$  GeV,

- forms a combined track (inner detector and muon spectrometer) with  $|\eta| \leq 2.5$ ,

- has a match  $\chi^2 < 100.0$  (5 D.O.F) between the parameters of the inner detector and muon spectrometer track segments.

The muons in the 1 TeV  $Z'$  sample have a most probable  $p_T$  of about 500 GeV. An efficiency of  $(95 \pm 0.2)\%$  with a resolution of approximately 5% is found with this selection. The results are consistent with previous studies [15] [16].

The muon identification efficiency as a function of  $p_T$  has been determined using two methods. The first method is the 'tag and probe' method, which has been used successfully at the Tevatron. In this method one uses a 'standard candle' as an in situ calibration point. It involves selecting  $Z \rightarrow \mu\mu$  events and evaluating the reconstruction efficiency from data on these events. One combined muon is used as the tag while an inner detector track is used as a probe track. One can then study how often the probe muon also has a combined track to get an unbiased measurement of the combined muon reconstruction efficiency. The reconstruction efficiency was measured by fitting to the dimuon invariant mass spectrum and finding the fraction of events where the probe track was found as a combined track. A comparison between this tag and probe method and Monte Carlo truth is shown in Fig. 2, demonstrating that we can extrapolate this method into the very high  $p_T$  range.

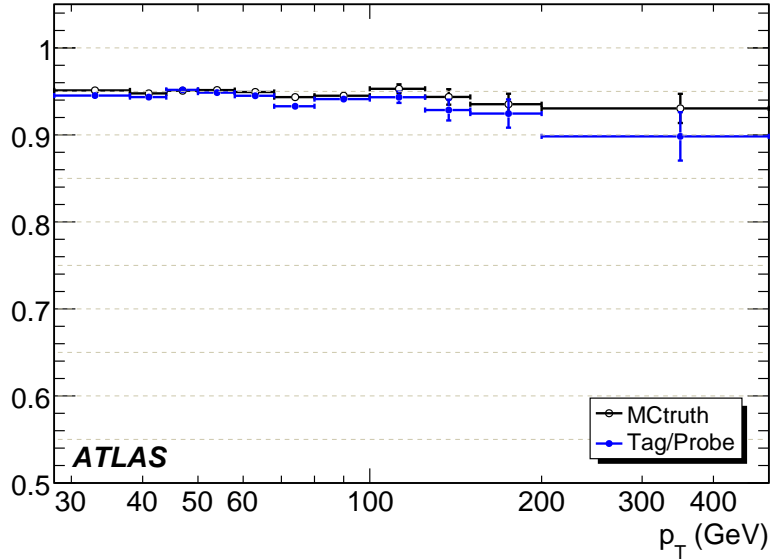


Figure 2: Efficiency of muon reconstruction and identification as a function of  $p_T$  from two different methods (see text).

### 2.3 Tau Identification

The algorithm to reconstruct hadronically decaying  $\tau$  lepton candidates is described in [17]. It is calorimeter based; it starts from a reconstructed cluster with a transverse energy<sup>2)</sup>  $E_T > 15$  GeV and then builds identification variables based on information both from the electromagnetic and hadronic calorimeters, as well as from the inner tracker. Finally, an electron and a muon veto are applied.

The reconstruction efficiency, defined as the probability of a true hadronically decaying  $\tau$  to be reconstructed as a cluster, and normalized to all true hadronically decaying  $\tau$  leptons with  $E_T > 15$  GeV

<sup>2)</sup>The transverse energy is defined as the energy multiplied by  $\sin \theta$ , where  $\theta$  is the angle between the beam axis and the direction from interaction point to the cluster.



inside the  $\eta$  acceptance, is flat as a function of  $\eta$  and  $\phi$ . The average efficiencies are summarized in Table 2. Efficiencies for electron and muon vetos are given with respect to all reconstructed  $\tau$  leptons. The electron and muon misidentification rates are normalized to true electrons or muons inside of the acceptance ( $|\eta| < 2.5$  and  $E_T > 15$  GeV), respectively.

|  |                     |
|--|---------------------|
| Events in $ \eta  \leq 2.5$                    | $(87.1 \pm 0.1) \%$ |
| Events in $ \eta  \leq 2.5$ AND $E_T > 15$ GeV | $(85.6 \pm 0.2) \%$ |
| Reconstruction                                 | $(98.8 \pm 0.1) \%$ |
| Electron veto                                  | $(99.3 \pm 0.1) \%$ |
| Muon veto                                      | $(99.9 \pm 0.0) \%$ |

Table 2: Reconstruction efficiency, efficiency of  $e/\mu$ - $\tau$ -jet overlap removal for hadronically decaying  $\tau$  leptons from  $Z'$  boson decays. The efficiencies for kinematic requirements are also given.

A likelihood is computed for each  $\tau$  candidate. The  $\tau$  likelihood combines information from the calorimeter describing the shower shape and tracking information in a multivariate likelihood to maximize the discrimination from background. Detailed studies were done to optimize the  $\tau$  lepton efficiency and jet rejection for the  $Z'$  boson search. The results (shown in Table 3) were to have a  $p_T$ -dependent likelihood requirement, a requirement on the number of tracks, and a requirement on the transverse energy.

| Requirement                        | Efficiency (%) |
|------------------------------------|----------------|
| $E_T > 60$ GeV                     | $89.8 \pm 0.2$ |
| AND $1 \leq N_{\text{trk}} \leq 3$ | $79.2 \pm 0.3$ |
| AND likelihood requirement         | $51.0 \pm 0.3$ |

Table 3: Preselection and identification efficiency for  $Z' \rightarrow \tau\tau$  ( $m = 600$  GeV). Efficiency is given with respect to reconstructed hadronically decaying  $\tau$  leptons (after removal of overlap with electrons or muons).

### 3 Trigger

At a nominal luminosity of  $\mathcal{L} = 10^{34} \text{ cm}^{-2}\text{s}^{-1}$  the interaction rate seen in the ATLAS detector will be 40 MHz with around 25 interactions per bunch crossing [18], which is far too high to be written to mass storage. The aim of the trigger systems is to reduce the rate to a more manageable 200 Hz while maintaining a highly efficient selection for rare signal processes. Even at the initial luminosity of  $\mathcal{L} = 10^{31} \text{ cm}^{-2}\text{s}^{-1}$  it will be a challenge to keep the trigger highly efficient for all important final states while reducing the event rate. Several detailed trigger studies were undertaken for the dilepton final state. In this section we summarize those results.

#### 3.1 Electron Triggers

There are several proposed triggers which in principle can be used for the dielectron analysis. We considered four triggers: e55 - requiring one electron with  $p_T \geq 60$  GeV, e22i - requiring one isolated electron with  $p_T \geq 25$  GeV, 2e12 - requiring two electrons with  $p_T \geq 15$  GeV, and 2e12i - requiring two isolated electrons with  $p_T \geq 15$  GeV.

Table 4 shows the efficiency at the three ATLAS trigger levels [18]: level 1 (L1), level 2 (L2), and the event filter (EF) for a sample of graviton events. As can be seen in this table, the most efficient triggers are the high  $p_T$  triggers that do not require isolation.

| <i>Signature</i> | Efficiency (L1/L2/EF) (%) |                |                | Total Trigger Efficiency (%) |
|------------------|---------------------------|----------------|----------------|------------------------------|
| e55              | $99.9 \pm 0.0$            | $95.9 \pm 0.2$ | $94.6 \pm 0.3$ | $90.8 \pm 0.3$               |
| e22i             | $85.9 \pm 0.3$            | $96.4 \pm 0.4$ | $83.9 \pm 0.3$ | $80.9 \pm 0.4$               |
| 2e12             | $99.9 \pm 0.1$            | $84.9 \pm 0.5$ | $85.5 \pm 0.3$ | $72.6 \pm 0.6$               |
| 2e12i            | $59.1 \pm 0.7$            | $86.1 \pm 0.7$ | $86.2 \pm 0.3$ | $43.9 \pm 0.7$               |

Table 4:  $G \rightarrow e^+ e^-$  ( $m = 500 \text{ GeV}$ ) event trigger efficiencies with respect to *loose* electron offline selection.

| <i>Sample</i>                          | mu20 Efficiency (L1/L2/EF) (%) |                |                | Total Trigger Efficiency (%) |
|--|--------------------------------|----------------|----------------|------------------------------|
| $m = 400 \text{ GeV } \rho_T/\omega_T$ | $97.6 \pm 0.1$                 | $98.8 \pm 0.1$ | $99.5 \pm 0.1$ | $96.0 \pm 0.1$               |
| $m = 600 \text{ GeV } \rho_T/\omega_T$ | $98.1 \pm 0.1$                 | $98.5 \pm 0.1$ | $99.2 \pm 0.1$ | $95.9 \pm 0.1$               |
| $m = 800 \text{ GeV } \rho_T/\omega_T$ | $97.6 \pm 0.1$                 | $98.7 \pm 0.1$ | $99.2 \pm 0.1$ | $95.6 \pm 0.1$               |
| $m = 1 \text{ TeV } \rho_T/\omega_T$   | $97.6 \pm 0.1$                 | $98.7 \pm 0.1$ | $99.2 \pm 0.1$ | $95.6 \pm 0.1$               |
| $m = 1 \text{ TeV } Z'_\chi$           | $97.8 \pm 0.1$                 | $98.9 \pm 0.1$ | $99.5 \pm 0.0$ | $96.3 \pm 0.1$               |
| $m = 2 \text{ TeV } Z'_{SSM}$          | $97.6 \pm 0.1$                 | $98.7 \pm 0.1$ | $98.9 \pm 0.1$ | $95.3 \pm 0.2$               |

Table 5: Simulated trigger efficiencies of dimuon resonance samples with respect to offline selection.

### 3.2 Muon Triggers

For the dimuon channel we investigated the trigger efficiency for dimuon events using the single muon 20 GeV  $p_T$  trigger mu20 [18]. Results for the various signal samples are shown in Table 5. Detailed studies on ways to estimate the trigger efficiency were carried out and presented in [19]. It was found that a tag and probe method, similar to the method described for the offline muon reconstruction, could be used to extrapolate  $Z \rightarrow \mu\mu$  results to high  $p_T$ . In addition, efficiencies were obtained using orthogonal triggers, giving a sample which was minimally biased with respect to the muon triggers. It was found in [19] that these estimates agreed with both the tag and probe method and the results from the simulated samples shown here. As can be seen from Table 5 the single muon triggers are highly efficient for any of our signal samples with a total trigger efficiency around 95%.

### 3.3 Triggers for Taus

The  $\tau$  lepton decays to hadronic states in 65% of the cases, and the rest of the time to lighter leptons ( $e$  or  $\mu$ ). In our studies of ditau final states we select events triggered with a single lepton ( $e/\mu$ ) trigger. Thus, we consider two true final states, which we denote  $e\tau_h$  and  $\mu\tau_h$ .

For the  $e\tau_h$  channel we consider two triggers: e22i and e55, as studied in section 3.1. The  $\mu\tau_h$  events are selected using the mu20 trigger already used in section 3.2. Note that the efficiencies shown here are lower than for the dimuon or dielectron channel. This arises because there is only one electron or muon in the final state considered here while in the dielectron or dimuon final state either electron/muon can trigger the event. Table 6 summarizes the trigger efficiencies.

| <i>Signature</i> | Efficiency (L1/L2/EF) (%) |                |                | Total Trigger Efficiency (%) |
|------------------|---------------------------|----------------|----------------|------------------------------|
| e22i             | $85.2 \pm 0.5$            | $89.8 \pm 0.4$ | $90.2 \pm 0.3$ | $69.1 \pm 0.6$               |
| e55              | $90.0 \pm 0.3$            | $74.2 \pm 0.4$ | $78.7 \pm 0.6$ | $52.6 \pm 0.8$               |
| e22i or e55      | $96.7 \pm 0.1$            | $88.7 \pm 0.4$ | $88.9 \pm 0.3$ | $75.5 \pm 0.5$               |
| mu20             | $79.8 \pm 0.6$            | $90.7 \pm 0.4$ | $97.5 \pm 0.4$ | $70.6 \pm 0.5$               |

Table 6: Trigger efficiency for different triggers for  $\tau$  leptons from  $m = 600 \text{ GeV } Z'$  bosons decaying to  $e\tau_h$  and  $\mu\tau_h$  final states with respect to offline selection.

## 4 Standard Model Predictions and Uncertainties

In this section, we investigate the main background sources. We show the clear dominance of the neutral Drell-Yan process. Then we investigate the Standard Model prediction for Drell-Yan production and estimate its uncertainties which will be used in the Exotic searches in the next section.

### 4.1 Background Sources

The neutral Drell-Yan (DY) process constitutes the irreducible background in the search of new heavy dilepton resonances. The dielectron reducible backgrounds result from the production of an electron in the decays of  $W \rightarrow e\nu$  and  $Z \rightarrow ee$  or from the contamination jet $\rightarrow$ electron or photon $\rightarrow$ electron. By combining these effects in the dielectron case, one can list these reducible background sources: inclusive jets, W+jets, W+photon, Z+jets, Z+photon, photon+jet and photon+photon. For a first estimation of these backgrounds, we have used the event generator PYTHIA [20] to compute the differential cross-sections as a function of the invariant mass of the object pair. On the left of Fig. 3 the resulting differential cross-sections for the different backgrounds is shown. Here, the neutral Drell-Yan process is far below most of the backgrounds. For each electron-candidate leg originating from a jet (photon) we apply a rejection factor of  $R_{e-jet} = 10^4$  ( $R_{e-\gamma} = 10$ ). We apply an additional requirement to take into account the geometrical acceptance in which the electrons are identified, i.e.  $|\eta| < 2.5$  and require at least one electron with  $p_T \geq 65$  GeV. Assuming that a photon or a jet faking an electron has a probability of 50% to be assigned a positive or a negative charge, we require the two electron-candidates to have opposite charges. The resulting differential cross-sections are shown on the right of Fig. 3. This figure shows that each contribution is at most 50 times smaller than the neutral Drell-Yan process. By loosening the rejection factor by a factor 2 the sum of all the reducible backgrounds constitutes slightly less than 10% of the neutral Drell-Yan process. Both the transverse momentum and the rapidity requirements play an important role in reducing the QCD-jet background because it is produced mainly in the  $t$ -channel resulting in jets with high rapidities. The top pair,  $WW$ ,  $WZ$  and  $ZZ$  backgrounds are negligible, especially when only their decay channel into two opposite charge electrons is taken into account.

The rejection factors  $\mu$ -jet and  $\mu$ -photon are higher than the ones corresponding to the electrons and the resulting reducible backgrounds are lower. In the following, only the neutral Drell-Yan is considered as a source of backgrounds in the dilepton channel. The ditau case is treated later.

### 4.2 Controlling the Standard Model Drell-Yan Cross-Section

The background estimations in the last section were performed with the PYTHIA event generator which uses tree-level calculations of the cross-sections. The tree-level dilepton cross-sections are subject to large higher order electroweak and QCD corrections. These are known at least to next-to-leading order (NLO) of perturbation theory, not only for the Standard Model Drell-Yan process, but also for a number of new physics processes. They have the additional benefit of reducing the uncertainty induced by the *a priori* unknown renormalization and factorization scales  $\mu_{R,F}$ . In the following, we discuss in detail the various known radiative corrections and the remaining theoretical uncertainties, focusing on the Standard Model Drell-Yan process and the corrections to the tree-level cross-section.

#### 4.2.1 NLO Electroweak Corrections

The electroweak corrections to the Drell-Yan process are known to NLO in the fine-structure constant  $\alpha$  [21, 22]. Initial-state (IS) photon radiation must be factorized into the parton density functions (PDFs), which in principle modifies the DGLAP evolution of quarks and gluons, but has in practice little effect on

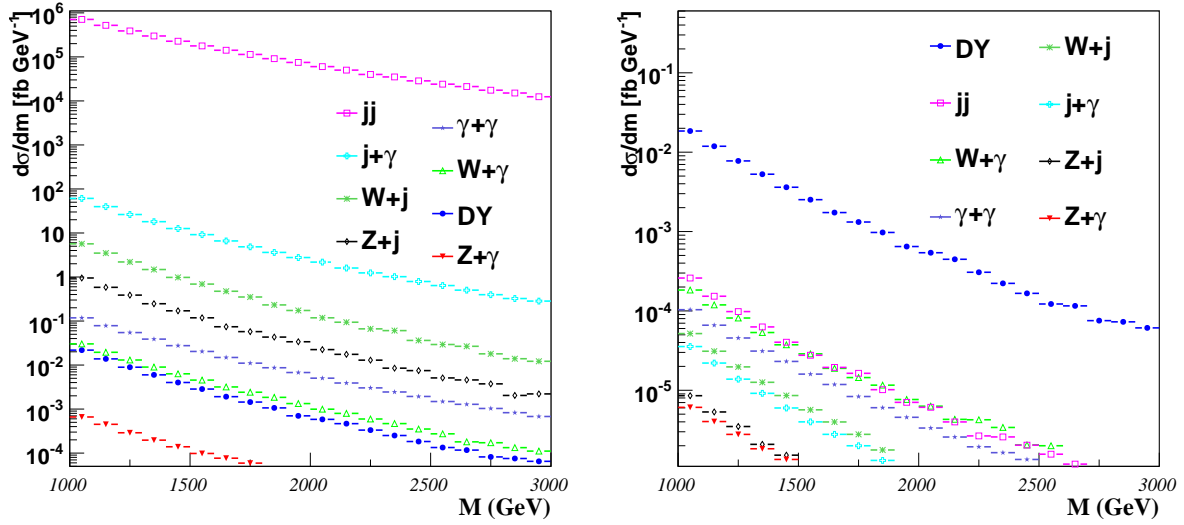


Figure 3: Background contribution to the  $e^+e^-$  invariant mass spectrum: before selection requirements (left) and after selection requirements (right)

the quality of the global fit [23]. Only at very large  $x$  and  $\mu_F^2$  can the correction become of the order of 1%. Multiple IS photon emission can also be resummed, leading to a 0.3% modification of the cross-section [24], or matched to parton showers [25]. The remaining IS QED contributions are also small, whereas the photon radiation emitted by the final state leptons can have a significant impact on their mass ( $M$ ) and transverse momentum spectra as well as the forward-backward asymmetry  $A_{FB}$  [26]. Fortunately, in the vector-boson resonance region(s) these and the universal parts of the weak corrections, which can amount to +80 (+40) % for electron (muon) pairs below and -18 (-10) % above the resonance (see Fig. 4), can be taken into account by using a running value of  $\alpha(M^2)$  or, more generally, effective vector and axial vector couplings in the Effective Born Approximation. While the presence of new physics can modify the running of the weak parameters, the QED corrections remain unaffected. The electroweak corrections coming from non-factorizable box diagrams with double-boson exchange are small in the resonance region(s), but they can be quite large away from the resonance(s) (-4 to -16 % for electron pairs, -12 to -38 % for muon pairs of invariant mass 300 GeV to 2 TeV at the LHC, see Fig. 5).

#### 4.2.2 NLO QCD Corrections

The QCD corrections to the Standard Model Drell-Yan process are known at NLO [27] and next-to-next-to-leading order (NNLO) [28, 29] in the strong coupling constant  $\alpha_s$ . The latter include in principle non-factorisable corrections through  $qq$  and  $gg$  initial states, which remain, however, smaller than 1% in practice, even at small values of  $x$ , where the gluon density is large. The effects of multiple soft-gluon radiation have been resummed simultaneously in the low- $p_T$  and high-mass (around 1 TeV) regions at next-to-leading logarithmic (NLL) accuracy not only for Standard Model Z-bosons [30], but also for  $Z'$  bosons [31], and shown to be in good agreement with the NNLO result as well as the one obtained by matching NLO QCD to parton showers in MC@NLO (see Fig. 6) [31, 32]. In contrast, the matching of tree-level matrix elements to parton showers in PYTHIA [20] requires the *ad hoc* application of a (slightly) mass-dependent correction ( $K$ ) factor and leads to an unsatisfactory description of the  $p_T$  spectrum. For resonant spin-2 graviton production, which involves not only color-triplet quark, but also color-octet gluon initial states, the NLO QCD corrections are substantially larger ( $K \simeq 1.6$ ) than those

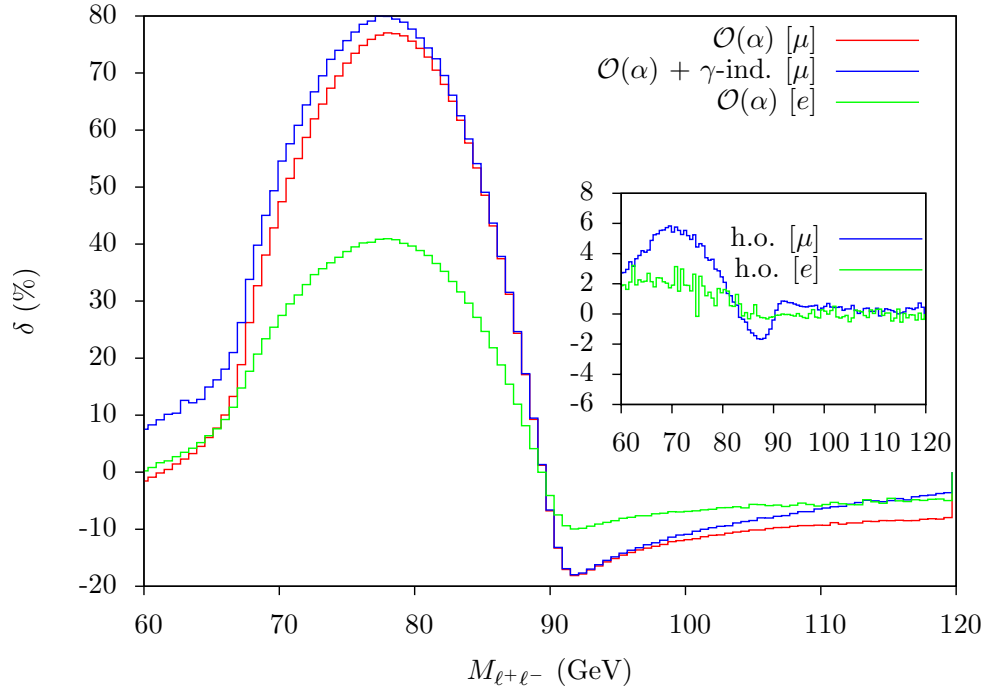


Figure 4: NLO electroweak corrections in the Z-boson resonance region for Standard Model electron and muon pair production at the LHC [25].

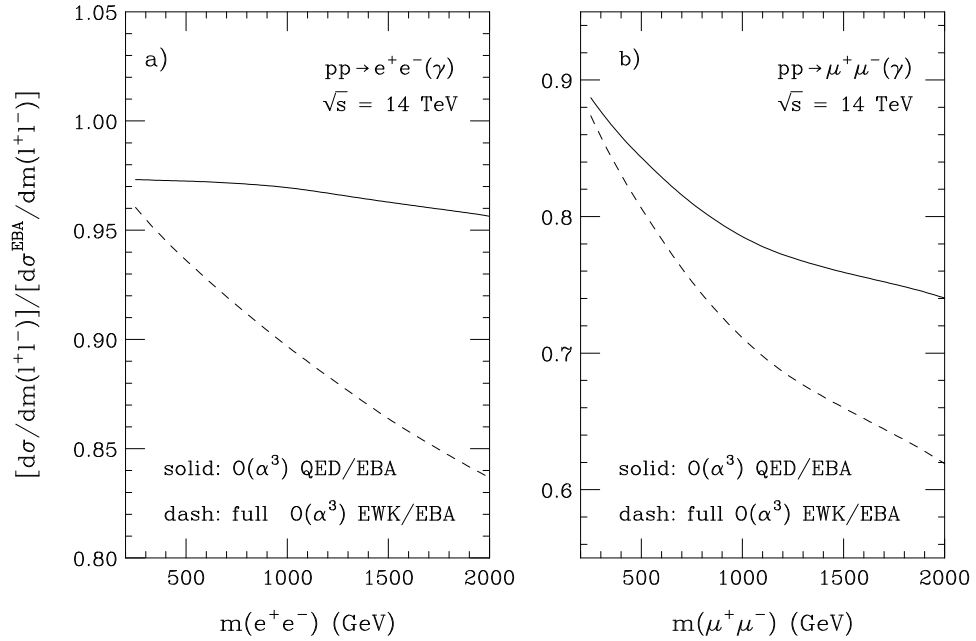


Figure 5: NLO electroweak corrections in the high-mass region for Standard Model electron and muon pair production at the LHC [21].

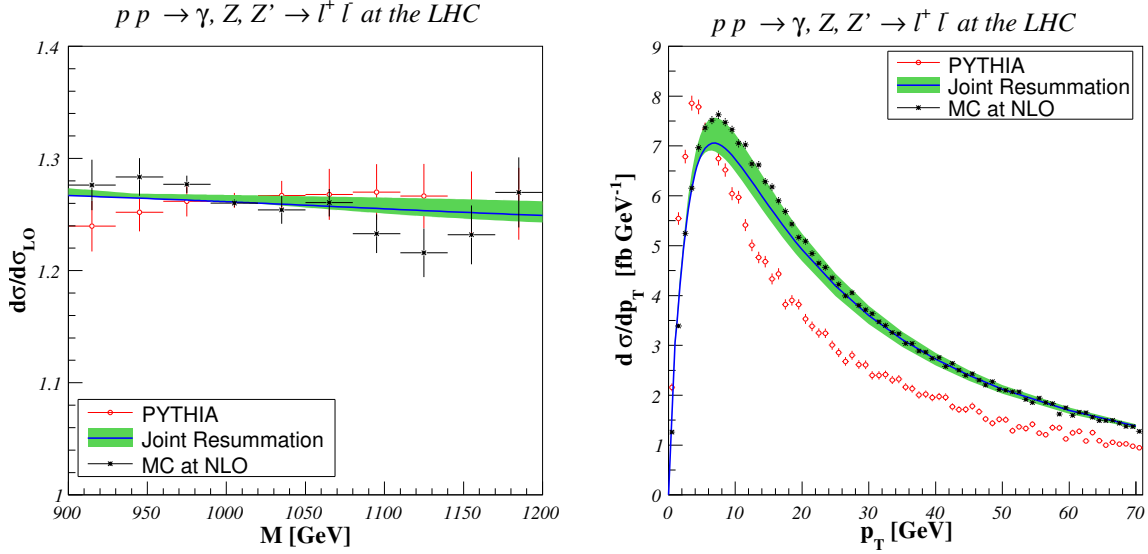


Figure 6: Mass (left) and transverse-momentum (right) spectra in PYTHIA with LO matrix elements matched to QCD parton showers (circles), in MC@NLO with NLO matrix elements matched to the HERWIG QCD parton shower (stars), and after matching the NLO QCD corrections to joint resummation (full line). The mass spectra have been normalized to the LO QCD prediction, and the renormalization and factorization scale uncertainties in the resummed predictions are indicated as shaded bands.

for Standard Model or extra neutral gauge bosons ( $K \simeq 1.26$ ) [33, 34]. In this case, the matching of matrix elements to parton showers has only been performed at the tree-level [35], and resummation has only been performed in the low- $p_T$  region [34].

While the NLO total cross-sections for vector bosons and gravitons still change substantially when the renormalization and factorization scales are varied simultaneously around the resonance mass  $M$  by a factor of two ( $\pm 9\%$ ) [31, 34], the scale uncertainty is reduced to the percent-level at NNLO [28, 29] or, alternatively, to  $+6$  and  $-3\%$  after joint resummation at the NLL order [31].

The theoretical uncertainty coming from different parameterizations of parton densities is estimated in Fig. 7 [31] for invariant masses around 1 TeV. Since the invariant mass of the lepton pair is correlated with the momentum fractions of the partons in the external protons, the normalized mass spectra (left) are indicative of the different shapes of the quark and gluon densities in the CTEQ6M [37] and MRST 2004 NLO [38] parameterizations. The latter also influence the transverse-momentum spectra (right), which are slightly harder for MRST 2004 NLO than for CTEQ6M. The shaded bands show the uncertainty induced by variations, added in quadrature, along the 20 independent directions that span the 90% confidence level of the data sets entering the CTEQ6 global fit [39]. With about  $\pm 5\%$ , the PDF uncertainty is slightly larger than the scale uncertainty, but remains modest [31, 40].

The uncertainty at low transverse momenta coming from non-perturbative effects in the PDFs is usually parameterized with a Gaussian form factor describing the intrinsic transverse momentum of partons in the proton. Three different parameterizations of this form factor have been proposed [41–43]. In all three cases the transverse-momentum distribution is changed by less than  $+3$  and  $-6\%$  for  $p_T > 5$  GeV [31].

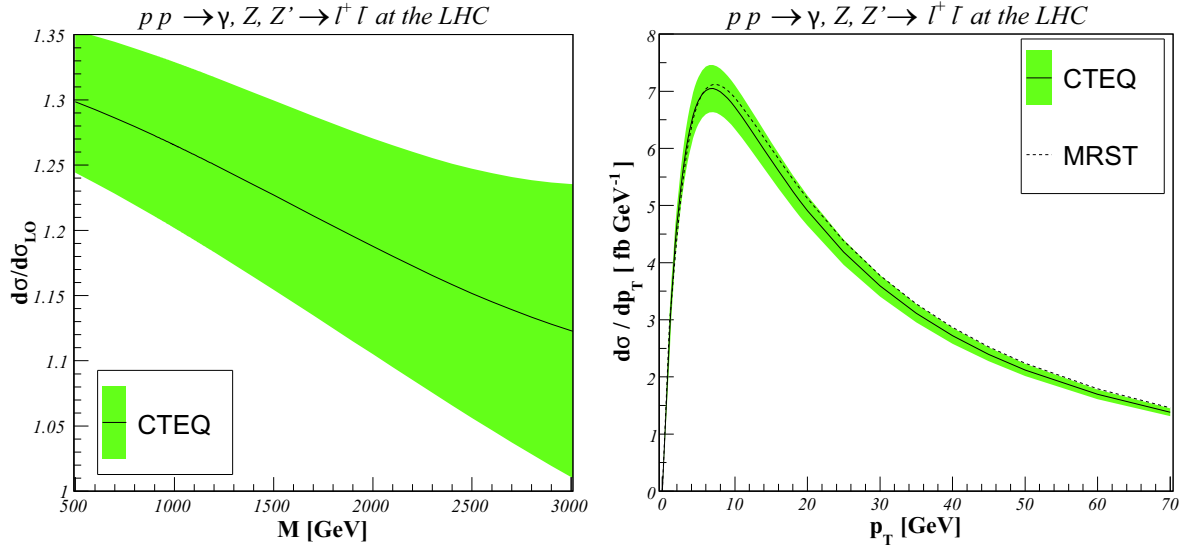


Figure 7: Mass (left) and transverse-momentum (right) spectra after matching the NLO QCD corrections to joint resummation with CTEQ6M (full) and MRST 2004 NLO (dashed) parton densities. The mass spectra have been normalized to the LO QCD prediction using CTEQ6L and MRST 2001 LO [36] parton densities, respectively. The shaded bands indicate the deviations allowed by the up and down variations along the 20 independent directions that span the 90% confidence level of the data sets entering the CTEQ6 global fit.

### 4.3 Effect of Muon Spectrometer Misalignment

At large  $p_T$  ( $\geq 100$  GeV), an important contribution to the muon resolution is the alignment of the muon spectrometer. In the early data period, the resolution is expected to be dominated by the alignment. The ultimate goal of the alignment system is to determine the position the chambers in the muon spectrometer to about 40 microns and  $\sigma_{rot}(mrad) = 0.5\sigma_{trans}(mm)$ .

A detailed study was carried out in order to determine the effect of possible larger uncertainties in the position of the chambers to the  $Z'$  search. For the analysis, we have chosen 7 different hypotheses of misalignment:  $(40\mu m, 20\mu rad)$ , corresponding to the target value of the alignment system,  $(100\mu m, 50\mu rad)$ ,  $(200\mu m, 100\mu rad)$ ,  $(300\mu m, 150\mu rad)$ ,  $(500\mu m, 250\mu rad)$ ,  $(700\mu m, 350\mu rad)$  and  $(1000\mu m, 500\mu rad)$ . In the last two cases, the alignment resolution is of the order of or higher than the track sagitta we want to measure.

As shown in Fig. 8, the dominant effect leading to a wash out of the signal is the resolution loss. The loss of resolution due to misalignment will deteriorate our ability to determine the charge of the muon. This was also studied as a function of the misalignment and is summarized in Table 7.

| Misalignment ( $\mu m$ ) | Nominal | 40    | 100   | 200  | 300   | 500   | 700   | 1000  |
|--------------------------|---------|-------|-------|------|-------|-------|-------|-------|
| Relative efficiency      | 0.984   | 0.984 | 0.984 | 0.98 | 0.973 | 0.948 | 0.918 | 0.877 |

Table 7: Loss in signal efficiency due to the charge misidentification for seven misalignment hypotheses.

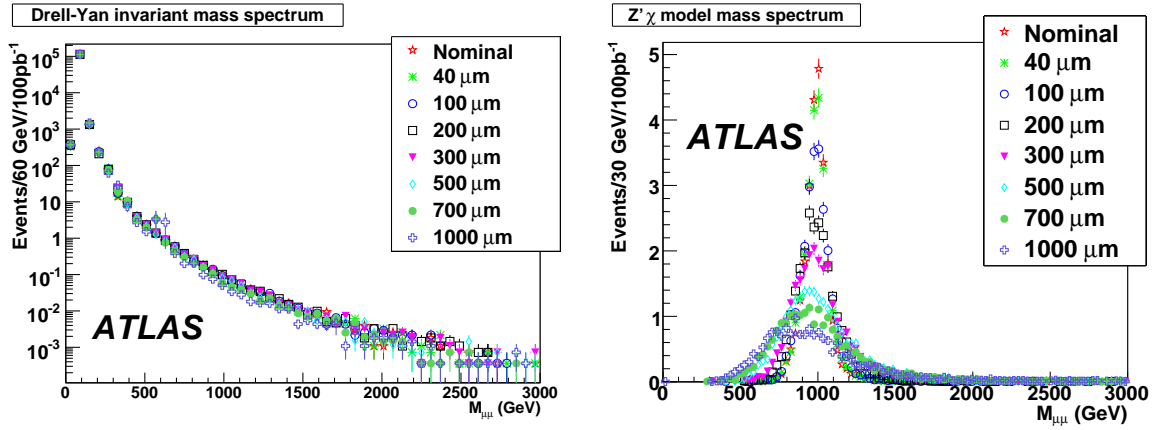


Figure 8: Left: reconstructed invariant mass distribution of Drell-Yan events for different misalignment hypotheses. The numbers corresponds to an integrated luminosity of  $100 \text{ pb}^{-1}$ . Right: reconstructed invariant mass of the  $Z'\chi$  model for the seven misalignment scenarios.

#### 4.4 Summary of Systematic Uncertainties

After implementing the dominant electroweak corrections in the vicinity of heavy resonances through effective couplings [21] and resumming the NLO QCD corrections or matching them to parton showers [31, 32], the remaining theoretical uncertainties on the total  $K$ -factor can be summarized as follows:

- Renormalization/factorization scale:  $^{+6\%}_{-3\%}$
- PDFs:  $\pm 5\%$  at 1 TeV to  $\pm 11\%$  at 3 TeV
- Non-perturbative form factor:  $^{+3\%}_{-6\%}$  (for  $p_T > 5 \text{ GeV}$ ).

Combining these contributions, the total theoretical uncertainty is  $\pm 8.5\%$  at 1 TeV,  $\pm 14\%$  at 3 TeV.

The experimental systematic uncertainties are listed as follows:

- the uncertainty on the efficiency of object identification was assumed to be 5% for muons, 1% for electrons, and 5% for  $\tau$  leptons;
- the uncertainty on the energy scale was assumed to be 1% for muons, 1% for electrons, and 5% for  $\tau$  leptons;
- the uncertainty on the resolution of the objects is as follows:  $\sigma(\frac{1}{p_T}) = \frac{0.011}{p_T} \oplus 0.00017$  for muons, 20 % for electrons, and 45% for  $\tau$  leptons.
- the uncertainty on the luminosity was assumed to be 20% with an integrated luminosity of  $100 \text{ pb}^{-1}$  of data and 3% for  $10 \text{ fb}^{-1}$ .

The effect of all the above on the discovery potential is discussed in the next section for individual channels.



## 5 Search for Exotic Physics

In this section we present the discovery potential for several resonant signatures in the early running with ATLAS. We focus on the reach with an integrated luminosity of up to  $10 \text{ fb}^{-1}$  of data.

The statistical significance of an expected signal can be evaluated in several ways. The simplest approach, “number counting” is based on the expected rate of events for the signal and background processes. From these rates, and assuming Poisson statistics, one can determine the probability that background fluctuations produce a signal-like result according to some estimator; e.g. the likelihood ratio. In the “shape analysis” approach, a detailed knowledge of the expected spectrum of the signal for one observable (like the invariant mass distribution for example) can be used to improve the sensitivity of the search by treating each mass bin as an independent search channel, and combining them accordingly.

The resulting sensitivity is in general higher in the shape analysis than the estimation given in the number counting approach. In the shape analysis, the data is fitted or compared to two models: a background-only model and a signal-plus-background model. These are also called “null hypothesis”, noted  $H_0$  and “test hypothesis”, noted  $H_1$ , respectively. For each of the models, a log-likelihood or a  $\chi^2$  is computed and the ratio of the two log-likelihoods (LLH) or the difference of two  $\chi^2$ s are estimated and used to compute the “confidence levels” noted  $CL_s$ , or significances, noted  $S$ .

The calculation of the significance is done using [44]:

$$S = \sqrt{2} \times \text{Erf}^{-1}\left(1 - \frac{1}{CL_s}\right) \quad \text{with} \quad CL_s = CL_{H1}/CL_{H0} \quad (1)$$

in the *double tail* convention. In this convention,  $1 - CL_b$  has to be lower than  $2.87 \times 10^{-7}$  to correspond to a  $5\sigma$  significance. The input signal and background shapes are given to the fitting algorithms either as histograms in the non-parameterized approach [44] or as functions in the parameterized approach.

A convenient way to compute the LLH ratio is to use the FFT method presented in [45]. The advantage of this method is that it does not require the generation of millions of pseudo-experiments needed for high significances and which can be time consuming. The sources of systematic uncertainties can then be incorporated as nuisance parameters.

The above methods have been investigated for the  $Z'$  boson in the dielectron and ditau channels, for the graviton in the dielectron channel, and for Technicolor in the dimuon channel. These are presented in the following sections.

### 5.1 Background Estimation

As shown in the previous section, the neutral Drell-Yan production of lepton pairs is the common dominant background for all the analyses. The available statistics in the Drell-Yan samples doesn't allow a total freedom in several analyses. Since different techniques are used to estimate the signal significance we also treat the Drell-Yan background in a few different but entirely consistent ways:

- In the “number counting” approach, we simply count the expected number of events under the resonance peak from various background sources, including the Drell-Yan process.
- In the non-parameterized  $CL_s$  method, we use the number and shape of the events by producing a histogram for the background.
- For several analyses, we perform a fit to the Drell-Yan background parameterizing the shape which allows to estimate the number of background events and extrapolate it to higher masses in case of lack of fully simulated events at high masses.

Each of these methods produces a complementary and consistent approach to estimating the background. When the Drell-Yan fit is needed, we parameterized the shape of the background by the formula  $ae^{-bM^c}$ , where  $M$  is the invariant mass of the lepton pair and  $a, b, c$  are parameters of the fit. Fits to the Drell-Yan spectrum presented in section 4.2 suggest that the parameterization  $\exp(-2.2M^{0.3})$  used by [46] describes the background shape well. It is this one which is used in the  $Z' \rightarrow \mu\mu$ ,  $G \rightarrow ee$  and technicolor analyses. In the  $Z' \rightarrow ee$  analysis, these parameters are allowed to vary in the individual ensemble tests. The fit to the entire spectrum letting all the parameters float is consistent with this prescription.

## 5.2 $Z' \rightarrow ee$ Using a Parameterized Fit Approach

### 5.2.1 Event Selection

The selection of events with two electrons coming from a  $Z'$  has been studied in samples of fully simulated  $Z'_\chi \rightarrow e^+e^-$  events with  $Z'$  boson masses of 1, 2 and 3 TeV, corresponding respectively to integrated luminosities of  $21 \text{ fb}^{-1}$ ,  $204 \text{ fb}^{-1}$  and  $2392 \text{ fb}^{-1}$ .

The first requirement is that the two highest  $p_T$  clusters in the event be in the geometrical acceptance. The next requirement is that these clusters be associated with a track; its efficiency is 67% at 1 TeV and decreases for higher masses<sup>3)</sup>. The third requirement is that these two reconstructed electron candidates be identified as *loose* electrons. The relative efficiency of such a selection is at least 94% and increases with invariant mass. The trigger studies have been normalized to events with two *loose* electrons. As shown in section 3.1, the highest trigger efficiency is obtained with a non-isolated single electron trigger (e55). Its efficiency is 90.8% per event. The last requirement is that the two electrons have opposite electric charges. The requirement flow is presented in Table 8, where the events are counted in a window of  $\pm 4 \Gamma_{Z'}$  around the center of the resonance. Although the opposite charge requirement is optional in the absence of a large background, especially at very high invariant mass, it allows to have a control sample (made of same sign dielectrons) for the background. The resulting overall efficiency is 48% at  $m = 1 \text{ TeV}$ , 42% at  $m = 2 \text{ TeV}$  and about 34% at  $m = 3 \text{ TeV}$ .

| Selection                            | Signal<br>at 1 TeV | DY<br>at 1 TeV | Signal<br>at 2 TeV | DY<br>at 2 TeV | Signal<br>at 3 TeV | DY<br>at 3 TeV |
|--------------------------------------|--------------------|----------------|--------------------|----------------|--------------------|----------------|
|                                      | 347.               | 3.56           | 14.7               | 0.16           | 1.22               | 0.015          |
| 2 generated $e^\pm$ , $ \eta  < 2.5$ | 299.               | 3.07           | 13.7               | 0.15           | 1.16               | 0.013          |
| 2 clusters with a track              | 201.               | 2.06           | 8.0                | 0.09           | 0.62               | 0.009          |
| 2 <i>loose</i> electrons             | 190.               | 1.96           | 7.2                | 0.08           | 0.52               | 0.008          |
| At least one $p_T > 65 \text{ GeV}$  | 190.               | 1.96           | 7.2                | 0.08           | 0.52               | 0.008          |
| Event triggered                      | 173.               | 1.77           | 6.6                | 0.07           | 0.47               | 0.007          |
| 2 opposite charges                   | 166.               | 1.70           | 6.2                | 0.07           | 0.43               | 0.007          |

Table 8: Requirement flow table for the  $Z' \rightarrow e^+e^-$  analysis: cross-sections in fb. The events are counted in a window of  $\pm 4 \Gamma_{Z'}$  around the resonance.

The above efficiencies, normalized to events in the geometrical acceptance ( $|\eta| < 2.5$ ), are shown on Fig. 9 (left) as a function of the invariant mass of the electrons. They do not depend on the model used to generate the  $Z'$  samples. Only the requirement that the two electrons be in the geometrical acceptance depend on the model. Indeed, the relative proportions of initial quark flavors depend on the couplings of the  $Z'$  to the quarks. The PDF of the up quarks being harder than that of the down quarks,  $Z'$  produced

<sup>3)</sup>As already stated in section 2.1, the efficiency of this criterion will be improved in future reconstruction versions.

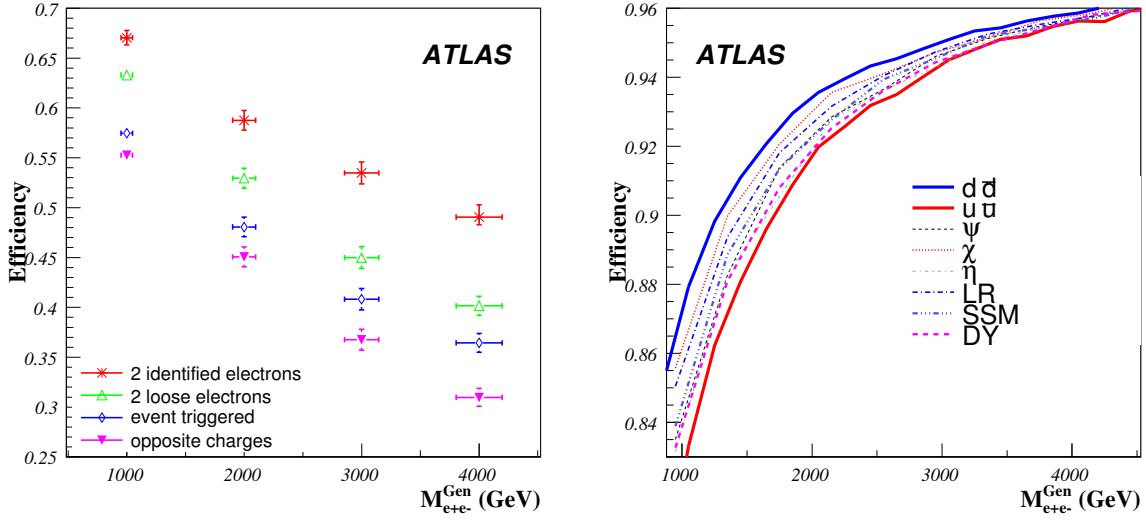


Figure 9:  $Z'_\chi \rightarrow e^+e^-$  selection efficiency as a function of the generated invariant mass. Left: all reconstruction selections, normalized to events in the geometrical acceptance; right:  $|\eta| < 2.5$  criteria for  $u\bar{u}$  and  $d\bar{d}$  events separately and for different  $Z'$  models (generator level).

by a  $u\bar{u}$  pair tend to be slightly more boosted, and therefore the electrons stemming from their decay tend to be produced at slightly higher pseudo-rapidities. This effect is visible in Fig. 9 (right) showing the efficiency of the  $|\eta|$  selection for  $u\bar{u}$  and  $d\bar{d}$  events separately, and for a number of benchmark  $Z'$  models: the Sequential Standard Model ( $Z'_{SSM}$ ), the  $E_6$  models  $Z'_\psi$ ,  $Z'_\chi$ ,  $Z'_\eta$ , and the left-right symmetric model ( $Z'_{LR}$ ). It is therefore possible to generalize the efficiencies that have been measured in the fully simulated samples to models which haven't been simulated as well as to intermediate masses.

## 5.2.2 Discovery Potential

**Modelization of the dilepton invariant mass spectrum.** In order to compute the significance for several  $Z'$  models, a parameterization of the mass spectrum of the signal and of the background has been used. The differential cross-section can be factorized with a good precision in a parton-level term  $\frac{d\hat{\sigma}}{dm}$  and a PDF-dependent term  $G_{PDF}(m)$ :

$$\frac{d\sigma}{dm}(m) = \frac{d\hat{\sigma}}{dm}(m) \times G_{PDF}(m) \quad (2)$$

Using this factorization, one can write:

$$\left. \frac{d\sigma}{dm} \right|_{\text{DY}}(m) = \frac{1}{m^2} \times G_{PDF}(m) \quad (3)$$

$$\begin{aligned} \left. \frac{d\sigma}{dm} \right|_{\text{Signal}}(m) &= \frac{1}{m^2} \times G_{PDF}(m) \\ &+ \mathcal{A}_{\text{peak}} \times \frac{\Gamma_{Z'}^2}{m_{Z'}^2} \frac{m^2}{(m^2 - m_{Z'}^2)^2 + m_{Z'}^2 \Gamma_{Z'}^2} \times G_{PDF}(m) \\ &+ \mathcal{A}_{\text{interf}} \times \frac{\Gamma_{Z'}^2}{m_{Z'}^2} \frac{m^2 - m_{Z'}^2}{(m^2 - m_{Z'}^2)^2 + m_{Z'}^2 \Gamma_{Z'}^2} \times G_{PDF}(m) \end{aligned} \quad (4)$$

where  $\mathcal{A}_{\text{peak}}$  is the amplitude of the  $Z'$  process and  $\mathcal{A}_{\text{interf}}$  is the amplitude of the interference  $Z'/Z$  and  $Z'/\gamma$ , both normalized to the Drell-Yan process. This parameterization only depends on four parameters:  $m_{Z'}$ ,  $\Gamma_{Z'}$ ,  $\mathcal{A}_{\text{peak}}$  and  $\mathcal{A}_{\text{interf}}$ . The differential cross-section is then multiplied by the appropriate  $K$ -factor (see section 4.2). The detector performance is accounted for as follows: the differential cross-section is multiplied by the efficiency computed above and convoluted by the invariant mass resolution (see section 2.1). The agreement between this parameterization and the full simulation is shown in Fig. 10 for a  $Z'_\chi$  at 1 TeV.

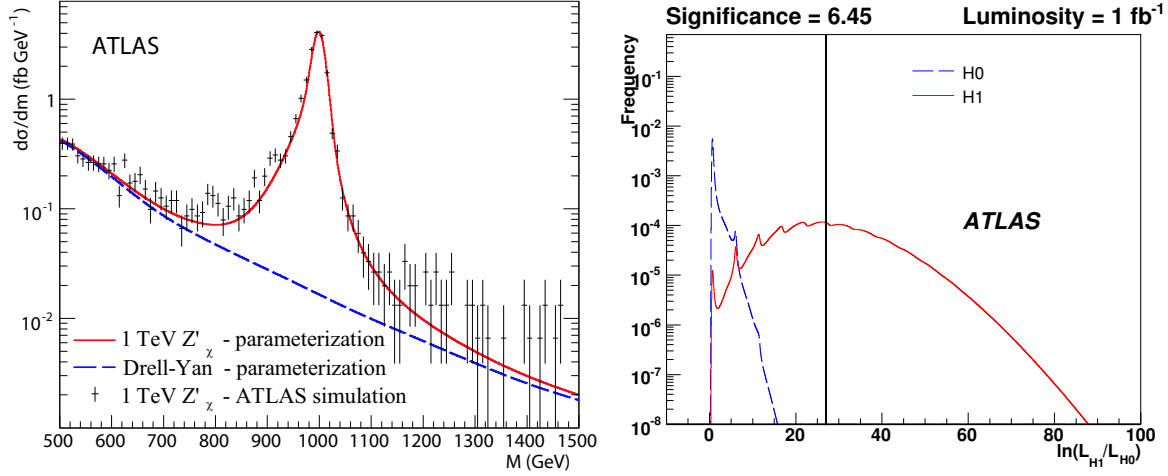


Figure 10: Left: mass spectrum for a  $m = 1 \text{ TeV } Z'_\chi \rightarrow e^+e^-$  obtained with ATLAS full simulation (histogram) and the parameterization (solid line). The dashed line corresponds to the parameterization of the Drell-Yan process (irreducible background). Right: Log-likelihood ratio densities with  $1 \text{ fb}^{-1}$  for a  $m = 2 \text{ TeV } Z'_\chi$  for the signal and background hypotheses. The vertical line is the median experiment in the H1 hypothesis.

**Results** Using the parameterization presented above to generate mass spectra for signal ( $\gamma/Z/Z' \rightarrow e^+e^-$ ) and background ( $\gamma/Z \rightarrow e^+e^-$ ), one can compute the distributions of the log-likelihood ratio (LLH) of the signal (H1) and background (H0) hypotheses.

Figure 10 shows the LLH distributions obtained for a  $2 \text{ TeV } Z'_\chi$  with  $1 \text{ fb}^{-1}$  as well as the median signal experiment used to calculate  $CL_s$ . The Fast Fourier Transform method (FFT) [45] was used in the computation of the LLH distributions. It is important to note that the mass window used to perform the analysis does not affect the result.

Figure 11 (left) shows the integrated luminosity needed for  $5\sigma$  discovery of the usual benchmark  $Z'$  models as a function of the  $Z'$  mass. Only statistical uncertainties were taken into account. The systematic uncertainties are discussed in the next paragraph. A fixed mass window of  $[500 \text{ GeV} - 4 \text{ TeV}]$  was used to compute the significance. Roughly speaking, less than  $100 \text{ pb}^{-1}$  are needed to discover a  $1 \text{ TeV } Z'$ , about  $1 \text{ fb}^{-1}$  are needed to discover a  $2 \text{ TeV } Z'$ , and about  $10 \text{ fb}^{-1}$  are needed to discover a  $3 \text{ TeV } Z'$ .

**Systematic Uncertainties** The sources of systematic uncertainties were listed in section 4. Since the main background is the Drell-Yan process, the systematic uncertainties from both the efficiencies and the theoretical predictions on the cross-section will affect the number of signal and background events in the same way, and can be added in quadrature. The uncertainties on the event selection efficiency

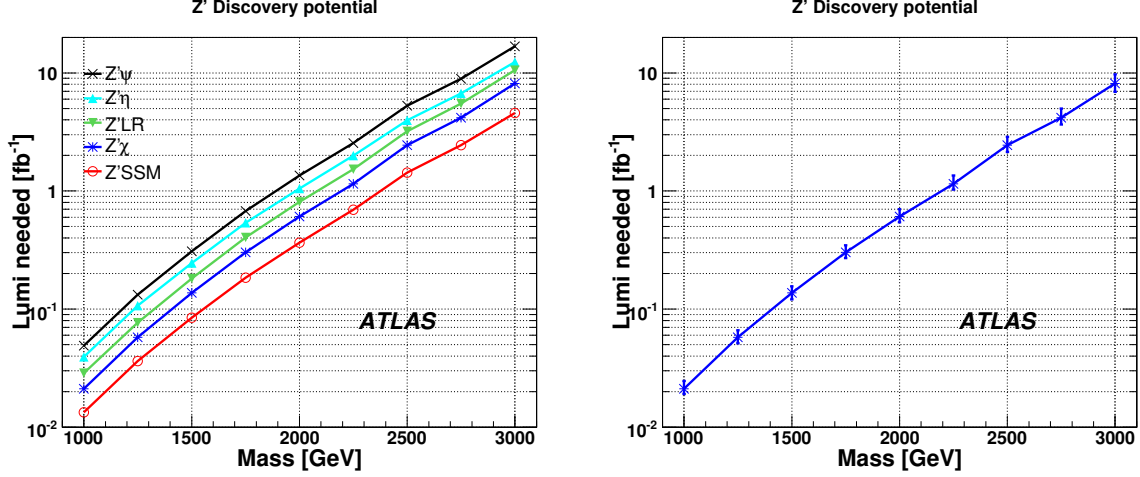


Figure 11: Integrated luminosity needed for a  $5\sigma$  discovery of  $Z' \rightarrow e^+e^-$  as a function of the  $Z'$  mass. Left: for various benchmark models with statistical uncertainties only; right: for the  $Z'_\chi$  with systematic uncertainties included.

mainly come from the electron identification and the geometrical acceptance. The former amounts to  $2 \times \pm 1\% = \pm 2\%$  for two electrons. Taking the extreme efficiencies for pure  $u\bar{u}$  and  $d\bar{d}$  events as a conservative estimate, the latter goes from  $\pm 3$  to  $\pm 0.5\%$ . Overall, this represents from  $\pm 3.6\%$  to  $\pm 0.6\%$  systematic uncertainty from the event selection. This is small as compared to the theoretical uncertainties, which represent  $\pm 8.5\%$  to  $^{+14}_{-12}\%$ . The effect of these combined uncertainties on the luminosity needed to discover 1, 2 and 3 TeV  $Z'$ s is  $^{+9}_{-10}\%$ ,  $^{+14}_{-10}\%$ ,  $^{+15}_{-13}\%$  (respectively).

The uncertainty on backgrounds other than the Drell-Yan process is another type of uncertainty. However, given that the Drell-Yan contribution is at the level of about 1% of the signal, any variation of the level of non-Drell-Yan background, which is more than ten times smaller, is negligible.

The uncertainty on the electron energy resolution is another type of uncertainty. In addition to the expected uncertainties on the energy resolution as measured in the calorimeter (see section 4), we have conservatively assumed that there was no increase in precision on the measured dielectron invariant mass coming from the angle measurement provided by the tracker. In this case, the resolution on the invariant mass increases from about 1% (see section 2.1) to about 1.5%. The effect of these uncertainties on the luminosity needed for a discovery is  $^{+5}_{-2}\%$  from the resolution, independent of the  $Z'$  mass.

The last type of uncertainty which has been considered is the electron energy scale. When varied within the expected uncertainties, the discovery luminosity varies by  $^{+2.5}_{-0}\%$ , independent of the  $Z'$  mass.

Combining all the above systematic uncertainties, the luminosity needed to discover, for example, a  $Z'_\chi$  is shown in Fig. 11 (right). It must be noted that the systematic effect coming from the fact that we do not know a priori the mass of the signal was not taken into account. This is addressed separately in appendix A.

### 5.3 $Z' \rightarrow \mu\mu$ Using a Parameterized Fit Approach

The dimuon channel represents an important complement to the dielectron channel. Although the resolution is expected to be up to an order of magnitude worse in the kinematic regime of interest, reducible backgrounds are expected to be considerably lower as discussed in Section 4.1. This feature makes the dimuon channel competitive especially with early data where the design background rejections may not be achieved. In this section we consider two signal models decaying into dimuons - the  $Z'_{\text{SSM}}$  and  $Z'_\chi$

424 bosons.

### 425 5.3.1 Event Selection

426 To select events from the  $Z' \rightarrow \mu\mu$  process we require two muons of opposite charge. The muons are  
 427 required to fulfill the muon identification criteria studied in Section 2.2, including  $p_T \geq 30$  GeV and  
 428  $|\eta| \leq 2.5$ . Events are triggered using the mu20 trigger described in Section 3.2. As seen in Section 4.1,  
 429 this should select a sample which consists mainly of  $Z/\gamma \rightarrow \mu\mu$  with limited contamination from other  
 430 sources of the order of a few percent. Table 9 indicates the effects of the various requirements on both  
 431 the signal and background samples.

| Sample              | $Z'_{SSM}$ (1 TeV) | $Z'_\chi$ (1 TeV) | Drell-Yan |
|---------------------|--------------------|-------------------|-----------|
| Generated           | 508.6              | 380.6             | 13.5      |
| $ \eta  \leq 2.5$   | 366.8              | 271.5             | 10.8      |
| $p_T \geq 30$ GeV   | 364.0              | 270.1             | 10.7      |
| Muon identification | 342.3              | 256.0             | 10.0      |
| Trigger             | 325.2              | 243.2             | 9.5       |
| Opposite charge     | 324.8              | 243.0             | 9.5       |

Table 9: Selection requirement flow for the  $Z' \rightarrow \mu\mu$  analysis - cross-sections in fb. Events are counted in a mass window of  $\pm 50$  GeV of the resonance mass (signal) and for  $m_{\mu\mu} > 800$  GeV (background).

### 432 5.3.2 Discovery Potential

433 To evaluate the discovery potential, we use the FFT method [45], as in section 5.2. The amount of  
 434 data required to discover a  $Z'$  boson is computed from the log-likelihood ratio (LLH) of the signal (H1)  
 435 and background (H0) hypotheses. Figure 12 shows the  $1 - CL_b$  obtained as a function of the integrated  
 436 luminosity for the two studied  $Z'$  boson models at  $m = 1$  TeV. The largest expected systematic uncertainty  
 437 (from misalignment of the muon spectrometer) is shown separately. One can see that the amount of  
 438 luminosity needed for a  $5\sigma$  discovery ranges from 20 to 40  $\text{pb}^{-1}$ , which is competitive with the dielectron  
 439 channel.

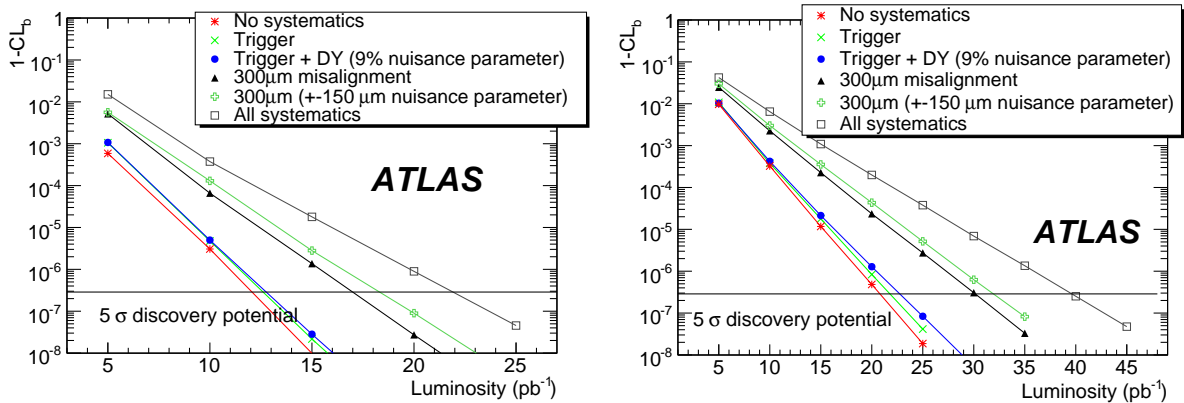


Figure 12: Results of the FFT computation of  $1 - CL_b$  for  $m = 1$  TeV  $Z'_{SSM}$  (left) and  $Z'_\chi$  (right) bosons. The horizontal line indicates the  $1 - CL_b$  value corresponding to  $5\sigma$ .

**Systematic Uncertainties** Section 4 describes the systematic uncertainties that were considered. As can be seen from Fig. 12 the effect of the nominal systematic uncertainties is modest in this channel. The largest theoretical uncertainty entering this study is the knowledge of the Standard Model Drell-Yan cross-section. In the dimuon channel, the largest experimental uncertainty is the resolution for high  $p_T$  muons which will be initially dominated by the alignment of the muon spectrometer. As already discussed, the nominal alignment precision may not be achievable with the integrated luminosities presented here and hence could significantly alter the conclusions. Figure 12 shows that the integrated luminosity needed to reach  $5\sigma$  increases from 13 to 20  $\text{pb}^{-1}$  if the muon spectrometer is aligned with a precision of  $300\text{ }\mu\text{m}$ . This takes into account an uncertainty of  $150\text{ }\mu\text{m}$  on the alignment precision estimate, which will have to be measured in data (e.g. from the  $Z \rightarrow \mu\mu$  sample) and which is treated as a nuisance parameter in the sensitivity computation.

## 5.4 $Z' \rightarrow \tau\tau$ Using a Number Counting Approach

The ditau signature is an important component to the high mass resonance search. In particular, there are models in which a hypothetical new resonance couples preferentially to the third generation [47]. For these models the branching ratios are such that the dielectron and dimuon channels are not viable - hence it is critical that we consider all possible channels including ditaus. In this section we discuss the discovery potential for such a resonance. Because of finite resources we restrict ourselves to the process  $Z' \rightarrow \tau\tau$  with a single mass point  $m = 600\text{ GeV}$  although much of the discussion generalizes to a generic ditau resonance search. The ditau final state can be divided into three final states: hadron-hadron (where both  $\tau$  leptons decay hadronically), hadron-lepton (where one  $\tau$  lepton decays hadronically and one decays leptonically), and lepton-lepton (where both decay leptonically). Here we consider the hadron-lepton ( $h - \ell$ ) final state. The possibility of observing the hadron-hadron final state using a hadronic  $\tau$  trigger will be examined later.

### 5.4.1 Event Selection

To select events in the hadron-lepton final state, we select events with a “hadronic  $\tau$ ” candidate, a charged lepton (muon or electron), and missing transverse energy ( $\cancel{E}_T$ ). As opposed to the dielectron or dimuon channel the backgrounds to the ditau channel are considerably larger and include Drell-Yan production,  $W$ +jets,  $t\bar{t}$  and dijet events. After the initial object selection several further requirements are needed to maximize the signal significance.

We consider hadronic  $\tau$  candidates with  $p_T > 60\text{ GeV}$  and impose a requirement on the likelihood as a function the  $\tau$  transverse energy as described in Section 2.3. To avoid double counting we remove candidates which overlap with an electron or muon.

For electron candidates we require a *medium* electron in this analysis (see Section 2.1). The initial muon selection is the same as described in Section 2.2. Since this channel only requires one high  $p_T$  lepton the backgrounds are considerably higher than for the dielectron or dimuon final states. To address this we make additional requirements on the isolation of the lepton. The isolation requirement imposed on electron candidates is  $\sum E_{T_{EM}}^{\Delta R < 0.2} / p_T < 0.1$  where  $\sum E_{T_{EM}}^{\Delta R < 0.2}$  is the sum of the energy deposits in the electromagnetic calorimeter within a cone of  $\Delta R = 0.2$  from the location in  $\eta$ - $\phi$  of the electron, less the electron candidate energy. Isolated electrons are required to have  $p_T > 27\text{ GeV}$ . We impose an isolation requirement similar to that of electrons on muon candidates:  $\sum E_{T_{EM}}^{\Delta R < 0.2} < 0.1$ . For isolated muons we require that the  $\chi^2$  lie between 0 and 20 and to be considered by the analysis muons must have  $p_T > 22\text{ GeV}$ .

After making the  $\tau$  candidate selection we make several further requirements to maximize the signal significance. First we require that  $\cancel{E}_T \geq 30\text{ GeV}$ . To greatly help with the rejection of the  $t\bar{t}$  backgrounds

| Selection                        | Signal | $t\bar{t}$ | Drell-Yan           | Multijet             | W+jet                |
|----------------------------------|--------|------------|---------------------|----------------------|----------------------|
| Trigger                          | 1356.  | 213600.    | $2.3950 \cdot 10^7$ | $4.19000 \cdot 10^6$ | $6.69400 \cdot 10^6$ |
| Lepton                           | 905.   | 150900.    | $1.2600 \cdot 10^7$ | $1.08230 \cdot 10^6$ | 120400.              |
| $\tau$ selection                 | 368.   | 7818.      | 145680              | 40080                | 4587.                |
| Opposite charge                  | 315.   | 2498.      | 5306                | 23240                | 771.                 |
| $\cancel{E}_T > 30$ GeV          | 270.   | 2040.      | 2562                | 835                  | 162.                 |
| $m_T < 35$ GeV                   | 203.2  | 302.4      | 388.0               | 436.4                | 83.8                 |
| $p_T^{tot} < 70$ GeV             | 155.0  | 106.7      | 331.5               | 221.6                | 28.4                 |
| $m_{vis} > 300$ GeV              | 132.5  | 26.2       | 105.6               | 33.8                 | 15.0                 |
| $\cos\Delta\phi_{\ell h} > -.99$ | 13.3   | 2.1        | 5.5                 | 2.3                  | 2.7                  |

Table 10: Requirement flow table for the  $m = 600$  GeV  $Z'_{SSM} \rightarrow \tau\tau \rightarrow \ell h$  analysis - cross-sections given in fb. The Drell-Yan process includes all flavors of leptons ( $e^+e^-$ ,  $\mu^+\mu^-$ ,  $\tau^+\tau^-$ ) with an invariant mass of at least 60 GeV.

we employ a requirement on the total event  $p_T$  which is defined as the sum of  $\cancel{E}_T$  and the vector sum of the hadronic  $\tau$  with the lepton transverse momentum. We require  $p_T^{tot} < 70$  GeV.

The transverse mass of the event is determined by using the lepton kinematics and the event  $\cancel{E}_T$ . Defining a four-vector for the missing energy:  $\cancel{p}_T = (\cancel{E}_{Tx}, \cancel{E}_{Ty}, 0, |\cancel{E}_T|)$ , the transverse mass is calculated as:

$$m_T = \sqrt{2p_{T,\ell}\cancel{p}_T(1 - \cos\Delta\phi_{\ell,\cancel{p}_T})}.$$

We require that  $m_T < 35$  GeV.

In the case of the lepton-hadron channel one cannot simply reconstruct the invariant mass of the resonance as energy is taken away from the event by the neutrinos. However, two quantities can be constructed

- A visible mass variable is calculated as defined by CDF [48] using the hadronic  $\tau$  and the lepton four-vector information:

$$m_{vis} = \sqrt{(\underline{p}_\ell + \underline{p}_h + \underline{\cancel{p}}_T)^2}$$

- The collinear approximation is used to build up the event-by-event invariant mass. The fraction of the  $\tau$  momentum carried by the visible decay daughters,  $x_\ell$  and  $x_h$ , are calculated with the following formulas:

$$x_\ell = \frac{p_{x,\ell}p_{y,h} - p_{x,h}p_{y,\ell}}{p_{y,h}p_{x,\ell} + p_{y,h}\cancel{p}_x - p_{x,h}p_{y,\ell} - p_{x,h}\cancel{p}_y}, \quad x_h = \frac{p_{x,\ell}p_{y,h} - p_{x,h}p_{y,\ell}}{p_{y,h}p_{x,\ell} + p_{x,\ell}\cancel{p}_y - p_{x,h}p_{y,\ell} - p_{y,\ell}\cancel{p}_x}.$$

The reconstructed mass is then calculated as  $m_{\tau\tau} = \frac{m_{\ell,h}}{\sqrt{x_\ell x_h}}$ .

To greatly help the background rejection and to restrict our search to the region of interest we require  $m_{vis} > 300$  GeV. Since the collinear approximation breaks down when the two  $\tau$  leptons are back-to-back, we impose the requirement that  $\cos\Delta\phi_{\ell h} > -.99$ . Of course, since a very heavy particle tends to be produced at rest, the decay objects are mostly back-to-back, leading to a highly inefficient mass reconstruction.

#### 5.4.2 Discovery Potential for $1 \text{ fb}^{-1}$ of Data

Table 10 shows the effect of the various selection requirements for the signal as well as all background processes considered. Distributions of the visible and reconstructed masses for signal and background



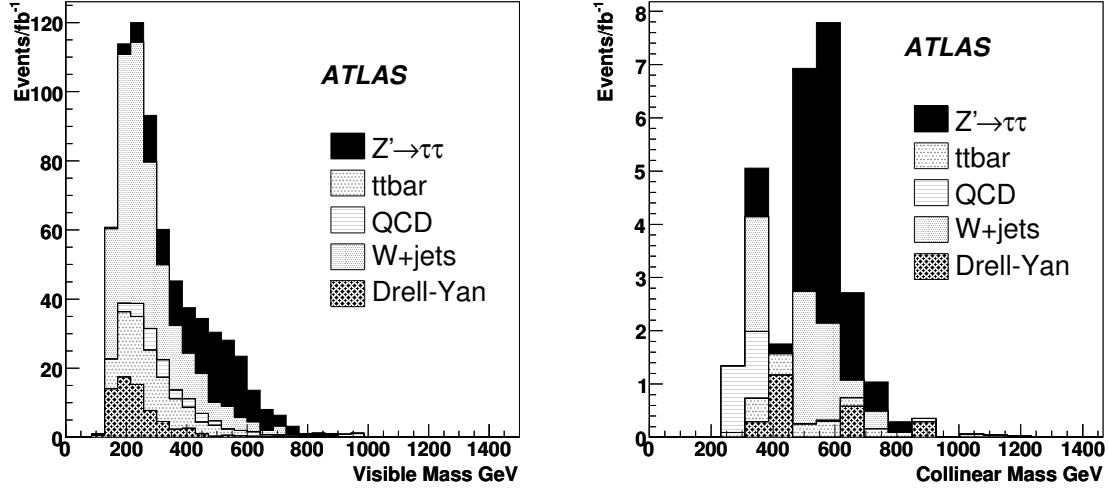


Figure 13: Left: the visible mass distribution in the  $Z' \rightarrow \tau\tau \rightarrow \ell h$  analysis for signal and background processes ( $1 \text{ fb}^{-1}$  of data is assumed). Right: the reconstructed invariant mass obtained using the collinear approximation.

are shown in Fig. 13. Here we assume a 600 GeV  $Z'$  and the SSM cross-section. In  $1 \text{ fb}^{-1}$  of ATLAS data we estimate 132.5 signal events and 180.6 background events after imposing the event selection up to the requirement on visible mass. Using  $S/\sqrt{B}$  we estimate the signal significance to be 9.9. The collinear approximation breaks down when the two  $\tau$  leptons are back-to-back, so that even a loose requirement (such as  $\cos\Delta\phi_{\ell h} > -.99$ ) reduces the signal by a large factor. Hence, we expect that the search will proceed by looking at the visible mass. If significant excess over background is seen, the collinear approximation will then be used to help establish the presence of a new resonance.

**Systematic uncertainties** The systematic uncertainties that were considered are described in Section 4. For an analysis of  $1 \text{ fb}^{-1}$  of data the dominant systematic source on the signal, just over  $\pm 18\%$ , comes from the uncertainty in the luminosity. The second most dominant systematic, the hadronic  $\tau$  energy scale, affects the signal at the  $\pm 10\%$  level. Summing in quadrature the effect of all systematic uncertainties on the signal Monte Carlo sample results in a total systematic uncertainty of about  $\pm 20\%$ . The current Monte Carlo samples available for the backgrounds to the ditau analysis are statistically limited and hence prevent a rigorous evaluation of the systematics at this time. As a conservative estimate, we assume that the total systematic uncertainty on the backgrounds is identical to that observed in the signal Monte Carlo. This is a conservative estimate because the majority of the backgrounds in the data have very large cross-sections (dijets, W+jets, etc.) and in principle the evaluation of systematic uncertainties there should be less sensitive to statistical fluctuations than for the signal events. Summing these systematic uncertainties in quadrature and using the formula  $S/\sqrt{B + \delta B^2}$  gives a significance of 3.4 in  $1 \text{ fb}^{-1}$ .

## 5.5 $G \rightarrow e^+e^-$ in a Parameterized Fit Approach

In this section we present a sensitivity study for the Randall-Sundrum  $G \rightarrow ee$  final state. In this channel, it is assumed that there is no interference between the  $G$  and the dilepton background. Table 11 shows the parameters of the different  $G$  samples used in this analysis.  $\Gamma_G$  is the simulated graviton resonance width and  $\sigma_m$  stands for the width of the observed resonance after convolution with detector resolutions.

524 For  $k/\bar{M}_{pl} < 0.06$  the resonance is narrow compared to the experimental resolution.

525 The main Standard Model background is neutral Drell-Yan production. Other backgrounds such as  
 526 dijets with both jets misidentified as electrons are expected to be small and neglected at this time.

| Model Parameters |                  | $\Gamma_G$ | $\sigma_m$ | $\sigma \cdot BR(G \rightarrow e^+e^-)$ |
|------------------|------------------|------------|------------|---|
| $m_G$            | $k/\bar{M}_{pl}$ | [GeV]      | [GeV]      | [fb]                                    |
| 500 GeV          | 0.01             | 0.08       | 4.6        | 187.4                                   |
| 750 GeV          | 0.01             | 0.10       | 6.4        | 27.7                                    |
| 1.0 TeV          | 0.02             | 0.57       | 7.9        | 26.0                                    |
| 1.2 TeV          | 0.03             | 1.62       | 10.3       | 22.4                                    |
| 1.3 TeV          | 0.04             | 2.98       | 11.4       | 25.3                                    |
| 1.4 TeV          | 0.05             | 5.02       | 13.1       | 26.8                                    |

Table 11: Parameters of the  $G \rightarrow ee$  samples used: natural width ( $\Gamma_G$ ), Gaussian width after detector effects ( $\sigma_m$ ) and leading order cross-section.

### 527 5.5.1 Event Selection

528 In reconstructing the resonance mass, we require a pair of electrons – we do not make any charge re-  
 529 quirements – with  $p_T \geq 65$  GeV using the *loose* electron selection criteria described in Section 2.1. We  
 530 require that the events pass the e55 single electron trigger (see section 3.1). Finally we require that  
 531 the two electrons are roughly back-to-back in  $\phi$  with  $\cos\Delta\phi_{ee} < 0$  between the two electrons. Table 12  
 532 shows the remaining cross-section at each stage of the selection and the total efficiency for different mass  
 533 points. The efficiency decreases at high graviton masses, due to the track match requirement, which is  
 534 consistent with the  $Z'$  boson analysis (see section 5.2). Table 13 shows the same requirement flow for  
 535 the Drell-Yan.

| Selection / Sample        | 500 GeV        | 750 GeV        | 1.0 TeV        | 1.2 TeV        | 1.3 TeV        | 1.4 TeV        |
|---------------------------|----------------|----------------|----------------|----------------|----------------|----------------|
| Generated                 | 187.4          | 27.7           | 26.0           | 22.4           | 25.3           | 26.8           |
| Acceptance                | 172.4          | 25.9           | 24.7           | 21.2           | 24.0           | 25.4           |
| Trigger                   | 168.7          | 25.0           | 22.6           | 19.1           | 21.4           | 22.3           |
| Electron Id.              | 127.9          | 18.3           | 16.4           | 12.8           | 14.6           | 14.7           |
| $p_T \geq 65$ GeV         | 125.7          | 18.2           | 16.3           | 12.7           | 14.5           | 14.6           |
| $\cos\Delta\phi_{ee} < 0$ | 123.0          | 17.8           | 16.0           | 12.6           | 14.3           | 14.4           |
| Selection efficiency (%)  | $65.6 \pm 1.1$ | $64.4 \pm 1.1$ | $61.7 \pm 1.1$ | $56.3 \pm 1.1$ | $56.4 \pm 1.1$ | $53.9 \pm 1.1$ |

Table 12: Requirement flow for the  $G \rightarrow ee$  analysis. The remaining cross-section (in fb) is given at each stage. The mass window is chosen as  $\pm 4\sigma_m$  around the signal peak.

| Selection/Sample          | 500 GeV | 750 GeV | 1.0 TeV | 1.2 TeV | 1.3 TeV | 1.4 TeV |
|---------------------------|---------|---------|---------|---------|---------|---------|
| Generated                 | 20.33   | 4.91    | 1.43    | 0.90    | 0.51    | 0.51    |
| Acceptance                | 18.53   | 4.50    | 1.36    | 0.87    | 0.48    | 0.49    |
| Trigger                   | 18.45   | 4.25    | 1.16    | 0.80    | 0.45    | 0.44    |
| Electron Id.              | 14.13   | 3.18    | 0.88    | 0.58    | 0.38    | 0.33    |
| $p_T \geq 65$ GeV         | 13.85   | 3.15    | 0.88    | 0.57    | 0.38    | 0.33    |
| $\cos\Delta\phi_{ee} < 0$ | 13.41   | 3.09    | 0.85    | 0.56    | 0.36    | 0.33    |

Table 13: Remaining Drell-Yan cross-section (in fb) at each stage of the  $G \rightarrow ee$  analysis. The mass window is chosen as  $\pm 4\sigma_m$  around the signal peak.

The Drell-Yan background distribution after this event selection is shown in Fig. 14 along with signal at  $m_G = 1$  TeV and coupling  $k/\bar{M}_{pl} = 0.02$ . The exponential described in Section 5.1 has been used to model the shape of the background.

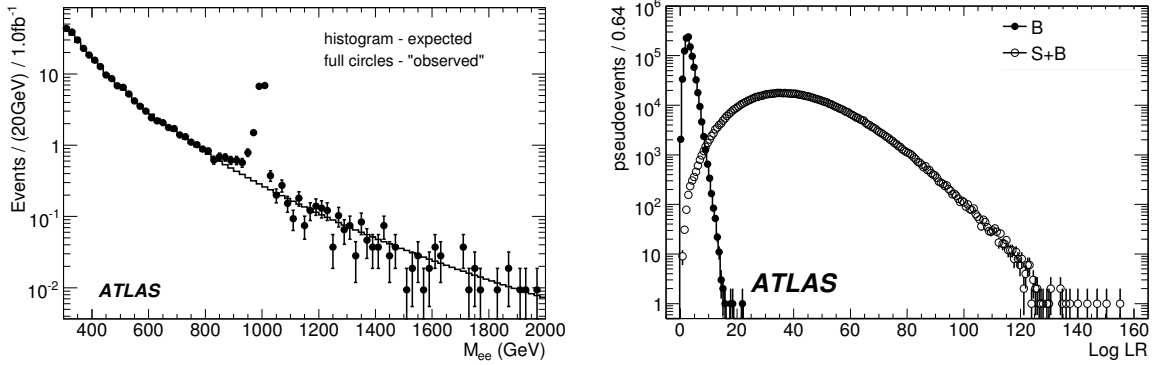


Figure 14: Left: expected (histogram) and “observed” (filled circles) Drell-Yan spectrum from full simulation. The observed distribution includes a graviton with mass of 1 TeV and coupling  $k/\bar{M}_{pl} = 0.02$ . Note that for the purposes of this plot the vertical axis has been rescaled: the error bars correspond to an integrated luminosity of  $100 \text{ fb}^{-1}$ . Right: Log likelihood ratio curves for one million pseudo-experiments generated with background only (filled circles), and signal plus background (empty circles) for the same  $m = 1$  TeV signal point.

### 5.5.2 Discovery Potential

We search for an excess of events in the mass range from 300 GeV up to 2 TeV and study the signal sensitivity by use of “extended maximum likelihood” fitting. We consider two hypotheses. The null hypothesis,  $H_0$ , is the hypothesis that the data are described by the Standard Model. The test hypothesis,  $H_1$ , is that the data are described by the sum of the background and a narrow Gaussian resonance.

To investigate the potential for discovery pseudo-experiments are generated from both the null and test hypothesis. Each pseudo-experiment is fit twice. The first fit assumes the data are described by the Standard Model using the function described in Section 5.1. The second fit assumes the data are

described by the sum of a Gaussian and the shape describing the Drell-Yan background. During this second fit the mean of the Gaussian is allowed to float throughout the entire mass region considered, and the width is fixed to the detector resolution.

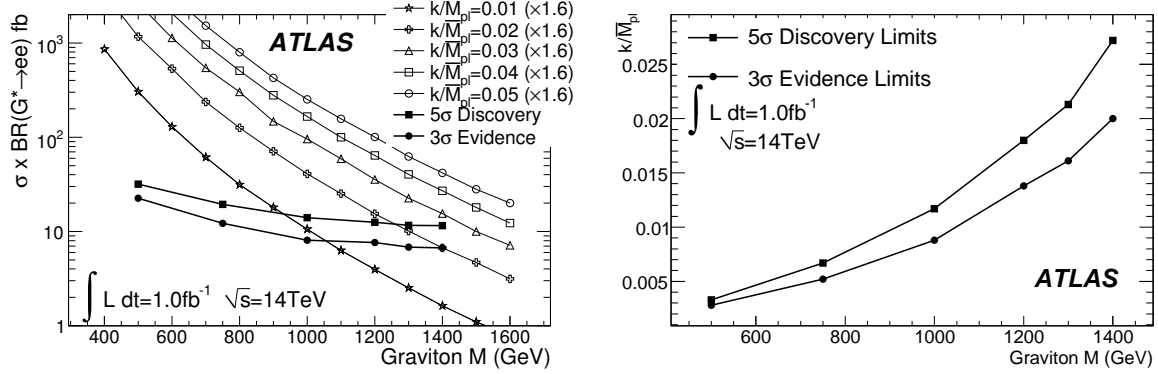


Figure 15:  $5\sigma$  discovery potential (full squares) as a function of the graviton mass. The  $3\sigma$  evidence potential is also shown (full circles). Left: shown with cross-sections as calculated by PYTHIA (LO) and multiplied by a  $K$  factor of 1.6 for several values of the coupling; right: dependence of the discovery potential on the coupling.

We can then compare the likelihood of the signal and background hypotheses. The distribution of the logarithm of the likelihood ratio between  $H_0$  and  $H_1$  is constructed, and shown for one signal point in Fig. 14. Based on this, we calculate the average expected discovery potential from the fraction of the likelihood ratio distribution for background-only pseudo-experiments that extends beyond the mean of the distribution for signal plus background experiments. Figure 15 shows the  $5\sigma$  discovery and  $3\sigma$  evidence reach in cross-section and  $k/\bar{M}_{pl}$  coupling constant as a function of graviton mass, estimated for an integrated luminosity of  $1 \text{ fb}^{-1}$ .

The LO cross-sections are multiplied by the  $K$ -factors discussed in section 4.2.2 for both signal and Drell-Yan background. Various sources of systematic uncertainties for signal and background are considered in the evaluation of the experimental sensitivity, including luminosity, energy scale, energy resolution, electron identification efficiency and Drell-Yan background uncertainties as listed in section 4.4. The combined effect of the systematic uncertainties is to increase the amount of integrated luminosity needed for discovery between 10 and 15 percent for the different parameter sets.

## 5.6 Technicolor Using a Non-Parameterized Approach

Topcolor-assisted Technicolor models with walking gauge coupling predict new technihadron states that are copiously produced at the LHC. The lowest mass states are the scalar technipions ( $\pi_T^{\pm,0}$ ) and the vector technirho and techniomega ( $\rho_T^{\pm,0}$  and  $\omega_T^0$ ). The vector mesons decay into a gauge boson plus technipion ( $\gamma\pi_T$ ,  $W\pi_T$  or  $Z\pi_T$ ), and fermion-antifermion pairs. This analysis searches for the decays  $\rho_T \rightarrow \mu^+\mu^-$  and  $\omega_T \rightarrow \mu^+\mu^-$ . The dimuon mode has a lower branching fraction than the modes involving technipions but the signal is clean, straightforward to trigger on, and can be readily observed with early ATLAS data.

The particular model studied here is the “Technicolor Strawman Model” or TCSM [11, 12]. In the TCSM, it is expected that techni-isospin is an approximate good symmetry and therefore the isotriplet  $\rho_T$  and isosinglet  $\omega_T$  will be nearly degenerate. We will assume for what follows that  $m_{\rho_T} = m_{\omega_T}$ . The technipions are also expected to be nearly degenerate. In the TCSM, the technipion masses are generi-

cally not small. In particular,  $m_{\pi_T} > m_{\rho_T}/2$  and therefore the decays of the  $\rho_T$  and  $\omega_T$  to technipions is kinematically forbidden. The dimuon rate is expected to come dominantly from the  $\omega_T$  with a smaller contribution from the  $\rho_T$ .

The event selection is summarized in Table 14.

In principle, the best search sensitivity is not obtained by examining the entire dimuon mass distribution for a bump all at once but by using an optimized mass window that maximizes the signal significance for a given assumed signal mass. A prescription for the optimal window size is taken from an analytic calculation in Ref. [49]. Assuming a narrow Gaussian peak on a linear background, the optimal window was found to be  $\pm 1.4\sigma$  about the peak mass. Since we are not really in the narrow resonance regime, we did a study using full-simulation ATLAS Monte Carlo for a Technicolor signal on a Drell-Yan background. Taking  $S/\sqrt{B}$  as our measure of significance, Fig. 16 (left) shows that a window size of  $\pm \sim 1.5\sigma$  or a bit larger is optimal. For this study, a window size of  $\pm 1.5\sigma$  about the peak mass is used.

| $m_{\rho_T, \omega_T}$ (GeV) | 400            | 600            | 800            | 1000           |
|------------------------------|----------------|----------------|----------------|----------------|
| Peak mass (GeV)              | 403            | 603            | 804            | 1004           |
| $\sigma(m)$ (GeV)            | 13             | 22             | 34             | 46             |
| Requirement                  |                |                |                |                |
| Generated                    | 201            | 60.8           | 23.0           | 10.1           |
| $ \eta  < 2.5$               | 116            | 39.8           | 15.8           | 7.3            |
| $p_T > 30$ GeV               | 114            | 39.5           | 15.7           | 7.2            |
| L1_MU20                      | 112            | 38.7           | 15.3           | 7.0            |
| L2_mu20                      | 110            | 38.0           | 15.1           | 6.9            |
| EF_mu20                      | 109            | 37.5           | 14.9           | 6.8            |
| Match $\chi^2 < 100$         | 104            | 35.7           | 14.0           | 6.4            |
| Opposite charge              | 104            | 35.7           | 14.0           | 6.4            |
| Mass window                  | 78.2           | 26.3           | 10.3           | 4.7            |
| Drell-Yan background         | 46.9           | 14.1           | 6.1            | 2.8            |
| Selection efficiency (%)     | $38.9 \pm 0.5$ | $43.2 \pm 0.5$ | $44.8 \pm 0.5$ | $46.8 \pm 0.5$ |

Table 14: Selection requirement flow for the analysis - cross-section in fb.

Figure 16 (right) shows the integrated luminosity necessary to observe either  $3\sigma$  evidence or a  $5\sigma$  discovery of technihadrons in this channel. The systematic uncertainties summarized in section 4.4 were included in this calculation of technihadron search sensitivity. It should be noted that the integrated luminosity needed for  $5\sigma$  discovery will be affected by the level of misalignment of the muon spectrometer. The contours in Fig. 16 were computed assuming the level of alignment we expect to achieve. The studies in sections 4.3 and 5.3 show that for an initial precision of 300 microns with an uncertainty of 150 microns the amount of data needed to reach  $5\sigma$  would increase by approximately 50%.

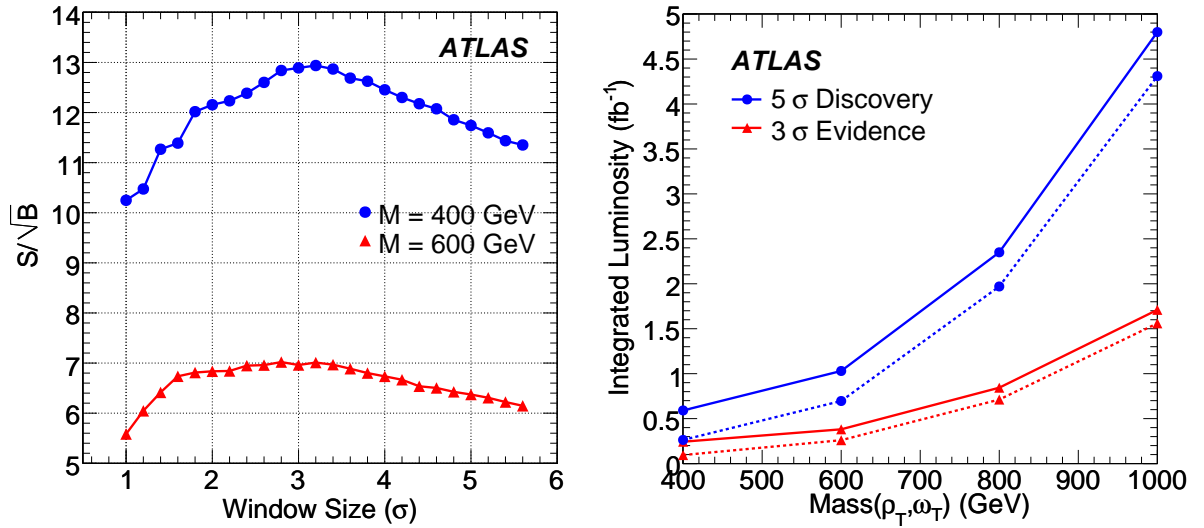


Figure 16: Left: for two different  $\rho_T, \omega_T$  signal masses,  $S/\sqrt{B}$  is plotted as a function of mass-window size for windows centered on the peak mass. Right: integrated luminosity needed for  $3\sigma$  evidence or  $5\sigma$  discovery as a function of  $\rho_T, \omega_T$  mass. The dashed lines include only statistical uncertainties while the solid lines contain the systematic uncertainties as well.

## 6 Summary and Conclusions

Several models which lead to resonances in the dilepton final state have been studied. Various systematic studies have been undertaken which estimate the effect of uncertainties from both theoretical knowledge of Standard Model processes as well as expected and assumed early detector performance. Data-driven methods have been developed to evaluate efficiencies, backgrounds, and uncertainties. It has been shown that even with early data the discovery potential can be dramatically increased from current limits. The discovery potential with an integrated luminosity of  $10 \text{ fb}^{-1}$  depends on the particular model and varies in the  $m = 1.0$  to  $3.5 \text{ TeV}$  range. It should be noted that resonance masses above  $1 \text{ TeV}$  which are unreachable by the Tevatron experiments could be discovered with as little as  $100 \text{ pb}^{-1}$  of data.

## Acknowledgments

We thank M. Klasen and B. Fuks for their work and discussion.

## A Effect of the Unknown Location and Rate

When estimating the significance of a local excess of events, the size of the region considered and uncertainties in the shape of the background can significantly reduce the sensitivity of the search. This appendix presents an assessment of the size of this effect for the  $Z'$  boson to dilepton searches. If an excess is found in the dilepton invariant mass, its significance needs to be evaluated in a way that takes into account the possibility of background fluctuations of different masses, cross-sections and widths. One possible way to do this is through the use of maximum likelihood fits, where these quantities are free parameters.

To estimate the effect on the sensitivity of the unknown rate and location of a dilepton resonance, the decay  $Z'_{SSM} \rightarrow ee$  and  $Z'_{SSM} \rightarrow \mu\mu$  were both generated for 16 true  $Z'$  masses between 1 and 4 TeV (evenly spaced every 200 GeV), with a lower cut on the true dilepton mass of 0.5 TeV in all cases. Each sample was simulated and reconstructed using fast simulation, and events were required to have two back-to-back ( $\Delta\phi > 2.9$ ) leptons of opposite charge with  $p_T > 20$  GeV and within  $|\eta| < 2.5$ . For an estimation of the expected background, Standard Model Drell-Yan production was used.

The dilepton resonance was modeled using an ad-hoc parameterization that models appropriately the shapes of both the  $Z' \rightarrow ee$  and  $Z' \rightarrow \mu\mu$  modes, consisting of a product between a Breit-Wigner and a Landau distribution with a common mean, and where the width of the Landau was parameterized as a function of the width of the Breit-Wigner<sup>4</sup>). The common mean, the width parameter and the amplitude of the signal are allowed to float in the fits.

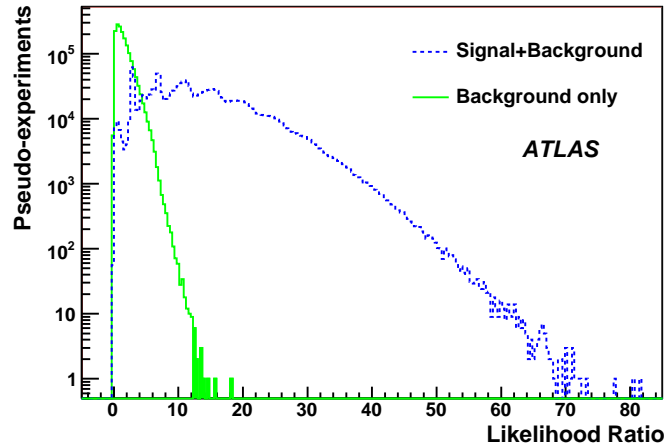


Figure 17: Likelihood ratio distribution for an  $m = 3$  TeV  $Z'_{SSM} \rightarrow ee$ ; the distribution on the left corresponds to background-only pseudo-experiments; the one on the right, to signal plus background.

Figure 17 shows the likelihood ratio distributions for an  $m = 3$  TeV  $Z'_{SSM} \rightarrow ee$  fit-based significance, where the signal rate, the peak's width and the mean mass all float in the fit, corresponding to an integrated luminosity of  $4 \text{ fb}^{-1}$ . The distributions of the log-likelihood ratio for fits to H0 pseudo-experiments. and for fits to H1 pseudo-experiments are shown. The fraction  $p$  of the H0 distribution that has a likelihood ratio larger than the mean of the H1 distribution is shaded. The value of  $p$  is then transformed into a significance following the convention under which  $p = 2.9 \times 10^{-7}$  corresponds to  $5\sigma$

<sup>4</sup>)The best motivated shape is a Breit-Wigner convoluted with a Gaussian resolution. Unfortunately, the convolution fit is very time consuming and for this study millions of fits were performed. Empirically the combination of a Breit-Wigner and a Landau were found to give essentially identical results.



(see section 5). The fraction shown in the plot corresponds to a significance of  $4.29\sigma$ .

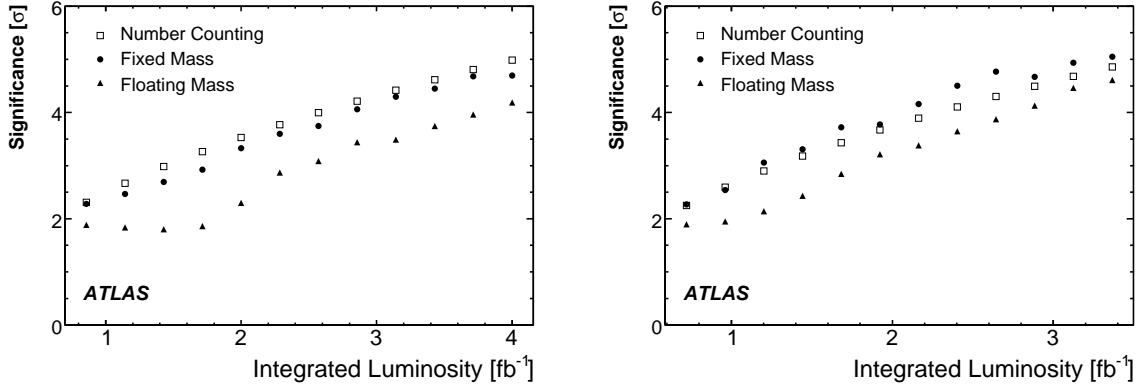


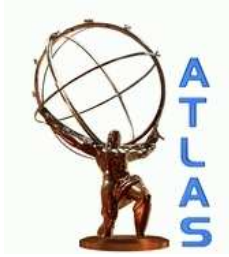
Figure 18: Comparison of the fit-based significance for fixed-mass (dots) and floating-mass (squares) fits for both cases,  $Z' \rightarrow ee$  (left) and  $Z' \rightarrow \mu\mu$  (right). Circles show the estimation from number counting.

Several million pseudo-experiments were generated and fit, covering different masses and luminosities. Figure 18 shows the significance for different approaches in the case of an  $m = 3$  TeV  $Z'_{SSM}$  for both the dielectron (left) and the dimuon (right) cases. The plots compare the significance as obtained from number counting (circles), fixed mass fits (dots) and floating mass fits (squares). The floating-mass significances are on average 20% lower than the fixed-mass calculations for  $Z' \rightarrow ee$ , and about 15% lower in the dimuon case (in obtaining these numbers, we exclude the region below  $2.25 \text{ fb}^{-1}$ , which is affected by low statistics effects).

## References

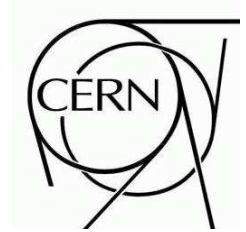
- [1] H. Georgi and S. L. Glashow, *Phys. Rev. Lett.* **32** (1974) 438–441.
- [2] K. D. Lane and E. Eichten, *Phys. Lett.* **B222** (1989) 274.
- [3] N. Arkani-Hamed, A. G. Cohen, and H. Georgi, *Phys. Lett.* **B513** (2001) 232–240.
- [4] L. Randall and R. Sundrum, *Phys. Rev. Lett.* **83** (1999) 3370–3373.
- [5] **D0** Collaboration, V. M. Abazov *et al.*, *Phys. Rev. Lett.* **95** (2005) 091801.
- [6] **CDF** Collaboration, A. Abulencia *et al.*, *Phys. Rev. Lett.* **96** (2006) 211801.
- [7] P5-Committee, “The case for run II: Submission to the particle physics project prioritization panel. the CDF and D0 experiments.” 2005.
- [8] F. Ledroit, J. Morel, and B. Trocmé, “ $Z'$  at the LHC.” ATL-PHYS-PUB-2006-024, 2006.
- [9] M. Cvetič, P. Langacker, and B. Kayser, *Phys. Rev. Lett.* **68** (1992) 2871–2874.
- [10] **Particle Data Group** Collaboration, W. M. Yao *et al.*, *J. Phys.* **G33** (2006) 1–1232.
- [11] K. D. Lane, *Phys. Rev.* **D60** (1999) 075007.
- [12] K. Lane and S. Mrenna, *Phys. Rev.* **D67** (2003) 115011.
- [13] **ATLAS** Collaboration, “Reconstruction and identification of electrons in ATLAS.” This volume.
- [14] **ATLAS** Collaboration, “The ATLAS Experiment at the CERN Large Hadron Collider.” Accepted by JINST, 2008.
- [15] **ATLAS** Collaboration, “The ATLAS Muon Spectrometer Technical Design Report.” 1997.
- [16] **ATLAS** Collaboration, “Muon Reconstruction and Identification Performance in ATLAS: Studies with Simulated Monte Carlo Samples.” This volume.
- [17] **ATLAS** Collaboration, “Reconstruction and identification of hadronic tau decays with ATLAS.” This volume.
- [18] **ATLAS** Collaboration, “The ATLAS Trigger for early running.” This volume.
- [19] **ATLAS** Collaboration, “Performance of the ATLAS Muon Trigger Slice with Simulated Data.” This volume.
- [20] T. Sjöstrand, S. Mrenna, and P. Skands, *JHEP* **0605** (2006) 026.
- [21] U. Baur, O. Brein, W. Hollik, C. Schappacher, and D. Wackeroth, *Phys. Rev. D* **65** (2002) 033007.
- [22] V. A. Zykunov, *Phys. Rev. D* **75** (2007) 073019.
- [23] A. D. Martin, R. G. Roberts, W. J. Stirling, and R. S. Thorne, *Eur. Phys. J. C* **39** (2005) 155.
- [24] C. Glosser, S. Jadach, B. F. L. Ward, and S. A. Yost, *Mod. Phys. Lett. A* **19** (2004) 2113.
- [25] C. M. C. Calame, G. Montagna, O. Nicrosini, and A. Vicini, *JHEP* **0710** (2007) 109.

- 669 [26] U. Baur, S. Keller, and W. K. Sakumoto, *Phys. Rev. D* **57** (1998) 199.
- 670 [27] G. Altarelli, R. K. Ellis, and G. Martinelli, *Nucl. Phys. B* **157** (1979) 461.
- 671 [28] R. Hamberg, W. L. van Neerven, and T. Matsuura, *Nucl. Phys. B* **359** (1991) 343. Erratum-ibid. *B*  
672 644:403, 2002.
- 673 [29] C. Anastasiou, L. J. Dixon, K. Melnikov, and F. Petriello, *Phys. Rev. D* **69** (2004) 094008.
- 674 [30] A. Kulesza, G. Sterman, and W. Vogelsang, *Phys. Rev. D* **66** (2002) 014011.
- 675 [31] B. Fuks, M. Klasen, F. Ledroit, Q. Li, and J. Morel, *Nucl. Phys.* **B797** (2008) 322–339.
- 676 [32] S. Frixione and B. R. Webber, *JHEP* **0206** (2002) 029.
- 677 [33] P. Mathews, V. Ravindran, and K. Sridhar, *JHEP* **0510** (2005) 031.
- 678 [34] Q. Li, C. S. Li, and L. L. Yang, *Phys. Rev. D* **74** (2006) 056002.
- 679 [35] J. Bijnens, P. Eerola, M. Maul, A. Møansson, and T. Sjöstrand, *Phys. Lett. B* **503** (2001) 341.
- 680 [36] A. D. Martin, R. G. Roberts, W. J. Stirling, and R. S. Thorne, *Phys. Lett. B* **531** (2002) 216.
- 681 [37] J. Pumplin *et al.*, *JHEP* **07** (2002) 012.
- 682 [38] A. D. Martin, R. G. Roberts, W. J. Stirling, and R. S. Thorne, *Phys. Lett. B* **604** (2004) 61.
- 683 [39] W. K. Tung, H. L. Lai, A. Belyaev, J. Pumplin, D. Stump, and C. P. Yuan, *JHEP* **0702** (2007) 053.
- 684 [40] F. Petriello and S. Quackenbush, *arXiv:0801.4389 [hep-ph]* .
- 685 [41] G. A. Ladinsky and C. P. Yuan, *Phys. Rev. D* **50** (1994) 4239.
- 686 [42] F. Landry, R. Brock, P. M. Nadolsky, and C. P. Yuan, *Phys. Rev. D* **67** (2003) 073016.
- 687 [43] A. V. Konychev and P. M. Nadolsky, *Phys. Lett. B* **633** (2006) 710.
- 688 [44] T. Junk, *Nucl. Instrum. Meth.* **A434** (1999) 435–443.
- 689 [45] H. Hu and J. Nielsen, *arXiv:physics/9906010*.  
690 <http://www.citebase.org/abstract?id=oai:arXiv.org:physics/9906010>.
- 691 [46] **CMS** Collaboration, G. L. Bayatian *et al.*, *J. Phys.* **G34** (2007) 995–1579.
- 692 [47] G. Altarelli, B. Mele, and M. Ruiz-Altaba, *Z. Phys.* **C45** (1989) 109.
- 693 [48] **CDF** Collaboration, D. E. Acosta *et al.*, *Phys. Rev. Lett.* **95** (2005) 131801.
- 694 [49] K.-M. Cheung and G. L. Landsberg, *Phys. Rev.* **D62** (2000) 076003.



# ATLAS NOTE

July 18, 2008



## Lepton plus Missing Transverse Energy Signals at High Mass

The ATLAS Collaboration

### Abstract

The prospects for the discovery of heavy lepton-neutrino resonances with the ATLAS detector are evaluated using full detector simulation. We discuss the performance of large missing transverse momentum measurement and its impact on the lepton-neutrino transverse mass reconstruction and backgrounds from large missing transverse momentum. As benchmark, we evaluate the sensitivity to the a Standard Model like  $W'$ . Emphasis is put on the discovery potential of ATLAS with early data, namely with an integrated luminosity of  $10 \text{ pb}^{-1}$  to  $10 \text{ fb}^{-1}$ .

# 1 Introduction

The Standard Model of particle physics has been able to predict or describe, within errors, almost all measurements performed within its domain. However, several fundamental questions remain unresolved. Its mechanism for electroweak symmetry breaking has not been experimentally confirmed, nor has the physical Higgs boson that it predicts been observed. The values of many constants in the model are still unconstrained and lack a fundamental explanation. There are indications, therefore, that the Standard Model is not a fundamental theory, but a good approximation of nature at the energy ranges that have been so far accessible to experiment. Thus, the search for physics beyond the Standard Model is an important part of the ATLAS physics program. In this document, a study is presented of the potential for the search of final states comprised of one electron or muon (*lepton*, in what follows) plus missing transverse energy.

A large variety of theories beyond the Standard Model, predict additional gauge bosons. Any charged, spin 1 gauge boson which is not included in the Standard Model is called  $W'$  boson and according to several predictions there is at least one  $W'$  boson detectable at the LHC. These theories and models which predict new charged gauge bosons range from the Grand Unified Theories [1–3], the various Left-Right Symmetric Models [1, 4–10], Kaluza-Klein theories [11–15], Little Higgs models [16–18], dynamical symmetry breaking models [19] and even models inspired from superstrings [20–22]. As an example, the 45 decompositions of the  $SO(10)$  gauge group, which is a candidate for large GUT symmetries, under the  $SU(3)_C \times SU(2)_L \times SU(2)_R \times U(1)_{B-L}$  gives rise to a (1,1,3,0) triplet coming from the  $SU(2)_R$  group. That is, a triplet of right-handed  $W^{\pm,0}$  fields, which carry weak (V+A) interactions. A theoretical model, based on the gauge group  $SU(3)_C \times SU(2)_L \times SU(2)_R \times U(1)_{B-L}$  which is called a Left-Right Symmetric Model (LRSM), after spontaneous symmetry breaking, predicts a right-handed  $W_R$  gauge boson mixes with the left-handed  $W_L$  boson of the Standard Model. A very attractive  $W'$  boson candidate is the  $W_R$  gauge boson. The search for these particles is an important part of the studies for new physics to be performed at LHC. Studies presented here are based on predictions of a “Standard Model-like”  $W'$  boson from so-called extended gauge models [23]. This  $W'$  boson has Standard Model-like couplings to fermions and its decays to  $WZ$  bosons are suppressed.

The D0 experiment, at Fermilab, has obtained the present lower limit for the  $W'$  boson mass [24] as  $m_{W'} > 1$  TeV at 95% C.L. The LHC, with a centre-of-mass energy of 14 TeV, is expected to increase the search reach even at early stages of data taking. Other ATLAS studies have evaluated the potential for discovery of  $W' \rightarrow \ell \nu_\ell$  where  $\ell = \mu, e$  [25]. This study is based on the most recent realistic detector description, including a complete simulation of the trigger chain.

## 2 Monte Carlo Samples

Table 1 summarizes the samples used in this study; a detailed account of the procedures, generators and settings used is given in [26]. Signal samples for masses other than 1 and 2 TeV were produced locally and validated against central production samples.

For the signal, samples of  $W' \rightarrow \ell \nu$  events were generated with PYTHIA v6.403 [27], based on the leading order cross sections and the parton distribution functions CTEQ6 [28], where  $\ell$  can be any type of lepton ( $\tau$  included), for true  $W'$  boson masses ranging from 1 to 4 TeV.

The main background for a  $W'$ -type state is the high-mass tail of Standard Model  $W$  boson production; in order to provide enough background to study also the higher  $W'$  boson masses, two samples of Standard Model  $W$  boson events were produced, with different requirements on the true invariant mass of the  $W$  boson: one with  $200 \text{ GeV} < m_W < 500 \text{ GeV}$ , and one with  $m_W > 500 \text{ GeV}$ . In these studies, the alignment and calibration of the detector is assumed to be well described in the reconstruction algorithms.

| Process                                 | Generator | $\sigma \times BR$ [fb] | Comments                                  | Events |
|---|-----------|-------------------------|---|--------|
| 1 TeV $W' \rightarrow \ell \nu$         | PYTHIA    | 9430                    | $\sqrt{s'} > 300$ GeV                     | 30K    |
| 2 TeV $W' \rightarrow \ell \nu$         | PYTHIA    | 437                     | $\sqrt{s'} > 300$ GeV                     | 30K    |
| 3 TeV $W' \rightarrow \ell \nu$         | PYTHIA    | 54                      | $\sqrt{s'} > 300$ GeV                     | 10K    |
| Standard Model $W \rightarrow \ell \nu$ | PYTHIA    | 18721.1                 | $200 \text{ GeV} < m_W < 500 \text{ GeV}$ | 20K    |
| Standard Model $W \rightarrow \ell \nu$ | PYTHIA    | 708.26                  | $m_W > 500 \text{ GeV}$                   | 20K    |
| $t\bar{t}$                              | MC@NLO    | 452000                  |   | 340K   |
| Dijet J0                                | PYTHIA    | $1.76 \times 10^{13}$   | $\hat{p}_T = 8 - 17 \text{ GeV}$          | 380K   |
| Dijet J1                                | PYTHIA    | $1.38 \times 10^{12}$   | $\hat{p}_T = 17 - 35 \text{ GeV}$         | 380K   |
| Dijet J2                                | PYTHIA    | $9.33 \times 10^{10}$   | $\hat{p}_T = 35 - 70 \text{ GeV}$         | 390K   |
| Dijet J3                                | PYTHIA    | $5.88 \times 10^9$      | $\hat{p}_T = 70 - 140 \text{ GeV}$        | 380K   |
| Dijet J4                                | PYTHIA    | $3.08 \times 10^8$      | $\hat{p}_T = 140 - 280 \text{ GeV}$       | 390K   |
| Dijet J5                                | PYTHIA    | $1.25 \times 10^7$      | $\hat{p}_T = 280 - 560 \text{ GeV}$       | 370K   |
| Dijet J6                                | PYTHIA    | $3.60 \times 10^5$      | $\hat{p}_T = 560 - 1120 \text{ GeV}$      | 380K   |
| Dijet J7                                | PYTHIA    | $5.71 \times 10^3$      | $\hat{p}_T = 1120 - 2240 \text{ GeV}$     | 430K   |

Table 1: Monte Carlo samples used for the study of  $W'$  bosons.  $\sqrt{s'}$  is the centre-of-mass energy of the two partons and  $\hat{p}_T$  represents the transverse momentum of the partons in their rest frame.

### 3 Reconstruction Performance

#### 3.1 Muon Reconstruction

Muon reconstruction in ATLAS uses all main detector subsystems. The Muon Spectrometer (MS) is designed to provide efficient and precise stand-alone momentum measurement for muons of transverse momentum up to  $O(p_T = 1 \text{ TeV})$ . During the back-tracking of the muon to the production vertex, energy loss fluctuations can be measured with the use of the calorimeters, which can also provide independent muon tagging to increase the identification efficiency. For optimum performance in momentum resolution, the MS information is combined with the track information obtained in the Inner Detector (ID). A full description of the algorithms for muon performance and identification can be found in [29] and [30].

Figure 1 shows the inverse transverse momentum ( $1/p_T$ ) resolution for muons from decays of a  $W'$  boson for muons below  $p_T = 400 \text{ GeV}$  and above  $p_T = 800 \text{ GeV}$ . Especially relevant for the analysis are the negative tails in these plots, since they correspond to reconstructed muon candidates that have a  $p_T$  larger than that of the true particle. The relative contribution of these tails can be assessed by the fraction of muon candidates separated by more than  $2\sigma$  from the mean of the distribution (which in both cases is consistent with zero, as it should). The fraction in that negative tail is  $(4.9 \pm 0.3)\%$  for muons with  $p_T < 400 \text{ GeV}$ , and  $(3.8 \pm 0.4)\%$  for  $p_T > 800 \text{ GeV}$  (to be compared with 2.275% for a gaussian distribution). The transverse momentum resolution achieved is shown as a function of the pseudo-rapidity  $\eta$  and  $p_T$  in Fig. 2. On average a resolution of 4.5 and 5.5% is recorded for muons from  $W'$  bosons of  $m = 1 \text{ TeV}$  and  $2 \text{ TeV}$  respectively.

Figures 3 and 4 show the efficiency for combined muon reconstruction as a function of pseudo-rapidity ( $\eta$ ), azimuthal angle ( $\phi$ ) and transverse momentum ( $p_T$ ) for muons from fully simulated  $W'$  boson decays. An overall efficiency of 93.6% and 92.4% is measured for  $m = 1 \text{ TeV}$  and  $2 \text{ TeV}$   $W'$  boson samples, respectively. The regions with lower efficiency in muon reconstruction are observed, as expected, in the middle plane ( $\eta = 0$ ) and in the transition regions between the barrel and the end-cap sections of the MS (at  $|\eta| \sim 1.2$ ). The regions with low efficiency in  $\phi$  correspond to the feet of the detector.

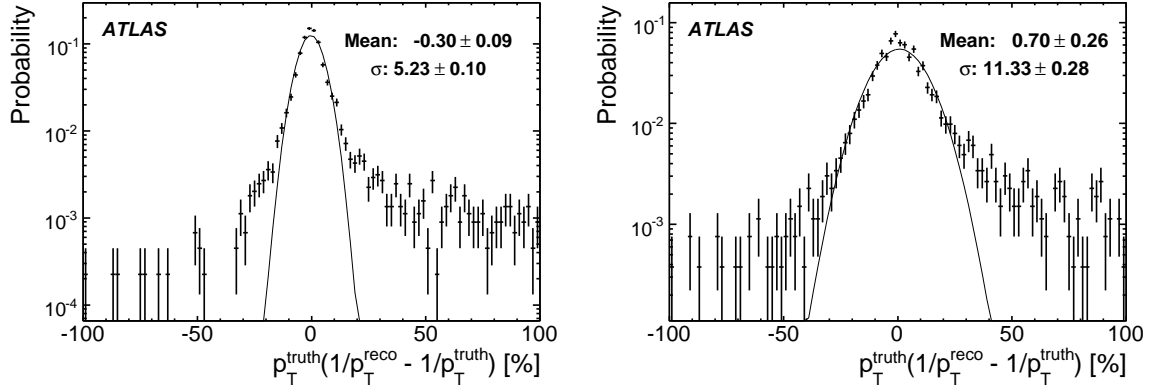


Figure 1: Inverse  $p_T$  resolution for muons from  $W'$  boson decays; left:  $p_T < 400$  GeV, right:  $p_T > 800$  GeV.

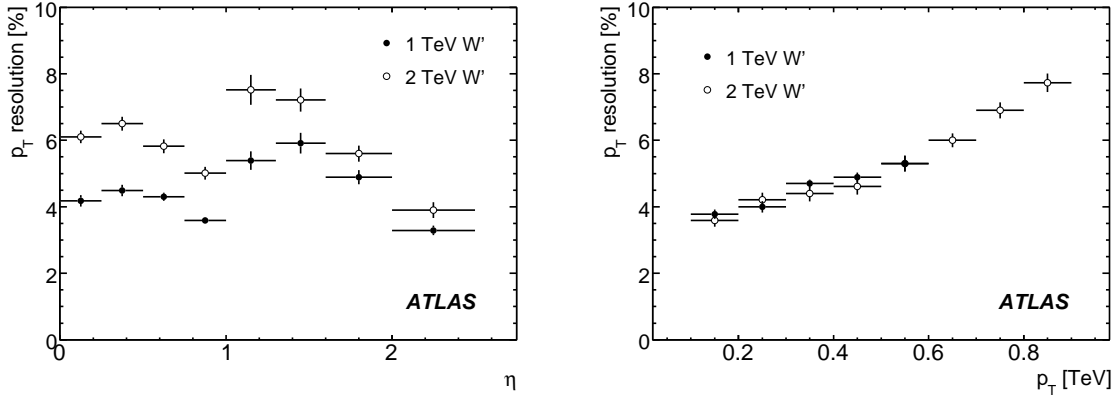


Figure 2: Muon transverse momentum resolution as a function of  $\eta$  (left) and  $p_T$  (right) in  $W'$  boson decays. Filled circles represent muons from  $m = 1$  TeV  $W'$  bosons, while open circles correspond to muons from  $m = 2$  TeV  $W'$  bosons.

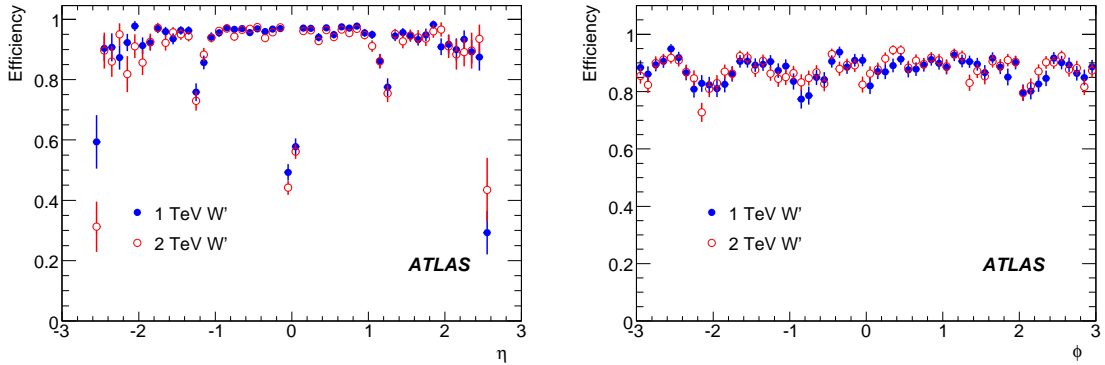


Figure 3: Combined muon reconstruction efficiency as a function of  $\eta$  and  $\phi$  for muons from  $W'$  boson decays.

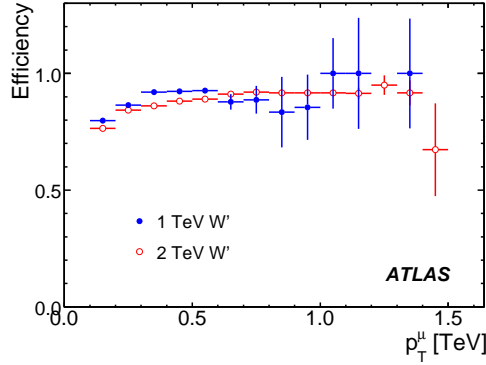


Figure 4: Combined muon reconstruction efficiency as a function of  $p_T$  for muons from  $W'$  boson decays.

One important issue in this study concerns the background that can rise from badly reconstructed muons. Their momentum being wrongly estimated upwards, can cause both the presence of a high  $p_T$  muon and, correspondingly, large missing transverse energy ( $\cancel{E}_T$ ). In the definition of the muon, extra quality criteria may be imposed in order to diminish this probability. In this study, the following mild requirements are adopted:

- A matching  $\chi^2$ , between MS and ID tracks, smaller than 100 (further discussed in [30]).
- An impact parameter in the  $z$ -axis (i.e. the beam axis) smaller than 200 mm.
- An impact parameter significance in the transverse ( $R$ - $\phi$ ) plane smaller than 10.

### 3.2 Electron Reconstruction

Electron candidates are built starting from clusters of calorimeter cell energy depositions, which are matched to a track from the inner detector. Electron identification and reconstruction are described in detail in [31] and [32], where three standard selections were developed to be used in physics searches. The present study uses the *medium* set of selection requirements, which consists in several requirements on the clusters used (size, containment, association with a track, shower shapes and quality of the track match).

Figure 5 shows the electron energy resolution (in percentage) as a function of pseudo-rapidity ( $|\eta|$ ) and true energy. The average energy resolution for electrons in this energy range is close to 1%, and is worse in the transition region between the two calorimeter systems. Figure 6 shows the relative difference between reconstructed and true transverse momenta of isolated electrons with true  $p_T$  lower than 400 GeV and higher than 800 GeV. The fractions of events in the upper tails (more than  $2\sigma$  over the fitted mean) are  $(11.8 \pm 0.6)\%$  and  $(5.3 \pm 0.5)\%$ , respectively. These non-Gaussian tails are due to the amount of material in the inner detector and are, therefore,  $\eta$ -dependent.

### 3.3 Reconstruction of the Missing Transverse Energy

The final state under consideration includes a neutrino, whose momentum information can be inferred only partially from the energy imbalance in the detector (since the total transverse momentum of the event has to add up to zero). The reconstruction of the missing transverse energy in ATLAS ( $\cancel{E}_T$ ) is described in detail in [33].



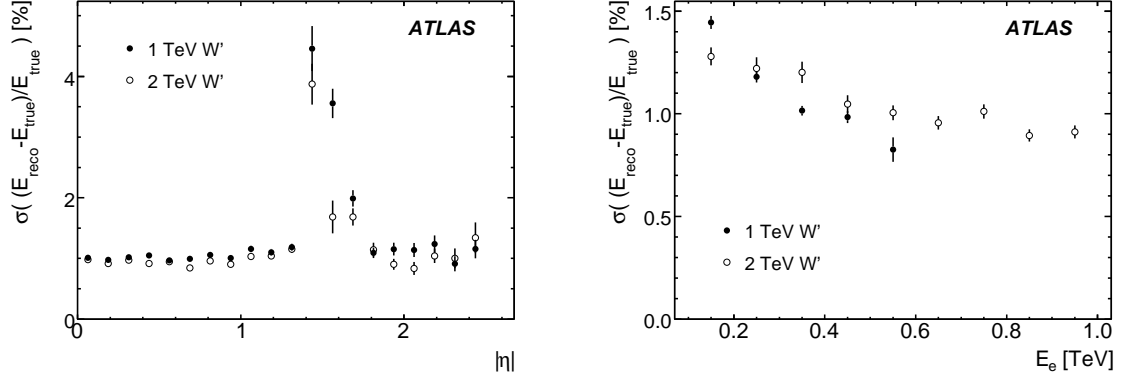


Figure 5: Electron energy resolution as a function of pseudo-rapidity (left) and energy (right) in  $W'$  boson decays. Filled circles represent electrons from  $m = 1$  TeV  $W'$  bosons, while open circles correspond to  $m = 2$  TeV  $W'$  bosons.

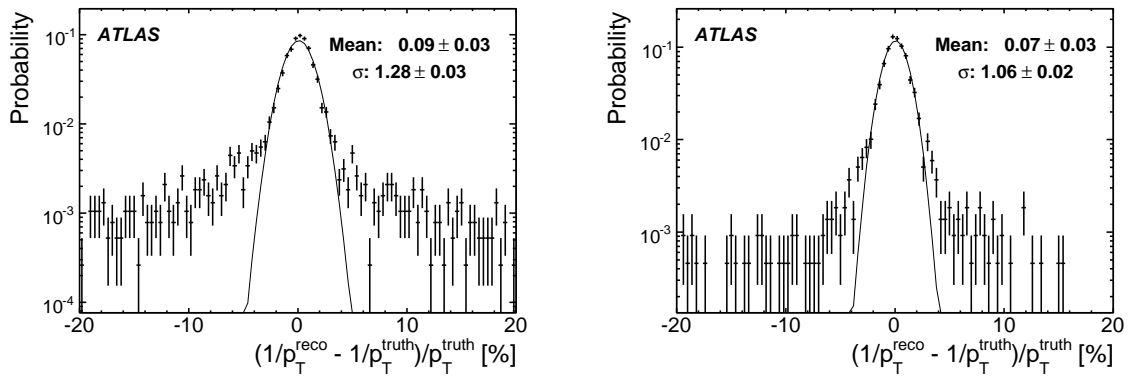


Figure 6: Electron  $p_T$  resolution in  $W'$  boson decays, for  $p_T < 400$  GeV (left) and  $p_T > 800$  GeV (right).

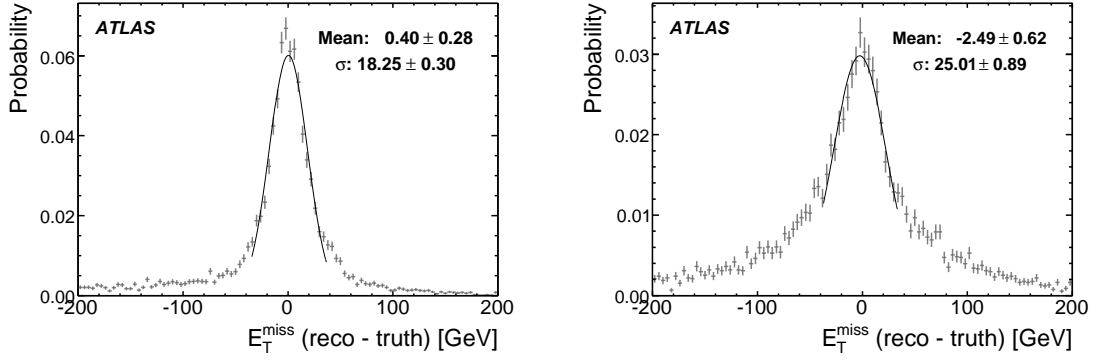


Figure 7:  $\cancel{E}_T$  resolution in muonic  $W'$  boson decays.  $m_{W'} = 1$  TeV (left) and 2 TeV (right).

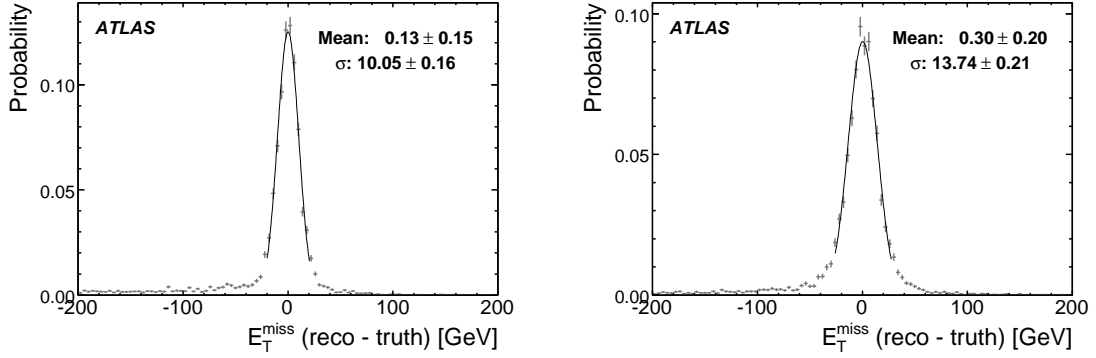


Figure 8:  $\cancel{E}_T$  resolution in  $W'$  boson decays to electrons.  $m_{W'} = 1$  TeV (left) and 2 TeV (right).

The resolution of  $\cancel{E}_T$  reconstruction in  $W'$  boson events containing muons can be seen in Fig. 7. An average resolution of  $\sim 18$  GeV (25 GeV for  $m_{W'} = 2$  TeV) is observed. In the case of  $m_{W'} = 2$  TeV the non-Gaussian tails in the resolution are more pronounced, and come from the degraded performance of muon reconstruction at high  $p_T$ .

Figure 8 shows the  $\cancel{E}_T$  resolution for events that contain one high- $p_T$  electron from a  $W'$  boson decay. The left plot corresponds to the  $m = 1$  TeV  $W'$  boson, and the right plot to 2 TeV; the resolutions are around 10 and 14 GeV, respectively. These values agree well with the expected  $\cancel{E}_T$  resolution from the mean of the scalar sum of transverse energy ( $\langle \sum E_T \rangle$ ) in each case; for the  $m = 1$  TeV sample,  $\langle \sum E_T \rangle$  for the selected events is 439 GeV, which yields an estimated  $\sigma(\cancel{E}_T) \sim 0.5\sqrt{\sum E_T} = 10.5$  GeV, while the  $\cancel{E}_T$  resolution for this sample, shown in Fig. 8, is 10.05 GeV; for  $m = 2$  TeV, the expected value (based on  $\langle \sum E_T \rangle$ ) is 13.3 GeV, while a fit to the  $\cancel{E}_T$  residuals returns 13.7 GeV.

### 3.4 Transverse Mass Reconstruction

In the  $W'$  boson search, the transverse momentum  $p_T$  of the single lepton in the event and the missing transverse energy  $\cancel{E}_T$  are combined to obtain the *transverse mass* as follows:

$$m_T = \sqrt{2p_T \cancel{E}_T (1 - \cos \Delta\phi_{\ell, \cancel{E}_T})} \quad (1)$$

where  $\Delta\phi_{\ell, \cancel{E}_T}$  is the angle between the momentum of the lepton and the missing transverse momentum, in the transverse plane. Figures 9 and 10 show the transverse mass distributions for  $m = 1$  and 2 TeV signals, respectively, as obtained from truth information (light gray filled histograms) and the degradation

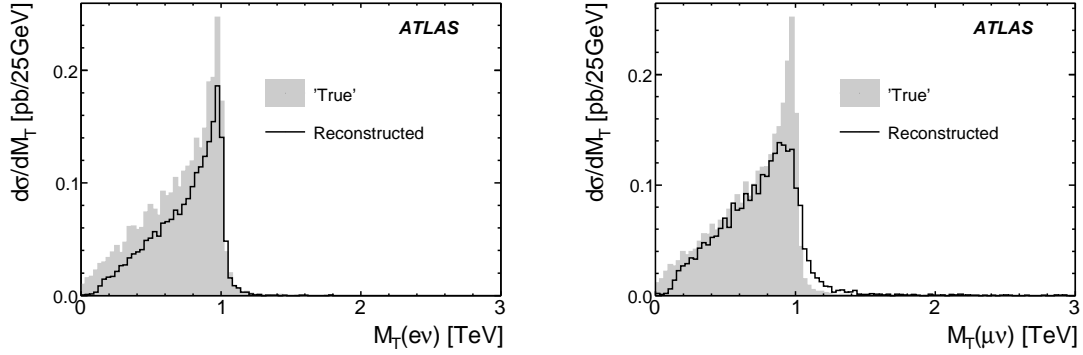


Figure 9: Transverse mass distribution for  $m = 1$  TeV  $W'$  bosons, as obtained from the true particles' momenta (filled histograms), and from reconstructed information after basic selection (black outline). Left: electron mode; right: muon mode.

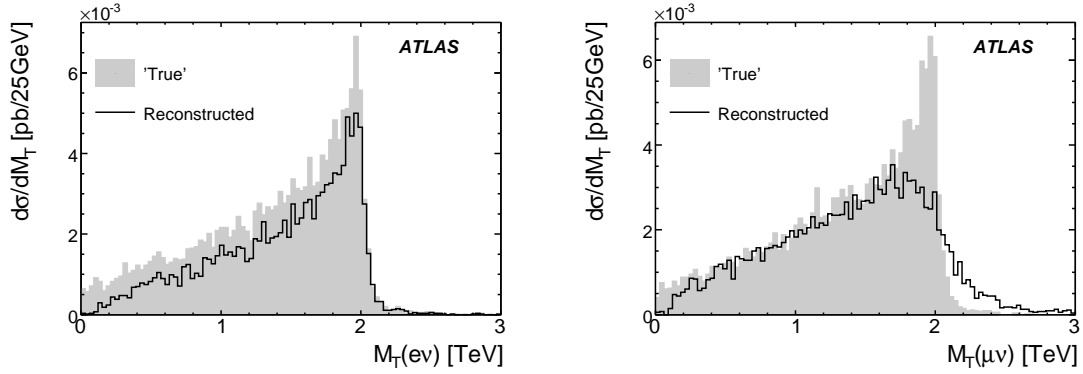


Figure 10: As Fig. 9, for  $m = 2$  TeV  $W'$  bosons, filled: from true information; outline: reconstructed transverse mass.

due to detector resolution and efficiency (black hollow histograms). As can be expected from Figs. 2 and 5, the shape of the transverse mass spectrum has a larger distortion in the muon channel than in the electron channel, with larger tails for higher  $W'$  boson masses. On the other hand, the reconstruction efficiency is higher in the muon channel (over 86% for each mass) than in the electron channel (about 72%).

Figures 11 and 12 show the distribution of the difference between the “true” transverse mass (i.e. as obtained from the true momenta of the lepton and the neutrino) and its reconstructed value, for electron and muon modes, and for  $m = 1$  and 2 TeV  $W'$  boson masses. In Fig. 11, single Gaussian fits are shown; a fitted width of 11.5 GeV is obtained for the electron channel, while the muon channel, besides having much larger non-Gaussian tails, has a fitted width close to 30 GeV.

Figure 12 shows the corresponding comparison for a 2 TeV signal; however, in this case, the muon channel (on the right) has a stronger non-Gaussian character, which is why no fit was performed.

## 4 Trigger

The ATLAS trigger [34] has three levels: events passed by the L1 (level 1) hardware trigger are partially reconstructed in L2 (level 2) processors and, if accepted there, are fully processed in the EF (event filter) processor farm. Only events accepted by the EF (and thus also by L1 and L2) are recorded for later

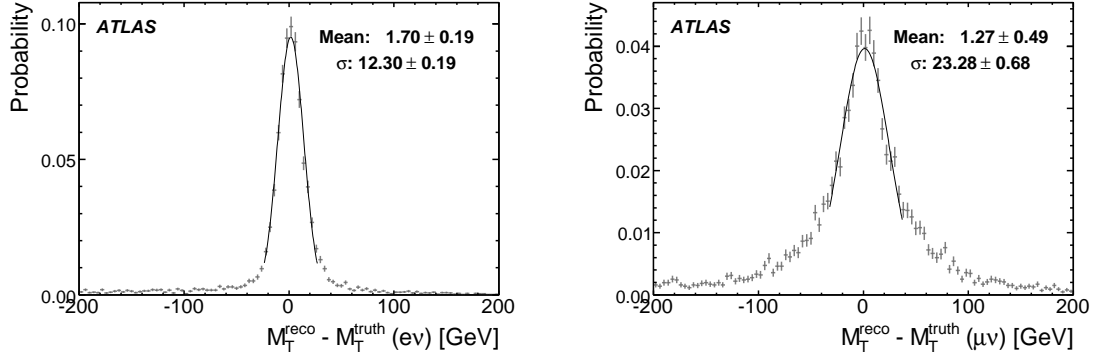


Figure 11: Distribution of the event-by-event difference between the reconstructed and “true” transverse mass for the electron and muon channel, for  $m = 1$  TeV  $W'$  bosons.

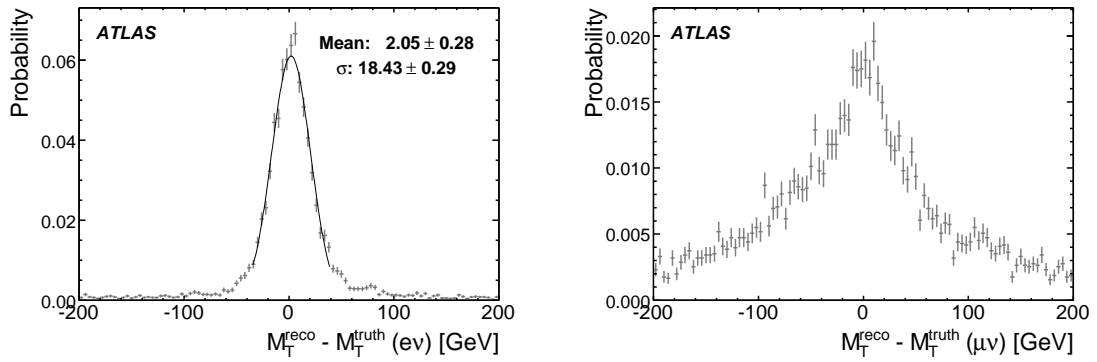


Figure 12: As Fig. 11, for  $m = 2$  TeV  $W'$  bosons.

reconstruction and analysis.

Trigger rates are estimated in separate studies of the electron [35] and muon [36] trigger systems. We have measured some of the rates directly in simulation using the dijet and top samples described earlier in this note. Especially for electrons, the trigger menu and algorithms in the simulated samples are quite different from those in the above notes which are much closer to those expected to be used during actual data acquisition. We additionally measured L1 rates and efficiencies for single-electron and single-muon triggers with thresholds higher than those defined in the simulated trigger menu. The errors we assign to our rate estimates are purely statistical.

#### 4.1 Electron trigger

For a single electron with an  $E_T$  threshold of 100 GeV, we measure a L1 rate of  $14 \pm 1$  Hz at an instantaneous luminosity of  $10^{32} \text{ cm}^{-2}\text{s}^{-1}$ , similar to the electron trigger study estimate of 10 Hz. The efficiency to trigger on  $W' \rightarrow e\nu$  events for  $|\eta| < 2.5$  is 98% for a mass of either 1 or 2 TeV. If the threshold is raised to 250 GeV, we measure a rate of  $25 \pm 4$  Hz at  $10^{33} \text{ cm}^{-2}\text{s}^{-1}$  and an efficiency of 96% for the 2 TeV mass.

Loose requirements in L2 and EF can further reduce these rates with a moderate degradation of the efficiency. For definiteness in the calculations in the following sections, we assume that a trigger efficiency (applied after all requirements) of  $0.90 \pm 0.10$  is achieved with an acceptable rate for all  $W'$  boson masses.

#### 4.2 Muon trigger

The trigger menu and algorithms in the simulation samples are similar to those in the muon trigger study and those expected for data acquisition. In contrast to the electron case, lower thresholds can be applied thanks to the lower fake rates. A significant decrease in rate is then obtained thanks to an improved measurement of  $p_T$  at each level. Applying a threshold of 20 GeV at each trigger level, we obtain an EF rate of  $20 \pm 10$  Hz for an instantaneous luminosity of  $10^{32} \text{ cm}^{-2}\text{s}^{-1}$ , consistent with the muon study prediction of 13 Hz. We measure a  $W' \rightarrow \mu\nu$  trigger efficiency for  $|\eta| < 2.5$  of 74% for  $m = 1$  TeV and 73% at 2 TeV. At  $10^{33} \text{ cm}^{-2}\text{s}^{-1}$ , we apply a  $p_T$  threshold of 40 GeV, the maximum L1 value, and obtain a trigger rate of  $4.1 \pm 0.7$  Hz close to the 5.6 Hz obtained in the trigger study. The corresponding trigger efficiency for the  $m = 2$  TeV  $W'$  boson is 69%.

It should be noted that most of the efficiency loss comes from holes in the coverage of the muon system, where the reconstruction is also inefficient.

### 5 Event Selection

The decay  $W' \rightarrow \ell\nu$  provides a rather clean signature consisting of a high-energy isolated lepton and large missing transverse energy. The largest backgrounds are the high- $p_T$  tail of the  $W \rightarrow \ell\nu$  decays and  $t\bar{t}$  production. Both these final states are accompanied by significant jet activity, but contain also leptons that are as isolated as those expected from  $W' \rightarrow \ell\nu$  decays.

A potentially dangerous background is the one arising from fake leptons; since this issue is more likely to be significant for electrons than for muons, the backgrounds will be presented separately for  $W' \rightarrow e\nu$  and  $W' \rightarrow \mu\nu$  final states.

#### 5.1 Event Preselection

In addition to the electron and muon identification criteria described above, events are required to have:

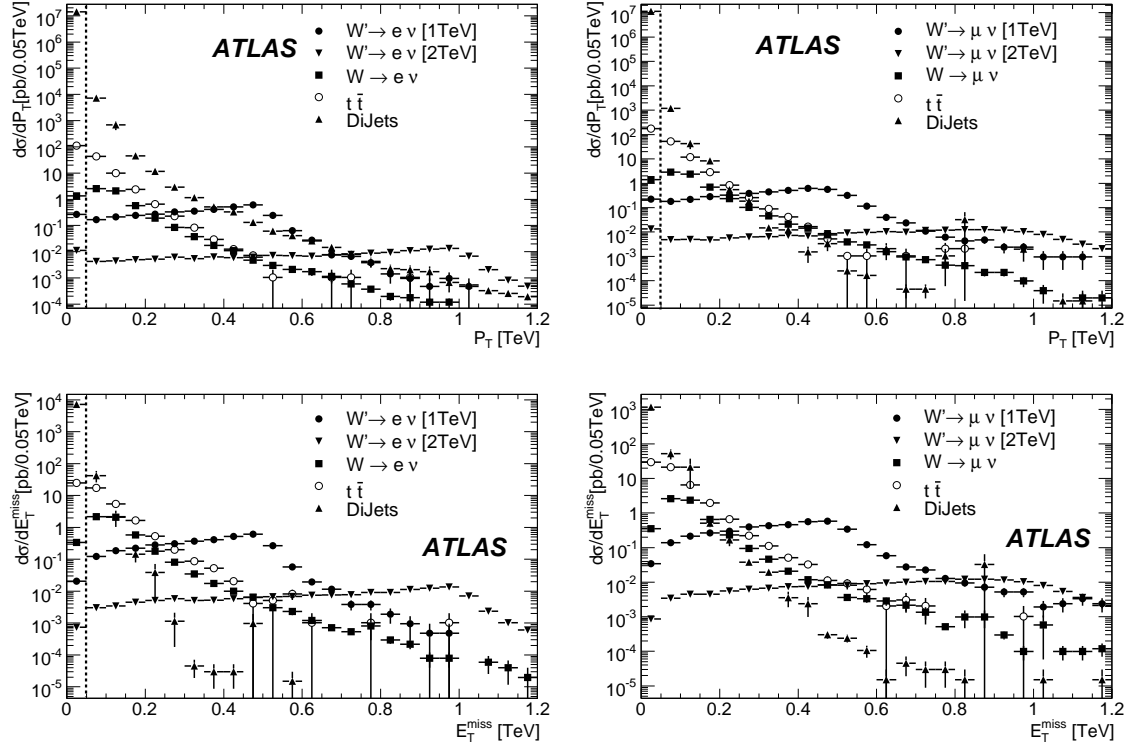


Figure 13: Top: leading lepton  $p_T$  distributions (left: electron events, right: muon events). Bottom:  $\cancel{E}_T$  distribution of events with only one reconstructed lepton with  $p_T > 50$  GeV (left: electron events, right: muon events).

- Only one reconstructed lepton with  $p_T > 50$  GeV within  $|\eta| < 2.5$ .
- Missing transverse energy  $\cancel{E}_T > 50$  GeV.

Figure 13 shows, on top, the lepton  $p_T$  distributions for the  $m = 1$  TeV and 2 TeV signal samples, Standard Model  $W$  boson,  $t\bar{t}$  and dijet production. The dashed vertical line shows the requirement value (50 GeV). The bottom plots in Fig. 13 show the  $\cancel{E}_T$  distributions for the same processes after requiring only one lepton with  $p_T > 50$  GeV; again, the requirement value (at 50 GeV) is shown with the dashed vertical line. This selection provides a relatively clean signal in the high transverse mass region, as shown in Fig. 14, which shows the transverse mass distributions after the requirements on  $p_T$  and  $\cancel{E}_T$ . The background can be further rejected by exploiting additional observables, described in next sections: lepton isolation, lepton fraction and jet veto criteria.

## 5.2 Background Rejection

After the kinematic requirements are applied, the  $t\bar{t}$  and dijets backgrounds are still larger than the high-mass tail of the Standard Model  $W$  boson close to the threshold value on the lepton  $p_T$  and on  $\cancel{E}_T$ . Since the uncertainties on the rate of these backgrounds are large, it is desirable to bring them below the irreducible background from  $W$  bosons. To achieve this, additional requirements are imposed on lepton isolation and on the lepton fraction, described below. A simpler selection strategy, based on a jet veto, is also explored, since it could prove useful during the first stages of data taking.

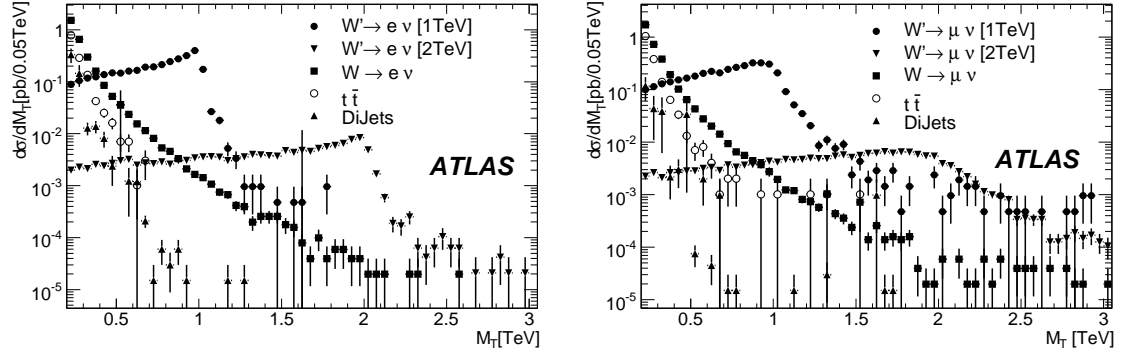


Figure 14: Transverse mass spectrum after the basic kinematic requirements for background and signal ( $m_{W'} = 1$  and 2 TeV). Left: electron mode; right: muon mode.

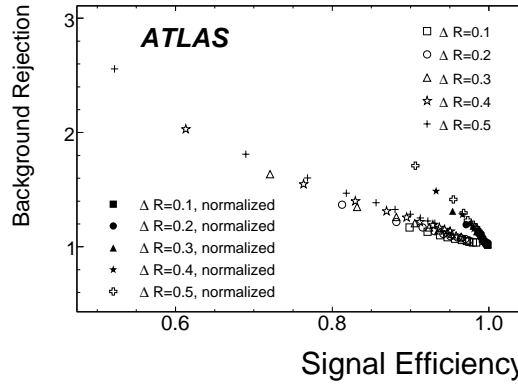


Figure 15:  $t\bar{t}$  background rejection and signal efficiency for different requirement values on the  $\Sigma p_T$  (squares) and  $(\Sigma p_T)/p_{T\text{lepton}}$  (triangles), for the muon channel. Each color corresponds to a different value for  $\Delta R$ , from 0.1 to 0.5.

### 5.2.1 Lepton Isolation

As the lepton from a  $W'$  boson decay is expected to be isolated, only events without high energy tracks around the lepton trajectory are accepted. The tracking isolation is done by requiring that the sum of the  $p_T$  of tracks in a  $\Delta R$ -cone around the lepton be below a threshold;  $\Delta R$  is defined as

$$\Delta R \equiv \sqrt{(\Delta\phi)^2 + (\Delta\eta)^2},$$

where  $\Delta\phi$  and  $\Delta\eta$  are the distances in azimuthal angle and in pseudo-rapidity, respectively, with the lepton under consideration.

Calorimeter isolation was also explored (the calorimetric energy deposited within the volume between two  $\Delta R$ -cones is required to be below a threshold).

Besides requiring a maximum value of  $\Sigma p_{T\text{tracks}}$ , the use of a *normalized* isolation requirement was also explored, in which the requirement is applied to the quantity  $\Sigma p_{T\text{tracks}}/p_{T\text{lepton}}$ . Five different  $\Delta R$  values were used in both cases; as shown in Fig. 15, the normalized isolation selection achieves a higher  $t\bar{t}$  rejection for the same efficiencies.

The calorimeter energy difference in two cones is not only of use in the electron case, but also in the muon one. High  $p_T$  muons coming from  $W'$  boson decays can also radiate a lot inside the material preceding the MS. This radiation appears as energy depositions close to the muon in the calorimeters.

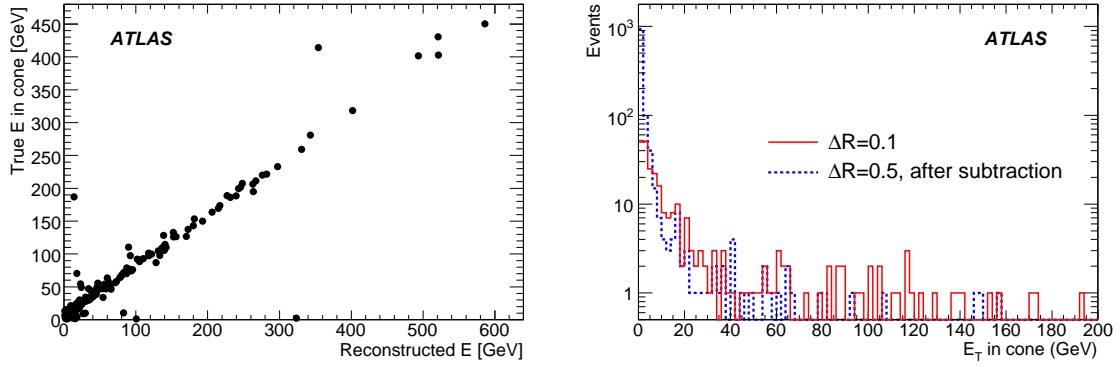


Figure 16: Left: the true energy deposition as a function of the reconstructed one in a cone of  $\Delta R=0.1$  for muons coming from decays of  $m = 2$  TeV  $W'$  bosons. Right: the solid histogram shows the energy recorded in a cone of  $\Delta R=0.1$  around the muon. The dashed histogram shows the energy recorded in a cone of  $\Delta R=0.5$  after the subtraction of the inner cone deposition.

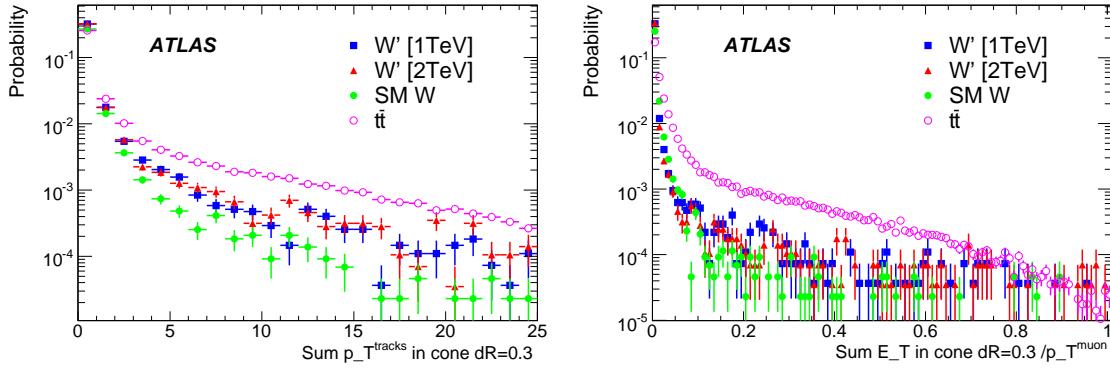


Figure 17: Left: distribution of an absolute track based isolation variable for muons. Right: distribution of a relative calorimetry based isolation variable for muons. In both cases the inner cone of  $\Delta R=0.1$  is subtracted.

As can be seen in Fig. 16 (right) the energy deposition in a cone of  $\Delta R < 0.1$  around the muon is much higher than the deposition in a cone of  $\Delta R < 0.5$  when the inner cone is subtracted. Moreover, in Fig. 16 (left) it is shown that in the majority of the cases the reconstructed energy deposition agrees well with the true one. Therefore, the energy deposition in an inner cone (e.g.  $\Delta R < 0.1$ ) must be subtracted also in the case of muons when isolation criteria based on calorimetry are applied. Also on track based isolation criteria an inner cone containing the muon track itself must be subtracted. In this case however, the inner cone can be much narrower, since it only needs to be able to exclude the track associated with the lepton under consideration. Figure 17 shows the distributions of the isolation energy for different event categories. For these plots, muons with  $p_T > 20$  GeV are considered.

For the analysis, a loose requirement of 0.05 is used on the normalized track-based isolation for both channels (electron and muon), and no requirement on the calorimeter-based isolation is applied. Tracks are included in the sum if  $0.02 < \Delta R(\text{track}, \text{lepton}) < 0.3$ . This requirement keeps about 99% of the signal for both masses ( $m_{W'} = 1$  and 2 TeV), rejects about 10% of the  $t\bar{t}$  events left after the basic selection and rejects over 99% of the dijet background.



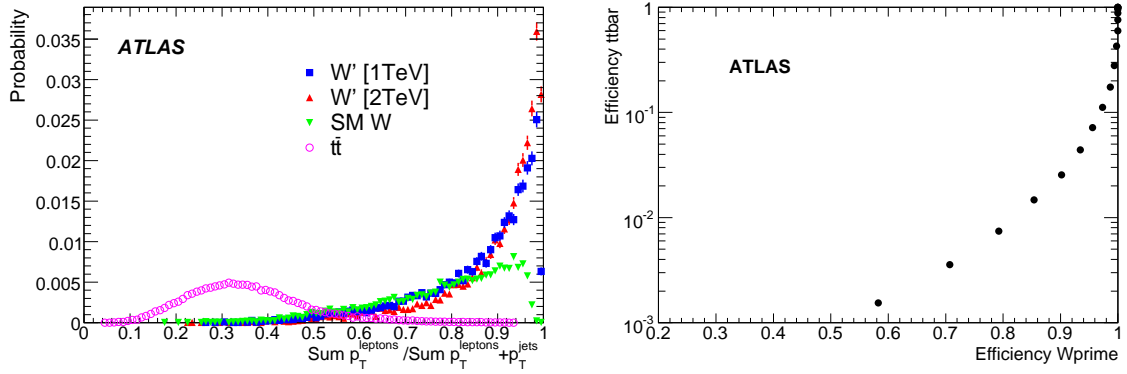


Figure 18: Left: distribution of the lepton fraction variable (see text) for different event categories. Right: signal efficiency versus  $t\bar{t}$  efficiency for different requirement values on the lepton fraction variable.

### 5.2.2 Lepton Fraction

Another variable that can be used to reduce the dijet and  $t\bar{t}$  backgrounds is the “lepton fraction” of the event, which can be expressed as  $\sum p_T^{\text{leptons}} / (\sum p_T^{\text{leptons}} + \sum E_T)$ , where the scalar sum on the lepton  $p_T$  sums over  $\cancel{E}_T$  as well. Essentially this variable measures the fraction of energy that can be attributed to leptons (including neutrinos, which are assumed to be the main contribution to  $\cancel{E}_T$ ) in an event. Here, out of the visible leptons, only the most energetic one is included in the sum (its  $p_T$  is added to the  $\cancel{E}_T$  to form  $\sum p_T^{\text{leptons}}$ ). The distribution of this variable is shown for different event categories in Fig. 18 (left). As expected, it shows a much lower value for  $t\bar{t}$  events (in pink) than for the rest of the samples used ( $W'$  boson signals and Standard Model  $W$  bosons). The efficiency for signal versus  $t\bar{t}$  events for different values of the variable, is shown in Fig. 18 (right). A requirement at 0.5 results in a signal efficiency of  $\sim 96\%$  in both channels and a rejection factor of  $\sim 45$  against the  $t\bar{t}$  background, and it suppresses all the remaining dijet events. This value will be used subsequently.

### 5.2.3 Jet Veto and Jet Multiplicity Requirements

A selection procedure based solely on veto-ing events with high jet activity could provide an alternative way to extract a signal in this search. Several requirements on jet activity were explored; in some, events were rejected if they include any jet over an energy threshold, in others, jet multiplicity information is used. The jet veto was applied just after the basic selection (i.e., lepton identification,  $p_T$  and  $\cancel{E}_T$  requirements).

Figure 19 shows the distribution of the  $p_T$  of the leading jets; the distribution on the left corresponds to the electron channel and the one on the right to the muon channel. Tables 2 and 3 show the expected rates for several jet veto criteria.

Figure 20 shows how after a 200 GeV jet veto requirement (and without isolation or lepton fraction requirements), most of the  $t\bar{t}$  and dijet background is rejected, and the signal to background ratio is good for high transverse mass values. Although the signal is reduced by between 20 and 30% with respect to selecting on isolation and lepton fraction, a jet veto requirement may be a good tool if the calibration of the  $\sum E_T$  (used to compute the lepton fraction) is not well understood in early data. However, in what follows, this requirement is not used.

| Requirement                           | $\sigma[\text{pb}]$ |            |           |            |             |
|---------------------------------------|---------------------|------------|-----------|------------|-------------|
|                                       | $W'$ 1 TeV          | $W'$ 2 TeV | $W$       | $t\bar{t}$ | Dijets      |
| No jets with $p_T > 100$ GeV          | 1.73(3)             | 0.069(1)   | 3.25(4)   | 2.79(5)    | $17 \pm 16$ |
| No jets with $p_T > 200$ GeV          | 2.37(3)             | 0.097(1)   | 4.12(5)   | 9.19(8)    | $21 \pm 16$ |
| No jets with $p_T > 500$ GeV          | 3.07(4)             | 0.131(2)   | 4.89(5)   | 15.4(1)    | $36 \pm 17$ |
| Less than 4 jets with $p_T > 40$ GeV  | 2.99(4)             | 0.130(2)   | 4.84(5)   | 3.85(5)    | $33 \pm 16$ |
| Less than 3 jets with $p_T > 100$ GeV | 3.01(4)             | 0.131(2)   | 4.85(5)   | 7.21(7)    | $34 \pm 16$ |
| Less than 2 jets with $p_T > 200$ GeV | 2.91(4)             | 0.126(2)   | 4.74(5)   | 9.28(8)    | $31 \pm 16$ |
| 200 GeV veto, $m_T > 0.7$ TeV         | 1.31(3)             |            | 0.0221(6) | 0          | 0           |
| 200 GeV veto, $m_T > 1.4$ TeV         |                     | 0.0473(1)  | 0.0008(1) | 0          | 0           |

Table 2: Cross-sections for signal and backgrounds for dijets,  $t\bar{t}$ ,  $W$  and  $W'$  boson samples for different requirements on jet content for the electron channel. The number in brackets is the error on the least significant digit.

| Requirement                           | $\sigma[\text{pb}]$ |            |          |            |               |
|---------------------------------------|---------------------|------------|----------|------------|---------------|
|                                       | $W'$ 1 TeV          | $W'$ 2 TeV | $W$      | $t\bar{t}$ | Dijets        |
| No jets with $p_T > 100$ GeV          | 1.99(3)             | 0.088(1)   | 3.76(4)  | 3.36(5)    | $0.8 \pm 0.8$ |
| No jets with $p_T > 200$ GeV          | 2.80(4)             | 0.123(2)   | 4.78(5)  | 11.19(9)   | $4.2 \pm 1.8$ |
| No jets with $p_T > 500$ GeV          | 3.63(4)             | 0.163(2)   | 5.69(5)  | 18.8(1)    | $22 \pm 4$    |
| Less than 4 jets with $p_T > 40$ GeV  | 3.49(4)             | 0.162(2)   | 5.64(5)  | 4.53(6)    | $22 \pm 4$    |
| Less than 3 jets with $p_T > 100$ GeV | 3.52(4)             | 0.164(2)   | 5.66(5)  | 8.52(8)    | $22 \pm 3$    |
| Less than 2 jets with $p_T > 200$ GeV | 3.42(4)             | 0.158(2)   | 5.51(5)  | 11.01(9)   | $18 \pm 3$    |
| 200 GeV veto, $m_T > 0.7$ TeV         | 1.56(3)             |            | 0.03(1)  | 0          | 0             |
| 200 GeV veto, $m_T > 1.4$ TeV         |                     | 0.062(1)   | 0.003(1) | 0          | 0             |

Table 3: Cross-sections for signal and backgrounds for dijets,  $t\bar{t}$ ,  $W$  and  $W'$  boson samples for different requirements on jet content for the muon channel. The number in brackets is the error on the least significant digit.

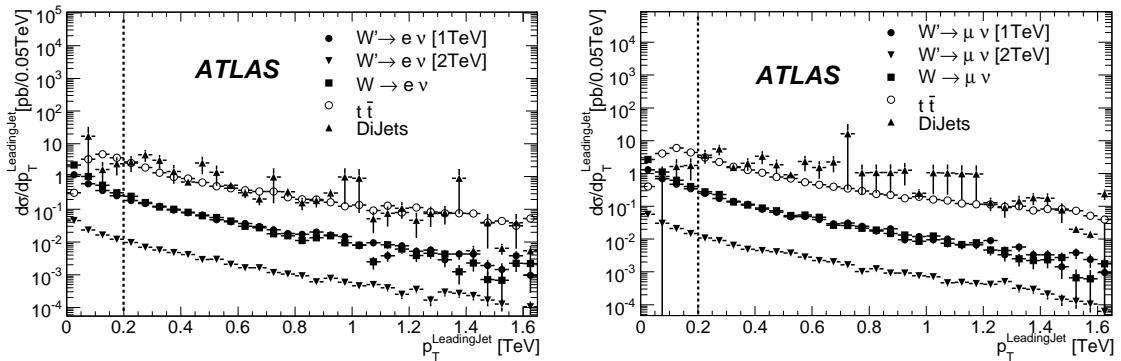


Figure 19: Distributions for the  $p_T$  of the leading jet. Left: electron selection. Right: muon selection.

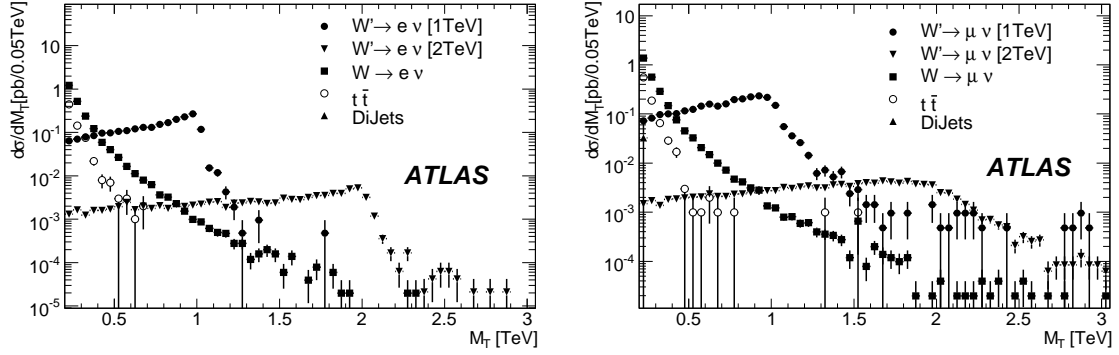


Figure 20:  $m_T$  spectrum after preselection requirements and a jet veto of  $E_T < 200$  GeV. Left: events with a high- $p_T$  electron; right: events with a high  $p_T$  muon.

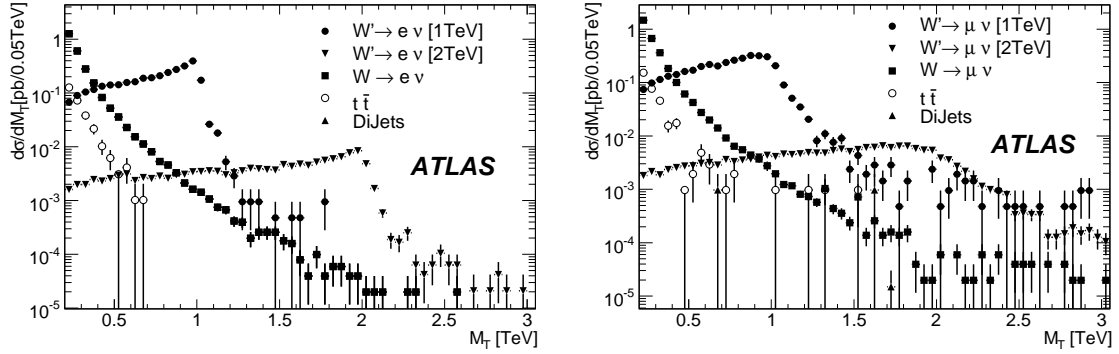


Figure 21: Expected transverse mass spectra after all requirements. Left: electron channel; right: muon channel.

### 5.3 Event Selection Results

Figure 21 shows the expected transverse momentum spectra for signal and background for both channels after all requirements (preselection, isolation, and lepton fraction). The selection requirement flow is shown in Tables 4 and 5. The transverse mass requirement has been chosen by maximizing the expected significance at the luminosity needed to get a  $5\sigma$  excess. The initial cross-sections for the  $W'$  boson signals and for the high mass  $W$  boson tail include the  $K$ -factor obtained in section 6.1.

| Requirement             | $\sigma$ [pb]   |                    |                     |                   |                              |
|-------------------------|-----------------|--------------------|---------------------|-------------------|------------------------------|
|                         | $W'$ (1 TeV)    | $W'$ (2 TeV)       | $W$ tail            | $t\bar{t}$        | Dijets[1-7]                  |
| (No requirement)        | 4.99            | 0.231              | 10.28               | 452               | $1.91 \times 10^{10}$        |
| Preselection            | $3.67 \pm 0.04$ | $0.160 \pm 0.002$  | $6.80 \pm 0.06$     | $150.57 \pm 0.40$ | $(13.6 \pm 0.2) \times 10^6$ |
| $p_T > 50$ GeV          | $3.43 \pm 0.04$ | $0.150 \pm 0.002$  | $5.53 \pm 0.05$     | $51.13 \pm 0.23$  | $(7.23 \pm 0.6) \times 10^3$ |
| $\cancel{E}_T > 50$ GeV | $3.40 \pm 0.04$ | $0.149 \pm 0.002$  | $5.19 \pm 0.05$     | $25.78 \pm 0.16$  | $45.33 \pm 16.65$            |
| Isolation               | $3.36 \pm 0.04$ | $0.148 \pm 0.002$  | $5.01 \pm 0.05$     | $23.30 \pm 0.16$  | $0.65 \pm 0.13$              |
| Lepton fraction         | $3.25 \pm 0.04$ | $0.145 \pm 0.002$  | $4.10 \pm 0.04$     | $0.50 \pm 0.02$   | 0                            |
| $m_T > 700$ GeV         | $1.86 \pm 0.03$ |                    | $0.0317 \pm 0.0008$ | 0                 | 0                            |
| $m_T > 1400$ GeV        |                 | $0.0740 \pm 0.001$ | $0.0014 \pm 0.0002$ | 0                 | 0                            |

Table 4: Cross-section for signal and backgrounds after each requirement. Electron mode.

| Requirement             | $\sigma$ [pb]   |                    |                     |                   |                                  |
|-------------------------|-----------------|--------------------|---------------------|-------------------|----------------------------------|
|                         | $W'$ (1 TeV)    | $W'$ (2 TeV)       | $W$ tail            | $t\bar{t}$        | Dijets[1-7]                      |
| (No requirement)        | 4.99            | 0.231              | 10.28               | 452               | $1.91 \times 10^{10}$            |
| Preselection            | $4.28 \pm 0.05$ | $0.199 \pm 0.002$  | $7.77 \pm 0.06$     | $205.30 \pm 0.46$ | $(11.2 \pm 0.19) \times 10^6$    |
| $p_T > 50$ GeV          | $4.03 \pm 0.04$ | $0.187 \pm 0.002$  | $6.40 \pm 0.06$     | $61.71 \pm 0.25$  | $(1.24 \pm 0.26) \times 10^3$    |
| $\cancel{E}_T > 50$ GeV | $4.00 \pm 0.04$ | $0.186 \pm 0.002$  | $6.04 \pm 0.05$     | $31.34 \pm 0.18$  | $74.32 \pm 23.28$                |
| Isolation               | $3.95 \pm 0.04$ | $0.185 \pm 0.002$  | $5.99 \pm 0.05$     | $28.70 \pm 0.17$  | $1.00 \pm 0.82$                  |
| Lepton fraction         | $3.81 \pm 0.04$ | $0.181 \pm 0.002$  | $4.85 \pm 0.05$     | $0.64 \pm 0.03$   | $(1.96 \pm 1.38) \times 10^{-3}$ |
| $m_T > 700$ GeV         | $2.20 \pm 0.03$ |                    | $0.043 \pm 0.002$   | $0.007 \pm 0.003$ | $0.001 \pm 0.001$                |
| $m_T > 1400$ GeV        |                 | $0.094 \pm 0.0001$ | $0.0031 \pm 0.0006$ | $0.001 \pm 0.001$ | $0.001 \pm 0.001$                |

Table 5: Cross-section for signal and backgrounds after each requirement. Muon mode.

## 6 Systematic Uncertainties

### 6.1 Generator-level Systematic Uncertainties

The input for the full simulation studies described in earlier sections was obtained by generating  $W'$  boson events using PYTHIA [27]. Events in the high-mass tail of the  $W$  boson were generated using PYTHIA as well. Both use the default PYTHIA parton distribution functions (PDFs), CTEQ6l, the CTEQ6 [37] LO (leading-order) fit with NLO (next-to-leading-order)  $\alpha_S$ . Here we report on generator-level studies which examine the effects of making use of the NLO matrix elements and varying the PDFs.

#### 6.1.1 Higher Orders

To evaluate contributions from higher order diagrams, we used MC@NLO [38] input to the HERWIG [39] event generator. Both  $W$  and  $W'$  boson events were generated using the  $W$  boson production process with the  $W$  boson mass set to the  $W'$  boson value for the latter. The  $W'$  boson widths were set to the values calculated by PYTHIA. The masses and widths used are listed in Table 6. Both MC@NLO and HERWIG were run using the default HERWIG PDFs, MRST2004nlo, the MRST 2004 fit using the standard  $\overline{\text{MS}}$  scheme at NLO [40].

One million events were generated for each generator at each of the masses. The cross-section is calculated for transverse mass above 70% of the  $W'$  boson mass, i.e. above the values listed in Table 6.

We define the  $K$ -factor to be the ratio of the MC@NLO cross-section to that from PYTHIA. These are shown as functions of  $\eta$  in Fig. 22.

| M (GeV) | $\Gamma$ (GeV) | Minimum $m_T$ (GeV) |
|---------|----------------|---------------------|
| 1000    | 34.739         | 700                 |
| 2000    | 70.540         | 1400                |
| 3000    | 106.390        | 2100                |

Table 6: Masses and widths used as input to MC@NLO/HERWIG generation of  $W'$  boson events. The third column gives the lower limit for the masses used to calculate cross-sections.

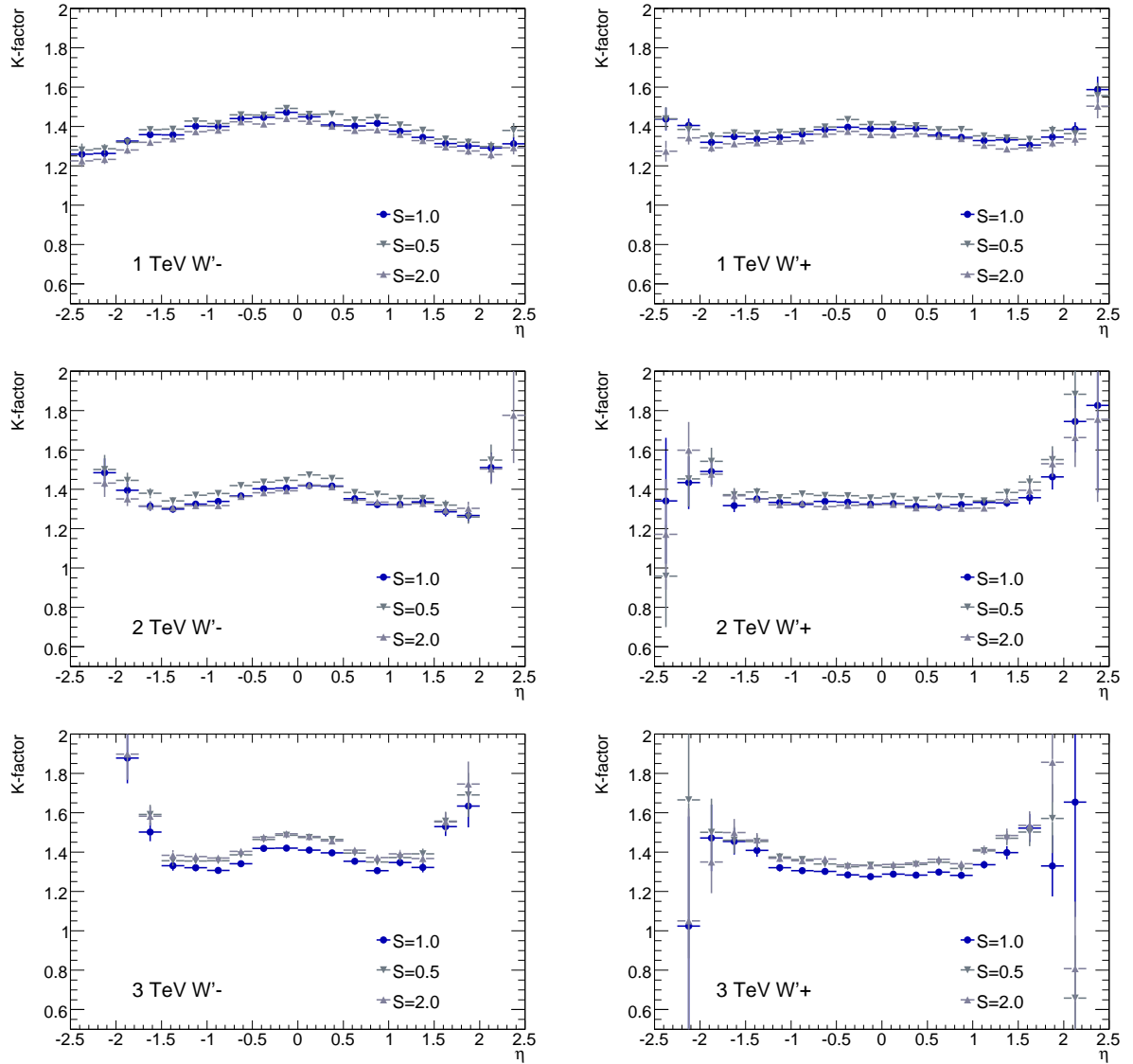


Figure 22:  $W'$  boson  $K$ -factors (ratios of MC@NLO and PYTHIA cross-sections) as functions of  $\eta$  for positive (left) and negative (right) charge for masses of 1 (top), 2 (middle) and 3 TeV (bottom).  $S$  is the common scale factor. The errors are statistical.

Integrals of the  $W'$  boson and  $W$  boson tail differential cross-sections are given in Table 7. The NLO predictions are 30-40% higher than those from PYTHIA, with little change with the variations in scale. Although the NLO/LO cross-section and acceptance ratios are of order 40%, the uncertainties on the NLO values are expected to be significantly smaller. Also, the QED corrections are partially included through PHOTOS [41] for FSR, and should have a small impact on the measurements in case of the observation of a signal.

| Process                  | Min. $m_T$ | PYTHIA $\sigma$ (fb) | NLO $\sigma$ (fb) | $K$ -factor | S=0.5    | S=2.0     |
|--------------------------|------------|----------------------|-------------------|-------------|----------|-----------|
| $W'(m = 1 \text{ TeV})+$ | 700        | 534. (1)             | 742. (1)          | 1.389 (4)   | 1.8% (2) | -1.8% (2) |
| $W'(m = 1 \text{ TeV})-$ | 700        | 1204. (1)            | 1644. (2)         | 1.365 (3)   | 1.7% (2) | -1.8% (2) |
| $W'(m = 2 \text{ TeV})+$ | 1400       | 62.6 (1)             | 83.0 (1)          | 1.327 (3)   | 2.7% (2) | -1.6% (2) |
| $W'(m = 2 \text{ TeV})-$ | 1400       | 20.3 (6)             | 27.7 (4)          | 1.362 (4)   | 3.0% (2) | -1.4% (2) |
| $W'(m = 3 \text{ TeV})+$ | 2100       | 6.73 (1)             | 8.69 (1)          | 1.292 (3)   | 3.7% (2) | 4.4% (2)  |
| $W'(m = 3 \text{ TeV})-$ | 2100       | 1.791 (6)            | 2.540 (4)         | 1.370 (5)   | 3.7% (2) | 4.4% (2)  |
| $W+$                     | 700        | 20.22 (7)            | 27.66 (8)         | 1.368 (6)   | 2.2% (4) | -0.6% (4) |
| $W-$                     | 700        | 8.93 (5)             | 12.56 (4)         | 1.407 (9)   | 2.6% (5) | -0.8% (5) |
| $W+$                     | 1400       | 1.042 (4)            | 1.424 (4)         | 1.366 (7)   | 2.2% (5) | -1.5% (5) |
| $W-$                     | 1400       | 0.354 (2)            | 0.499 (2)         | 1.41 (1)    | 1.8% (6) | -1.6% (5) |
| $W+$                     | 2100       | 0.1231 (3)           | 0.1657 (3)        | 1.346 (4)   | 3.0% (3) | 2.4% (3)  |
| $W-$                     | 2100       | 0.0346 (1)           | 0.0492 (1)        | 1.421 (6)   | 3.1% (3) | 2.5% (3)  |

Table 7: Integrated  $W'$  boson and  $W$  boson tail cross-sections for PYTHIA and MC@NLO with common scale factor  $S=1$ . Integral is over the full  $\eta$  range  $-2.5 < \eta < 2.5$ . The listed  $K$ -factors are the ratios of the integrated MC@NLO and PYTHIA cross-sections. The last two columns give the change in the MC@NLO cross-section when the common scale factor is changed by a factor of two. The statistical error in the last digit of each calculated quantity is shown in parentheses.

### 6.1.2 Parton Distribution Functions

The LHC will take data in a new energy regime and so we expect significant uncertainty in signal and background predictions due to our uncertainty in knowledge of the PDFs.

The CTEQ6.1 fits include 40 error PDFs corresponding to the two limits on each of 20 eigenvectors. These can be used to estimate the uncertainty in predictions obtained with the fit. Figure 23 shows the PYTHIA prediction for the  $m = 1 \text{ TeV}$   $W'$  boson differential cross-section as a function of  $\eta$  for the CTEQ6.1 central value and each of the 40 error sets. Events are required to have transverse mass above the threshold in Table 6.

We calculated cross sections for  $W'$  boson production with mass of 1 TeV using the CTEQ6.1 central value and error PDFs by integrating over the full  $\eta$  range ( $|\eta| < 2.5$ ) in Fig. 23. To estimate the overall uncertainty, the positive and negative deviations for each eigenvector were summed separately in quadrature for each charge sign. Where both deviations for an eigenvector had the same sign, only the larger magnitude was included in the sums. Table 8 shows the results.

Combining all the above, we assign a common  $K$ -factor of 1.37 for all masses and charges and assign an 8% uncertainty on this factor.

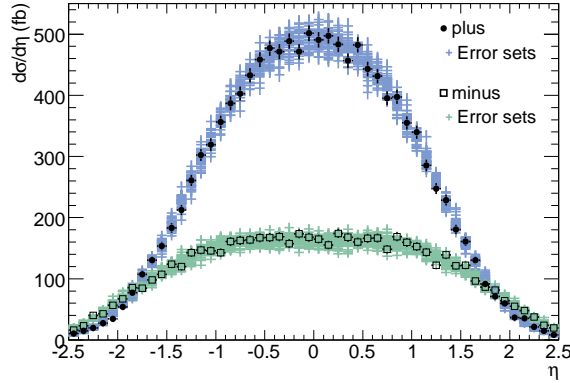


Figure 23: Muon  $\eta$  distributions for positively- and negatively-charged  $m = 1$  TeV  $W'$  bosons using the CTEQ 6.1 PDF central value (black) and 40 error sets.

| Process                  | Min. $m_T$ | $W+$                 | $W-$                  |
|--------------------------|------------|----------------------|-----------------------|
| $W' (m = 1 \text{ TeV})$ | 700        | -4.1% (5), +8.2% (5) | -11.1% (7), +3.5% (8) |

Table 8: CTEQ6.1 combined error set deviations for  $W'$  boson cross-sections. The statistical error on the last digit is shown in parentheses.

## 6.2 Instrumental Uncertainties

Detector related uncertainties for these studies can be easily divided in two categories: the ones related to the Reconstruction of the leptons and the ones corresponding to the global event activity as the  $\cancel{E}_T$  and the jet characteristics. However, the lepton reconstruction uncertainties can be the dominant factor in the  $\cancel{E}_T$  resolution

### 6.2.1 Lepton Reconstruction

Three main contributions can be easily identified in this category. The efficiency of lepton identification, as well as the fake rates associated with this, the  $p_T$  or  $E_T$  scale and its measurement resolution.

Systematic errors on the momentum scale of the muons can arise for instance due to the non-perfect knowledge of the magnetic field. To take into account such effects, a variation of  $\pm 1\%$  is applied to the  $p_T$  of the reconstructed muons. Positive and negative variations are considered separately. In a similar way but for energy, a variation of  $\pm 0.5\%$  was made for electrons.

An incomplete understanding of the material distributions inside the detector as well as possible misalignments in the MS can lead to an additional smearing of the momentum measurement resolution. To evaluate the impact of such contributions on the analysis, a smearing, based on early calibrations of  $\sigma(1/p_T) = 0.011/p_T \oplus 0.00017$  is applied. The first term enhances the Coulomb scattering smearing, while the second enhances the alignment contribution, and is the crucial factor in this study.

For the energy measurement resolution for electrons, the total  $\sigma(E_T)$  is smeared by  $0.0073 \times E_T$ , which enhances the constant term only.

Lepton identification efficiency is obviously important for this analysis. The identification efficiency can be estimated from the data, using the tag-and-probe method described in [42] for muons in the region  $20 < p_T < 50$  GeV and extrapolated to higher  $p_T$  using simulated data. A value of  $\pm 5\%$  has been chosen

for the evaluation of this uncertainty, corresponding to the early running period of integrated luminosities  $\mathcal{L} < 100 \text{ pb}^{-1}$ . In the case of electrons a  $\pm 1\%$  variation has been applied.

### 6.2.2 Jet Reconstruction

An uncertainty on the jet energy scale of  $\pm 7\%$  was imposed, together with an uncertainty on its resolution of  $\sigma(E_T) = 0.45 \times \sqrt{E_T} \oplus 5\%$ .

### 6.2.3 Missing Energy

If jets or leptons are systematically shifted, then missing transverse energy should be systematically shifted in a known direction. Based on the jet and leptons performance, the missing energy is shifted as follows:

$$\begin{aligned}
 \bullet \quad \cancel{E}_{T(\text{shifted})}(x) &= \cancel{E}_T(x) + E^{\text{lepton/jet}}(x) - E_{\text{shifted}}^{\text{lepton/jet}}(x) \\
 \bullet \quad \cancel{E}_{T(\text{shifted})}(y) &= \cancel{E}_T(y) + E^{\text{lepton/jet}}(y) - E_{\text{shifted}}^{\text{lepton/jet}}(y) \\
 \bullet \quad \sum E_{T(\text{shifted})} &= \sum E_T + E_T^{\text{lepton/jet}} - E_{T(\text{shifted})}^{\text{lepton/jet}}
 \end{aligned}$$

In the case of muons, momentum is used instead of energy.

## 6.3 Summary of Systematic Uncertainties

The effects of the experimental uncertainties are summarized in Tables 9 and 10.

| Description of systematic | electrons            |                      | muons                |                      |
|---------------------------|----------------------|----------------------|----------------------|----------------------|
|                           | $\delta\sigma_s$ [%] | $\delta\sigma_b$ [%] | $\delta\sigma_s$ [%] | $\delta\sigma_b$ [%] |
| lepton energy scale +     | +0.8                 | +1.8                 | +1.2                 | +4.6                 |
| lepton energy scale -     | -0.7                 | -2.1                 | -1.2                 | -4.4                 |
| lepton energy resolution  | +0.1                 | +0.2                 | -1.0                 | +3.7                 |
| efficiency +              | +1.0                 | +1.0                 | +5.                  | +5.                  |
| efficiency -              | -1.0                 | -1.0                 | -5.                  | -5.                  |
| Jet energy scale +        | +0.1                 | -0.2                 | -0.1                 | +0.1                 |
| Jet energy scale -        | +0.1                 | -0.2                 | +0.1                 | +0.7                 |
| Jet energy resolution     | +0.0                 | +0.1                 | -0.1                 | +0.3                 |
| Luminosity                | $\pm 3.$             |                      | $\pm 3.$             |                      |

Table 9: Effect of the detector systematics in percentage for  $m_{W'} = 1 \text{ TeV}$ .

## 7 Discovery Potential

In order to assess the ATLAS discovery potential in the search for a  $W' \rightarrow \ell + \cancel{E}_T$  signal, the luminosity needed for a  $5\sigma$  excess is obtained as a function of the mass of the  $W'$  boson.

The significance is obtained from the expected number of signal and background events in the region  $m_T > 0.7m_{W'}$ , where  $m_{W'}$  is the mass of the hypothesized  $W'$  boson. Calling these expected numbers  $s$  and  $b$ , respectively, the significance  $S$  is obtained as

$$S = \sqrt{2((s+b)\ln(1+s/b) - s)}$$



| Description of systematic | electrons            |                      | muons                |                      |
|---------------------------|----------------------|----------------------|----------------------|----------------------|
|                           | $\delta\sigma_s$ [%] | $\delta\sigma_b$ [%] | $\delta\sigma_s$ [%] | $\delta\sigma_b$ [%] |
| lepton energy scale +     | +0.7                 | +1.2                 | +1.5                 | +3.4                 |
| lepton energy scale -     | -0.4                 | -3.7                 | -1.7                 | -2.5                 |
| lepton energy resolution  | -0.03                | 0.0                  | -4.2                 | +6.8                 |
| efficiency +              | +1.0                 | +1.0                 | +5.                  | +5.                  |
| efficiency -              | -1.0                 | -1.0                 | -5.                  | -5.                  |
| Jet energy scale +        | +0.1                 | 1.2                  | +0.1                 | +0.8                 |
| Jet energy scale -        | -0.1                 | 0                    | -0.3                 | -0.1                 |
| Jet energy resolution     | -0.1                 | 0                    | +0.1                 | -0.1                 |
| Luminosity                | $\pm 3.$             |                      | $\pm 3.$             |                      |

Table 10: Effect of the detector systematics in percentage for  $m_{W'} = 2$  TeV.

which gives a good approximation to the likelihood-ratio based significance in the low statistics regime. Figure 24 shows the expected integrated luminosity needed for a 5-sigma excess as a function of the mass of the  $W'$  boson.

Higher order corrections for  $W'/W \rightarrow \ell\nu$  processes are taken into account as stated in section 6.1. Systematic uncertainties listed in Tables 9 and 10 are taken into account by increasing the expected background by the sum in quadrature of its positive expected variations, and by reducing the signal by the sum in quadrature of its expected negative variations; this assumes no correlations of the expected signal and background expectations and, as a result, produces a conservative estimate.

For comparison, the integrated luminosity values for a  $5\sigma$  significance were also obtained taking into account the shape of the signal and background  $m_T$  distributions. This was done using a technique in which, instead of an ensemble of Monte Carlo pseudo-experiments [43], a Fast Fourier Transform (FFT) is used to calculate the experimental estimator distributions [44]. This method allows a fast determination of the probability that background fluctuations produce a signal-like result, but it depends on the assumption that both the location of the signal and its shape are well known. Treating each bin of the transverse mass distribution as an independent search channel, and combining them accordingly, the resulting sensitivity is in general higher than the estimation given in the number counting approach. With this method, the luminosity required for a  $5\sigma$  effect was reduced between 20 and 35% with respect to the values shown in Fig. 24.

Even for very low integrated luminosities (of the order of picobarns), a  $W'$  boson with a mass above the current experimental limits could be found with a significance in excess of  $5\sigma$ , while, with  $1 \text{ fb}^{-1}$ , masses of the order of 3 TeV can be reached. As an illustration, Figs 25 and 26 show Monte Carlo outcomes of pseudo-experiments corresponding to  $10 \text{ pb}^{-1}$  and  $100 \text{ pb}^{-1}$ , respectively, for both channels. The solid line histograms depict the expected background, those in dotted lines the  $m = 1$  TeV  $W'$  boson signal and the dashed-dotted line histograms show possible  $m = 2$  TeV  $W'$  boson signals.

## 8 Summary and Conclusion

The potential for the ATLAS experiment to reconstruct and identify the decay of a heavy, charged gauge boson into a lepton and a neutrino has been studied. Various systematic and theoretical uncertainties have been considered, as well as plausible estimations of our uncertainties about the performance of the detector in the early stages of data taking. These studies show that, even with integrated luminosities as low as  $10 \text{ pb}^{-1}$  of data, it would be possible to discover this type of bosons, should they exist not far beyond the current experimental limits. With an integrated luminosity of a few  $\text{fb}^{-1}$ , ATLAS has the

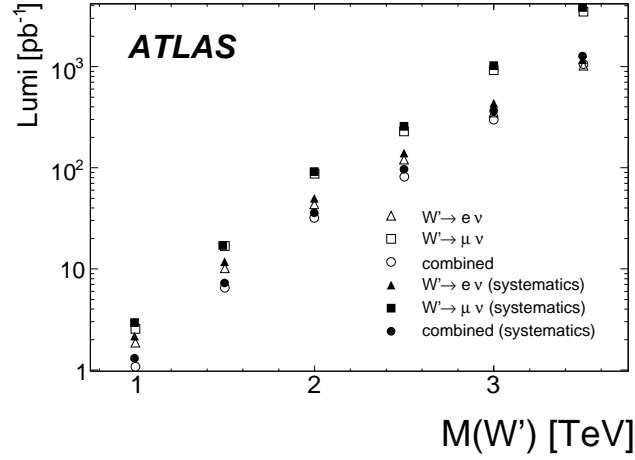


Figure 24: Integrated luminosity needed to have a  $5\sigma$  discovery as a function of the mass of the  $W'$  bosons; triangles correspond to the  $e\nu$  search, squares to  $\mu\nu$ , circles to the combined search. Filled markers include the effect of systematic uncertainties.

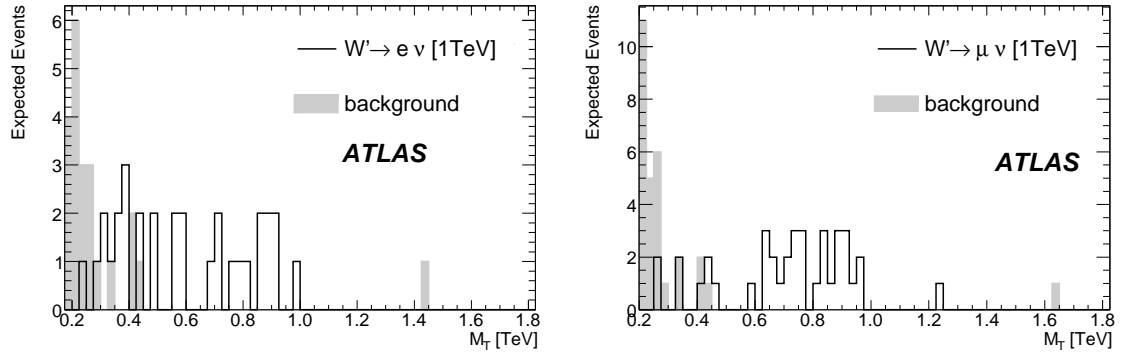


Figure 25: Monte Carlo pseudo-experiment for  $10 \text{ pb}^{-1}$ . Left: electron channel; right: muon channel.

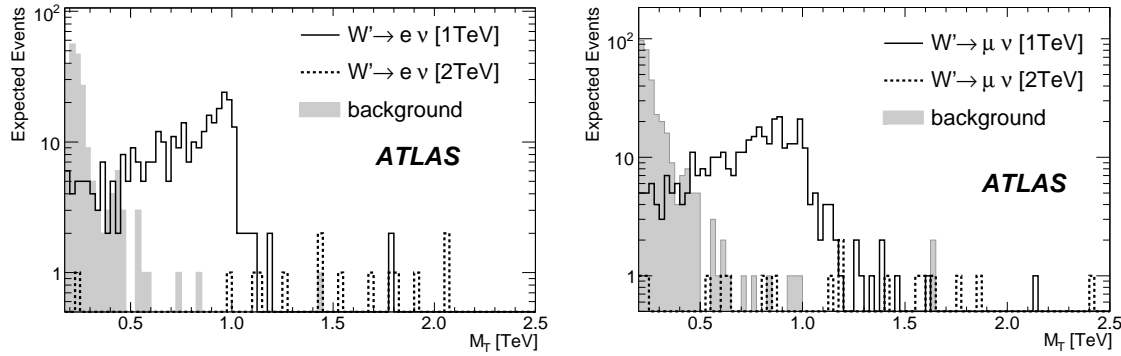


Figure 26: Monte Carlo pseudo-experiment for  $100 \text{ pb}^{-1}$ . Left: electron channel; right: muon channel.

potential to discover these particles for masses up to 4 TeV.

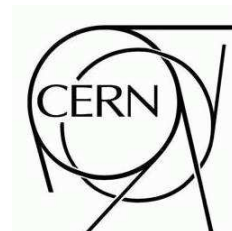
## References

- [1] P. Langacker, R. W. Robinett, and J. L. Rosner, *Phys. Rev.* **D30** (1984) 1470.
- [2] F. Buccella, G. Mangano, O. Pisanti, and L. Rosa, *Phys. Atom. Nucl.* **61** (1998) 983–990.
- [3] R. W. Robinett, *Phys. Rev.* **D26** (1982) 2388.
- [4] J. C. Pati and A. Salam, *Phys. Rev.* **D10** (1974) 275–289.
- [5] R. N. Mohapatra and J. C. Pati, *Phys. Rev.* **D11** (1975) 2558.
- [6] G. Senjanovic and R. N. Mohapatra, *Phys. Rev.* **D12** (1975) 1502.
- [7] G. Azuelos, K. Benslama, and J. Ferland, *J. Phys.* **G32** (2006) 73–92.
- [8] G. Beall, M. Bander, and A. Soni, *Phys. Rev. Lett.* **48** (1982) 848.
- [9] P. L. Cho and M. Misiak, *Phys. Rev.* **D49** (1994) 5894–5903.
- [10] M. Cvetič and S. Godfrey, [arXiv:hep-ph/9504216](https://arxiv.org/abs/hep-ph/9504216).
- [11] N. Arkani-Hamed, S. Dimopoulos, and G. R. Dvali, *Phys. Rev.* **D59** (1999) 086004.
- [12] G. Azuelos and G. Polesello, *Eur. Phys. J.* **C39S2** (2005) 1–11.
- [13] G. Polesello and M. Prata, *Eur. Phys. J.* **C32S2** (2003) 55–67.
- [14] T. G. Rizzo, *AIP Conf. Proc.* **530** (2000) 290–307, [arXiv:hep-ph/9911229](https://arxiv.org/abs/hep-ph/9911229).
- [15] M. J. Duff, [arXiv:hep-th/9410046](https://arxiv.org/abs/hep-th/9410046).
- [16] H. Georgi, E. E. Jenkins, and E. H. Simmons, *Phys. Rev. Lett.* **62** (1989) 2789.
- [17] N. Arkani-Hamed *et al.*, *JHEP* **08** (2002) 021.
- [18] G. Azuelos *et al.*, *Eur. Phys. J.* **C39S2** (2005) 13–24.
- [19] P. Chiappetta, [arXiv:hep-ph/9405251](https://arxiv.org/abs/hep-ph/9405251).
- [20] D. J. Gross, J. A. Harvey, E. J. Martinec, and R. Rohm, *Phys. Rev. Lett.* **54** (1985) 502–505.
- [21] K. S. Babu, X.-G. He, and E. Ma, *Phys. Rev.* **D36** (1987) 878.
- [22] F. Aversa, S. Bellucci, M. Greco, and P. Chiappetta, *Phys. Lett.* **B254** (1991) 478–484.
- [23] G. Altarelli, B. Mele, and M. Ruiz-Altaba, *Z. Phys.* **C45** (1989) 109.
- [24] **D0** Collaboration, V. M. Abazov *et al.*, *Phys. Rev. Lett.* **100** (2008) 031804.
- [25] **ATLAS** Collaboration, *CERN/LHCC* **99-15** (1999) .
- [26] **ATLAS** Collaboration, “Monte Carlo Generators for the ATLAS Computing System Commissioning.” This volume.

- 390 [27] T. Sjostrand, S. Mrenna, and P. Skands, *JHEP* **05** (2006) 026.
- 391 [28] J. Pumplin *et al.*, *JHEP* **07** (2002) 012.
- 392 [29] **ATLAS** Collaboration, *CERN/LHCC 97-22* (1997) .
- 393 [30] **ATLAS** Collaboration, “Muon Reconstruction and Identification Performance in ATLAS: Studies  
394 with Simulated Monte Carlo Samples.” This volume.
- 395 [31] **ATLAS** Collaboration, “Reconstruction and Identification of Electrons in ATLAS.” This volume.
- 396 [32] **ATLAS** Collaboration, “EM Calorimeter Calibration and Performance.” This volume.
- 397 [33] **ATLAS** Collaboration, “Measurement of Missing Transverse Energy in ATLAS.” This volume.
- 398 [34] **ATLAS** Collaboration, “The ATLAS Experiment at the CERN Large Hadron Collider.” Accepted  
399 by JINST, 2008.
- 400 [35] **ATLAS** Collaboration, “Overall Trigger Strategy for the Electron and Photon Selection.” This  
401 volume.
- 402 [36] **ATLAS** Collaboration, “Performance of the ATLAS Muon Trigger Slice with Simulated Data.”  
403 This volume.
- 404 [37] J. Pumplin, A. Belyaev, J. Huston, D. Stump, and W. K. Tung, *JHEP* **02** (2006) 032.
- 405 [38] S. Frixione, P. Nason, and B. R. Webber, *JHEP* **08** (2003) 007.
- 406 [39] G. Corcella *et al.*, arXiv:hep-ph/0210213.
- 407 [40] A. D. Martin, R. G. Roberts, W. J. Stirling, and R. S. Thorne, *Phys. Lett.* **B604** (2004) 61–68.
- 408 [41] P. Golonka and Z. Was, *Eur. Phys. J.* **C45** (2006) 97–107.
- 409 [42] **ATLAS** Collaboration, “In-Situ Determination of the Performance of the ATLAS Muon  
410 Spectrometer.” This volume.
- 411 [43] T. Junk, *Nucl. Instrum. Meth.* **A434** (1999) 435–443.
- 412 [44] H. Hu and J. Nielsen, arXiv:physics/9906010.  
413 <http://www.citebase.org/abstract?id=oai:arXiv.org:physics/9906010>.



# ATLAS NOTE



July 16, 2008

## Search for Scalar Leptoquarks and Right-handed $W$ Bosons and Neutrinos in Dilepton-Jets Final States

The ATLAS Collaboration

### Abstract

Final states with high- $p_T$  leptons and jets are predicted by many Beyond the Standard Model (BSM) scenarios. Two prominent models are used here as guides to understanding the event topologies: the scalar leptoquarks and the Left-Right Symmetry. In contrast to many SUSY signatures, their topologies rarely contain missing energy. Their discovery potential with early ATLAS data, corresponding to an integrated luminosity of a few hundred inverse picobarns, is discussed.

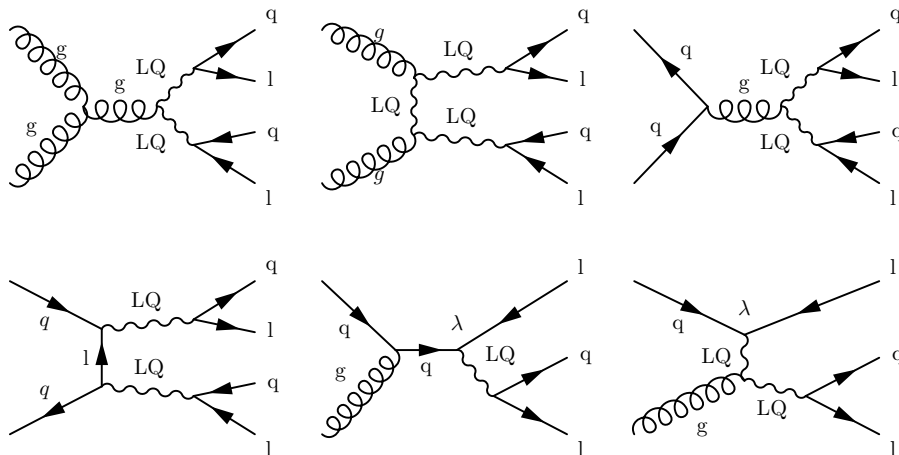


Figure 1: Feynman diagrams for leptoquark production.

## 1 Introduction

Grand Unification has inspired many extensions of the Standard Model. Such models introduce new, usually very heavy particles and previous searches for Grand Unification Theory (GUT) signatures have placed limits on masses and interaction strengths of the new particles. The LHC will probe new regions of parameter space, allowing for a direct search for these particles. Decays characterized by final states with two highly energetic leptons, two jets and no missing transverse energy are studied in this note. The models for new physics considered for this note are described below. The simulation of signal and background processes is described in section 2. In section 4 the baseline selection that is used for all analyses is explained. After the trigger requirements are given (section 3), section 5 details the specifics of each of the analyses. The systematics are described in section 6 and the final sensitivity estimates are given in section 7.

### 1.1 Leptoquarks

The experimentally observed symmetry between leptons and quarks has motivated the search for leptoquarks (LQ), hypothetical bosons carrying both quark and lepton quantum numbers, as well as fractional electric charge [1–5]. Leptoquarks could, in principle, decay into any combination of a lepton and a quark. Experimental limits on lepton number violation, flavor-changing neutral currents, and proton decay favour three generations of leptoquarks. In such a scenario, each leptoquark couples to a lepton and a quark from the same Standard Model generation [6]. Leptoquarks can either be produced in pairs by the strong interaction or in association with a lepton via the leptoquark-quark-lepton coupling. Figure 1 shows the Feynman diagrams for leptoquark production processes available at the LHC.

This note describes the search for leptoquarks decaying to either an electron and a quark or a muon and a quark. The branching ratio of a leptoquark to a charged lepton and a quark is denoted as  $\beta$ . Decays to neutrinos are not considered, and events are not explicitly selected based on the flavor of the quark. The experiments at the Tevatron have searched for first (decaying to  $eq$ ), second (decaying to  $\mu q$ ), and third (decaying to  $\tau q$ ) generation scalar leptoquarks. For  $\beta = \mathcal{B}(LQ \rightarrow \ell^\pm q) = 1$ , the DØ [7] and CDF [8] collaborations have set 95%CL limits for first generation scalar leptoquarks of  $m_{LQ_1} > 256$  GeV and  $m_{LQ_1} > 236$  GeV, respectively. These limits are based on integrated  $p\bar{p}$  luminosities of approximately  $250 \text{ pb}^{-1}$  and  $200 \text{ pb}^{-1}$ . The results for second generation leptoquarks,  $m_{LQ_2} > 251$  GeV and  $m_{LQ_2} > 226$  GeV, were obtained with  $300 \text{ pb}^{-1}$  and  $200 \text{ pb}^{-1}$  by the DØ [9]

and CDF [10] experiments, respectively.

The Tevatron exclusion limits are expected to reach 300-350 GeV in the near future.

## 1.2 Left-Right Symmetry

Left-Right Symmetric Models (LRSMs) of the weak interaction address two important topics: the nonzero masses of the three known left-handed neutrinos [11] and baryogenesis. LRSMs conserve parity at high energies by introducing three new heavy right-handed Majorana neutrinos  $N_e$ ,  $N_\mu$  and  $N_\tau$ . The smallest gauge group that implements a LRSM is  $SU(2)_L \times SU(2)_R \times U(1)_{B-L}$ . At low energies, the left-right symmetry is broken and parity is violated. The Majorana nature of the new heavy neutrinos explains the masses of the three left-handed neutrinos through the see-saw mechanism [12]. The lepton number  $L$  could be violated in processes that involve the Majorana neutrinos. This opens a window to the very attractive theoretical scenario for baryogenesis via leptogenesis, where baryon and lepton numbers  $B$  and  $L$  are violated but  $B - L$  is conserved.

In addition to the Majorana neutrinos, most general LRSMs also introduce the new intermediate vector bosons  $W_R$  and  $Z'$ , Higgs bosons, and a left-right mixing parameter. The most restrictive lower limit on the mass of the  $W_R$  boson comes from the  $K_L - K_S$  mass difference which requires  $m_{W_R} > 1.6$  TeV. This lower limit is subject to large corrections from higher-order QCD effects. Heavy right-handed Majorana neutrinos with masses of about a few hundred GeV would be consistent with the data from supernova SN1987A. Such heavy neutrinos would allow for a  $W_R$  boson at the TeV mass scale. This scenario would also be consistent with LEP data on the invisible width of the  $Z$  boson. Present experimental data on neutral currents imply a lower limit on the mass of a  $Z'$  boson of approximately 400 GeV. Recent direct searches [13] for the  $W_R$  boson at DØ give a lower mass limit of 739 GeV and 768 GeV, assuming the  $W_R$  boson could decay to both lepton pairs and quark pairs, or only to quark pairs, respectively. However, heavy Majorana neutrinos decaying to a lepton and a pair of quarks (detected as jets) were not searched for in those analyses.

The new intermediate vector bosons  $W_R$  and  $Z'$  would be produced at the LHC via the Drell-Yan (DY) process like normal  $W$  and  $Z$  bosons. Their decays would be a source of new Majorana neutrinos. The Feynman diagram for  $W_R$  boson production and its subsequent decay to a Majorana neutrino is shown in Fig. 2. This note describes an analysis of  $W_R$  boson production and its decays  $W_R \rightarrow eN_e$  and  $W_R \rightarrow \mu N_\mu$ , followed by the decays  $N_e \rightarrow eq'\bar{q}$  and  $N_\mu \rightarrow \mu q'\bar{q}$ , which can be detected in final states with (at least) two leptons and two jets.

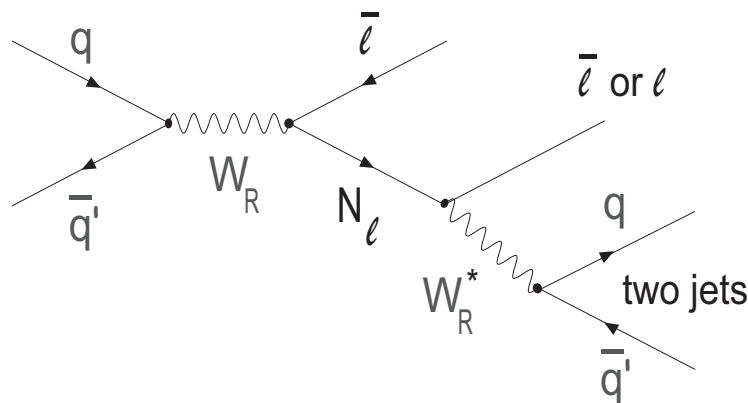


Figure 2: Feynman diagram for  $W_R$  boson production and its decay to the a Majorana neutrino  $N_\ell$ .

| $m_{LQ}$ in GeV | $\sigma(pp \rightarrow LQ\bar{L}\bar{Q})$ (NLO) in pb |
|-----------------|---|
| 300             | $10.1 \pm 1.5$  |
| 400             | $2.24 \pm 0.376$                                      |
| 600             | $0.225 \pm 0.048$                                     |
| 800             | $0.0378 \pm 0.0105$                                   |

Table 1: NLO cross-sections for scalar leptoquark pair production at the LHC.

## 2 Simulation of Physics Processes

### 2.1 Leptoquarks

The signals have been studied using samples of first generation (1st gen.) and second generation (2nd gen.) scalar leptoquarks simulated with the Monte Carlo (MC) generator PYTHIA [14]. The next to leading order (NLO) cross-sections for leptoquark pair production at 14 TeV  $pp$  centre-of-mass energy are shown in Table 1 for the four simulated leptoquark masses.

### 2.2 Left-Right Symmetry

Studies of the discovery potential for  $W_R$  bosons and the Majorana neutrinos,  $N_e$  and  $N_\mu$  produced in their decays, were performed using datasets simulated with the MC generator PYTHIA according to a particular implementation [15] of a LRSM described in [16]. The Standard Model axial and vector couplings, the CKM matrix for the quark sector, no mixing between the new and Standard Model intermediate vector bosons, and phase space isotropic decays of Majorana neutrinos are assumed for the right-handed sector in this model. The products of leading-order production cross-sections  $\sigma(pp \rightarrow W_R X)$  and branching fractions to studied final states  $W_R \rightarrow \ell N_\ell \rightarrow \ell \ell j j$  are 24.8 pb for  $m_{W_R} = 1800$  GeV,  $m_{N_e} = m_{N_\mu} = 300$  GeV and 47.0 pb for  $m_{W_R} = 1500$  GeV,  $m_{N_e} = m_{N_\mu} = 500$  GeV. In the rest of this note, these samples are referred to as LRSM\_18\_3 and LRSM\_15\_5, respectively. The Majorana nature of the new heavy neutrinos allows for same-sign and opposite-sign dileptons.

### 2.3 Background Processes

The main sources of background for the analyses presented here are  $t\bar{t}$  and  $Z/\gamma^* + \text{jets}$  production processes. Multijet production where two jets are misidentified as leptons represents another background. In addition, minor contributions arise from diboson production. Other potential background sources, such as single-top production, were also studied. Their contribution was found to be insignificant.

- $Z/\gamma^*$  background was studied using a combination of two MC samples with generator-level dilepton invariant mass preselections of  $m_{\ell\ell} > 60$  GeV and  $m_{\ell\ell} > 150$  GeV, the latter sample corresponding to a much larger integrated luminosity than the former. The samples were normalized to the given luminosity using their partial cross-sections and the NLO estimate  $\sigma(pp \rightarrow Z) \times \mathcal{B}(Z \rightarrow \ell^+ \ell^-) = 2032$  pb, obtained with the MC generator FEWZ [17, 18].

For logistical reasons, the sample with the lower mass preselection was generated using the MC generator PYTHIA [14], and the sample with higher mass preselection was generated using HERWIG [19]. In both cases, the CTEQ6L1 [20] parton distribution functions were used. The consistency between the two samples was verified at high dilepton masses.

- $t\bar{t}$  background was simulated using the MC generator MC@NLO [21] using the CTEQ6M [20] parton distribution functions. It was normalized to the given integrated luminosity using a production cross-section of 833 pb estimated to the next-to-leading order (NLO+NLL) [22].



- The diboson samples were generated using HERWIG with a generator-level preselection on the invariant mass of  $Z/\gamma^* > 20$  GeV. With this requirement, the NLO partial cross-sections for  $WW$ ,  $WZ$  and  $ZZ$  boson pair production processes were numerically estimated (using MC@NLO) to be 117.6 pb, 56.4 pb, 17.8 pb, respectively. The CTEQ6L1 parton distribution functions were used for event generation.
- The multijet background was simulated using PYTHIA with the CTEQ6L1 structure functions. The normalization was based on PYTHIA cross-section estimates. After lepton identification requirements, the statistics of these samples are very limited, such that no reliable estimate of this background could be made at this time.

### 3 Trigger Requirements

The trigger system [27] of the ATLAS experiment has three levels, L1, L2 and the Event Filter (EF). To ensure high overall trigger efficiencies, our analyses rely on single lepton trigger streams with relatively low thresholds. The dielectron analyses rely on the single electron-based trigger called e55 which has a threshold of around 60 GeV [27]. When selected events fail this trigger, the analyses rely on the lower-threshold (about 25 GeV) single electron trigger called e22i [27] in which the electron is required to be isolated. A single muon trigger with threshold about 20 GeV (mu20 [27]) is used in the dimuon analyses.

Final states studied in this note always contain two high- $p_T$  leptons. While the baseline selection described in section 4 requires two leptons with  $p_T > 20$  GeV, most signal events contain at least one lepton with significantly higher  $p_T$ . As a result, the overall trigger efficiency for events that satisfy all analysis selection criteria (section 5) exceeds 95%. The trigger efficiencies for signal MC events that satisfy all selection criteria are shown in Table 2.

| Process   | L1     | L2    | EF    | L1*L2*EF |
|---|--------|-------|-------|----------|
| 1st gen. leptoquarks $m_{LQ} = 400$ GeV                       | 100.0% | 99.4% | 97.6% | 97.0%    |
| 2nd gen. leptoquarks $m_{LQ} = 400$ GeV                       | 97.7%  | 99.1% | 99.7% | 96.5%    |
| LRSM (ee) $m_{W_R} = 1800$ GeV, $m_{N_e} = 300$ GeV           | 100.0% | 99.2% | 97.2% | 96.4%    |
| LRSM ( $\mu\mu$ ) $m_{W_R} = 1800$ GeV, $m_{N_\mu} = 300$ GeV | 96.8%  | 98.7% | 98.9% | 94.5%    |

Table 2: Overall trigger efficiencies for signal events that satisfy all selection criteria.

### 4 Baseline Event Selection

The baseline event selection, common for all analyses presented in this note, requires two leptons and two jets. All analyses use the same selection criteria for signal electron, muon, and jet candidates. The baseline selection criteria for these reconstructed objects are summarized below. Performance studies are described elsewhere [23–26].

Electron candidates are identified as energy clusters reconstructed in the liquid argon electromagnetic calorimeter that match tracks reconstructed in the inner tracking detector and satisfy the *medium* electron identification requirements [23].

Muon candidates are identified as tracks in the inner tracking detector whose extrapolations match tracks in the muon spectrometer [24] and satisfy relative isolation energy requirements  $E_T^{iso}/p_T^\mu \leq 0.3$ .  $p_T^\mu$  is the muon candidate’s transverse momentum and  $E_T^{iso}$  is the energy detected in the calorimeters in a cone of  $\Delta R = \sqrt{\Delta\eta^2 + \Delta\phi^2} = 0.2$  around the muon candidate’s reconstructed trajectory, corrected for the expected energy deposition by a muon.

Jets are identified as energy clusters reconstructed in the calorimeters using a  $\Delta R=0.4$  cone algorithm [25].  $\Delta R$  between a jet and any electron candidate (as defined above) must be larger than 0.1. This veto is imposed to avoid electrons being misidentified as jets. It is applied in all analyses, regardless of whether electrons are explicitly considered in the final states or not. The jet energy scale calibration is performed using full MC simulation and requires that the average reconstructed jet energy agrees with the average predicted jet energy. The same jet reconstruction algorithm, with cone size  $\Delta R = 0.4$ , is used for both reconstruction and calibration.

All objects are requested to have  $p_T \geq 20$  GeV, the leptons must have an absolute pseudo-rapidity  $|\eta|$  smaller than 2.5 and jets must have  $\eta \leq 4.5$ .

To suppress contributions from Drell-Yan backgrounds, the dilepton invariant mass is required to be at least 70 GeV. Tighter analysis-specific requirements are later applied to this and other variables in order to achieve the best sensitivities in individual studies, as described in the following section.

## 5 Individual Analyses

### 5.1 Search for Leptoquark Pair Production

Following the baseline object identification criteria described above, the leptoquark pair analyses require events to have at least two oppositely charged leptons of the same flavour and at least two jets. Signal sensitivity and discovery potential are estimated using a sliding mass window algorithm: only events in the mass region around the assumed mass of the leptoquark are analyzed.

For large leptoquark masses, leptons and jets have larger transverse momenta in signal events than background events. The following kinematic quantities are used to separate the signal from backgrounds: The transverse momentum of the leptons ( $p_T$ ), the scalar sum of the transverse momenta of the two most energetic jets and leptons ( $S_T = \sum |\vec{p}_T|_{jet} + \sum |\vec{p}_T|_{lep}$ ), the dilepton invariant mass ( $m_{\ell\ell}$ ), and lepton-jet invariant mass. The lepton-jet invariant mass represents the mass of the leptoquark if the correct lepton-jet combination is chosen. Since there are two leptons and two jets there are two possible combinations, and we choose the combination which gives the smallest difference between the masses of the first and second leptoquark candidates.

| Physics sample           | Before selection | Baseline selection | $S_T \geq 490$ GeV | $m_{ee} \geq 120$ GeV | $m_{lj}^1 - m_{lj}^2$ window (GeV)<br>[320-480] - [700-900]<br>[320-480] [700-900] |         |
|--------------------------|------------------|--------------------|--------------------|-----------------------|--|---------|
| $LQ$ ( $m = 400$ GeV)    | 2.24             | 1.12               | 1.07               | 1.00                  | 0.534  | -       |
| $LQ$ ( $m = 800$ GeV)    | 0.0378           | 0.0177             | 0.0177             | 0.0174                | -  | 0.0075  |
| $Z/\gamma^* \geq 60$ GeV | 2032.            | 49.77              | 0.722              | 0.0664                | 0.0036   | 0.00045 |
| $t\bar{t}$               | 833.             | 3.23               | 0.298              | 0.215                 | 0.0144   | 0.0     |
| Vector Boson pairs       | 60.94            | 0.610              | 0.0174             | 0.00384               | 0.00049  | 0.0     |
| Multijet                 | $10^8$           | 20.51              | 0.229              | 0.184                 | 0.0  | 0.0     |

Table 3: 1st generation leptoquark analysis. Partial cross-sections (pb) that survive selection criteria.

In both channels, the values of these selection criteria are optimized to achieve discovery with  $5\sigma$  significance at the lowest luminosity possible. Tables 3 and 4 list these selection values and resulting signal and background cross-sections for 1st and 2nd generation channels, respectively. One important difference between the two channels is the background due to jets being misidentified as electrons. This background can be significantly reduced by requiring both reconstructed jet-electron masses,  $(m_{lj}^1, m_{lj}^2)$ , to be close to the tested leptoquark mass. However, such a selection in the 2nd generation analysis would significantly reduce the signal efficiency, especially for larger leptoquark

| Physics sample           | Before selection | Baseline selection | $p_T^\mu \geq 60$ GeV<br>$p_T^{jet} \geq 25$ GeV | $S_T \geq 600$ GeV | $m_{\mu\mu} \geq 110$ GeV | $m_{lj}$ window (GeV)<br>[300-500] [600-1000] |         |
|--------------------------|------------------|--------------------|--|--------------------|---------------------------|---|---------|
| LQ (400 GeV)             | 2.24             | 1.70               | 1.53   | 1.27               | 1.23                      | 0.974   | -       |
| LQ (800 GeV)             | 0.0378           | 0.0313             | 0.0306   | 0.0304             | 0.030                     | -   | 0.0217  |
| $Z/\gamma^* \geq 60$ GeV | 2032.            | 79.99              | 2.975  | 0.338              | 0.0611                    | 0.021   | 0.014   |
| $t\bar{t}$               | 833.             | 4.17               | 0.698  | 0.0791             | 0.0758                    | 0.0271  | 0.0065  |
| VB pairs                 | 60.94            | 0.876              | 0.0654   | 0.00864            | 0.00316                   | 0.00185                                       | 0.00076 |
| Multijet                 | $10^8$           | 0.0                | 0.0  | 0.0                | 0.0                       | 0.0   | 0.0     |

Table 4: 2nd generation leptoquark analysis. Partial cross-sections (pb) that survive selection criteria.

masses. Therefore, only the average of the two muon-jet masses ( $m_{lj}^{av}$ ) is required to be near the tested leptoquark mass.

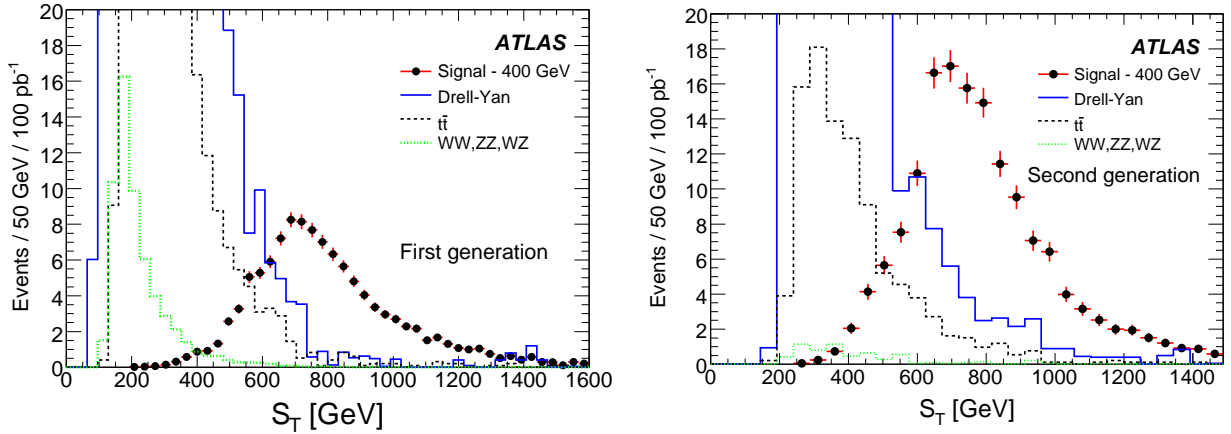

 Figure 3:  $S_T$  in leptoquark MC events ( $m_{LQ} = 400$  GeV) after baseline selection. Left: 1st generation, right: 2nd generation with the additional requirements  $p_T^\mu > 60$  GeV and  $p_T^{jet} > 25$  GeV.

Figure 3 shows the  $S_T$  variable distribution with  $m_{LQ} = 400$  GeV, along with the main backgrounds, Drell-Yan and  $t\bar{t}$  production, after baseline selection plus, for the 2nd generation case, the requirements  $p_T^\mu > 60$  GeV and  $p_T^{jet} > 25$  GeV.

The dilepton mass distribution after the  $S_T$  selection can be seen in Figure 4.

Figures 5 and 6 show the reconstructed invariant mass of leptoquark candidates ( $m_{LQ}=400$  GeV) in signal events and the main backgrounds, Drell-Yan and  $t\bar{t}$  production, after the subsequent selections on dimuon mass and  $S_T$ . Due to gluon radiation, quarks produced in the decays of heavy particles are not equivalent to standard jets. This shifts the peak of the jet energy resolution function towards smaller energies and results in a shoulder at low values for the reconstructed heavy particle mass. Figure 5 shows two entries per event corresponding to the two reconstructed electron-jet objects obtained by adding x and y mass projections of  $(m_{lj}^1, m_{lj}^2)$  on a common axis,  $m_{lj}$ .

Events in all of the histograms are given for an integrated luminosity of  $100 \text{ pb}^{-1}$ .

The trigger efficiency is not included in the plots and tables shown in this section. However events satisfying all selection criteria would trigger with an efficiency exceeding 95%, as discussed in Section 3.

## 5.2 Search for New Particles from Left-Right Symmetric Models

Signal event candidates are required to contain (at least) two electron or muon candidates and two or more jets that pass the baseline selection criteria. As previously described, the minimum separation

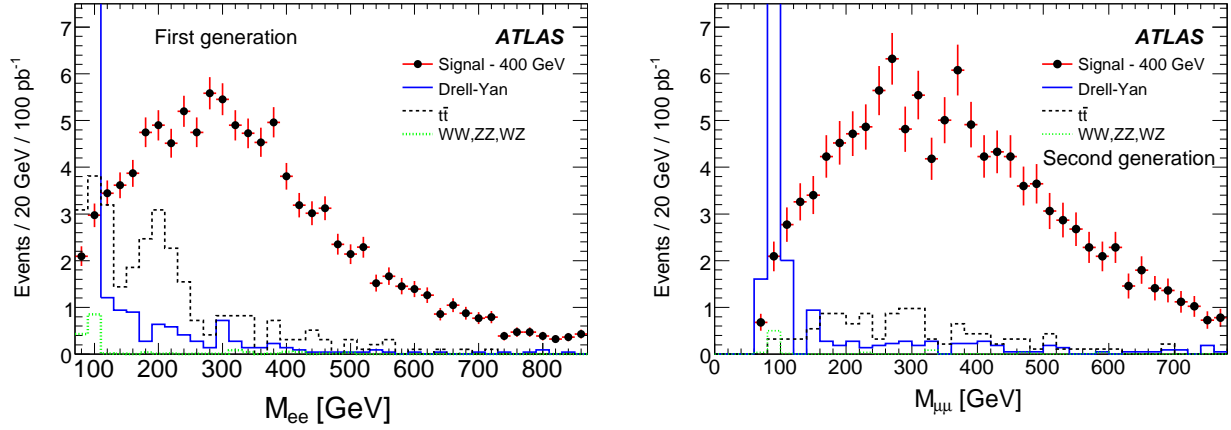


Figure 4:  $m_{\ell\ell}$  of the selected lepton pair after  $S_T$  selection in leptoquark 1st generation (left) and 2nd generation (right) events ( $m_{LQ} = 400$  GeV).

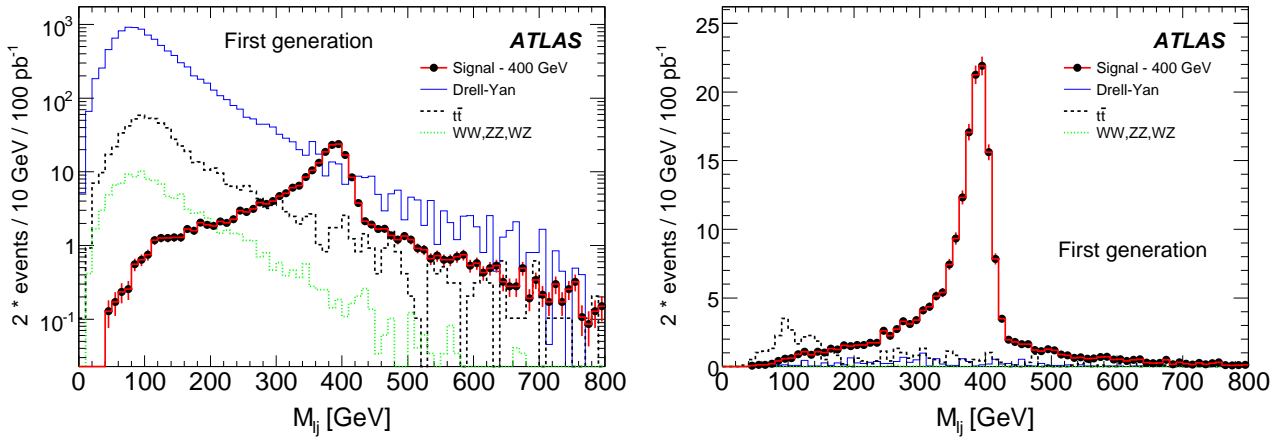


Figure 5: Reconstructed electron-jet invariant mass in the 1st generation leptoquark ( $m_{LQ}=400$  GeV) analysis for signal and background MC events after baseline selection (left) and after all selection criteria (right). All distributions are given for  $100 \text{ pb}^{-1}$  of integrated luminosity.

between a jet and an electron candidate  $\Delta R \geq 0.1$  is required. The two leading  $p_T$  lepton candidates and the two leading  $p_T$  jets are assumed to be the decay products of the  $W_R$  boson. The signal jet candidates are combined with each signal lepton and the combination that gives the smallest invariant mass is considered as the new heavy neutrino. This assignment is correct in more than 99% of signal MC events. The other lepton is assumed to come directly from the decay of the  $W_R$  boson.

When the  $W_R$  boson is at least twice as heavy as the Majorana neutrino, the daughter lepton from the neutrino's decay often begins to partially merge with one of the daughter jets. In the dielectron analysis, when the separation between this lepton and a signal jet candidate is in the range  $0.1 \leq \Delta R \leq 0.4$ , using all three reconstructed objects to estimate the invariant mass of the neutrino would often result in double-counting. To solve this problem, signal event candidates in the dielectron analysis are divided into two groups. When the separation is outside the discussed range, *i.e.*  $\Delta R > 0.4$ , all three objects are used. However, when the separation is in the critical range, *i.e.*  $0.1 \leq \Delta R \leq 0.4$ , only jets are used to estimate the mass of the  $N_e$  neutrino. No such problem exists in the dimuon analysis because muon reconstruction is possible even when the reconstructed trajectory's projection into the calorimeters randomly coincides with jet activity. The mass of the Majorana neutrino can be reconstructed with a relative resolution of about 6%, and the mass of the  $W_R$  boson can be reconstructed with a relative resolution of 5% to 8%; better resolution on the latter

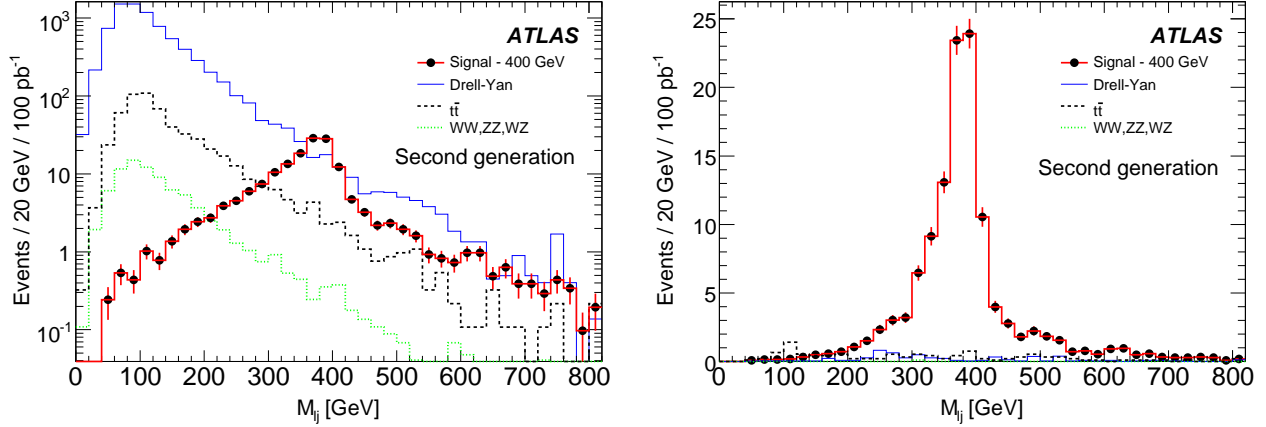


Figure 6: Reconstructed muon-jet invariant mass for 2nd generation leptoquarks ( $m_{LQ} = 400$  GeV) in signal and background MC events after baseline selection (left) and after all selection criteria (right). All distributions are given for  $100 \text{ pb}^{-1}$  of integrated luminosity.

199 is achieved in the dielectron analyses because the muon spectrometer resolution is degraded at high  
 200 transverse momenta.

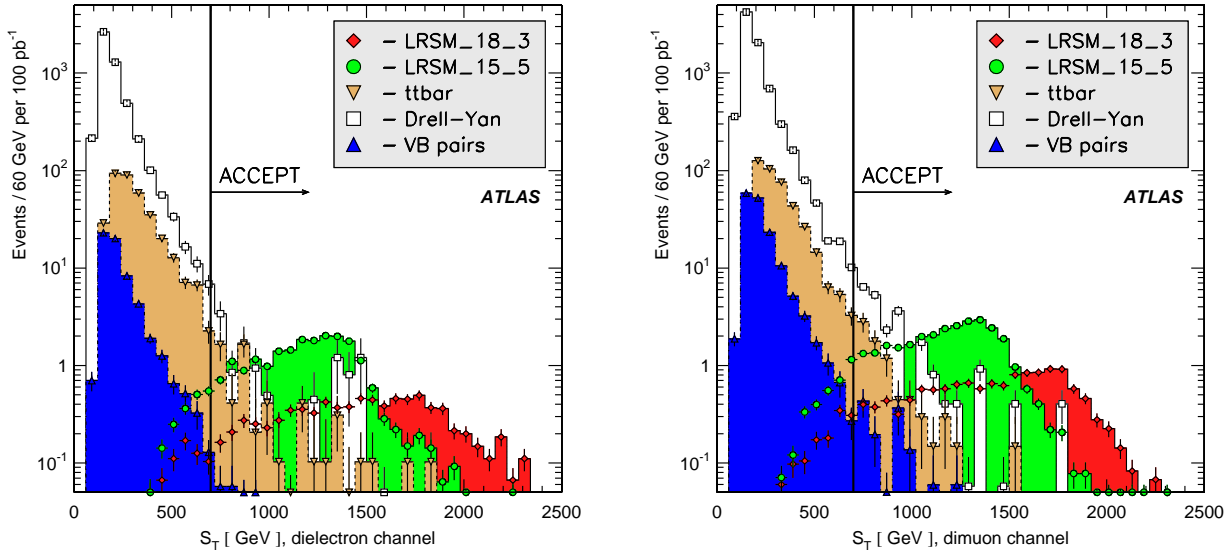


Figure 7: LRSM analysis.  $S_T$  distributions for signals and backgrounds normalized to  $100 \text{ pb}^{-1}$  of integrated luminosity after baseline selection in dielectron (left) and dimuon (right) analyses. Vertical lines indicate the value of the selection used in the analysis.

201 While the main background sources in LRSM analyses are  $t\bar{t}$ ,  $Z/\gamma^*$ , and vector boson pair pro-  
 202 duction processes, multijets were also identified as a source of potentially dangerous background in  
 203 the dielectron analysis. The distributions of the scalar sum of signal object candidates' transverse  
 204 momenta  $S_T$ , and the reconstructed dilepton invariant mass  $m_{\ell\ell}$  for signal and background events,  
 205 normalized to an integrated luminosity of  $100 \text{ pb}^{-1}$ , are shown in Figs. 7 and 8.

206 The choice of the selection criteria  $S_T \geq 700$  GeV and  $m_{\ell\ell} \geq 300$  GeV is made in order  
 207 to maintain good efficiency not only for mass values used in this study, but also for signals with

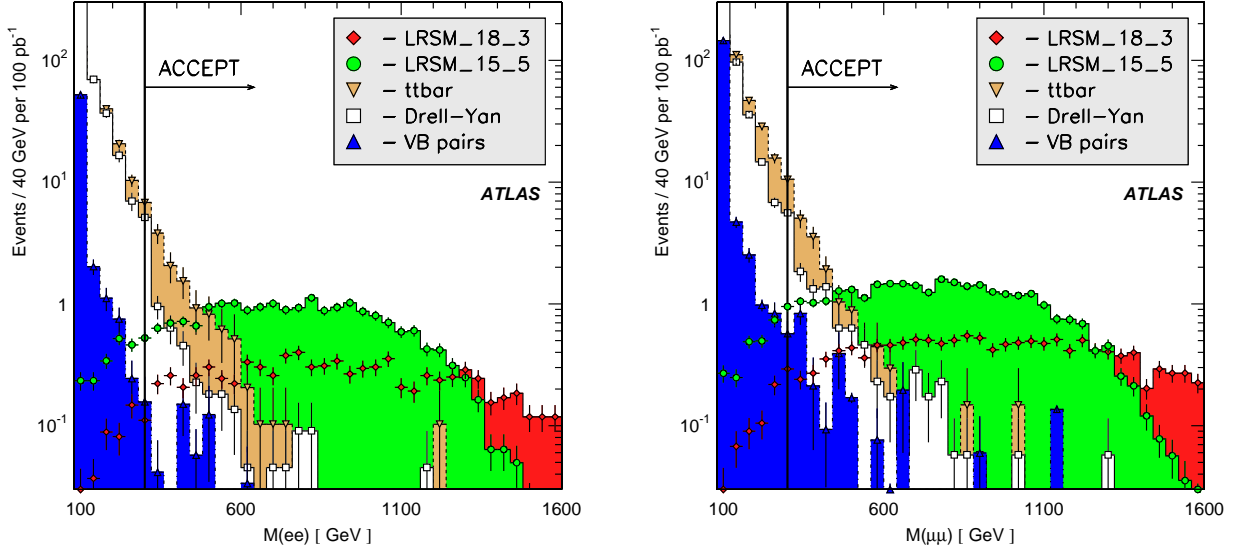


Figure 8: LRS M analysis. The distributions of  $m_{\ell\ell}$  for signals and backgrounds normalized to  $100 \text{ pb}^{-1}$  of integrated luminosity after baseline selection in dielectron (left) and dimuon (right) analyses. Vertical lines indicate the value of the selection used in the analysis.

208  $m_{W_R} \geq 1000 \text{ GeV}$ .

| Physics sample                      | Before selection | Baseline selection | $m_{ejj} \geq 100 \text{ GeV}$ | $m_{eejj} \geq 1000 \text{ GeV}$ | $m_{ee} \geq 300 \text{ GeV}$ | $S_T \geq 700 \text{ GeV}$ |
|-------------------------------------|------------------|--------------------|--------------------------------|----------------------------------|-------------------------------|----------------------------|
| LRS M_18_3                          | 0.248            | 0.0882             | 0.0882                         | 0.0861                           | 0.0828                        | 0.0786                     |
| LRS M_15_5                          | 0.470            | 0.220              | 0.220                          | 0.215                            | 0.196                         | 0.184                      |
| $Z/\gamma^*, m \geq 60 \text{ GeV}$ | 1808.            | 49.77              | 43.36                          | 0.801                            | 0.0132                        | 0.0064                     |
| $t\bar{t}$                          | 450.             | 3.23               | 3.13                           | 0.215                            | 0.0422                        | 0.0165                     |
| VB pairs                            | 60.94            | 0.610              | 0.522                          | 0.0160                           | 0.0016                        | 0.0002                     |
| Multijet                            | $10^8$           | 20.51              | 19.67                          | 0.0490                           | 0.0444                        | 0.0444                     |

Table 5: LRS M dielectron analysis. Partial cross-sections (pb) that survive the selection criteria.

| Physics sample                      | Before selection | Baseline selection | $m_{\mu jj} \geq 100 \text{ GeV}$ | $m_{\mu\mu jj} \geq 1000 \text{ GeV}$ | $m_{\mu\mu} \geq 300 \text{ GeV}$ | $S_T \geq 700 \text{ GeV}$ |
|-------------------------------------|------------------|--------------------|-----------------------------------|---------------------------------------|-----------------------------------|----------------------------|
| LRS M_18_3                          | 0.248            | 0.145              | 0.145                             | 0.141                                 | 0.136                             | 0.128                      |
| LRS M_15_5                          | 0.470            | 0.328              | 0.328                             | 0.319                                 | 0.295                             | 0.274                      |
| $Z/\gamma^*, m \geq 60 \text{ GeV}$ | 1808.00          | 79.99              | 69.13                             | 1.46                                  | 0.0231                            | 0.0127                     |
| $t\bar{t}$                          | 450.             | 4.17               | 4.11                              | 0.275                                 | 0.0527                            | 0.0161                     |
| VB pairs                            | 60.94            | 0.876              | 0.824                             | 0.0257                                | 0.0047                            | 0.0015                     |
| Multijet                            | $10^8$           | 0.0                | 0.0                               | 0.0                                   | 0.0                               | 0.0                        |

Table 6: LRS M dimuon analysis. Partial cross-sections (pb) that survive selection criteria.

209 Partial cross-sections for signal and background processes passing the selection criteria are shown

in Tables 5 and 6. Some remarks are in order concerning the selection criteria's efficiencies. First, the dimuon channel is more efficient than the dielectron channel. This is due to the jet-electron merging discussed previously. This issue becomes especially important for a larger ratio of masses  $m_{W_R}/m_{N_e}$ . However, for a very heavy  $W_R$  boson, the dielectron channel could become more significant because the  $W_R$  boson mass resolution does not become as wide in the dielectron channel as it does in the dimuon channel. Also, because of its heavy mass, the potential to discover the  $W_R$  boson and the heavy neutrino together is much better than in the inclusive search for the new heavy neutrino (assuming the same production mechanism) because of backgrounds.

Figures 9 and 10 show the distributions of the reconstructed invariant masses of the heavy neutrino and  $W_R$  boson candidates for signal and background MC samples before and after the selection criteria are applied. All distributions are normalized to  $100 \text{ pb}^{-1}$  of integrated luminosity. It should be remarked that the trigger efficiency is not included in the plots and tables shown in this section. However, events satisfying all selection criteria would trigger with an efficiency exceeding 95%, as discussed in Section 3.

Background contributions to signal invariant mass spectra could also arise from jets that are misidentified as signal electrons. In principle such misidentified jets are efficiently suppressed because at least two signal electron candidates are required, but at present this background remains poorly understood because larger statistics of multijet MC, or better, real data, would be necessary to evaluate its contribution reliably. If needed, a better suppression of events with multijets that are misidentified as electrons is possible by applying a more sophisticated isolation energy requirement. The multijet background does not pose a problem in the dimuon analysis, where estimates of the misidentification rate predict a vanishing contribution from multijet to dimuon events.

Finally, the analyses described in this note do not discriminate between same-sign and opposite-sign dileptons. Same-sign dileptons, however, are a very important signature of Majorana neutrinos, which, being their own anti-particles, could decay to a lepton of either charge. The background contribution to same-sign dileptons is much smaller than to opposite-sign dileptons. Of course, both channels would have to be studied if the discovery is made. The studies of charge misidentification performed in the framework of the presented analyses, predict a rate as high as 5% for high- $p_T$  leptons which is strongly  $\eta$ -dependent.

## 6 Systematic Uncertainties

The following sources of systematic uncertainties have been considered in the described analyses:

- 20% uncertainty was assumed on the integrated luminosity.
- In the dielectron analyses, 1% was used for the uncertainty in overall trigger efficiency.
- For electron identification and reconstruction efficiency, an uncertainty of 1% was assumed.
- For muon identification, including trigger and reconstruction efficiencies, an uncertainty of 5% was assumed.
- The uncertainty on the electron energy scale was assumed to be  $\pm 1\%$ .
- The uncertainty on the muon momentum scale was assumed to be  $\pm 1\%$ .
- The uncertainty on the jet energy scale was estimated by changing the energies of all jets simultaneously by  $\pm 10\%$  and  $\pm 20\%$ , for  $|\eta_{jet}| \leq 3.2$  and  $|\eta_{jet}| > 3.2$ , respectively.
- The 20% uncertainty in electron  $p_T$  resolution was estimated using a Gaussian smearing of  $p_T$  with a relative width of  $0.66 * (0.10/\sqrt{p_T} \oplus 0.007)$ , where  $p_T$  is in GeV.

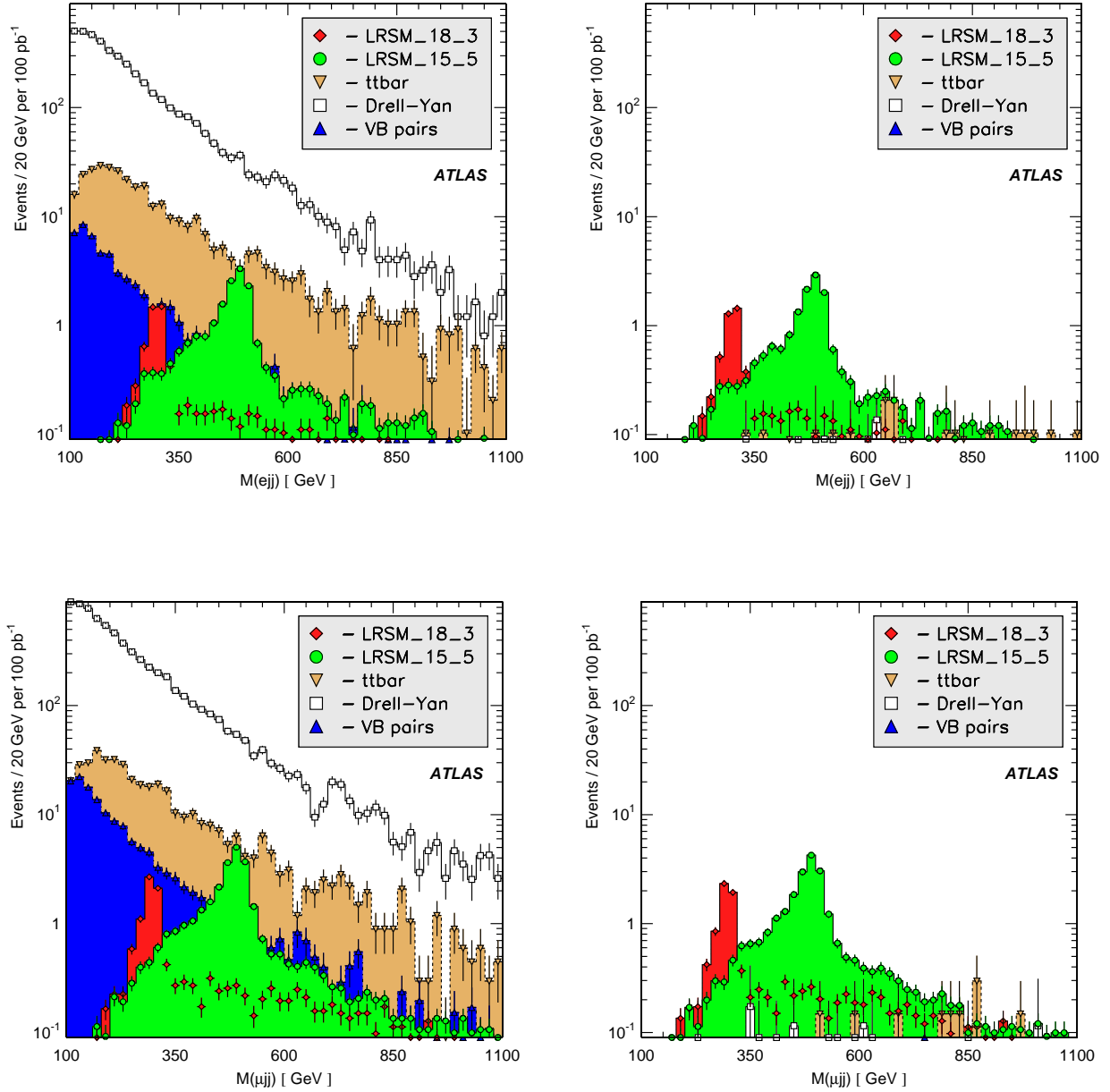


Figure 9: LRSM analysis. The distributions of the reconstructed invariant masses for  $N_e$  (top) and  $N_\mu$  (bottom) candidates in background and signal (LRSM\_18.3 and LRSM\_15.5) events before (left) and after (right) background suppression is performed in dielectron and dimuon analyses. All distributions are normalized to 100 pb<sup>-1</sup> of integrated luminosity. LRSM\_15.5 and LRSM\_18.3 refer to two sets of LRSM mass hypotheses. See the text for more information.

- The uncertainty due to muon  $1/p_T$  resolution was estimated using a Gaussian smearing of  $1/p_T$  with a width of  $0.011/p_T \oplus 0.00017$ , where  $p_T$  is in GeV.
- The uncertainty due to jet energy resolution was estimated using a Gaussian smearing of jet energies in such a way that the relative jet energy resolution widens from  $0.60/\sqrt{E} \oplus 0.05$  to  $0.75/\sqrt{E} \oplus 0.07$  for  $|\eta_{jet}| \leq 3.2$ , and from  $0.90/\sqrt{E} \oplus 0.07$  to  $1.10/\sqrt{E} \oplus 0.10$  for  $|\eta_{jet}| > 3.2$ , where  $E$  is in GeV.



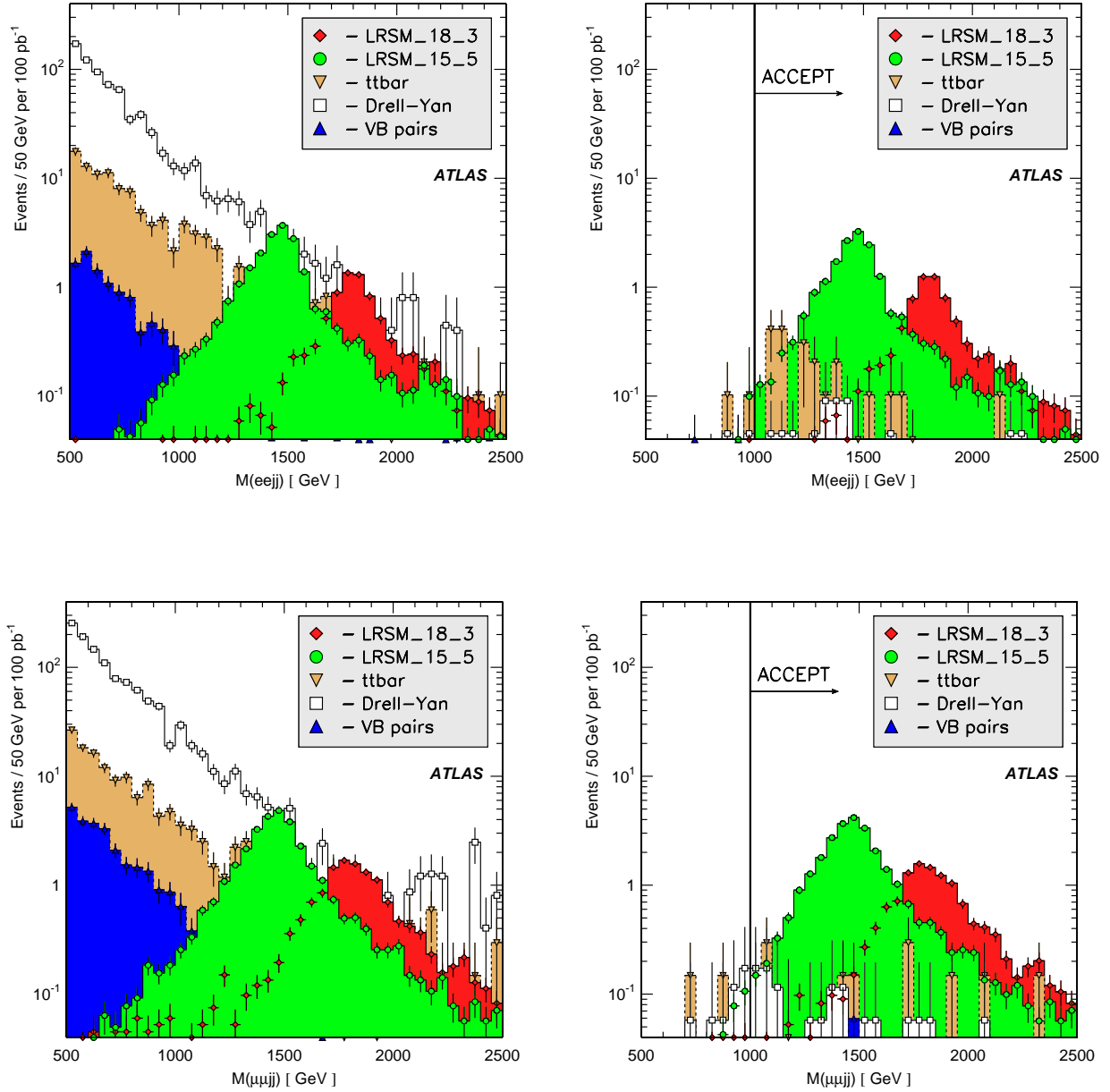


Figure 10: LRSB analysis. The distributions of the reconstructed invariant masses for  $W_R \rightarrow eN_e$  (top) and  $W_R \rightarrow \mu N_\mu$  (bottom) candidates in background and signal (LRSB\_18.3 and LRSB\_15.5) events before (left) and after (right) background suppression is performed in dielectron and dimuon analyses. All distributions are normalized to 100 pb<sup>-1</sup> of integrated luminosity. Notice that the invariant mass of the  $W_R$  boson is shown *before* the requirement  $m_{\ell\ell jj} \geq 1000$  GeV is imposed. This variable is strongly correlated with the background-suppressing variables  $S_T$  and  $m_{\ell\ell}$ . LRSB\_15.5 and LRSB\_18.3 refer to two sets of LRSB mass hypotheses. See the text for more information.

- Statistical uncertainties on the number of background MC events were considered as systematic uncertainties on the number of background events.
- The systematic uncertainty on the leptoquark cross-section (NLO) [28] was calculated by taking the 40 PDF CTEQ6M tables (two per eigenvector of PDF variations, provided by the CTEQ group for calculating uncertainties [20]), recalculating the leptoquark cross-section with each of

these tables, and taking the largest difference of the two variations for each of the 20 eigenvectors to the cross-section calculated with the standard CTEQ6M table. The estimate shown is the sum in quadrature of these 20 differences and the relative difference in cross-section obtained by varying renormalization and factorization scales by a factor of 2. The systematic uncertainty is between 15% and 28% for the tested leptoquark masses.

- The uncertainty of the jet modeling in  $Z\gamma^*$  events was estimated by comparing the background predictions obtained using MC samples produced with PYTHIA to MC samples produced with ALPGEN. For the leptoquark pair analysis, this results in an uncertainty of about 30% on the background from  $Z/\gamma^*$  events.
- Background cross-sections for  $t\bar{t}$  and  $Z/\gamma^*$  processes were assumed to have uncertainties of 12% and 10%, respectively.

Systematic uncertainties affect both signal and background efficiencies, however the significance computation (next section) will be mainly affected by the uncertainty on the background. The dominant systematic effects on the background are due to the uncertainties in integrated luminosity (20%), the jet energy scale (16%-35%), jet energy resolution (6%-28%), and the limited statistics of background MC samples (15%-30%). The total systematic uncertainties for signals and backgrounds are summarized in Table 7.

| analysis   | effect on signal events |            | effect on background events |            |
|------------|-------------------------|------------|-----------------------------|------------|
|            | 1st gen.                | 2nd gen.   | 1st gen.                    | 2nd gen.   |
| leptoquark | $\pm 27\%$              | $\pm 29\%$ | $\pm 53\%$                  | $\pm 51\%$ |
| LRSM       | $\pm 23\%$              | $\pm 25\%$ | $\pm 45\%$                  | $\pm 40\%$ |

Table 7: Summary of total systematic uncertainties (%) for 100 pb<sup>-1</sup> luminosity.

## 7 Results

The program  $S_{cp}$  [29] is used to calculate the significances of possible observations of the signals studied in this note. The significance is defined in units of Gaussian standard deviations, corresponding to the (one-sided) probability of observing a certain number of events exceeding the MC-predicted background  $N_b$  at a given integrated luminosity. This probability is usually referred to as  $CL_b(N)$ , where  $N$  is the number of observed events. The  $5\sigma$  discovery corresponds to  $CL_b(N_s + N_b)$ , where  $N_s$  is the expected number of signal events. Systematic uncertainties in the number of background events were also included in the significance calculations. For second generation leptoquarks, the signal selection was optimized at each point to minimize the cross-section times branching ratio needed to reach a  $5\sigma$  discovery, while for all other analyses the selection cuts presented in earlier sections were used.

The overall reconstruction and trigger efficiencies discussed are used to estimate ATLAS' sensitivity and discovery potential for the studied final states below. Note that in these results the trigger efficiency is applied to the expected number of signal and background events in the signal region, as discussed in Section 5, Table 2.

### 7.1 Leptoquarks

The integrated luminosities needed for a  $5\sigma$  discovery of the 1st and 2nd gen. scalar leptoquark signals are shown in Table 8 as function of leptoquark mass, assuming  $\beta = 1$ . Also, Fig. 11 predicts the

| Leptoquark mass | Expected luminosity needed for a $5\sigma$ discovery |                       |
|-----------------|--|-----------------------|
|                 | 1st gen.   | 2nd gen.              |
| 300 GeV         | $2.8 \text{ pb}^{-1}$                                | $1.6 \text{ pb}^{-1}$ |
| 400 GeV         | $11.8 \text{ pb}^{-1}$                               | $7.7 \text{ pb}^{-1}$ |
| 600 GeV         | $123 \text{ pb}^{-1}$                                | $103 \text{ pb}^{-1}$ |
| 800 GeV         | $1094 \text{ pb}^{-1}$                               | $664 \text{ pb}^{-1}$ |

Table 8: The integrated luminosities needed for a  $5\sigma$  discovery of 1st and 2nd gen. scalar leptoquarks for different mass hypotheses.

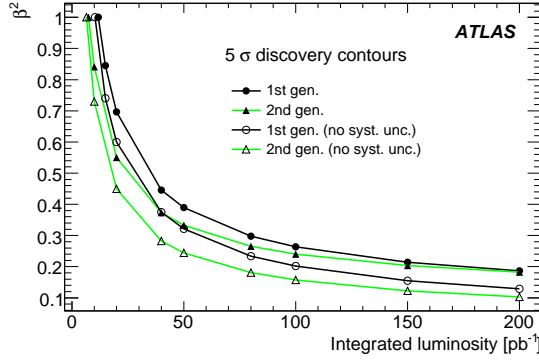


Figure 11:  $5\sigma$  discovery potential for 1st and 2nd gen.  $m = 400 \text{ GeV}$  scalar leptoquarks versus  $\beta^2$  with and without background systematic uncertainty included.

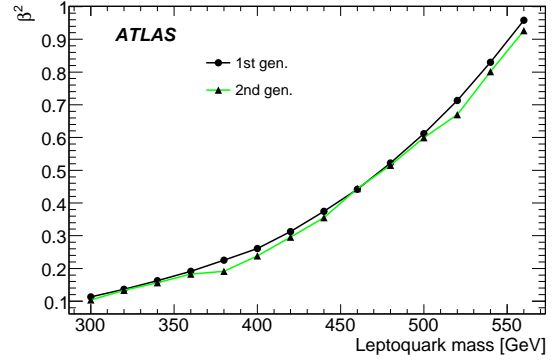


Figure 12: Minimum  $\beta^2$  of scalar leptoquarks versus leptoquark mass for  $100 \text{ pb}^{-1}$  of integrated luminosity at  $5\sigma$  (background systematic uncertainty included.)

integrated luminosities needed for a 400 GeV leptoquark mass hypothesis, with various values of  $\beta^2$ , at a  $5\sigma$  level.

Finally, Fig. 12 shows the minimum  $\beta^2$  that can be probed with ATLAS with  $100 \text{ pb}^{-1}$  of integrated luminosity as a function of leptoquark mass. Lighter leptoquark masses can be probed with a smaller  $\beta$  because of their larger cross-section. It is evident from this figure that ATLAS is sensitive to leptoquark masses of about 565 GeV and 575 GeV for 1st gen. and 2nd gen., respectively, at the given integrated luminosity, provided they always decay into charged leptons and quarks.

## 7.2 Left-Right Symmetry

The significances of studied signals versus integrated luminosity are shown in Fig. 13. Figure 14 shows the product of signal cross-section and dilepton branching fraction versus the integrated luminosity necessary for a  $5\sigma$  discovery. The overall relative systematic uncertainty on Drell-Yan and  $t\bar{t}$  production backgrounds is approximately 45% and 40% in the dielectron and dimuon analyses, respectively. This estimate is dominated by contributions from jet reconstruction, uncertainty in integrated luminosity and insufficient MC statistics. Currently multijet background is poorly understood and is not included in the presented sensitivity estimates for the dielectron channel.

## 8 Summary and Conclusions

Studies of final states with two leptons and multiple jets have been discussed, considering both electrons and muons. The early-data discovery potential for BSM physics predicted by two prominent GUT-inspired models has been investigated.

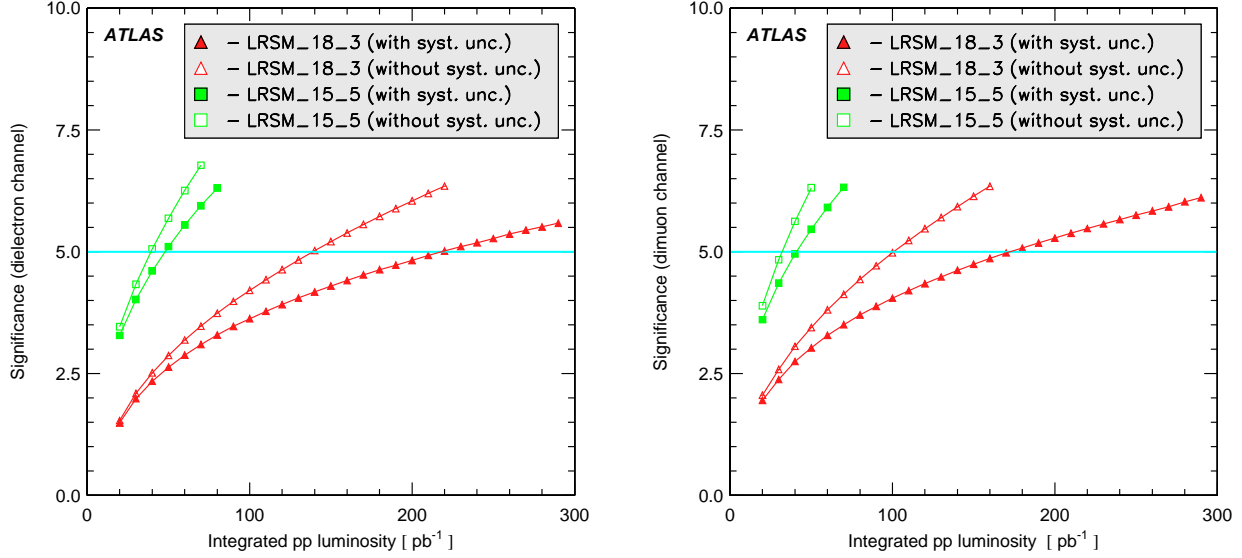


Figure 13: LRS\_M analysis. Expected signal significances versus integrated luminosity for  $N_e$ ,  $N_\mu$  neutrino and  $W_R$  boson mass hypotheses, according to signal MC samples LRS\_M\_18.3 and LRS\_M\_15.5. Open symbols show sensitivities without systematic uncertainties. Sensitivities shown with closed symbols include an overall relative uncertainty of 45% (40%) estimated for background contributions in the dielectron (dimuon) analysis. LRS\_M\_15.5 and LRS\_M\_18.3 refer to two sets of LRS\_M mass hypotheses. See the text for more information.

Both 1st and 2nd gen. scalar leptoquark pair production could be discovered with less than 100  $\text{pb}^{-1}$  of integrated luminosity, provided that the mass of the leptoquarks is smaller than 500 GeV and the branching ratio into a charged lepton and a quark is 100%.

Two LRS\_M mass points ( $m_{W_R} = 1.8 \text{ TeV}, m_{N_\ell} = 300 \text{ GeV}$  and  $m_{W_R} = 1.5 \text{ TeV}, m_{N_\ell} = 500 \text{ GeV}$ ) for the right-handed  $W_R$  boson and Majorana neutrinos  $N_\ell$  have been studied in the dielectron and dimuon channels. It was found that discovery of these new particles at these mass points would require integrated luminosities of 150  $\text{pb}^{-1}$  and 40  $\text{pb}^{-1}$ , respectively.

## References

- [1] J. C. Pati and A. Salam, *Phys. Rev.* **D10** (1974) 275–289.
- [2] E. Eichten, I. Hinchliffe, K. D. Lane, and C. Quigg, *Phys. Rev.* **D34** (1986) 1547.
- [3] E. Eichten, K. D. Lane, and M. E. Peskin, *Phys. Rev. Lett.* **50** (1983) 811–814.
- [4] W. Buchmuller and D. Wyler, *Phys. Lett.* **B177** (1986) 377.
- [5] H. Georgi and S. L. Glashow, *Phys. Rev. Lett.* **32** (1974) 438–441.
- [6] M. Leurer, *Phys. Rev.* **D49** (1994) 333–342, [arXiv:hep-ph/9309266](#).
- [7] **D0** Collaboration, V. M. Abazov *et al.*, *Phys. Rev.* **D71** (2005) 071104, [arXiv:hep-ex/0412029](#).
- [8] **CDF** Collaboration, D. E. Acosta *et al.*, *Phys. Rev.* **D72** (2005) 051107, [arXiv:hep-ex/0506074](#).

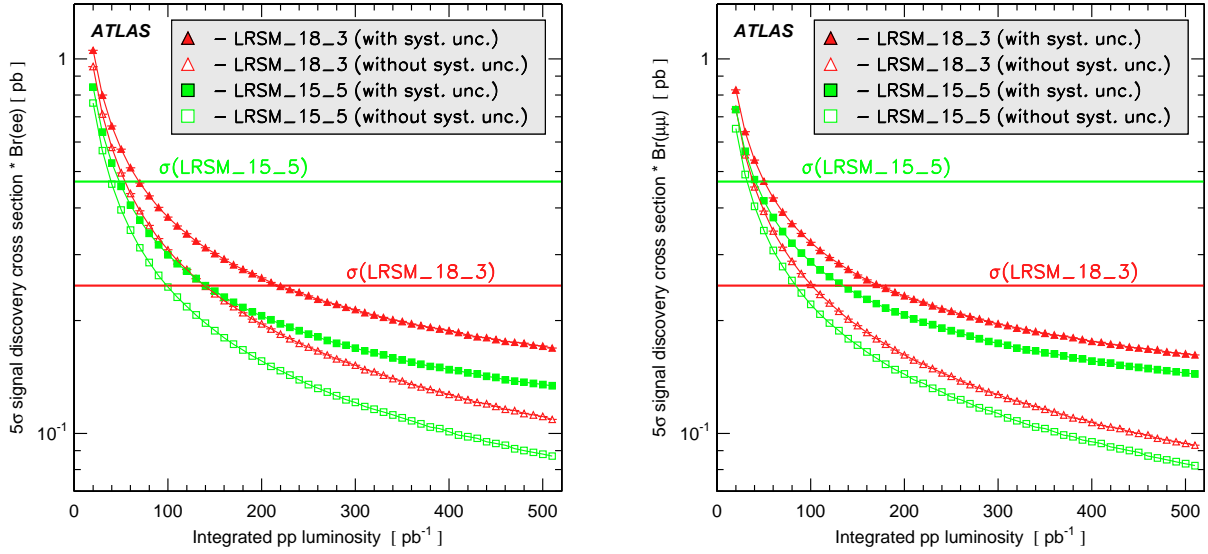


Figure 14: LRSB analysis. The product of signal cross-section and branching fraction to dielectron and dimuon final states versus integrated luminosity necessary for a  $5\sigma$  discovery.  $N_e$ ,  $N_\mu$  neutrino and  $W_R$  boson mass hypotheses are for signal MC samples LRSB\_18.3 and LRSB\_15.5. Horizontal lines indicate nominal cross-sections for two signal MC samples, according to the LRSB implementation in the MC simulation. Open symbols show discovery potentials without systematic uncertainties. Discovery potentials shown with closed symbols include an overall relative uncertainty of 45% (40%) assumed for the background contribution in the dielectron (dimuon) analysis. LRSB\_15.5 and LRSB\_18.3 refer to two sets of LRSB mass hypotheses. See the text for more information.

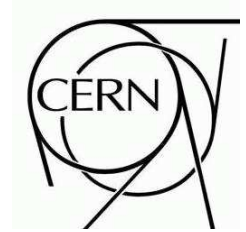
- 334 [9] **D0** Collaboration, V. M. Abazov *et al.*, *Phys. Lett.* **B636** (2006) 183–190,  
335 [arXiv:hep-ex/0601047](#).
- 336 [10] **CDF** Collaboration, A. Abulencia *et al.*, *Phys. Rev.* **D73** (2006) 051102,  
337 [arXiv:hep-ex/0512055](#).
- 338 [11] T. Ahrens, *Boston, USA, Kluwer Acad. Publ.* (2000) . 177p.
- 339 [12] R. N. Mohapatra and P. B. Pal, *World Sci. Lect. Notes Phys.* **60** (1998) 1–397.
- 340 [13] **D0** Collaboration, V. M. Abazov *et al.*, [arXiv:0803.3256 \[hep-ex\]](#).
- 341 [14] T. Sjostrand, S. Mrenna, and P. Skands, *JHEP* **05** (2006) 026, [arXiv:hep-ph/0603175](#).
- 342 [15] A. Ferrari *et al.*, *Phys. Rev.* **D62** (2000) 013001.
- 343 [16] K. Huitu, J. Maalampi, A. Pietila, and M. Raidal, *Nucl. Phys.* **B487** (1997) 27–42,  
344 [arXiv:hep-ph/9606311](#).
- 345 [17] K. Melnikov and F. Petriello, *Phys. Rev. Lett.* **96** (2006) 231803, [arXiv:hep-ph/0603182](#).
- 346 [18] C. Anastasiou, L. J. Dixon, K. Melnikov, and F. Petriello, *Phys. Rev.* **D69** (2004) 094008,  
347 [arXiv:hep-ph/0312266](#).
- 348 [19] G. Corcella *et al.*, *JHEP* **01** (2001) 010, [arXiv:hep-ph/0011363](#).
- 349 [20] J. Pumplin *et al.*, *JHEP* **07** (2002) 012, [arXiv:hep-ph/0201195](#).

- 350 [21] S. Frixione and B. R. Webber, *JHEP* **06** (2002) 029, [arXiv:hep-ph/0204244](#).
- 351 [22] R. Bonciani, S. Catani, M. L. Mangano, and P. Nason, *Nucl. Phys.* **B529** (1998) 424–450,  
352 [arXiv:hep-ph/9801375](#).
- 353 [23] **ATLAS** Collaboration, “Reconstruction and identification of electrons in ATLAS.” This  
354 volume.
- 355 [24] **ATLAS** Collaboration, “Muon Reconstruction and Identification Performance in ATLAS:  
356 Studies with Simulated Monte Carlo Samples.” This volume.
- 357 [25] **ATLAS** Collaboration, “Jet5: Reconstruction Algorithms and Performance.” This volume.
- 358 [26] **ATLAS** Collaboration, “b-tagging performance.” This volume.
- 359 [27] **ATLAS** Collaboration, “The ATLAS Trigger for early running.” This volume.
- 360 [28] M. Kramer, T. Plehn, M. Spira, and P. M. Zerwas, *Phys. Rev.* **D71** (2005) 057503,  
361 [arXiv:hep-ph/0411038](#).
- 362 [29] S. I. Bityukov, S. E. Erofeeva, N. V. Krasnikov, and A. N. Nikitenko. Prepared for  
363 PHYSTATO5: Statistical Problems in Particle Physics, Astrophysics and Cosmology, Oxford,  
364 England, United Kingdom, 12-15 Sep 2005.



# ATLAS NOTE

July 12, 2008



## Vector Boson Scattering at High Mass

The ATLAS Collaboration

### Abstract

In the absence of a light Higgs boson, the mechanism of electroweak symmetry breaking will be best studied in processes of vector boson scattering at high mass. Various models predict resonances in this channel. Here, we investigate  $WW$  scalar and vector resonances,  $WZ$  vector resonances and a  $ZZ$  scalar resonance over a range of diboson centre-of-mass energies. Particular attention is paid to the application of forward jet tagging and to the reconstruction of dijet pairs with low opening angle resulting from the decay of highly boosted vector bosons. The performance of different jet algorithms is compared. We find that resonances in vector boson scattering can be discovered with a few tens of inverse femtobarns of integrated luminosity.

# 1 Introduction

In the absence of a light Higgs boson, an alternative scenario to the Standard Model, Supersymmetry, or Little Higgs models must be invoked. In particular, Electroweak Symmetry Breaking (EWSB) could result from a strong coupling interaction. Here, we will make no assumptions about the underlying dynamics of EWSB; we treat the Standard Model as a low energy effective theory, and evaluate the potential for measuring vector boson scattering. In the Standard Model, perturbative unitarity is violated [1] in vector boson scattering at high energy for a Higgs mass  $m_H > 870$  GeV or, if there is no Higgs ( $m_H \rightarrow \infty$ ), for a centre-of-mass energy above a critical value of around 1.7 TeV. The only way to avoid a light Higgs boson is therefore to presume new physics at high energy [2], possibly in the form of vector boson pair resonances. Such resonances are predicted in many models such as QCD-like technicolour models with the required Goldstone bosons resulting from chiral symmetry breaking [3]; Higgsless extra dimension models [4], where Kaluza-Klein states of gauge bosons are exchanged in the  $s$ -channel [5]; as well as in models with extra vector bosons, from GUT or from strong interaction (BESS models [6]) mixing with the Standard Model vector bosons. The present search for resonances in vector boson scattering can be considered generic and may be interpreted in terms of any of these models.

## 1.1 The Chiral Lagrangian Model

The Chiral Lagrangian (ChL) model is an effective theory valid up to  $4\pi v \sim 3$  TeV, where  $v = 246$  GeV is the vacuum expectation value of the Standard Model Higgs field, which can provide a description of longitudinal gauge boson scattering at the TeV scale when no light scalar Higgs boson is present. Electroweak symmetry breaking is realised non-linearly. A set of dimension-4 effective operators describe the low energy interactions (see for example [7]). Since, at the LHC, vector boson scattering can occur at the TeV energy scale where the interaction becomes strong, it is necessary to unitarise the scattering amplitudes. One popular unitarisation prescription is the so-called Padé prescription, or Inverse Amplitude Method [8]. This is based on meson scattering in QCD, where it gives an excellent description [9], reproducing observed resonances. Among the terms of the Lagrangian which describe vector boson scattering, under some basic assumptions (custodial symmetry and CP conservation), only 2 parameters (namely  $a_4$  and  $a_5$ ) are important for this process. Depending on the values of these two parameters, one can obtain Higgs-like scalar resonances and/or technicolour-like vector resonances [10]. The resulting properly-unitarised amplitudes for vector boson scattering may therefore give information in a higher energy range. They yield poles for certain values of  $a_4$  and  $a_5$  that can be interpreted as resonances, as shown in Fig. 1.

Other unitarisation procedures are possible, such as the K-matrix method [11] or the  $N/D$  method [12]. In general, resonances are not necessarily produced. In non-resonant cases, it remains vital to measure the vector boson scattering cross-section, but high luminosity and a very good understanding of backgrounds will be required in order to measure the regularisation of the cross-section.

## 1.2 Characteristic Signatures of Vector Boson Scattering

Discovery of the physics signals studied here will, in general, require high integrated luminosity. It will require also extremely large samples of simulated backgrounds, fine tuning of all reconstruction algorithms, and a good understanding of the detector performance, which will only gradually develop after the first few years of LHC running. The main purpose of this note is not, therefore, to evaluate with precision the discovery potential of ChL resonances, but to



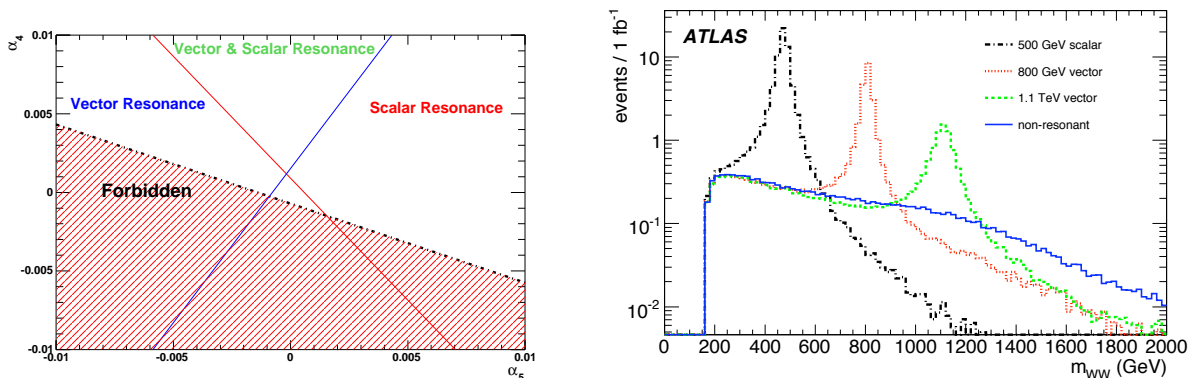


Figure 1: Left: regions in the  $(a_4, a_5)$  parameter space indicating which values exhibit vector and/or scalar resonances in the Padé unitarisation scheme. Right: number of events per  $\text{fb}^{-1}$  as a function of the di-boson invariant mass for different resonance masses studied here.

establish some strategy for the search of this important signal. The main emphasis will be put on those aspects most particular to the high mass vector boson scattering process; that is, the reconstruction of hadronically decaying vector bosons at high  $p_T$ , and the reconstruction of the high rapidity tag jets.

The decay of a high mass ChL resonance will produce two highly boosted vector bosons in the central rapidity region of the detector. For transverse momenta greater than about 250 GeV, a hadronically decaying vector boson will be seen as one single wide and heavy jet. Methods of distinguishing such jets from single-parton jets will be investigated with different jet algorithms.

A characteristic signature of vector boson scattering is the presence of two high rapidity and high energy “tag” jets [13], arising from the quarks which radiate the incoming vector bosons. The process can thus be efficiently distinguished from contributions to the production of (mostly transversely polarised) final state vector bosons due to bremsstrahlung of these vector bosons from the quarks. In that case, the accompanying jets are softer and more central. A further component of the signature is the suppression of QCD radiation in the rapidity interval between the tag jets due to the fact that no colour is exchanged between the protons in these processes [14]. This characteristic feature allows for efficient use of central jet veto to suppress backgrounds.

The high QCD background at the LHC naturally leads us to focus on “semi-leptonic” vector boson events; that is, those events when one  $W$  or  $Z$  boson decays leptonically, and the other decays hadronically. These channels represent the best compromise in that there is only at most one neutrino, and so the diboson mass may be reconstructed with reasonable resolution, and the backgrounds can be reduced to a manageable level by the requirement of leptons and/or missing transverse energy ( $\cancel{E}_T$ ). Fully-leptonic events are also useful in cases where clear resonances are present, where a kinematic edge may be visible and the backgrounds may be reduced even further. The case of resonant  $ZZ \rightarrow \ell^+ \ell^- \nu \bar{\nu}$  can also lead to a clean signature. Fully hadronic events may be useable at very high diboson energies, but this possibility is not considered further here. Thus, the study of vector boson scattering events will also require a good understanding of detector performance for electrons, muons and  $\cancel{E}_T$ . Although many ATLAS analyses will depend on the reconstruction of these objects, the quality of such reconstruction is evaluated here for the case of high energy leptons.

The note is organised as follows. In the next section (2) we describe the Monte Carlo simulations and the samples used. Next, the trigger is discussed (Section 3), then the detector

performance with particular focus on the challenges of this analysis (Section 4). After this, the event selections, efficiencies and purities for the various final states are given (Section 5). An attempt to evaluate the expected sensitivity is made (Section 6), and the systematic uncertainties are discussed (Section 7), before a final summary and conclusion.

## 2 Signals and Background Simulation

### 2.1 Definition of signal

A resonance *signal* will be defined here as events in the resonance mass region in excess of the number expected from the Standard Model continuum when the Higgs boson mass is 100 GeV. This ensures that the assumed continuum production is gauge invariant while, at the same time, longitudinal vector boson scattering diagrams will contribute negligibly. This definition follows the prescription of [15]. However, we note that measurement of even a continuum cross-section for this process at such high energies would be of great importance, and study whether this is also possible with the luminosity considered.

### 2.2 Overview of Generators

The Monte Carlo (MC) generators used in the main analysis are as follows.

- PYTHIA [16] version 6.4.0.3 was used for the signal, with the CTEQ6L parton distribution function and the renormalisation and factorisation scale  $Q^2 = M_W^2$ . The hard process was modified to include new vector boson scattering amplitudes (see below).
- MADGRAPH [17], version 3.95, with PYTHIA for parton shower, hadronisation and underlying event, was used for  $W$ +jets and  $Z$ +jets backgrounds. The default values of fixed renormalisation and factorisation scales of  $Q^2 = m_Z^2$  were set and CTEQ6L1 parton distribution functions were used.
- MC@NLO [18], with HERWIG [19], for parton shower and hadronisation and JIMMY [20,21] for underlying event, was used for  $t\bar{t}$  background.

The underlying event samples were tuned to data from previous experiments [21]. All samples use PHOTOS [22] to simulate final state radiation. WHIZARD [23] and ALPGEN [24, 25] are also used for some generator level comparisons. WHIZARD uses PYTHIA for parton showering, hadronisation, and underlying event. ALPGEN uses HERWIG/JIMMY.

The different choice of scales for MADGRAPH and PYTHIA is not ideal, but retained for historical reasons since large samples were generated with these choices. However, studies showed that the major effect is on the cross-section rather than on event shapes, and the cross section normalisation is determined independently as described below.

Further details specific to the samples are given below.

### 2.3 List of samples

Table 1 lists the Monte Carlo samples, produced with full detector simulation, used in the present analysis.

The first set of samples represents different reference cases of vector boson scattering signals:

| Sample name  | Generator  | $\sigma \times Br$ , fb |
|--|------------|-------------------------|
| $qqWZ \rightarrow qqjj\ell\ell$ , $m = 500$ GeV      | PYTHIA-73  | 25.2                    |
| $qqWZ \rightarrow qq\ell\nu jj$ , $m = 500$ GeV      | PYTHIA-73  | 83.9                    |
| $qqWZ \rightarrow qq\ell\nu\ell\ell$ , $m = 500$ GeV | PYTHIA-73  | 8.0                     |
| $qqWZ \rightarrow qqjj\ell\ell$ , $m = 800$ GeV      | PYTHIA-ChL | 10.5                    |
| $qqWZ \rightarrow qq\ell\nu jj$ , $m = 800$ GeV      | PYTHIA-ChL | 35.2                    |
| $qqWZ \rightarrow qq\ell\nu\ell\ell$ , $m = 800$ GeV | PYTHIA-ChL | 3.4                     |
| $qqWZ \rightarrow qqjj\ell\ell$ , $m = 1.1$ TeV      | PYTHIA-ChL | 3.7                     |
| $qqWZ \rightarrow qq\ell\nu jj$ , $m = 1.1$ TeV      | PYTHIA-ChL | 12.3                    |
| $qqWZ \rightarrow qq\ell\nu\ell\ell$ , $m = 1.1$ TeV | PYTHIA-ChL | 1.18                    |
| $qqWW \rightarrow qq\ell\nu jj$ , $m = 499$ GeV (s)  | PYTHIA-ChL | 66.5                    |
| $qqWW \rightarrow qq\ell\nu jj$ , $m = 821$ GeV (s)  | PYTHIA-ChL | 27.5                    |
| $qqWW \rightarrow qq\ell\nu jj$ , $m = 1134$ GeV (s) | PYTHIA-ChL | 17.0                    |
| $qqWW \rightarrow qq\ell\nu jj$ , $m = 808$ GeV (v)  | PYTHIA-ChL | 29.8                    |
| $qqWW \rightarrow qq\ell\nu jj$ , $m = 1115$ GeV (v) | PYTHIA-ChL | 17.9                    |
| $qqWW \rightarrow qq\ell\nu jj$ , non-resonant       | PYTHIA-ChL | 10.0                    |
| $qqZZ \rightarrow qq\nu\nu\ell\ell$ , $m = 500$ GeV  | PYTHIA-ChL | 4.0                     |
| $jjWZ \rightarrow jj\ell\nu\ell\ell$ , background    | MADGRAPH   | 96                      |
| $jjZZ \rightarrow jj\nu\nu\ell\ell$ , background     | MADGRAPH   | 45.5                    |
|  |            | $\sigma$ (no Br), pb    |
| $W^+ + 4$ jets, QCD diagrams                         | MADGRAPH   | $163.3 \pm 0.1$         |
| $W^+ + 4$ jets, EW diagrams                          | MADGRAPH   | $1.76 \pm 0.03$         |
| $Z + 4$ jets, QCD                                    | MADGRAPH   | $85.7 \pm 0.7$          |
| $Z + 4$ jets, EW                                     | MADGRAPH   | $1.04 \pm 0.02$         |
| $W^+ + 3$ jets, QCD                                  | MADGRAPH   | $6.08 \pm 0.02$         |
| $W^+ + 3$ jets, EW                                   | MADGRAPH   | $0.219 \pm 0.001$       |
| $Z + 3$ jets, QCD                                    | MADGRAPH   | $3.72 \pm 0.02$         |
| $Z + 3$ jets, EW                                     | MADGRAPH   | $0.106 \pm 0.006$       |
| $t\bar{t}$   | MC@NLO     | $833 \pm 100$           |

Table 1: Table of samples and generators used

- PYTHIA-73: For the samples labelled “PYTHIA-73”, the process 73 (longitudinal  $WZ$  scattering) was selected, with MSTP(46)=5 (QCD-like model of [26] with Padé unitarisation). All other switches were left as default. This is meant to represent a generic narrow  $WZ$  resonance.
- PYTHIA-ChL: datasets with generator labelled “PYTHIA-ChL” in the table use a modified version of PYTHIA routine PYSGHG. The modification involves replacing the scattering amplitudes calculated for processes 73–77 by those given by Dobado et al [10] with parameters  $a_4$  and  $a_5$ . These parameters were chosen so as to produce a vector or scalar (indicated by a (v) or an (s) in the table) resonance at the desired mass, or signal with no resonances at all. Note that only vector  $WZ$  and scalar  $ZZ$  resonances are possible, but both scalar and vector  $WW$  resonances can be produced. A continuum sample was also generated using this model.

Background samples include events with two vector bosons and two jets in the final state, arising from gluon or electroweak vector boson exchange between incoming quarks. The vector bosons are here mostly transverse and emitted more centrally than in the case of longitudinal vector boson pair scattering.

- $jjWZ$  final state, where  $j$  is a quark or gluon: The decays of the vector bosons are performed in PYTHIA. Note that the semi-leptonic cases are already included in samples  $W$ +jets and  $Z$ + jets. Only the purely leptonic cases make use of this background.
- The background process:  $\ell\ell\nu\nu$  with a pair of jets (quark or gluons). The cross section shown in Table 1 is for non-hadronic decay of the  $ZZ$ ’s, with a filter requiring two leptons with  $p_T > 5$  GeV and  $|\eta| < 2.8$ .
- $W/Z + 3$  jets and  $W/Z + 4$  jets: they constitute backgrounds for the cases of high mass and lower mass resonances respectively since, in the former case, we expect that most of the vector bosons which decay hadronically will be reconstructed as a single jet. A correction factor of 1.38 is applied to the  $W^+$ +jets cross sections to account for  $W^-$ +j process. These datasets include all tree level diagrams leading to  $W+4j$ ,  $Z+4j$ ,  $W+3j$  and  $Z+3j$ , with the vector bosons decaying leptonically, but are separated into QCD diagrams or QED diagrams. To keep the cross-section manageable, preselection cuts were applied at MADGRAPH level. For the  $W, Z + 4$  jets case, we tag the highest rapidity jet (fjet), backward jet (bjet) and 2 central jets by requiring that  $|\eta_{fjet}| > 1.5$ ,  $|\eta_{bjet}| > 1.5$ , that the forward and backward jet candidates be on different hemispheres:  $\eta_{fjet}\eta_{bjet} < 0$ , that at least one forward jet have energy  $E > 300$  GeV, and that the invariant mass of the combined forward jets be  $m_{jj} > 250$  GeV. We further require  $p_T$  of at least one of the central jets to be  $p_T^j > 50$  GeV, the  $p_T$  of the vectorial addition of the central jets to be  $p_T^{jj} > 60$  GeV and the invariant mass of the combined central jets  $m_{jj} > 60$  GeV. For the case  $W, Z + 3$  jets, we add the requirements:  $p_T$  of the  $W$  or  $Z$  boson  $p_T > 200$  GeV,  $|\eta_{W/Z}| < 2$ , and  $p_T$  of one jet (central)  $p_T^j > 200$  GeV,  $|\eta_j| < 2$ .

Additional samples were produced with fast detector simulation to improve background statistics.

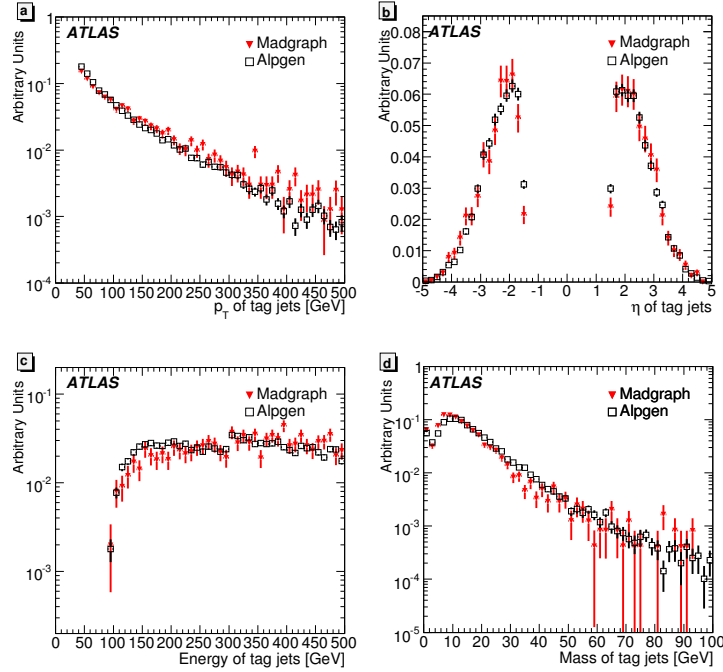


Figure 2: Distributions of the forward jets in the  $W + 4\text{jet}$  background for MADGRAPH (red) and ALPGEN (black) samples (area normalised). The error bars show the statistical error in each sample.

## 2.4 Comparative studies of generators

### 2.4.1 Parton shower matching to matrix elements

Here, MADGRAPH was used to generate the  $W + \text{jets}$  background. A better evaluation of this background would be obtained using a generator for which  $W + n$  partons,  $n=0, 1, 2, 3$  or  $4$  inclusive, are combined in a manner which avoids double counting of jets produced by the parton shower in PYTHIA. ALPGEN is one such generator (and in fact such matching is now implemented in more recent versions of MADGRAPH). However, due to time constraints, and in order to have a manageable size of background samples, it was not practical to use this technique. In order to validate the use of MADGRAPH, a comparison was made of the  $W + 4\text{jets}$  sample with an appropriate ALPGEN sample, with some analysis cuts applied. The ALPGEN samples are not used in the final analysis since they lack sufficient statistics.

Distributions of the vector bosons and jets were compared. As an example, the distributions for the forward jets are shown in Fig. 2. The overall conclusion is that the shapes of the distributions are in reasonable agreement, and therefore no great error is made in the description of the event topology by neglecting the effect of parton-shower double-counting. To the extent that such an error is made, the tag jets in the ALPGEN sample have a lower energy (leading to a depletion with respect to the MADGRAPH samples at high energies of a few %) and so the backgrounds in this analysis can be considered to be conservatively over estimated. The difference in  $Q^2$  scale of the two samples (ALPGEN uses  $Q^2 = m_W^2 + p_T(W)^2$ ) leads to about a factor two in cross section. This was confirmed by running MADGRAPH on a small sample with the same scale as ALPGEN, yielding cross-sections smaller by factors 2.05 and 1.77 for the QCD and QED processes respectively. These factors will be applied in the present analysis.

### 2.4.2 Effective $W$ Approximation

WHIZARD [23] is a relatively new event generator originally developed for the ILC. It is able to calculate the full  $2 \rightarrow 6$  matrix element needed for the vector boson scattering processes and it implements the Chiral Lagrangian model with the K-Matrix unitarisation scheme [26] which does not lead to vector boson resonances. Further unitarisation schemes in the form of arbitrary resonances are planned.

The generator does not assume an effective  $W$  approximation, whereby the bosons emitted from the quarks are treated as partons, allowing vector boson scattering diagrams to form a gauge-invariant subset. This approximation is made in the PYTHIA signal samples, and might be expected to particularly affect the tag jet kinematics. Comparisons between the tag jet distributions from WHIZARD and PYTHIA are shown in Fig. 3. The two samples are not strictly comparable since here, WHIZARD simulates the  $2 \rightarrow 4$  processes including non-scattering electroweak diagrams and applies K-matrix unitarisation. Although there are differences (e.g. the tag jets from WHIZARD are somewhat harder than those from PYTHIA) they do not strongly depend upon the vector boson centre-of-mass, and thus the effective  $W$  approximation is unlikely to be the culprit. The harder tag jets in WHIZARD mean that if the signal looks more like WHIZARD than PYTHIA, it would be more likely to pass the selection cuts, thus improving the sensitivity. The potential size of the effect was investigated and estimated to be at the few per cent level.

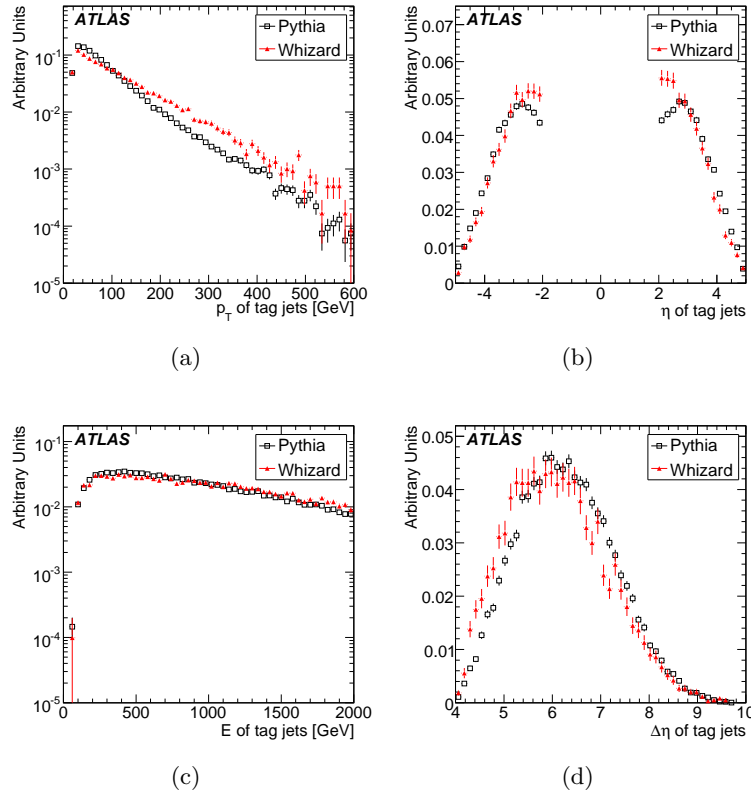


Figure 3: Differences between WHIZARD (red) and PYTHIA (black) for vanishing anomalous couplings for tag jet distributions of: transverse momentum (a), pseudo rapidity (b), energy (c) and pseudo rapidity difference (d).

### 3 Trigger

As a first step in the analysis, it is important to evaluate the efficiency of the basic trigger menus for a luminosity of  $10^{33} \text{ cm}^{-2}\text{s}^{-1}$ . The triggers chosen were based on an early menu [27] as an example, and the real physics menu is likely to be very different. However, since the signal is at relatively high  $p_T$ , and triggering on vector bosons is a high priority, this is not likely to have a large impact. To evaluate this efficiency, we apply the following cuts: for electrons and muons we require single leptons to have  $p_T$  greater than the value corresponding to the threshold dictated by the trigger signature and  $|\eta| < 2.5$ ; similarly for jets, but with a pseudorapidity cut of  $|\eta| < 3.2$ . This is necessary because trigger signatures for forward jets exist separately, but unfortunately that trigger information was not available in the simulation version used for this study. The trigger efficiency is defined as the number of times the trigger passed (with the corresponding cuts applied) divided by the number of truth events in the samples (with the same cuts applied). In Table 2 we present a detailed list of efficiencies for the signals  $qqWZ \rightarrow qqjj\ell\ell$  ( $m = 1.1 \text{ TeV}$ ) in the left column and  $qqWW \rightarrow qqjj\ell\nu$  (non-resonant) in the right<sup>1)</sup>.

The poor efficiency of the **e22i** (see Fig. 4, left) and **2e12i** triggers is understood to be due to the isolation criterion, which was not optimised for high energy electrons.

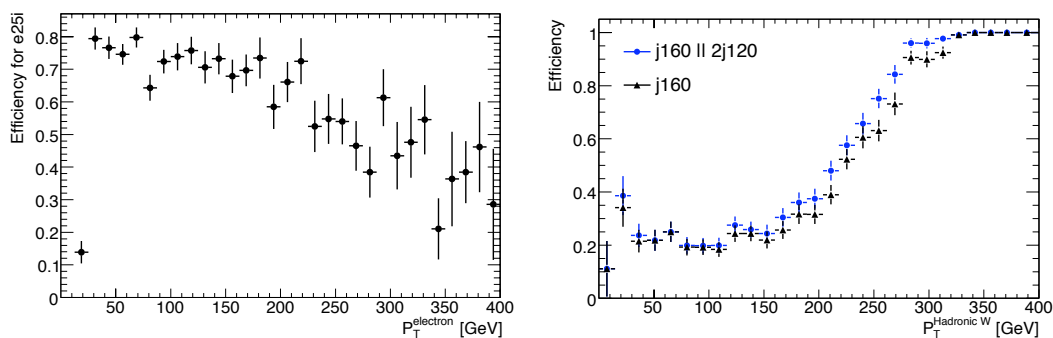


Figure 4: Trigger efficiencies computed with the  $WW$  continuum signal. Left: efficiency of the **e22i** trigger as a function of the  $p_T$  of electrons from the true leptonically-decaying  $W$  boson. Right: efficiency of the **j160** trigger (black triangles) as a function of the  $p_T$  of the true hadronically-decaying  $W$  boson. Also shown with blue circles is the efficiency when the **j160** and **2j120** triggers are logically OR'ed.

It is worth mentioning that the efficiency for the **2j120** trigger (Fig. 4, right), which requires two jets with  $p_T > 120 \text{ GeV}$  suffers partly from the fact that the two jets from the vector boson decay are merged due to the boost as described in Section 4.1. It is also significantly higher for events with true electrons than for those with true muons, probably because the electrons themselves are also reconstructed as jets in the calorimeter.

Finally, various combinations of the trigger signatures might be explored in the future to improve the efficiency. For instance, the **e60** trigger might be used in conjunction with the **e22i** to compensate the low efficiency of the latter for high-momentum electrons (Fig. 4). Likewise, the **2j120** trigger might be used together with **j160**, since the efficiency of the latter drops significantly when the hadronically-decaying vector boson has  $p_T < 300 \text{ GeV}$  and decays into two distinctly resolvable jets.

<sup>1)</sup>Triggers **2j120** and **j160** have been removed from the menu as they are expected to give too high a rate. More recent developments in the electron trigger has resulted in improved efficiency.

|                   | <i>WZ</i> signal |            | <i>WW</i> signal |            |
|-------------------|------------------|------------|------------------|------------|
| Trigger Signature | Cut Loss         | Efficiency | Cut Loss         | Efficiency |
| <i>Electrons</i>  |                  |            |                  |            |
| 2e12i             | 13%              | 36%        | > 99%            | —          |
| e22i              | 1%               | 78%        | 11%              | 65%        |
| e60               | 5%               | 82%        | 29%              | 73%        |
| <i>Muons</i>      |                  |            |                  |            |
| mu6               | 5%               | 95%        | 6%               | 80%        |
| mu20              | 5%               | 92%        | 9%               | 73%        |
| <i>Jets</i>       |                  |            |                  |            |
| 2j120             | 67%              | 73%        | 50%              | 80%        |
| j160              | 34%              | 96%        | 30%              | 86%        |

Table 2: Table of high level trigger efficiencies for  $qqWZ \rightarrow qqjj\ell\ell$  ( $m = 1.1$  TeV) and  $qqWW \rightarrow qqjj\ell\nu$  (non-resonant). The “Cut Loss” columns indicate the fraction of true events that would be lost by applying the  $p_T$  requirements of each trigger signature on the true electrons, muons and jets. Since such events are unlikely to satisfy the trigger conditions, they are not taken into account when the trigger efficiencies are evaluated.

## 4 Reconstruction Challenges

In this section, we focus on those parts of the reconstruction which are most particular to vector boson fusion at high masses. We discuss the following:

- Reconstruction of hadronically-decaying vector bosons. In our regime these typically have high  $p_T$  and the decay products are very collimated. We discuss two alternative methods, using  $k_\perp$  jets and subjets, and using cone jets with different radii.
- Leptonically decaying vector bosons. These require good lepton and  $\cancel{E}_T$  measurement, but the challenges here are not unique to these channels.
- Forward ‘tag’ jets. Measuring jets close to the edge of the detector rapidity acceptance is a challenge in common with low mass Higgs searches in vector boson fusion.
- Central jet veto. Since the vector boson scattering process involves no colour exchange between the protons, a suppression of QCD radiation is expected. This can be used to distinguish between signal and background, but is sensitive to underlying event and pile-up.
- Top veto.  $t\bar{t}$  production is a major background for the channels which do not contain leptonic  $Z$  boson decays. A large fraction of this is removed by explicitly rejecting events containing top candidates.

### 4.1 Hadronic Vector Boson Identification

At lower masses and  $p_T$ , the hadronically decaying vector bosons are identified as dijet pairs. However, for events where a hadronically decaying vector boson is highly boosted, the decay products are often collimated into a single jet. Cuts such as a dijet invariant mass window are no longer applicable in this scenario, but a single jet mass cut can be used.



The single jet mass is defined as the invariant mass evaluated from the 4-vectors of the constituents of the jet. In the ATLAS detector, these constituents are at present calorimeter objects, either topologically defined clusters with some local hadronic calibration, called here *topoclusters*, or calorimeter towers. For jets containing the decay products of a boosted vector boson, this single jet mass is near the mass of the parent boson. For light quark and gluon jets this mass is generally much lower. Since the background to hadronic vector boson identification is so severe, further cuts may be applied on the subjet structure of the candidate jet.

In addition, the transition between the dijet and single jet case as  $p_T$  increases needs to be dealt with. Two methods are used, as follows;

1. Dynamically select the appropriate method. To do this, we first look at the highest  $p_T$  jet. If this passes the mass window cut, then the single jet selection is applied, as described below. If it does not, then combinations of jet pairs in the event are considered. The vector boson is still expected to be the highest  $p_T$  hadronic system, and so the  $p_T$  of all jet pairs is evaluated, and the highest  $p_T$  pair is taken to be the vector boson candidate. A mass window cut (dependent upon the jet algorithm) is then applied to this pair. Thus a single analysis can be used to scan the data for signs of resonances without bias.
2. When the single jet and jet pair cases yield very different signal to background ratios, it is preferable to choose a priori which mass region is being investigated, and to use the single jet reconstruction for high masses and the dijet reconstruction for low masses. This approach is used in the cone algorithm analysis. For the  $m = 800$  GeV resonance, both the dijet and single jet approaches are tried independently.

#### 4.1.1 $K_{\perp}$ Algorithm

The  $k_{\perp}$  algorithm is run with an  $R$ -parameter (which determines the “jet size”) of 0.6 on calibrated topoclusters. The algorithm [28] merges pairs of constituents.

The  $k_{\perp}$  analysis uses the dynamic selection technique described above to decide whether to use a dijet or a single jet for the vector boson candidate. The fraction of vector bosons reconstructed as a single jet, as a function of  $p_T$  of the vector boson candidate, is given in Fig. 5. The transition between dijet and single jet takes place between  $p_T = 200$  and 300 GeV for this algorithm.

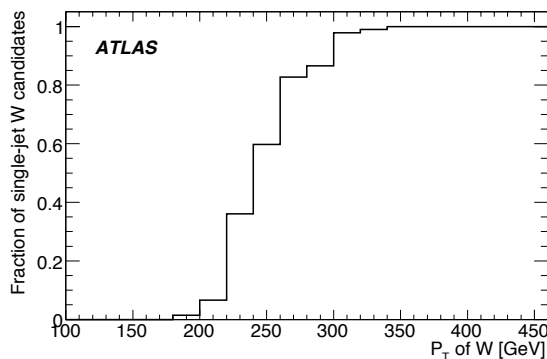


Figure 5: Fraction of  $W$  boson candidates reconstructed from a single jet, as a function of the transverse momentum of the reconstructed vector boson, for the  $WW$   $m = 1.1$  TeV signal sample.

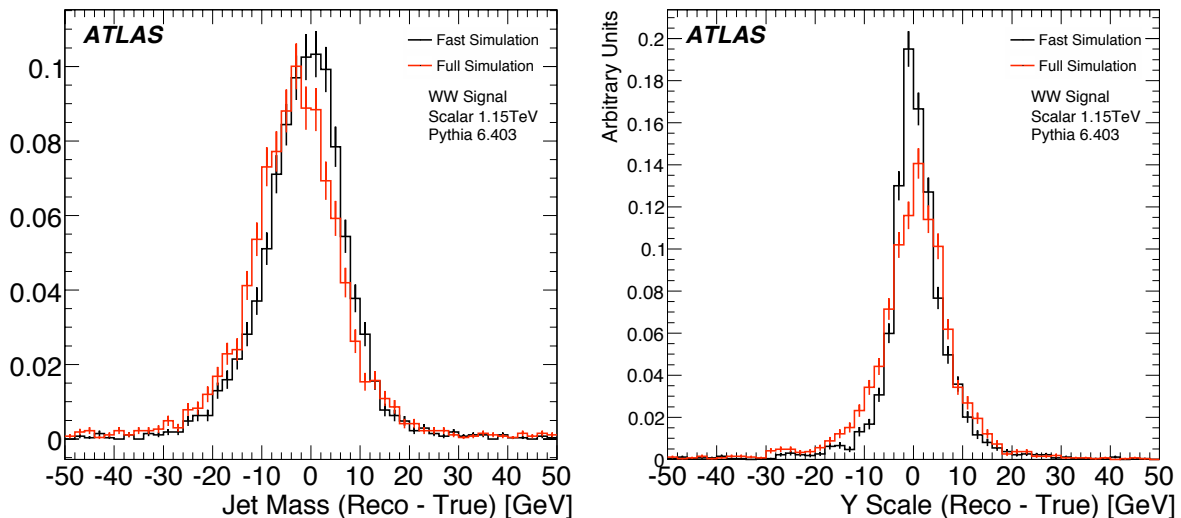


Figure 6: Single jet mass resolutions (left) and Y scale resolutions (right) from different detector simulations, using the  $k_{\perp}$  algorithm. The truth is defined by running the jet algorithm on the hadronic final state of the MC generator.

### Single jet mode

The resolution of the single jet mass for the  $k_{\perp}$  algorithm has been evaluated for both detector simulations (full and fast) for several samples. For the sample with a  $WW$  resonance at  $m = 1.1$  TeV (Fig. 6 left) for example, the  $W$  boson singlet jet mass resolution was found to be  $9.2 \pm 0.2\%$  and  $9.1 \pm 0.2\%$  from full and fast detector simulation respectively.

A mass cut around the window from  $m = 68.4$  GeV to  $97.2$  GeV is applied to  $W$  boson candidates, and from  $m = 68.7$  GeV to  $106.3$  GeV for hadronic  $Z$  boson candidates reconstructed in the single jet mode. This mass window is determined by considering the resolution, the tails, and the background contamination.

The  $k_{\perp}$  merging is intrinsically ordered in scale, making the final merging the hardest. The algorithm provides a  $y$  value for this final merging, which is a measure of the highest scale at which a jet can be resolved into two subjets. The  $y$  value can be converted into a “Y scale” in GeV using the relation  $Y \text{ scale} = E_T \times \sqrt{y}$ , where  $E_T$  is the jet transverse energy. This Y scale is expected to be  $\mathcal{O}(m_V/2)$  (where  $m_V$  is the mass of the vector boson) for boosted vector boson jets, and much lower than  $E_T$  for light jets [29]. At the truth and fast simulation levels this variable has been shown to have discriminating power even after a single jet mass cut [29–32]. The resolution of the ATLAS detector for this variable is presented in Fig. 6 (right). The resolutions, for the same sample as above, are  $12.3\% \pm 0.3\%$  and  $8.8\% \pm 0.2\%$  with full and fast detector simulation, respectively.

Based on the resolution, the tails, and the background contamination, a Y scale cut around the window from 30 GeV to 100 GeV is applied to  $W$  and  $Z$  boson candidates reconstructed in the single jet mode. To evaluate the benefit of cutting on Y scale, a sample of single jet vector boson candidates is selected in signal and background by applying a  $p_T > 300$  GeV cut, motivated by Fig. 5, and a mass window cut. Starting from this sample, the efficiency of the Y scale cut is given in Table 3 for full and fast simulation. The numbers suggest that for the  $W$ +jets background, an additional rejection factor of approximately 2 is provided by the Y scale cut even after a single jet mass cut has been applied. This is achieved with a signal efficiency of

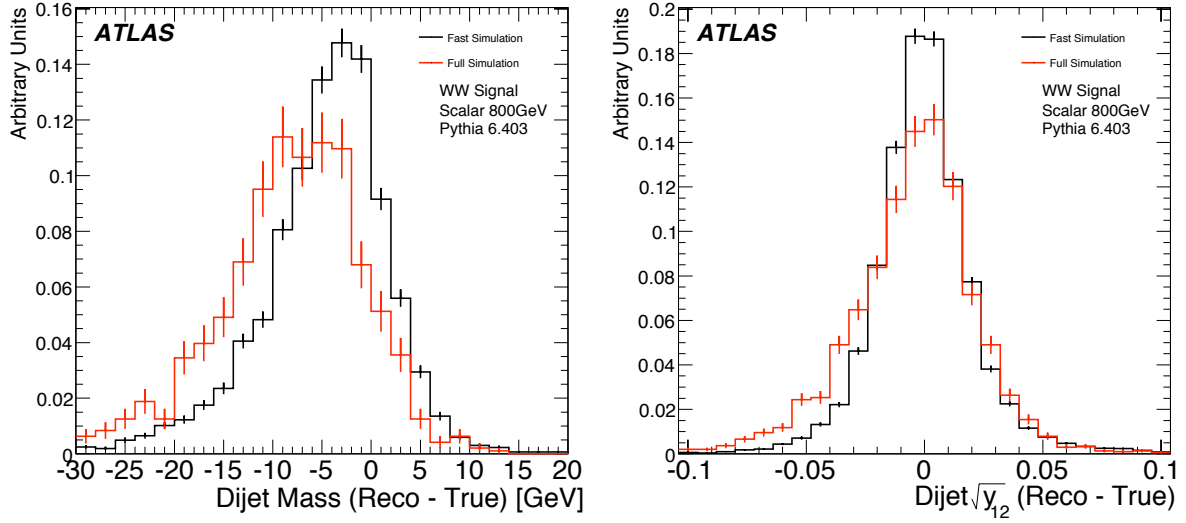


Figure 7: Dijet mass resolutions (left) and  $y$  resolutions (right) from different detector simulations, using the  $k_{\perp}$  algorithm. The truth is defined by running the jet algorithm on the hadronic final state of the MC generator.

|          | 1.1 TeV Vector Resonance | $W+4$ jets | $t\bar{t}$ |
|----------|--------------------------|------------|------------|
| Jet Mass | 68% (67%)                | 14% (14%)  | 28% (28%)  |
| Y Scale  | 77% (84%)                | 29% (40%)  | 63% (70%)  |

Table 3: Efficiency of the Y-scale cut in the 1 jet case for full (fast) simulation.

approximately 80%.

### Dijet mode

A mass cut around the window from  $m = 62$  GeV to 94 GeV is applied to  $W$  boson candidates, and from  $m = 66.6$  GeV to 106.2 GeV for hadronic  $Z$  boson candidates reconstructed in the dijet mode.

A variable analogous to the  $y$  may be calculated, using the relative  $p_T$  of the dijets. This variable is required to be in the range  $0.1 < \sqrt{y} < 0.45$ . The efficiency is shown in Table 4.

The mass and  $y$  windows are again determined by considering the resolution, the tails, and the background contamination.

The resolution of the dijet mass and the  $y$  variable for dijet vector boson candidates are shown in Fig. 7. The resolution for the full (fast) simulation is found to be approximately 5% (6%) for the mass and 5% (4%) for the  $y$  variable.

|          | 800 GeV Scalar Resonance | $W+4$ jets | $t\bar{t}$ |
|----------|--------------------------|------------|------------|
| Jet Mass | 17% (20%)                | 6% ( 7%)   | 14% (14%)  |
| Y Scale  | 79% (83%)                | 48% (49%)  | 84% (82%)  |

Table 4: Efficiency of the Y-scale cut in the 2 jet case for full (fast) simulation.

### 4.1.2 Cone Algorithm

Figure 8 shows an example of  $W$  boson reconstruction using the cone algorithm for the jet-pair case ( $m = 500$  GeV resonance) and single jet case ( $m = 800$  GeV resonance). A cone size of 0.8 is used for selecting a single jet  $W$  boson and 0.4 for the case of a jet pair. There is a small difference in the  $W$  boson mass peak reconstruction for the two cases. The jets chosen for this selection have a minimum  $p_T$  cut of  $p_T > 20$  GeV, and those overlapping with electrons have been removed.

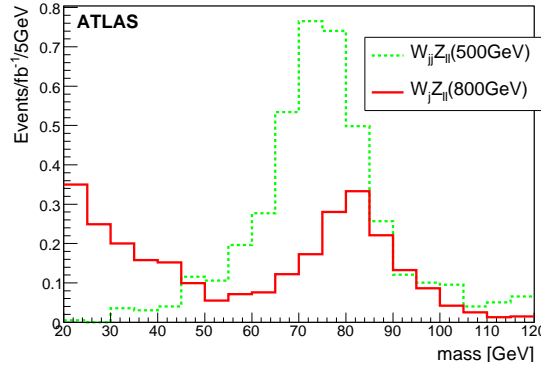


Figure 8: Reconstructed  $W$  boson for cases where it forms two separated jets (500 GeV) and a single jet (800 GeV). The samples used are the  $m = 500$  GeV resonance (in green) and  $m = 800$  GeV resonance (in red).

Single jet hadronic  $W$  boson candidates are identified with the highest  $p_T$  object in the central region, after having removed overlaps with all electrons in the event within a  $\Delta R$  of 0.1. A mass cut in a window around the reconstructed  $W$  boson mass is applied.

The problem of the two jets from a boosted hadronically decaying vector boson merging into a single jet has also been studied for jets reconstructed using the Cone Algorithm. With this algorithm, jet reconstruction starts from *seeds* i.e. constituents (clusters) with  $p_T > 1$  GeV. The algorithm collects all constituents around a seed within  $\Delta R = \sqrt{(\Delta\eta)^2 + \Delta\phi^2} < R_0$  (where  $R_0$  can be, for instance 0.4) and adds their momenta vectorially. Then it repeats the procedure over the collection around the direction of the sum, and computes a new sum. It continues repeating this operation until the resulting sum direction is stable.

The exploration of the substructure of a wide jet (typically of size 0.8) is done by searching for 2 narrow jets (size  $\sim 0.2$ ) fitting inside the big jet. Various variables can then be studied, among which are the energy ratio of the narrow jets, their invariant mass, the distance  $\Delta R$  between the leading narrow jet and the wide jet, or the momentum component of this narrow jet transverse to the wide jet direction. The discriminating power is illustrated for the  $WZ \rightarrow \ell\ell jj$  channel (1.1 TeV resonance) and its principal background in Fig. 9 which shows the latter variable (called here ‘ $p$  transverse’) versus the invariant mass reconstructed from two narrow jets. Cutting in the ( $p_T$ , invariant mass) plane gives results comparable to those obtained with the Y scale method above, as illustrated in Table 5. Similarly, Fig. 10 shows the  $p_T$  versus  $\Delta R$  between the leading narrow jet and the wide jet.

|                | 1.1 TeV Vector Resonance | $W+4\text{jets}$ (QCD) | $t\bar{t}$ | $Z+3\text{jets}$ (QED) |
|----------------|--------------------------|------------------------|------------|------------------------|
| small jets cut | 76.3%                    | 15.2%                  | 38.6%      | 13.8%                  |

Table 5: Comparison of efficiencies for the jet sub-structure selection for a typical signal and backgrounds. Efficiencies are relative to the selection of a single jet as described in the Y scale method (Table 3). For the subjet selection, we require 2 small jets with  $p_T > 15$  GeV and invariant mass  $> 60$  GeV (see text).

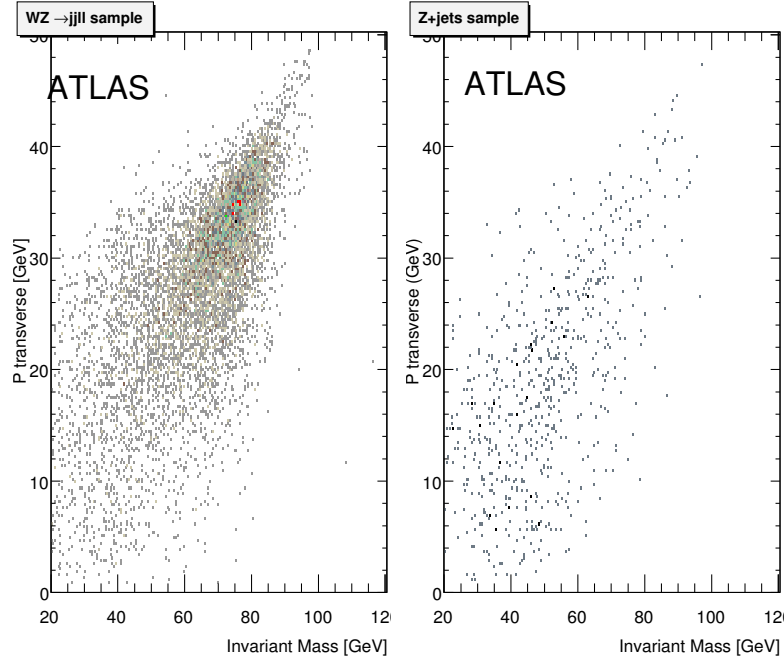


Figure 9: Momentum of the narrow jet orthogonal to the wide jet direction vs invariant mass of narrow jets, for  $W$  boson hadronic decay of the resonance signal  $qqW_{jj}Z_{\ell\ell}$  of  $m = 1.1$  TeV (left) and for  $Z+3$  jets sample (right).

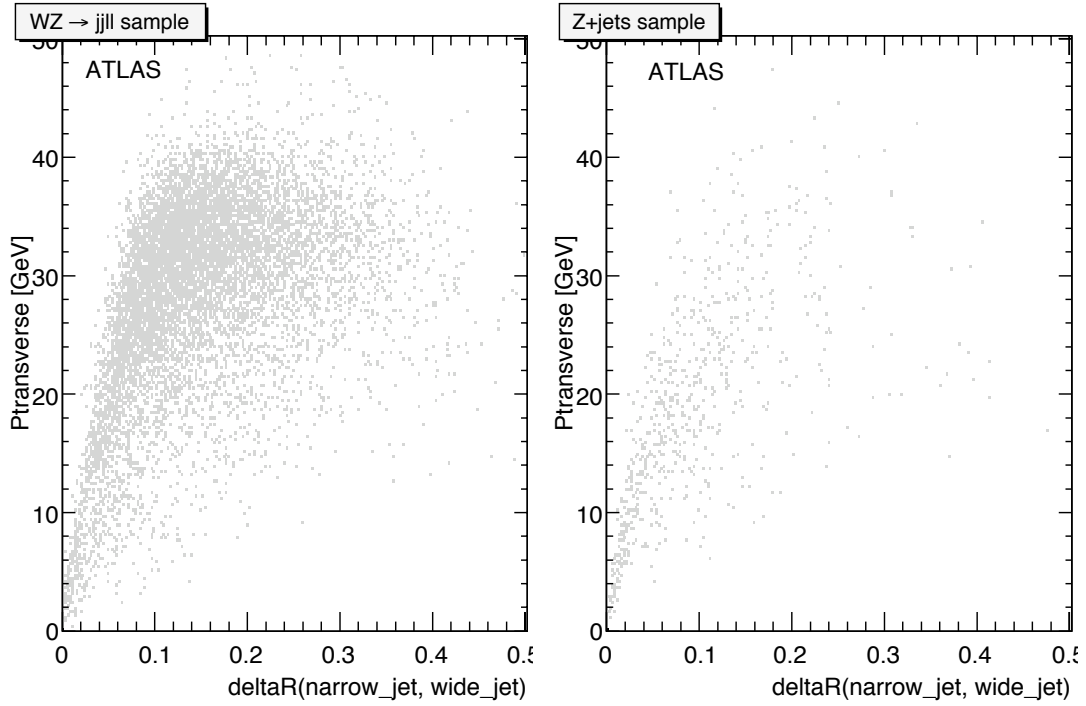


Figure 10: Momentum of the narrow jet orthogonal to the wide jet direction versus distance (narrow jets, wide jet), for  $W$  boson hadronic decay of the resonance signal  $qqW_{jj}Z_{\ell\ell}$  of  $m = 1.1$  TeV (left) and for  $Z+3$  jets sample (right).

## 4.2 Leptonic Vector Boson Identification

### 4.2.1 Lepton Reconstruction Efficiencies

All the signals studied in this note involve at least one leptonic vector boson decay. Electrons and muons are selected using standard ATLAS criteria [33], [34]. Figure 11 shows the efficiency for  $W$  boson daughter leptons. The results for different electron selection criteria are given. The loss of efficiency occurs in the forward regions, near the limits of the tracking detectors and at  $p_T$  values close to the applied cut. The efficiencies for the leptonic  $Z$  boson channels have been found to be similar.

### 4.2.2 Leptonic $Z$ Boson Reconstruction

The  $Z$  boson candidates are reconstructed from pairs of  $e^+e^-$  or  $\mu^+\mu^-$ . In the electron case, the mass resolution is about 2.7 GeV as is shown in Fig. 12 left, suggesting a mass window selection between  $m = 85$  GeV and 97 GeV for  $m_{ee}$ . In the case of muons, the resolution for the  $Z$  mass reconstruction is 3.6 GeV (see Fig. 12 right), so the mass requirement is loosened to be between  $m = 83$  GeV and 99 GeV. Furthermore, to reduce the backgrounds (particularly the background from  $t\bar{t}$  events), the  $p_T$  of one of the leptons is required to be  $p_T > 50$  GeV, and of the other  $p_T > 35$  GeV. In the unlikely case that more than one combination of leptons satisfy all these requirements, we choose the composite  $Z_{\ell^+\ell^-}$  with the mass closest to the actual  $Z$  boson mass.

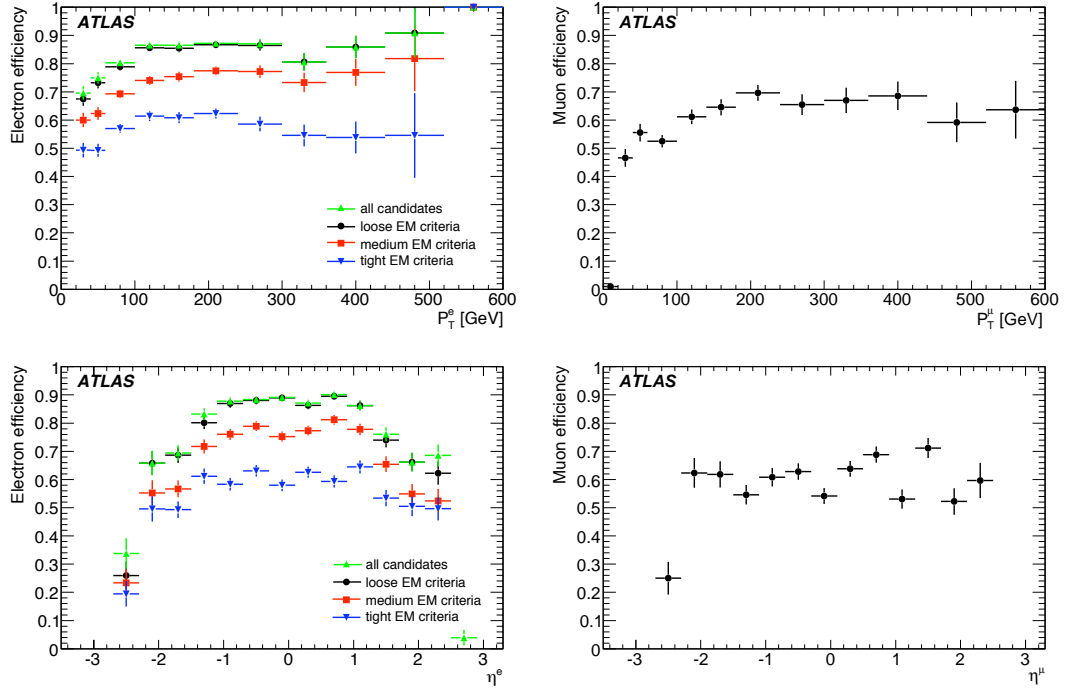


Figure 11: Efficiency of reconstructing and identifying  $W$ -daughter electrons (left) and muons (right) as functions of true lepton momentum (top) and pseudo-rapidity (bottom). The electron plots show the efficiency for 4 different electron selection criteria: All candidate objects (green), *loose* (black circles), *medium* (red squares), and *tight* (blue triangles).

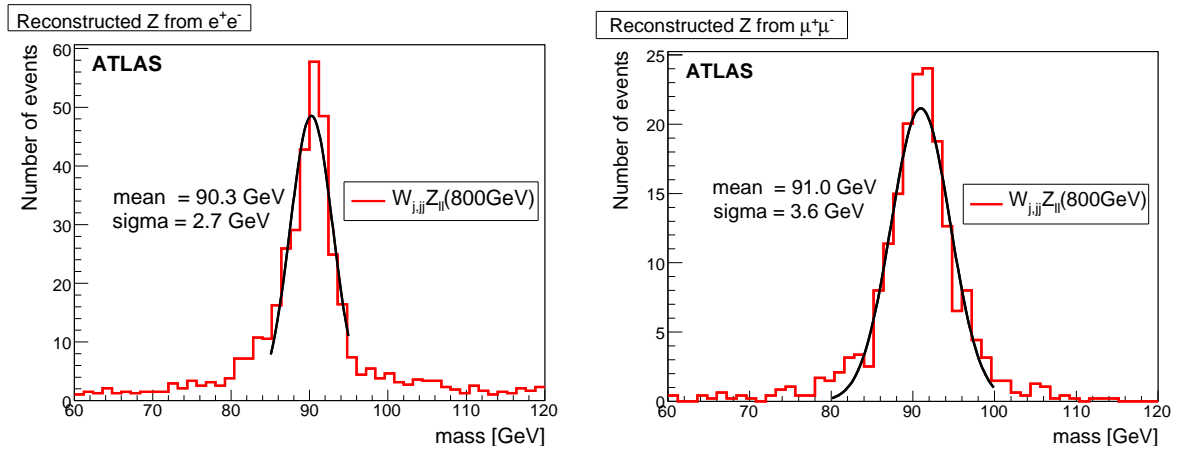


Figure 12: Reconstructed  $Z$  boson from electron pairs (left) and muon pairs (right).

### 4.2.3 Leptonic $W$ Boson Reconstruction

The  $W$  boson reconstruction uses the transverse components of the missing 3-momentum of the highest- $p_T$  lepton ( $e$  or  $\mu$ ) in the event. For the signal, after reconstruction of the hadronic vector boson candidate, the highest  $p_T$  lepton corresponds to the lepton from the  $W$  boson decay in 96% of cases. Attributing the missing momentum to the neutrino, and taking the nominal  $W$  boson mass ( $m_W = 80.42$  GeV) as a constraint, a quadratic equation is obtained for the  $z$ -component of the neutrino's momentum. The  $z$  component is required in order to reconstruct the diboson mass in the final analysis. Only events for which at least one real solution exists for this quadratic equation are retained. When there are two possible solutions, one is chosen at random to avoid kinematic bias on the resonance mass. Options such as selecting the reconstructed  $W$  boson which is more central have also been considered, and little difference was found in the purity of the reconstruction. In the fully leptonic case, the leptonic  $Z$  boson is reconstructed and its daughter leptons removed before applying the above procedure.

### 4.3 Tagged Forward Jets

One of the well known characteristic features of vector boson scattering is the presence of high energy forward jets [13], resulting from the primary quarks from which the vector bosons have radiated (see Fig. 13). Such forward jets are expected to be much less prominent in processes involving gluon or electroweak boson exchange with bremsstrahlung of vector bosons. In the latter case, these vector bosons are mostly transverse and have a harder  $p_T$  spectrum than in  $W_L W_L$  scattering. Correspondingly, the outgoing primary quarks have a harder  $p_T$  and are therefore less forward.

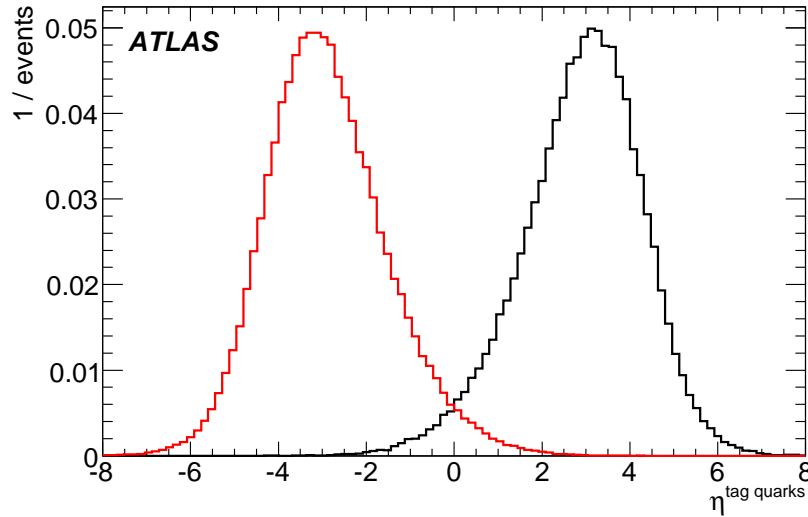


Figure 13: Pseudo-rapidity for the two quarks in signal events after they radiate the vector bosons, obtained from PYTHIA before any showering, fragmentation, etc.

Many different strategies are possible for implementing a tag-jet selection. A number of these were compared, and the best rejection factors for a given efficiency were obtained as follows:

1. Require two jets with

- $|\eta(jet)| > \eta_{\text{cut}}$  and  $p_T(jet) > p_{T\text{cut}}$  GeV.



- opposite signed rapidity
- at least one of them has an energy greater than a critical value  $E_{\text{cut}}$  GeV

2. If more than one jet with the same sign rapidity satisfies the above cuts, choose the most energetic, labelled FJ1. The next one is labelled FJ2.

- Require the tag-jet with the opposite sign of rapidity to satisfy  $\Delta\eta(FJ1, FJ2) > \Delta\eta_{\text{cut}}$  and  $E(FJ2) > E_{2\text{cut}}$  GeV.

In addition a dijet mass cut is currently applied in the cone algorithm analyses. The specific values of the cuts in each case are to be optimised depending upon the kinematic region under study.

#### 4.4 Central Jet Veto

A useful analysis strategy to suppress backgrounds such as  $t\bar{t}$  is to apply a central jet veto [14, 35, 36]. For vector boson scattering, one expects little QCD radiation in the central region since only colourless electroweak vector bosons are produced and the forward jets are not colour connected. Given the forward jet cut definition, we unambiguously define the central region of the event as the  $\eta$  region between them. The central jet veto then simply requires that no other high  $p_T$  jet (here taken as  $p_T > 30$  GeV) other than those resulting from the hadronically decaying vector boson lie in the central region.

Specifically in these analyses, where it is applied the central jet veto rejects events if there are any additional jets with a chosen maximum value for  $|\eta|$  and minimum value for  $p_T$ .

#### 4.5 Top Quark Rejection

While the final states from a leptonically decaying  $Z$  boson are mostly free of background from top processes,  $t\bar{t}$  and  $tW$  events form an important source of background for the  $WW$  signals. To suppress them, events can be vetoed if a reconstructed  $W$  boson candidate, combined with another jet in the event (excluding those overlapping with an identified electron or within  $\Delta R < 0.8$  of a  $W$  candidate), leads to an invariant mass close to that of the top quark [29]. A typical mass window is  $130 < m_t < 240$  GeV.

In a future analysis it is likely that this cut can be improved using  $b$ -tag information and better jet mass reconstruction, but this has not been investigated here.

### 5 Event Selection

Using the tools outlined in the previous section, we now characterise the samples and outline the specific cuts applied for each final state considered.

#### 5.1 $W^+W^- \rightarrow \ell^\pm \nu jj$ and $W^\pm Z \rightarrow \ell^\pm \nu jj$

The hadronic vector boson candidates and the tag jets are obtained using the  $k_\perp$  algorithm as discussed in Section 4.1. The leptonic  $W$  is identified as described in Section 4.2.3. Both vector boson candidates are required to have  $p_T > 200$  GeV,  $|\eta| < 2$ . Tag jet cuts are made as described in Section 4.3, with  $p_{T\text{cut}} = 10$  GeV,  $E_{\text{cut}} = E_{2\text{cut}} = 300$  GeV and  $\Delta\eta_{\text{cut}} = 5$ . The top veto (Section 4.5) and the central jet veto (Section 4.4) are applied.

The kinematic distributions for the  $WW$  channel are shown in Fig. 14. Note that these are significantly biased by the generator-level cuts. The selection efficiencies of the cuts on

$WW$  events from four example scenarios are summarised in Table 6, along with the efficiency of the combined trigger selection described in Section 3. No significant differences are observed between the scalar and vector resonances, nor between the  $WZ$  and  $WW$  channels, except for the  $m = 500$  GeV-resonant samples, where the  $p_T$  requirements are found to be less efficient for the  $WZ$  sample. The QCD-like model of [26] tends to predict softer vector bosons.

Due to the small background statistics available with full simulation, the full-simulation signal samples are used together with fast-simulation background samples in obtaining the final results. The modelling of the kinematics is good, as shown in Fig. 14 <sup>2)</sup>. However, in general the efficiency for selecting both signal and background is higher in fast simulation by about 25% compared to full simulation. To account for this, a constant scaling factor is applied to the fast-simulation samples in estimating the significance of the signal over the background (Section 6).

Figure 15 shows a comparison of the final  $WW$  mass for the signal samples using fast and full simulation.

The final  $WW$  mass spectra obtained using this analysis are shown in Fig. 16. The backgrounds shown have been obtained from the fast-simulation samples and the above mentioned scaling factor has been applied.

## 5.2 $W^\pm Z \rightarrow jj \ell^+ \ell^-$

This channel benefits from a very good resolution on the  $Z$  boson leptonic reconstruction, which allows good suppression of the  $t\bar{t}$  background.

For the  $m = 1.1$  TeV  $WZ$  resonance, only the case of a single heavy jet from the  $W$  boson decay will be considered as it constitutes the majority of the events. For the  $m = 800$  GeV resonance, not all  $W$  bosons are boosted sufficiently to produce a single jet. We therefore consider separately the cases of a  $W$  boson from a single heavy jet and from a jet pair. Finally, for the  $m = 500$  GeV resonance, we only consider the jet pair case. In this section, the cone algorithm will be used and compared with an analysis using the  $k_\perp$  jet algorithm.

### 5.2.1 $W$ boson from a single jet

The main backgrounds will here be  $Z + 3$  jets and  $t\bar{t}$ .

Table 7 shows the cut flow for the electron-based and the muon-based analyses for the ChL  $WZ$  resonances of mass  $m = 1.1$  TeV and  $m = 800$  GeV. The  $m = 500$  GeV case is not considered here since the  $W$  and  $Z$  bosons will not be sufficiently boosted, in general, to produce a single jet. The  $Z \rightarrow e^+e^-$  and  $Z \rightarrow \mu^+\mu^-$  selections are shown, which correspond each to about 50% of the sample events. After applying electron quality cuts (*medium* electrons) we select the two highest  $p_T$  leptons which should satisfy respectively:  $p_T(e, \mu) > 50$  GeV and  $p_T(e, \mu) > 35$  GeV. The low efficiency of the lepton pair cut is approximately consistent with the expected selection efficiency per lepton, as shown in Fig. 11, as well as the detector acceptance. As can be seen in Fig. 17, the  $p_T$  cut suppresses mostly the  $t\bar{t}$  background. A leptonic  $Z_{e^+e^-}$  or  $Z_{\mu^+\mu^-}$  is afterwards reconstructed as described in Section 4.2.2, almost eliminating completely this background. The efficiency of this cut is somewhat poorer for the signal than for the background because most of the background events have  $Z$  bosons of relatively low  $p_T$ , with different lepton pair energies and opening angle.

<sup>2)</sup>To achieve this agreement it was necessary to correct the lepton-finding efficiency in the fast simulation by fitting a function to the efficiency from fast and full simulation as a function of lepton  $p_T$  and correcting the fast simulation by the ratio of the functions.

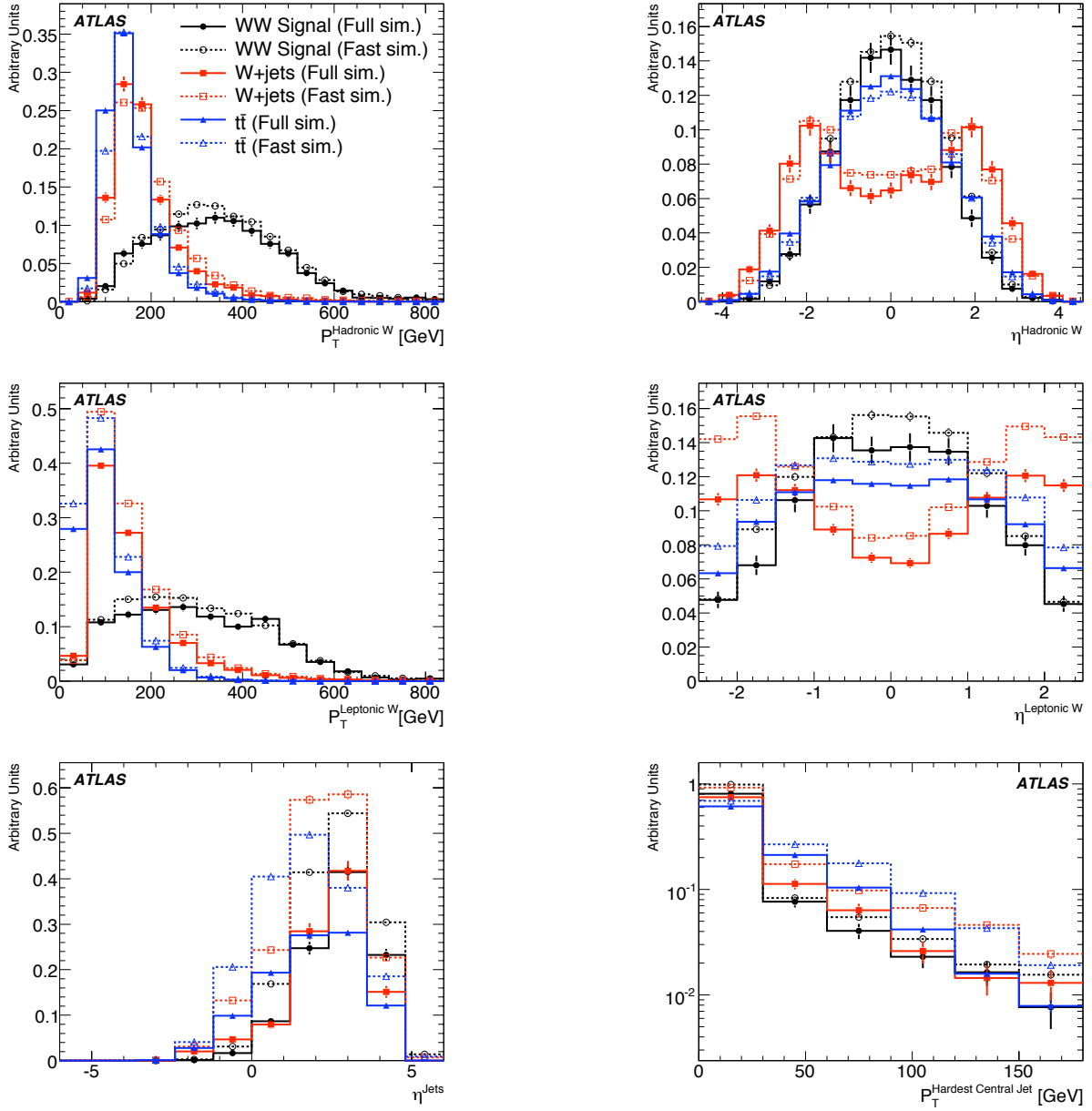


Figure 14: Kinematic distributions for the generated signal and backgrounds ( $t\bar{t}$  and  $W+4$  jets QCD) in the  $W^+W^- \rightarrow \ell^\pm \nu j(j)$  channel. The top two plots show the  $p_T$  and  $\eta$  for the hadronic  $W$  boson candidate. The middle two show the same variables for the leptonic  $W$  boson candidate. The bottom two plots show the  $\eta$  distribution of all jets which are at higher rapidity than the  $W$  boson candidates, and the  $p_T$  distribution of the highest- $p_T$  central jet. In each plot, the full-simulation histograms (solid lines) have been normalised to unit area and the fast-simulation histograms (dashed lines) have been normalised to the same cross-section as their full-simulation counterparts.

| Cut  | $m = 500 \text{ GeV}$ Scalar Resonance |               | $m = 800 \text{ GeV}$ Scalar Resonance |                 | $m = 1.1 \text{ TeV}$ Vector Resonance |               |
|--|--|---------------|--|-----------------|--|---------------|
|  | Efficiency (%)                         | $\sigma$ (fb) | Efficiency (%)                         | $\sigma$ (fb)   | Efficiency (%)                         | $\sigma$ (fb) |
| <b>Starting sample</b><br>$\equiv 1$ Hadronic $W$<br>$\equiv 1$ Leptonic $W$<br>$p_T$ (Had. $W$ ) $> 200 \text{ GeV}$<br>$ \eta $ (Had. $W$ ) $< 2$<br>$p_T$ (Lep. $W$ ) $> 200 \text{ GeV}$<br>$ \eta $ (Lep. $W$ ) $< 2$<br>$\equiv 2$ tag jets<br>$\equiv 0$ top candidates<br>Central jet veto<br>Trigger efficiency | –                                      | 66            | –                                      | 28              | –                                      | 18            |
|  | $32.1 \pm 0.5$ ( 34)                   | 21 ( 23)      | $40.0 \pm 0.5$ ( 45)                   | 11 ( 13)        | $39.5 \pm 0.7$ ( 43)                   | 7.1 ( 7.8)    |
|  | $45.4 \pm 0.9$ ( 54)                   | 9.6 ( 12)     | $48.5 \pm 0.8$ ( 57)                   | 5.4 ( 7.1)      | $48.8 \pm 1.2$ ( 55)                   | 3.5 ( 4.3)    |
|  | $57.6 \pm 1.3$ ( 69)                   | 5.5 ( 8.5)    | $88.2 \pm 0.7$ ( 90)                   | 4.8 ( 6.4)      | $86.6 \pm 1.1$ ( 88)                   | 3.0 ( 3.8)    |
|  | $91.9 \pm 0.9$ ( 93)                   | 5.1 ( 7.9)    | $95.3 \pm 0.5$ ( 95)                   | 4.6 ( 6.1)      | $93.4 \pm 0.9$ ( 92)                   | 2.8 ( 3.5)    |
|  | $43.8 \pm 1.8$ ( 42)                   | 2.2 ( 3.3)    | $91.3 \pm 0.7$ ( 89)                   | 4.2 ( 5.4)      | $92.4 \pm 1.0$ ( 89)                   | 2.6 ( 3.1)    |
|  | $95.5 \pm 1.1$ ( 94)                   | 2.1 ( 3.1)    | $95.3 \pm 0.6$ ( 95)                   | 4.0 ( 5.1)      | $92.8 \pm 1.0$ ( 93)                   | 2.4 ( 2.9)    |
|  | $32.0 \pm 2.6$ ( 37)                   | 0.7 ( 1.1)    | $42.4 \pm 1.3$ ( 49)                   | 1.7 ( 2.5)      | $43.7 \pm 2.0$ ( 55)                   | 1.1 ( 1.6)    |
|  | $50.0 \pm 5.0$ ( 40)                   | 0.3 ( 0.5)    | $52.0 \pm 2.1$ ( 41)                   | 0.9 ( 1.0)      | $51.4 \pm 3.0$ ( 44)                   | 0.5 ( 0.7)    |
|  | $100.0 \pm 0.0$ ( 98)                  | 0.3 ( 0.4)    | $96.7 \pm 1.0$ ( 97)                   | 0.8 ( 1.0)      | $91.6 \pm 2.3$ ( 93)                   | 0.5 ( 0.7)    |
|  | $96 \pm 3$                             | 0.3 ( 0.4)    | $98 \pm 1$                             | 0.8 ( 1.0)      | $98 \pm 1$                             | 0.5 ( 0.7)    |
| Cut  | Non-resonant Signal                    |               | $t\bar{t}$ Background                  |                 | $W$ +jets Backgrounds                  |               |
|  | Efficiency (%)                         | $\sigma$ (fb) | Efficiency (%)                         | $\sigma$ (fb)   | Efficiency (%)                         | $\sigma$ (fb) |
| <b>Starting sample</b><br>$\equiv 1$ Hadronic $W$<br>$\equiv 1$ Leptonic $W$<br>$p_T$ (Had. $W$ ) $> 200 \text{ GeV}$<br>$ \eta $ (Had. $W$ ) $< 2$<br>$p_T$ (Lep. $W$ ) $> 200 \text{ GeV}$<br>$ \eta $ (Lep. $W$ ) $< 2$<br>$\equiv 2$ tag jets<br>$\equiv 0$ top candidates<br>Central jet veto<br>Trigger efficiency | –                                      | 10            | –                                      | 450000          | –                                      | 21365         |
|  | $38.0 \pm 0.7$ ( 41)                   | 3.8 ( 4.1)    | $18.9 \pm 0.1$ ( 19)                   | 85000 ( 84000)  | $8.3 \pm 0.1$ ( 9)                     | 1760 ( 1820)  |
|  | $48.2 \pm 1.1$ ( 55)                   | 1.8 ( 2.3)    | $22.1 \pm 0.2$ ( 29)                   | 19000 ( 25000)  | $23.3 \pm 0.7$ ( 31)                   | 410 ( 570)    |
|  | $82.1 \pm 1.3$ ( 86)                   | 1.5 ( 1.9)    | $16.8 \pm 0.4$ ( 20)                   | 3200 ( 5000)    | $34.4 \pm 1.7$ ( 43)                   | 140 ( 240)    |
|  | $94.4 \pm 0.8$ ( 94)                   | 1.4 ( 1.8)    | $90.3 \pm 0.7$ ( 90)                   | 2900 ( 4500)    | $80.1 \pm 2.4$ ( 77)                   | 110 ( 190)    |
|  | $90.4 \pm 1.1$ ( 87)                   | 1.3 ( 1.6)    | $34.5 \pm 1.3$ ( 29)                   | 990 ( 1300)     | $48.5 \pm 3.3$ ( 40)                   | 55 ( 75)      |
|  | $96.0 \pm 0.8$ ( 96)                   | 1.2 ( 1.5)    | $94.6 \pm 1.0$ ( 90)                   | 930 ( 1200)     | $80.4 \pm 3.9$ ( 79)                   | 44 ( 59)      |
|  | $45.1 \pm 2.0$ ( 54)                   | 0.6 ( 0.8)    | $8.1 \pm 1.3$ ( 10)                    | 76 ( 120)       | $13.9 \pm 3.5$ ( 22)                   | 6 ( 13)       |
|  | $56.5 \pm 3.0$ ( 47)                   | 0.3 ( 0.4)    | $7.9 \pm 4.4$ ( 2)                     | 5 ( 2)          | $60.5 \pm 13.1$ ( 23)                  | 4 ( 3)        |
|  | $91.1 \pm 2.3$ ( 94)                   | 0.3 ( 0.4)    | $< 50$ ( $< 25$ )                      | $< 5$ ( $< 1$ ) | $84.9 \pm 13.7$ ( 91)                  | 3 ( 3)        |
|  | $98 \pm 1$                             | 0.3 ( 0.4)    | $\sim 100$                             | $< 5$ ( $< 1$ ) | $82 \pm 16$                            | 3 ( 3)        |

Table 6: Efficiencies of the cuts for four different  $qqWW \rightarrow qq\ell\nu qq$  signal samples and the backgrounds. The trigger efficiency row shows the efficiency of the logical OR of mu20i, e25i and jet160 signatures on the samples after all the cuts have been consecutively applied. The numbers in brackets are from the fast simulation.

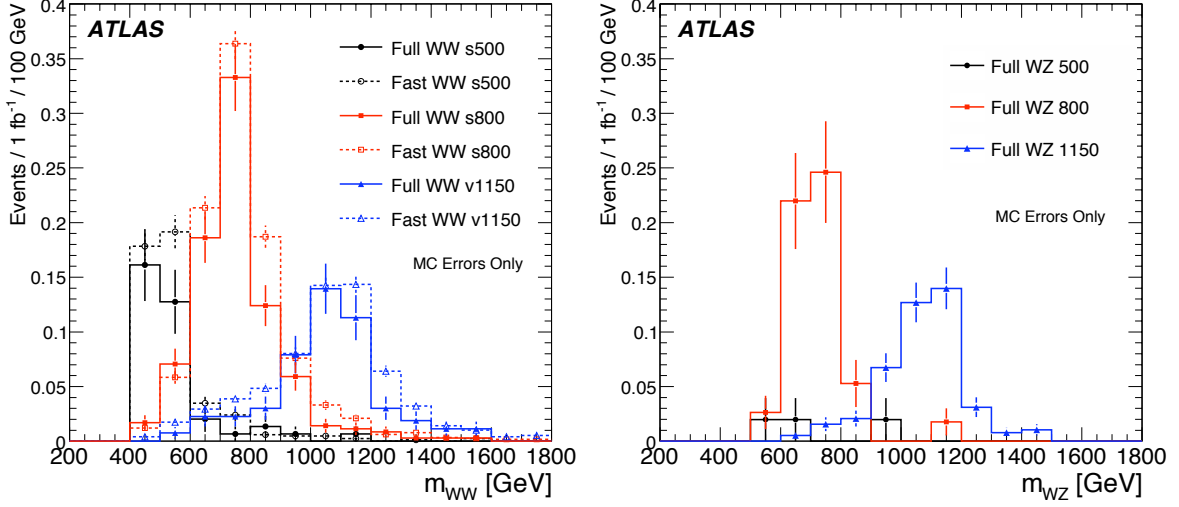


Figure 15:  $WW$  (left) and  $WZ$  (right) invariant mass spectra in the  $\ell\nu j(j)$  semileptonic channel for the three resonant signal samples. The  $WW$  plot shows a comparison of the fast- and full-simulation results.

Using the cone algorithm, size 0.8, the hadronic  $W$  boson candidate is identified as a heavy single jet having a mass between 70 and 100 GeV, and separated in azimuthal angle from the  $Z$  boson candidate by  $\Delta\phi(W, Z) > 2$ , as described in Section 4.1 (see Fig. 18). At this stage, considering that the fraction of single jet  $W$  bosons becomes important for  $p_T > 250$  GeV (see Fig. 5), and in order to be consistent with the preselection cuts on the  $Z+3$  jets background, we apply the following cuts to the reconstructed  $W$  and  $Z$  bosons:  $p_T^{W,Z} > 250$  GeV and  $|\eta^{W,Z}| < 2.0$ .

After a forward jet selection, (see Section 4.3,  $p_{T\text{cut}} = 20$  GeV,  $E_{\text{cut}} = E_{2\text{cut}} = 300$  GeV,  $\eta_{\text{cut}} = 1.5$ ,  $|\eta_{fjet}| > \eta_{\text{central jet}}$ ,  $\Delta\eta_{\text{cut}} = 4.5$ ), the invariant mass of these two jets is required to be greater than 700 GeV. Note that the efficiency of the forward jet cuts appearing in Table 7 appears artificially good for the background because a preselection was already applied.

A central jet veto was found to be unnecessary, as no  $t\bar{t}$  event survived the selection. Because of the lack of statistics for the  $t\bar{t}$  sample, it is not possible to exclude completely a contribution from this background. The normalisation factor is 4.9, meaning that  $t\bar{t}$  is excluded, over the whole mass range, at the level of 11.3 fb at 90% C.L. To have an estimate of the efficiency of the last two cuts at rejecting this background, the mass window for the cut on the  $Z$  boson mass was loosened:  $60 < m_Z < 120$  GeV, allowing 44 events (215 fb) to pass for the  $Z \rightarrow ee$  channel and 38 events (185 fb) for the  $Z \rightarrow \mu\mu$  channel. The  $W$  boson mass cut alone is found to have an efficiency of 12% and the forward jet cut alone lets no event survive. Assuming that the cuts are independent, the overall efficiency of the heavy jet mass cut and forward jet tagging combined is higher than 0.15%. The exclusion limit at 95% C.L. ( $1.64 \sigma$ ) for the  $t\bar{t}$  background is shown in Table 7 and it will be assumed that this is negligible in the mass window of the resonance. The  $Z+4$  jets background was not included here because it may be double-counting with  $Z+3$  jets with parton shower. In order to evaluate the level of this background, an average over the high mass region was taken because of the relatively poor Monte Carlo statistics, yielding about 0.03 fb/100 GeV.

For the  $m = 1.1$  TeV case, it was found that the trigger efficiency, based on the OR of e60,

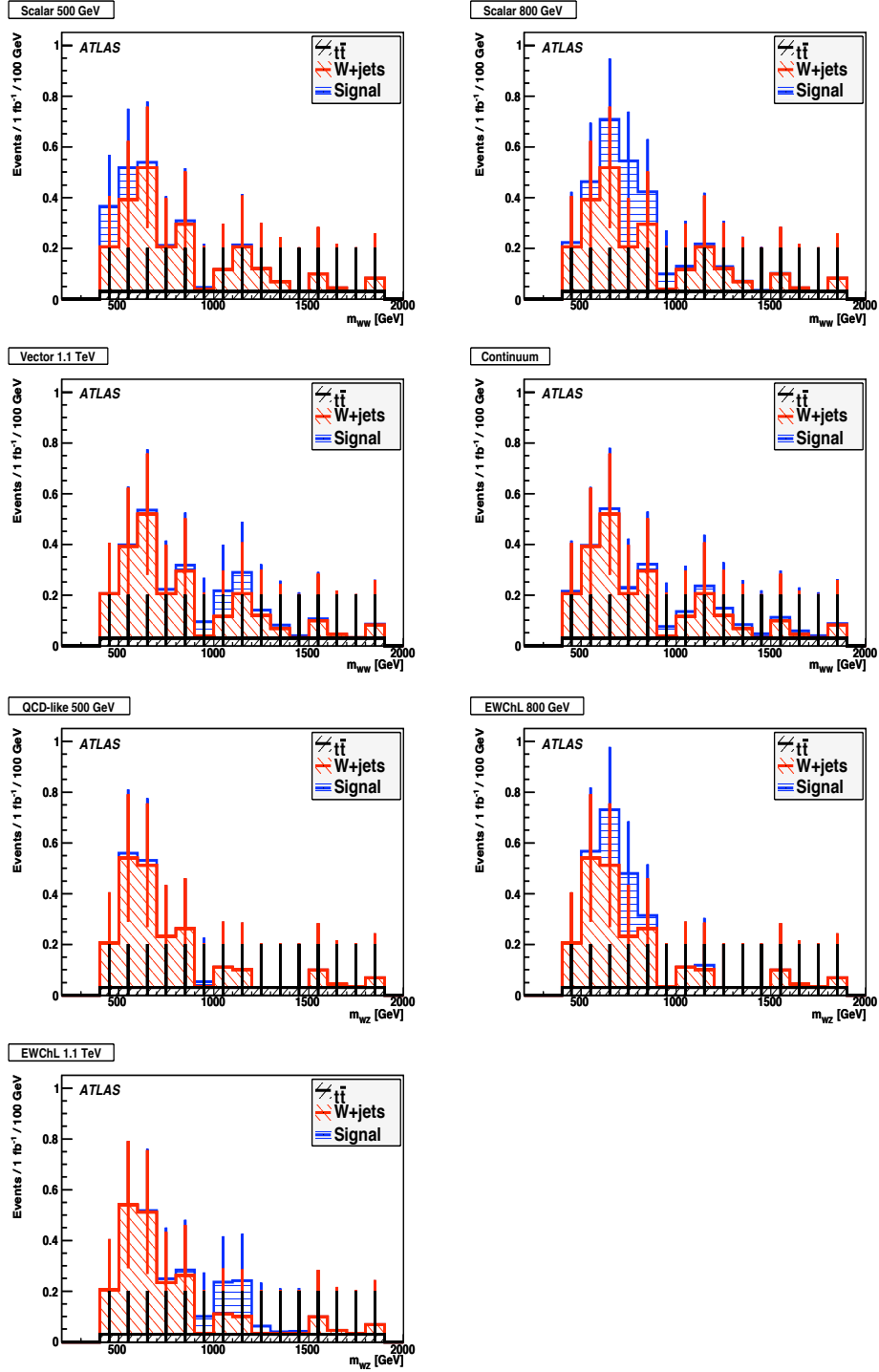


Figure 16:  $WW$  (top 4) and  $WZ$  (bottom 3) invariant mass spectra in the  $\ell\nu j(j)$  semileptonic channel, showing the total  $W$ +jets and  $t\bar{t}$  backgrounds and the signal for the three resonant signal samples and the continuum sample. The error bars reflect the uncertainty from the Monte Carlo statistics.

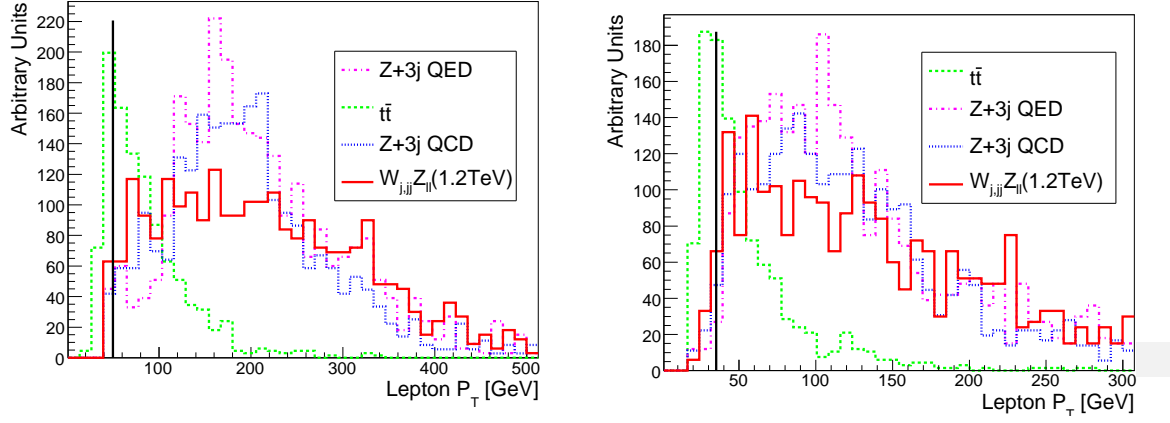


Figure 17:  $p_T$  of the highest  $p_T$  and second highest  $p_T$  electrons from reconstructed  $Z$  bosons in the  $m = 1.1$  TeV resonance sample. Distributions are arbitrarily normalised. The line indicates the cut value.

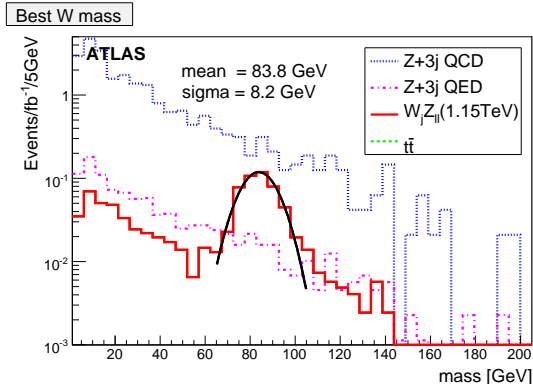


Figure 18: Mass of the heavy jet for the  $m = 1.1$  TeV ChL resonance and corresponding backgrounds. No  $t\bar{t}$  event is left.

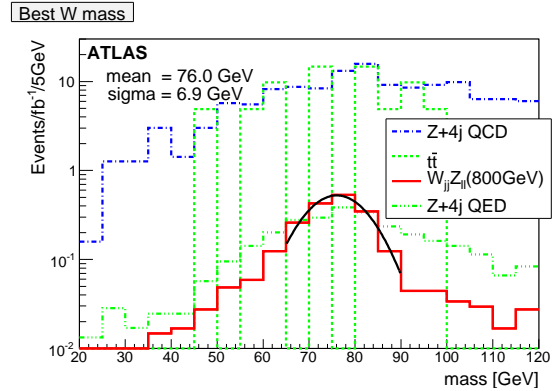


Figure 19: Reconstructed  $W$  boson mass from a jet pair for the  $m = 800$  GeV resonance.

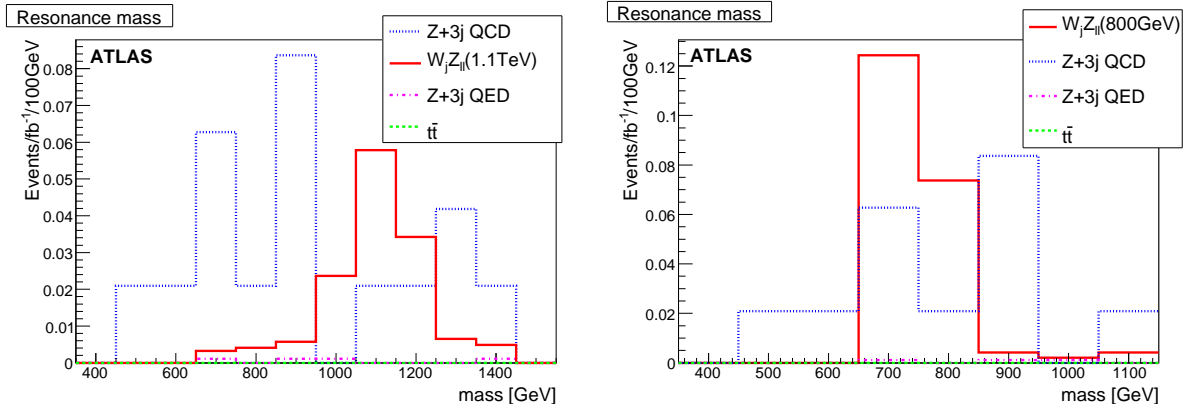


Figure 20: Reconstruction of ChL resonance at  $m = 1.1$  TeV (left) and  $m = 800$  GeV (right) in the channel  $qqW_jZ_{\ell\ell}$  (with  $\ell = e, \mu$ ), where a single jet cone 0.8 has been used to reconstruct the  $W$ .

mu20 and j160, was 100% at the end of the selection.

Figure 20 shows the resonance mass resulting when the  $Z$  boson has been reconstructed from electrons or muons and the  $W$  boson from a single jet of size 0.8.

### 5.2.2 $W$ boson from a jet pair

As above, after applying electron quality cuts, the lepton transverse momenta are required to satisfy  $p_T(e_1, \mu_1) > 50$  GeV and  $p_T(e_2, \mu_2) > 35$  GeV, and a  $Z_{e^+e^-}$  ( $Z_{\mu^+\mu^-}$ ) boson having a mass between 85 and 97 GeV (83 and 99 GeV) is then reconstructed. Considering all pairs of jets with  $p_T > 30$  GeV in the central region ( $|\eta| < 3.0$ ) not overlapping with the electron jets from the  $Z$  decay, the one yielding an invariant mass closest to the mass of a  $W$  boson will be the  $W$  boson candidate (see Fig. 19). The low efficiency of this cut can be explained in part by the fact that a good fraction of events are constituted of a single jet  $W$  boson. Forward and backward jet selection proceeds as in 5.2.1. A central jet veto is also applied: we exclude events with an extra jet, having a  $p_T > 30$  GeV, not corresponding to the jets from the  $W$  boson or the forward and backward jets and we require the  $W$  and  $Z$  directions to be in the central region  $|\eta| < 2$ . Figure 21 show the resulting reconstructed resonance masses. Table 7 summarizes the cut flow for this analysis. Here, by using the technique of widening the  $Z$  boson mass window as in Sect. 5.2.1, it is estimated that the  $t\bar{t}$  background could be approximately 0.13 fb and it will be assumed that this is negligible in the mass window of the resonance.

### 5.2.3 Comparison to $k_\perp$ analysis

This channel was also studied with the analysis techniques described in Section 5.1, with the  $k_\perp$  algorithm but using the leptonic  $Z$  boson identification (Section 4.2.2) instead of the leptonic  $W$  boson identification (Section 4.2.3). The hadronically-decaying  $W$  boson is reconstructed dynamically from one or two jets (Section 4.1).

The signal mass distributions for fast and full simulation are shown in Fig. 22. The final mass distributions are shown in Fig. 23, and are comparable to the results from the cone algorithm method for the 1.1 TeV case which is not sensitive to the cut on the  $p_T$  of the VB's of 200 GeV.



|   | $m = 1.1 \text{ TeV}$ |      | $m = 800 \text{ GeV}$ |      | $m = 500 \text{ GeV}$ |       | $Z + 3j$              |      | $Z + 4j$              |      | $t\bar{t}$            |       |
|---|-----------------------|------|-----------------------|------|-----------------------|-------|-----------------------|------|-----------------------|------|-----------------------|-------|
|   | $\sigma \text{ (fb)}$ | eff. | $\sigma \text{ (fb)}$ | eff. | $\sigma \text{ (fb)}$ | eff.  | $\sigma \text{ (fb)}$ | eff. | $\sigma \text{ (fb)}$ | eff. | $\sigma \text{ (fb)}$ | eff.  |
| $Z \rightarrow e^+e^-$  |                       |      |                       |      |                       |       |                       |      |                       |      |                       |       |
| $p_T(e1) > 50 \text{ GeV}, p_T(e2) > 35 \text{ GeV}$                            | 0.79                  | 22%  | 2.14                  | 20%  | 4.15                  | 16%   | 22.2                  | 20%  | 195                   | 7.9% | 1055                  | 29%   |
| $85 \text{ GeV} < m_Z < 97 \text{ GeV}$   | 0.63                  | 80%  | 1.69                  | 79%  | 3.34                  | 80%   | 18.5                  | 87%  | 176                   | 90%  | 39                    | 3.7%  |
| $Z \rightarrow \mu^+\mu^-$  |                       |      |                       |      |                       |       |                       |      |                       |      |                       |       |
| $p_T(\mu_1) > 50 \text{ GeV}, p_T(\mu_2) > 35 \text{ GeV}$                      | 0.60                  | 16%  | 1.67                  | 16%  | 3.11                  | 12.4% | 17.2                  | 16%  | 170                   | 7.0% | 821                   | 0.22% |
| $83 \text{ GeV} < m_Z < 99 \text{ GeV}$   | 0.48                  | 81%  | 1.40                  | 84%  | 2.68                  | 86%   | 15.8                  | 90%  | 163                   | 95%  | 64                    | 7.8%  |
| $Z \rightarrow e^+e^- \text{ and } Z \rightarrow \mu^+\mu^-$                    |                       |      |                       |      |                       |       |                       |      |                       |      |                       |       |
| $W_j Z u$   |                       |      |                       |      |                       |       |                       |      |                       |      |                       |       |
| Heavy jet mass $W \rightarrow j$  | 0.40                  | 36%  | 0.63                  | 20%  | —                     | —     | 1.16                  | 3.4% | —                     | —    | 0                     | 0%    |
| Forward jet tagging   | 0.29                  | 58%  | 0.23                  | 36%  | —                     | —     | 0.36                  | 31%  | —                     | —    | < 0.25                | —     |
| $W_{jj} Z u$  |                       |      |                       |      |                       |       |                       |      |                       |      |                       |       |
| $65 \text{ GeV} < m_{jj} < 90 \text{ GeV}$<br>and $\Delta\phi(W_{jj}, Z) > 2.0$ | —                     | —    | 1.51                  | 25%  | 2.21                  | 37%   | —                     | —    | 37.6                  | 11%  | 9.8                   | 9.5%  |
| Forward jet tagging   | —                     | —    | 0.62                  | 41%  | 0.68                  | 31%   | —                     | —    | 9.57                  | 25%  | —                     | —     |
| Central jet veto  | —                     | —    | 0.29                  | 47%  | 0.32                  | 47%   | —                     | —    | 4.85                  | 51%  | —                     | —     |

Table 7: Cut flow for the  $W_{jj}Z_{\ell\ell}$ ,  $m = 1.1 \text{ TeV}$ , 800 and 500 GeV signals. For each process, the cross-section (fb) surviving the successive application of the cuts is shown, as well as the efficiency of each cut. The upper limit for  $t\bar{t}$  in the last lines is for 95% C.L.

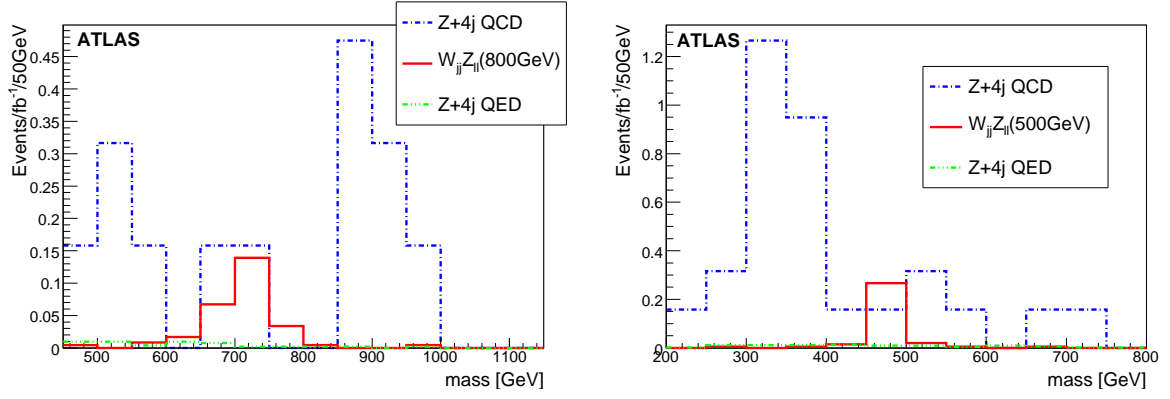


Figure 21: Reconstructed ChL resonance at  $m = 800$  GeV (left) and  $m = 500$  GeV (right) in the channel  $qqW_{jj}Z_{\ell\ell}$  (with  $\ell = e, \mu$ ) where two jets of cone size 0.4 have been used to reconstruct the  $W$  boson. No  $t\bar{t}$  events survive the selection.

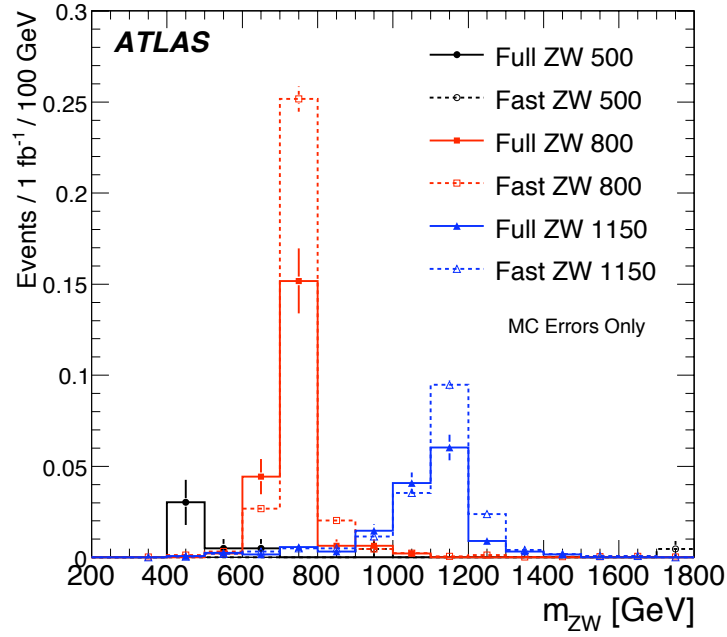


Figure 22:  $WZ$  invariant mass spectrum in the semileptonic channel for the three resonant signal samples obtained using  $k_{\perp}$  algorithm approach. Dotted lines indicate the fast simulation results.

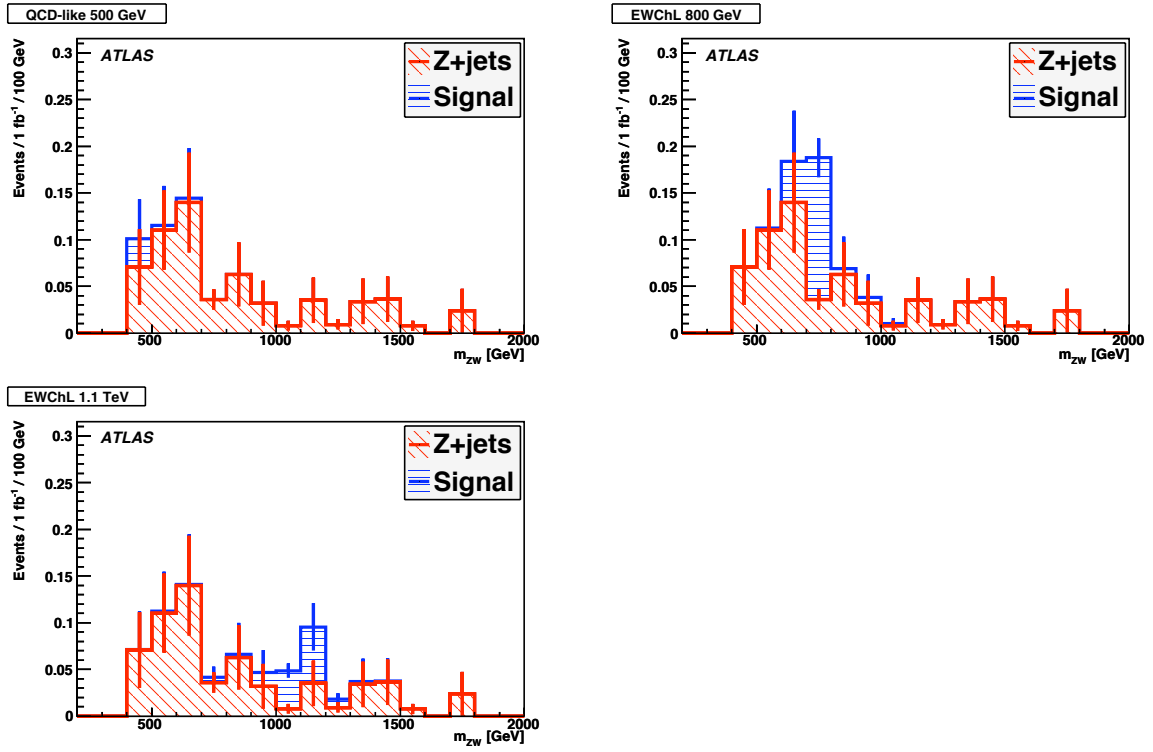
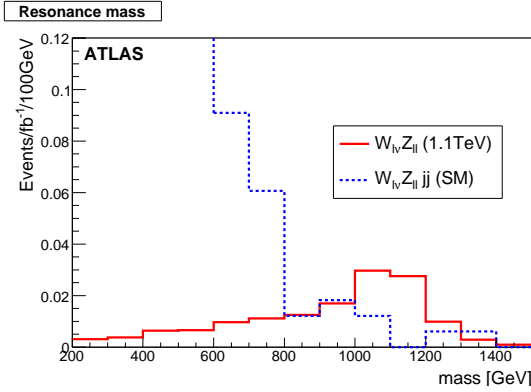
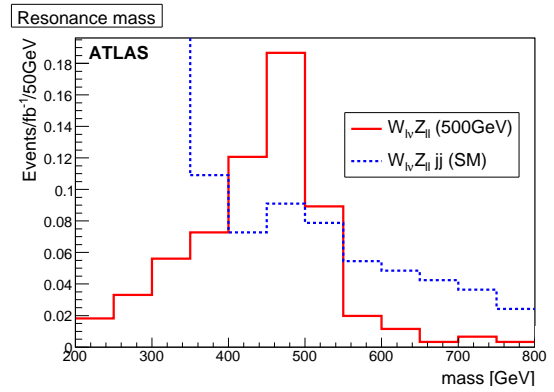


Figure 23:  $WZ$  invariant mass spectrum in the semileptonic channel for the three resonant signal samples obtained using  $k_{\perp}$  algorithm approach.  $Z$ +jet histogram (in red) represents a direct sum of all  $Z$ +3 or 4 jets backgrounds with no matching, and hence is a conservative estimate. The background from  $t\bar{t}$  events has been found to be negligible.


 Figure 24: Full reconstruction of ChL resonance  $m \sim 1.1$  TeV ( $W_{\ell^\pm\nu}Z_{\ell^\pm\ell^\mp}$ ).

 Figure 25: Full reconstruction of QCD-like resonance  $m \sim 500$  GeV ( $W_{\ell^\pm\nu}Z_{\ell^\pm\ell^\mp}$ ).

|                     | $W_{\ell\nu}Z_{\ell\ell}$ ( $m = 500$ GeV) |      | $W_{\ell\nu}Z_{\ell\ell}$ ( $m = 1.1$ TeV) |      | $W_{\ell\nu}Z_{\ell\ell}jj(SM)$ |      |
|---------------------|--|------|--|------|---------------------------------|------|
|                     | $\sigma$ (fb)                              | eff. | $\sigma$ (fb)                              | eff. | $\sigma$ (fb)                   | eff. |
| $Z_{ee}$            | 1.47                                       | 18%  | 0.23                                       | 20%  | 20.7                            | 16%  |
| $Z_{\mu\mu}$        | 1.09                                       | 14%  | 0.18                                       | 15%  | 16.7                            | 13%  |
| $W$ reconstruction  | 1.43                                       | 56%  | 0.25                                       | 61%  | 18.9                            | 51%  |
| Forward jet tagging | 0.63                                       | 44%  | 0.14                                       | 56%  | 1.6                             | 8.5% |

 Table 8: Cut flow for the  $W_{\ell\nu}Z_{\ell\ell}$  ( $m = 500$  GeV and 1.1 TeV) signals. All the cuts are described in detail in this section.

### 5.3 $W^\pm Z \rightarrow \ell^\pm \nu \ell^+ \ell^-$

This purely leptonic channel consists of four different signatures:  $W_{\ell^\pm\nu}Z_{\ell^\pm\ell^\mp}$  with  $\ell = e, \mu$ . The main background will be  $WZjj$  production from the Standard Model. The analysis starts by identifying leptonic  $Z_{e^+e^-}$  ( $Z_{\mu^+\mu^-}$ ) bosons as described in Section 4.2.2, after requiring two leptons with  $p_T$  greater than 50 and 35 GeV.

As a second step, we proceed to reconstruct the  $W$  boson from the highest  $p_T$  lepton among those remaining in the event, if there is one, and the measured missing transverse energy, as described in Section 4.2.3. The solution which yields the highest  $p_T$   $W$  boson is kept.

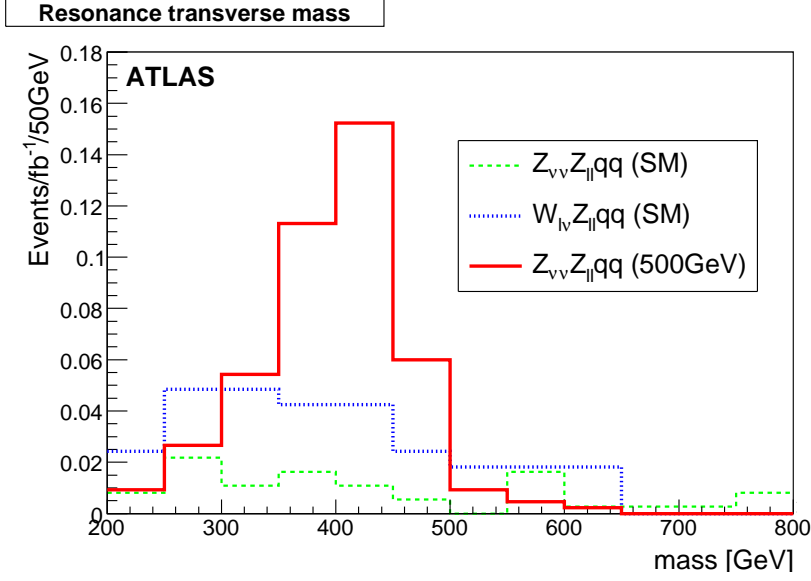
The forward and backward jet selection follows the prescription of the Section 4.3 ( $p_{T\text{cut}} = 20$  GeV,  $E_{\text{cut}} = E_{2\text{cut}} = 300$  GeV,  $\eta_{\text{cut}} = 1.5$ ,  $|\eta_{f\text{jet}}| > \eta_{\text{central jet}}$ ,  $\Delta\eta_{\text{cut}} = 4.5$ ).

In Table 8 we present the cut flow of the reconstruction of the resonances for 1.1 TeV and 500 GeV. Also in Fig. 24 and Fig. 25 we present the reconstructed resonance and the background  $WZjj$  for the same resonance mass.

### 5.4 $ZZ \rightarrow \nu\nu \ell^+ \ell^-$

This scalar resonance can be interpreted as a Standard Model Higgs boson produced by vector boson fusion. At leading order, the cross-section times branching ratio would be 6 fb, compared to 4 fb obtained for the ChL model. This signal is characterised by a leptonic  $Z$  boson accompanied by large  $\cancel{E}_T$ , yielding a large transverse mass. The backgrounds considered are:  $ZZjj \rightarrow \ell\ell\nu\nu jj$  and  $WZjj \rightarrow \ell\nu\ell\ell jj$ . Other background can result from  $Z$ +jets production, where the tail of the missing transverse energy distribution can fake a signal.

After selecting the leptonically decaying  $Z_{e^+e^-}$  ( $Z_{\mu^+\mu^-}$ ) boson as usual, with mass between 85


 Figure 26: Transverse mass of the  $m = 500$  GeV resonance  $Z_{\nu\nu}Z_{\ell\ell}$ .

|                          | $Z_{\nu\nu}Z_{\ell\ell}qq$ ( $m = 500\text{GeV}$ ) |       | $W_{\ell\nu}Z_{\ell\ell}jj$ (SM) |      | $Z_{\nu\nu}Z_{\ell\ell}jj$ (SM) |      |
|--------------------------|--|-------|----------------------------------|------|---------------------------------|------|
|                          | $\sigma$ (fb)                                      | eff.  | $\sigma$ (fb)                    | eff. | $\sigma$ (fb)                   | eff. |
| $Z_{ee}$                 | 0.72   | 17.6% | 20.78                            | 22%  | 9.1                             | 20%  |
| $Z_{\mu\mu}$             | 0.58   | 15%   | 16.7                             | 17%  | 6.6                             | 15%  |
| Forward jet tagging      | 0.58   | 45%   | 3.2                              | 8.6% | 0.47                            | 3%   |
| $\cancel{E}_T > 150$ GeV | 0.44   | 75%   | 0.46                             | 14%  | 0.12                            | 26%  |

 Table 9: Cut flow for the  $Z_{\nu\nu}Z_{\ell\ell}qq$  ( $m = 500$  GeV) signal. All the cuts are described in detail in this section.

and 97 GeV (83 and 99 GeV), a minimum  $\cancel{E}_T$  of 150 GeV is required. For this high value of  $\cancel{E}_T$ ,  $Z$ +jets background is expected to be negligible for a Standard Model Higgs boson signal [36]. The forward jet selection is applied (see Section 4.3,  $p_{T\text{cut}} = 20$  GeV,  $E_{\text{cut}} = E_{2\text{cut}} = 300$  GeV,  $\eta_{\text{cut}} = 1.5$ ,  $\Delta\eta_{\text{cut}} = 4.5$ ).

The transverse mass, defined as:

$$m_T^2 = (\sqrt{p_T(Z)^2 + m_Z^2} + \cancel{E}_T)^2 - (\vec{p}_T(Z) + \vec{\cancel{p}}_T)^2 \quad (1)$$

is shown in Fig. 26 and the cut flow can be found in Table 9.

## 6 Results

The significance of the signals and the luminosity required for a possible discovery is estimated here. From the reconstructed resonance mass distributions in Section 5 one can evaluate the size of the signal and background in the resonance mass window. Table 10 summarises the approximate cross-sections expected after the analyses described above. The table also gives the luminosity required to observe a significant excess over the background, showing the uncertainty from MC statistics only, and the significance of a signal for an integrated luminosity of  $100 \text{ fb}^{-1}$ .

| Process   | Cross-section (fb) |                   | Luminosity (fb <sup>-1</sup> ) |                | Significance<br>for 100 fb <sup>-1</sup> |
|---|--------------------|-------------------|--------------------------------|----------------|--|
|   | signal             | background        | for 3 $\sigma$                 | for 5 $\sigma$ |  |
| $WW/WZ \rightarrow \ell\nu jj$ ,<br>$m = 500$ GeV | $0.31 \pm 0.05$    | $0.79 \pm 0.26$   | 85                             | 235            | $3.3 \pm 0.7$                            |
| $WW/WZ \rightarrow \ell\nu jj$ ,<br>$m = 800$ GeV | $0.65 \pm 0.04$    | $0.87 \pm 0.28$   | 20                             | 60             | $6.3 \pm 0.9$                            |
| $WW/WZ \rightarrow \ell\nu jj$ ,<br>$m = 1.1$ TeV | $0.24 \pm 0.03$    | $0.46 \pm 0.25$   | 85                             | 230            | $3.3 \pm 0.8$                            |
| $W_{jj}Z_{\ell\ell}$ , $m = 500$ GeV              | $0.28 \pm 0.04$    | $0.20 \pm 0.18$   | 30                             | 90             | $5.3 \pm 1.9$                            |
| $W_{\ell\nu}Z_{\ell\ell}$ , $m = 500$ GeV         | $0.40 \pm 0.03$    | $0.25 \pm 0.03$   | 20                             | 55             | $6.6 \pm 0.5$                            |
| $W_{jj}Z_{\ell\ell}$ , $m = 800$ GeV              | $0.24 \pm 0.02$    | $0.30 \pm 0.22$   | 60                             | 160            | $3.9 \pm 1.2$                            |
| $W_jZ_{\ell\ell}$ , $m = 800$ GeV                 | $0.20 \pm 0.02$    | $0.09 \pm 0.06$   | 30                             | 90             | $5.3 \pm 1.3$                            |
| $W_jZ_{\ell\ell}$ , $m = 1.1$ TeV                 | $0.11 \pm 0.01$    | $0.10 \pm 0.06$   | 90                             | 250            | $3.1 \pm 0.8$                            |
| $W_{\ell\nu}Z_{\ell\ell}$ , $m = 1.1$ TeV         | $0.070 \pm 0.004$  | $0.020 \pm 0.009$ | 70                             | 200            | $3.6 \pm 0.5$                            |
| $Z_{\nu\nu}Z_{\ell\ell}$ , $m = 500$ GeV          | $0.32 \pm 0.02$    | $0.15 \pm 0.03$   | 20                             | 60             | $6.6 \pm 0.6$                            |

Table 10: Approximate signal and background cross-sections expected after the analyses. An approximate value of the luminosity required for 3 $\sigma$  and 5 $\sigma$  significance, and the expected significance for 100 fb<sup>-1</sup> are shown. The uncertainties, when given, are due to Monte Carlo statistics only.

Because of the large statistical and systematic uncertainties (see Section 7), the numbers given here must be taken as an approximate indication of the reach of the LHC for such resonances.

The significance is calculated as

$$\text{significance} = \sqrt{2((S + B) \ln(1 + S/B) - S)} \quad , \quad (2)$$

where S (B) is the number of expected signal (background) events in the signal *peak* region, which is defined as the three consecutive bins (of size given in the figures, chosen to represent the resolution), with the highest total number of signal events. The background is averaged over this region.

In the  $WW$  case, only the semileptonic channel is accessible. Thus, as shown in Table 10, around 25 fb<sup>-1</sup> is needed to start seeing indications of a resonance even in the most optimistic case studied here, and around 70 fb<sup>-1</sup> is needed for a discovery.

In the continuum case, the “signal” is spread over an extended mass region with a total of about 0.3 events expected for each fb<sup>-1</sup> in the mass range  $m = 400$ –1900 GeV, compared to about 2.5 background events. Measuring this cross-section with any accuracy using the techniques developed here would required an integrated luminosity of several hundred fb<sup>-1</sup>.

Since the mass windows for hadronic  $W$  and  $Z$  boson decays overlap, in practice these scenarios can probably not be distinguished in this channel, and a combined analysis would in reality have to be performed, which would then be compared to those channels containing a leptonic  $Z$  boson decay.

For each of the  $WZ$  resonances, results of the different channels,  $W_{\ell\nu}Z_{\ell\ell}$ ,  $W_{jj}Z_{\ell\ell}$  and  $W_{\ell\nu}Z_{jj}$  can, in principle, be combined. From Table 10, one can conclude that for two of three mass regions,  $m = 500$  GeV and 800 GeV, a chiral Lagrangian vector resonance can be discovered with less than 100 fb<sup>-1</sup>. The expectations with the alternative  $k_{\perp}$  analysis described in Section 5.2.3 are not far from the values in Table 10. As an example, the integrated luminosity needed for 3 $\sigma$  observation of the  $m = 800$  GeV signal is 63 fb<sup>-1</sup>, and of the  $m = 1.1$  TeV signal is 81 fb<sup>-1</sup>.

A scalar resonance at  $m = 500 \text{ GeV}$  will require about  $60 \text{ fb}^{-1}$  to be seen in the  $ZZ \rightarrow \nu\nu\ell\ell$  channel.

## 7 Systematic Uncertainties

A number of large systematic uncertainties affect the signals studied here. Because of the small cross-sections and the important backgrounds, it is difficult to estimate them with precision from Monte Carlo simulations. Data driven tests will be required to understand better the systematic effects. Some discussion of the most significant effects is given here.

### 7.1 Background Cross-sections

As was discussed in Section 2, the renormalisation and factorisation scales,  $Q^2$ , can affect the cross-section by as much as a factor of two. This is especially true at high centre of mass energies, where the degree of virtuality of partons and choice of scale for  $\alpha_s$  are quite critical [37]. At present this represents a theoretical uncertainty on the current sensitivity estimate. While the predictions may improve in future, in an eventual analysis, the backgrounds would have to be measured from data and the eventual size of the associated systematic uncertainty has not been studied here.

Another consideration is that for the analyses which dynamically move between the dijet and single jet reconstruction technique for the hadronically decaying vector boson (see Section 4.1), to evaluate the background with the samples available both  $W+3$  jet and  $W+4$  jet samples must be used. This implies some double-counting due to the lack of parton-shower matching in these samples, and so the background will be overestimated. This is in addition to the fact that as shown in Section 2.4.1, the MADGRAPH samples used overestimate slightly the energy of the tag jets. The effect is expected to be at the few per cent level.

### 7.2 Signal Cross-sections

The PYTHIA signal generation produces softer tag jets than the more exact WHIZARD MC, and thus the signal efficiencies are likely to be underestimated.

### 7.3 Monte Carlo Statistics

We are limited by the very large size of the background samples required. Fast MC simulation was shown to be in good agreement with full simulation and was used to evaluate  $t\bar{t}$  background for the  $WW$  signals. In some cases, only upper limits on the backgrounds can be given, although it is expected that these limits are very conservative. Again, this represents a systematic uncertainty on the current sensitivity estimates, but will not be present in a final data analysis, assuming sufficient simulated data will eventually be available.

### 7.4 Pile-up and Underlying Event

Pile-up and underlying event are separate effects which have potentially similar and crucial impact on the efficiency of the forward jet cuts, the central jet veto and the top veto, as well as on the jet mass resolution.

Of particular concern is the fact that the top veto in the  $WW$  analysis uses jets down to  $p_T = 10 \text{ GeV}$ , expected to be strongly affected by these effects [38]. Simply raising the cut to  $20 \text{ GeV}$  admits significantly larger background. Some of this can be removed for the higher mass

resonances by raising the  $p_T$  cut on the vector boson. However, a more promising approach is likely to be to exploit  $b$ -tagging and improved jet mass reconstruction to improve the veto.

#### 7.4.1 Pile-up

Fully simulated samples with pile-up at low luminosity ( $10^{33}\text{cm}^{-2}\text{s}^{-1}$ ) were available, but with much lower statistics: we restricted the analysis to one signal and one background samples. However pile-up effects should be approximately independent of the underlying physics sample, and we assume we can safely generalise the results obtained here.

We compared the same events of the  $W_{jj}Z_{\ell\ell}$  at  $m = 1.1\text{ TeV}$  sample reconstructed with and without pile-up simulation. This allows computation of the fraction of events with pile-up having tagged forward jets with respect to corresponding non-pile-up events which fail the tagged jet criterion, thus defining a ‘fake’ rate. The reciprocal fraction defines a ‘miss’ rate. The effect of pile-up increases with increasing jet radius and decreasing energy threshold, as would be expected. We found that both ‘fake’ and ‘miss’ effects are essentially due to the degradation of energy resolution in presence of pile-up and that their combination contributes to an uncertainty on the efficiency of the order of 5%.

#### 7.4.2 Underlying Event

Current simulations use underlying event models tuned to Tevatron and other data [21], but there is a large extrapolation needed to 14 TeV. The underlying event would be have to be measured in LHC data, and its level is not currently known.

#### 7.5 Other Systematic Effects

Systematic effects, such as uncertainties in the luminosity, in efficiencies and resolutions, jet energy scale, etc. are of the order of a few percent and will therefore be completely dominated by the above effects and by statistical uncertainties.

### 8 Summary and Conclusion

The Chiral Lagrangian model with Padé unitarisation provides a framework for studying vector boson scattering at high mass, in case a light Higgs boson is not found at the LHC in the first years of running. With full detector simulation, the search for vector and scalar resonances of masses  $m = 500, 800$  and  $1100\text{ GeV}$  is studied. To suppress the very high backgrounds from  $W$ +jets and  $Z$ +jets to acceptable levels requires special techniques investigated here. In particular, at these high masses, hadronic vector boson decay results in a single jet. The reconstruction of the jet mass is found to be generally quite efficient at rejecting QCD jets. The  $k_{\perp}$  and the cone algorithms can be applied to this heavy jet to resolve it into two light jets, suppressing further the background. Other conventional techniques for the study of vector boson fusion are also found essential for the present analysis: forward jet tagging, central jet veto and top-jet veto.

The cut-based analysis presented here is performed with realistic simulation and reconstruction of leptons and jets. Improvements can be expected by more sophisticated analysis and, with real data and a good understanding of the detector, further gains can be achieved by improvements in the reconstruction efficiencies.

The discovery of resonances in vector boson scattering at high mass will take a few tens of  $\text{fb}^{-1}$ , but the different decay channels of the vector boson pairs allow a cross-check of the



presence of a resonance. These results can be considered generic of vector boson scattering and can therefore be interpreted in terms of other theoretical models with possibly different cross-sections.

## References

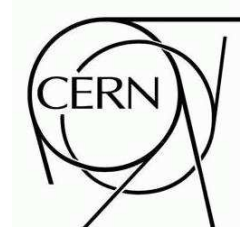
- [1] S. Dawson, [hep-ph/9901280](#).
- [2] M. S. Chanowitz. Presented at the 23rd International Conference on High Energy Physics, Berkeley, Calif., Jul 16-23, 1986.
- [3] K. Lane and S. Mrenna, *Phys. Rev.* **D67** (2003) 115011, [hep-ph/0210299](#).
- [4] C. Csaki, C. Grojean, H. Murayama, L. Pilo, and J. Terning, *Phys. Rev.* **D69** (2004) 055006, [hep-ph/0305237](#).  
C. Csaki, C. Grojean, L. Pilo, and J. Terning, *Phys. Rev. Lett.* **92** (2004) 101802, [hep-ph/0308038](#).  
G. Cacciapaglia, C. Csaki, C. Grojean, and J. Terning, *Phys. Rev.* **D71** (2005) 035015, [hep-ph/0409126](#).
- [5] C. Csaki, [hep-ph/0412339](#). Talk presented at SUSY 2004, Tsukuba, Japan, June 17-23 2004, [arXiv:hep-ph/0412339](#).  
A. Birkedal, K. T. Matchev, and M. Perelstein, [hep-ph/0508185](#).  
R. Sekhar Chivukula *et al.*, *Phys. Rev.* **D74** (2006) 075011, [hep-ph/0607124](#).
- [6] R. Casalbuoni, S. De Curtis, and M. Redi, *Eur. Phys. J.* **C18** (2000) 65–71, [hep-ph/0007097](#).
- [7] W. Kilian, *Springer Tracts Mod. Phys.* **198** (2003) 1–113.  
W. Kilian, [hep-ph/0303015](#).
- [8] A. Dobado and J. R. Pelaez, *Phys. Rev.* **D56** (1997) 3057–3073, [hep-ph/9604416](#).
- [9] A. Gomez Nicola and J. R. Pelaez, *Phys. Rev.* **D65** (2002) 054009, [hep-ph/0109056](#).
- [10] A. Dobado, M. J. Herrero, J. R. Pelaez, and E. Ruiz Morales, *Phys. Rev.* **D62** (2000) 055011, [hep-ph/9912224](#).
- [11] M. S. Chanowitz, *Phys. Rept.* **320** (1999) 139–146, [hep-ph/9903522](#).
- [12] J. A. Oller, E. Oset, and J. R. Pelaez, *Phys. Rev.* **D59** (1999) 074001, [hep-ph/9804209](#).
- [13] R. N. Cahn, S. D. Ellis, R. Kleiss, and W. J. Stirling, *Phys. Rev.* **D35** (1987) 1626.  
R. Kleiss and W. J. Stirling, *Phys. Lett.* **B200** (1988) 193.  
V. D. Barger, T. Han, and R. J. N. Phillips, *Phys. Rev.* **D37** (1988) 2005–2008.
- [14] V. D. Barger, K.-M. Cheung, T. Han, and D. Zeppenfeld, *Phys. Rev.* **D44** (1991) 2701–2716.
- [15] J. Bagger *et al.*, *Phys. Rev.* **D52** (1995) 3878–3889, [hep-ph/9504426](#).

- 686 [16] T. Sjostrand, S. Mrenna, and P. Skands, *JHEP* **05** (2006) 026, [hep-ph/0603175](#).
- 687 [17] F. Maltoni and T. Stelzer, *JHEP* **02** (2003) 027, [hep-ph/0208156](#).
- 688 [18] S. Frixione and B. R. Webber, *JHEP* **06** (2002) 029, [hep-ph/0204244](#).
- 689 S. Frixione, P. Nason, and B. R. Webber, *JHEP* **08** (2003) 007, [hep-ph/0305252](#).
- 690 [19] G. Corcella *et al.*, [hep-ph/0210213](#).
- 691 G. Corcella *et al.*, *JHEP* **01** (2001) 010, [hep-ph/0011363](#).
- 692 [20] J. M. Butterworth, J. R. Forshaw, and M. H. Seymour, *Z. Phys.* **C72** (1996) 637–646,
- 693 [hep-ph/9601371](#).
- 694 [21] S. Alekhin *et al.*, [hep-ph/0601012](#).
- 695 [22] P. Golonka *et al.*, *Comput. Phys. Commun.* **174** (2006) 818–835, [hep-ph/0312240](#).
- 696 [23] W. Kilian, T. Ohl, and J. Reuter, [arXiv:0708.4233 \[hep-ph\]](#).
- 697 [24] M. L. Mangano, M. Moretti, F. Piccinini, R. Pittau, and A. D. Polosa, *JHEP* **07** (2003)
- 698 001, [hep-ph/0206293](#).
- 699 M. L. Mangano, M. Moretti, and R. Pittau, *Nucl. Phys.* **B632** (2002) 343–362,
- 700 [hep-ph/0108069](#).
- 701 [25] F. Caravaglios, M. L. Mangano, M. Moretti, and R. Pittau, *Nucl. Phys.* **B539** (1999)
- 702 215–232, [hep-ph/9807570](#).
- 703 [26] A. Dobado, M. J. Herrero, and J. Terron, *Z. Phys.* **C50** (1991) 465–472.
- 704 [27] **ATLAS** Collaboration, “The ATLAS Trigger for early running.” This volume.
- 705 [28] S. Catani, Y. L. Dokshitzer, M. H. Seymour, and B. R. Webber, *Nucl. Phys.* **B406** (1993)
- 706 187–224.
- 707 J. M. Butterworth, J. P. Couchman, B. E. Cox, and B. M. Waugh, *Comput. Phys.*
- 708 *Commun.* **153** (2003) 85–96, [hep-ph/0210022](#).
- 709 M. Cacciari and G. P. Salam, *Phys. Lett.* **B641** (2006) 57–61, [hep-ph/0512210](#).
- 710 [29] J. M. Butterworth, B. E. Cox, and J. R. Forshaw, *Phys. Rev. D* **65** (2002) ,
- 711 [hep-ph/0201098](#).
- 712 [30] S. Allwood. Manchester PhD Thesis, 2006.
- 713 [31] E. Stefanidis. UCL PhD Thesis, 2007.
- 714 [32] J. M. Butterworth, J. R. Ellis, and A. R. Raklev, *JHEP* **05** (2007) 033, [hep-ph/0702150](#).
- 715 [33] **ATLAS** Collaboration, “Reconstruction and identification of electrons in ATLAS.” This
- 716 volume.
- 717 [34] **ATLAS** Collaboration, “Muon Reconstruction and Identification Performance in ATLAS:
- 718 Studies with Simulated Monte Carlo Samples.” This volume.
- 719 [35] V. D. Barger, K.-M. Cheung, T. Han, J. Ohnemus, and D. Zeppenfeld, *Phys. Rev.* **D44**
- 720 (1991) 1426–1437.

- 721 [36] **ATLAS** Collaboration, *CERN/LHCC 99-15* (1999) .  
722 **CMS** Collaboration, *CERN/LHCC 94-33* (1994) .  
723 K. Iordanidis and D. Zeppenfeld, *Phys. Rev.* **D57** (1998) 3072–3083, [hep-ph/9709506](#).  
724 D. L. Rainwater and D. Zeppenfeld, *Phys. Rev.* **D60** (1999) 113004, [hep-ph/9906218](#).  
725 [37] V. D. Barger, T. Han, J. Ohnemus, and D. Zeppenfeld, *Phys. Rev.* **D40** (1989) 2888.  
726 Erratum-ibid.D41:1715,1990.  
727 [38] S. Asai *et al.*, *Eur. Phys. J.* **C32S2** (2004) 19–54, [hep-ph/0402254](#).



# ATLAS NOTE



July 10, 2008

## Discovery Reach for Black Hole Production

The ATLAS Collaboration

### Abstract

Models with extra space dimensions, in which our Universe exists on a 4-dimensional brane embedded in a higher dimensional bulk space-time, offer a new way to address outstanding problems in and beyond the Standard Model physics. In such models the Planck scale in the bulk can be of the order of the electroweak symmetry breaking scale. This allows the coupling strength of gravity to increase to a size similar to the other interactions, opening the way to the unification of gravity and the gauge interactions. The increased strength of gravity in the bulk space-time means that quantum gravity effects would be observable in the TeV energy range reachable by the LHC. The most spectacular phenomenon would be the production of black holes, which would decay semi-classically by Hawking radiation emitting high energy particles. In this note, we discuss the potential for the ATLAS experiment to discover such black holes in the early data ( $1\text{--}1000\text{ pb}^{-1}$ )

# 1 Introduction

In this study we simulate the search for black holes in the first  $100 \text{ pb}^{-1}$  of LHC data with the ATLAS detector and software framework.

The document's structure is as follows: Section 2 gives an overview of the extra dimension models, present limits on the size of the extra dimensions and a discussion of black hole production and decay. In Section 3 the Monte Carlo simulation samples are described. Section 4 presents basic event properties, and is followed by Sections 5 and 6 dealing with the triggering and analysis selection, respectively. The expected systematic uncertainties are given in Section 7. Finally, the extraction of model parameters, especially of black hole properties, is covered in Section 8. A summary is given in Section 9.

## 2 Theory

### 2.1 Theoretical Motivation

The electroweak energy scale and the Planck scale, at which gravitational interactions become strong, differ by about sixteen orders of magnitude. This large difference between the scales of the two fundamental interactions is known as the hierarchy problem. Explaining the hierarchy problem is one of the outstanding challenges in particle physics.

Arkani-Hamed, Dimopoulos and Dvali (ADD) [1–3], and Randall and Sundrum (RS) [4, 5] have pioneered approaches to solving the hierarchy problem by using extra-dimensional space. The hierarchy is generated by the geometry of the additional spatial dimensions. ADD models postulate additional flat extra dimensions, while RS models invoke a single warped extra dimension. The observed weakness of gravity is thus due to the gravitational field being allowed to expand into the higher-dimensional space (bulk), while the Standard Model particles are confined to our familiar three-dimensional space (3-brane). Extra-dimensional models can also be motivated by string theory.

In extra-dimensional models, the  $D$ -dimensional Planck scale  $M_D$  is the fundamental scale from which the Planck scale  $M_{\text{Pl}} = 1.22 \times 10^{19} \text{ GeV}$  in four dimensions is derived<sup>1)</sup>. The relationship between the two scales is determined by the volume of the extra dimensions in ADD models or by the warp factor in RS models. For large extra dimensions or a strongly warped extra dimension, the fundamental scale of gravity can be as low as the electroweak scale. If the Planck scale is low enough, black holes could be produced at the Large Hadron Collider (LHC) [9, 10]. Detecting them will not only test general relativity and probe extra dimensions, but would also teach us about quantum gravity.

### 2.2 Experimental Limits

Assuming that low-scale gravity is due to the existence of extra dimensions<sup>2)</sup>, most experimental searches for unusual low-scale gravity effects have focused on detecting evidence for extra dimensions. Current experimental limits allow the fundamental scale of gravity to be as low as about 1 TeV. In testing the ADD models and deriving limits in these models, the compactification radius of all extra dimensions is assumed to be the same. ADD models have been tested at length scales comparable to the radius of the compactified (i.e. curled-up) dimensions  $R$ . Were the effective number of large extra dimensions to be  $n = D - 4$ , the inverse-square law would smoothly change from the  $1/r^2$  form for  $r \gg R$  to a  $1/r^{2+n}$  form for  $r \ll R$ . Searches have been performed and constraints on the Planck scale have been set by

<sup>1)</sup>Several conventions exist for the  $D$ -dimensional Planck scale in the ADD model. We denote by  $M_D$  the parameter defined by Giudice, Rattazzi and Wells [6] and used by the PDG [7]:  $M_D^{D-2} = (2\pi)^{D-4}/(8\pi G_D)$ , where  $G_D$  is the  $D$ -dimensional Newton gravity constant. In an alternative convention given by Dimopoulos and Landsberg [8] the  $D$ -dimensional Planck scale  $M_{\text{DL}}$  is defined via  $M_{\text{DL}}^{D-2} = 1/G_D$ .

<sup>2)</sup>See Ref. [11] for a model of TeV gravity in four dimensions.

tabletop and particle accelerator experiments, astrophysical observations, cosmic-ray measurements and cosmological considerations. Direct searches for black holes at collider experiments have not yet been performed. The only direct limits on black hole production in high energy interactions were obtained using cosmic-ray data. Table top experiments lead to an upper bound of  $R \leq 44 \mu\text{m}$ , at the 95% confidence level [12]. The LEP bounds obtained with direct searches vary from 1.5 TeV for  $n = 2$  extra dimensions to 0.75 TeV for 5 extra dimensions [13]. The latest direct search result from the CDF collaboration has set lower bounds with  $1.1 \text{ fb}^{-1}$  of Run II data on  $M_D$  of 1.33 TeV for  $n = 2$  to 0.88 TeV for  $n = 6$  [14]. All four LEP experiments combined set a lower limit on  $M_D$  of 1.2 TeV for positive interference, or 1.1 TeV for negative interference between Standard Model diagrams and graviton exchange [15, 16]. Indirect searches by the DØ [17] collaboration set lower limits around 1.28 TeV were derived<sup>3)</sup>. Astrophysics places the most stringent lower limits on  $M_D$  in ADD models which however fall sharply with increasing number of extra dimension [18–24]. Considerations of neutron star imposes the strongest constraints:  $M_D > 1760, 77, 9$  and 2 TeV for  $n = 2, 3, 4$  and 5 extra dimensions, respectively [18]. One should note that all astrophysical and cosmological constraints are based on a number of assumptions, whose uncertainties are not included in the limit derivations, so the results are reliable only as order of magnitude estimates. Ultra high-energy cosmic-ray neutrinos ( $E_\nu \sim 10^{19} \text{ eV}$ ) in their interaction with the Earth’s atmosphere offer a complementary probe of extra dimensions. Cosmic-rays interact with the atmosphere and earth’s crust with centre-of-mass energies of the order of 100 TeV. The neutrinos can produce black holes deep in the atmosphere, leading to quasi-horizontal giant air showers. So far a lower bound on  $M_D$  in the ADD model, ranging from 1.0 to 1.4 TeV for scenarios with 4 to 7 extra dimensions has been set at 95% confidence level [25]. It is expected that the Pierre Auger Observatory will be able to set more stringent limits during the first five years of operation; the estimates place  $M_D \gtrsim 3 \text{ TeV}$  for  $n \geq 4$  [26].

### 2.3 Working Model

Our working model for black holes uses the black disk cross-section, which depends only on the horizon radius. The  $(4 + n)$ -dimensional Myers-Perry solution [27], similar to the 4-dimensional Schwarzschild radius, is chosen for the horizon radius  $r_h$ . It depends only on the number of dimensions and the Planck scale. The classical black hole cross-section at the parton level is

$$\hat{\sigma}_{ab \rightarrow \text{BH}} = \pi r_h^2, \quad (1)$$

where  $a$  and  $b$  are the parton types. In most cases, we work with initial black hole masses at least five times higher than the Planck scale at which the expression for the cross section should be valid.

The total cross-section is obtained by convoluting the parton-level cross-section with the parton distribution functions (PDFs), integrating over the phase space, and summing over the parton types.

Throughout this study we use the CTEQ6L1 (leading order with leading order  $\alpha_s$ ) parton distribution functions [28] within the LHAPDF framework [29]. The momentum scale for the PDFs is set equal to the black hole mass for convenience.

The transition from the parton-level to the hadron-level cross-section is based on a factorisation ansatz. The validity of this formula for the energy region above the Planck scale is unclear. Even if factorisation is valid, the extrapolation of the parton distribution functions into this transplanckian region based on Standard Model evolution from present energies is questionable, since the evolution equations neglect gravity and possible KK states in the proton.

The details of horizon formation, and the balding and spin-down phases have been ignored. The important effects of angular momentum in the production and decay of the black hole in extra dimensions are not accounted for in the Monte Carlo event generator. The black holes are considered as

---

<sup>3)</sup>This lower limit uses the Hewett approach for the calculation of  $M_D$  and implies a positive interference term  $\lambda$  with the Standard Model diagrams.

$D$ -dimensional Schwarzschild solutions. Only the Hawking evaporation phase is generated by the simulation.

We can view the Hawking evaporation phase as consisting of two parts: determination of the particle species and assigning energy to the decay products. A particle species is selected randomly with a probability determined by its number of degrees of freedom and the ratio of emissivities. The degrees of freedom take into account polarisation, charge and colour. The emitted charge is chosen such that the magnitude of the black hole charge decreases. All Standard Model particles are considered, including a Higgs boson<sup>4)</sup>. The particles are treated as massless, including the gauge bosons and heavy quarks.

Gravitons have not been included in the simulation, which is another drawback of the current model. Because the graviton lives in the bulk, the number of degrees of freedom of the graviton becomes significant for high numbers of dimensions. In addition, the graviton emissivity is highly enhanced as the space-time dimensionality increases. Therefore the black hole may lose a significant fraction of its mass into the bulk, resulting in missing transverse energy.

The energy assignment to the decay particles in the Hawking evaporation phase has been implemented as follows. The particle species selected by the model described above is given an energy randomly according to its extra-dimensional decay spectrum. A different decay spectrum is used for scalars, fermions and vector bosons, i.e. the spin statistics factor is taken into account. Grey-body spectra are used without approximations [30]. The grey-body factors depend on the number of dimensions. The Hawking temperature is updated after each decay. It is assumed the decay is quasi-stationary in the sense that the black hole has time to come into equilibrium at each new temperature before the next particle is emitted. The energy of the particle given by the spectrum must be constrained to conserve energy and momentum at each step.

The evaporation phase ends when the chosen energy for the emitted particle is ruled out by the kinematics of a two-body decay. At this point an isotropic two-body phase-space decay is performed. In our simulation, the decay is performed totally to Standard Model particles and no stable exotic remnants survive.

Baryon number, colour and electric charge are conserved in the black hole production and decay in this model. Missing transverse energy in the generator comes only from the neutrinos, while in reality missing transverse energy is also possible due to the lost energy in inelastic production, graviton emission, a non-detectable black hole remnant and the possibility that the black hole can leave the Standard Model brane. For the black holes we consider, only a small amount of energy, on average, is lost due to neutrinos. If gravitons were considered, the average energy loss would be approximately 9% [31].

### 3 Monte Carlo Simulations

#### 3.1 Production of Signal and Background Events

The event generator CHARYBDIS [32, 33] version 1.003 was used within the ATLAS software framework to generate Monte Carlo signal samples. It was interfaced via the Les Houches accord [29] to HERWIG [34, 35] which provides the parton evolution and hadronisation, as well as Standard Model particle decays.

Table 1 shows the default CHARYBDIS parameters used, for which approximately 25000 events were generated. Three other black hole signal samples were generated with variations in the number of dimensions and in the black hole minimum mass. In all simulations, the parameter MSSDEF was set equal to 2, setting the Planck scale MPLNCK to be the  $D$ -dimensional Planck scale  $M_{DL}$  in the convention of Ref. [8]. The above samples subsequently underwent the full ATLAS detector simulation and reconstruction. Fast simulation using ATLFAST [36] was employed to widen the range of signal

<sup>4)</sup>Including a scalar Higgs boson is not significant since it has only one degree of freedom.

| Name   | Description  | Value  |
|--------|--|--------|
| MINMSS | Minimum mass of black holes                        | 5 TeV  |
| MAXMSS | Maximum mass of black holes                        | 14 TeV |
| MPLNCK | Planck scale                                       | 1 TeV  |
| MSSDEF | Convention for Planck scale                        | 2      |
| TOTDIM | Total number of dimensions                         | 6      |
| NBODY  | Number of particles in remnant decay               | 2      |
| GTSCA  | Black hole mass used as PDF momentum scale         | True   |
| TIMVAR | Allow $T_H$ to change with time                    | True   |
| MSSDEC | Use all Standard Model particles as decay products | True   |
| GRYBDY | Include grey-body effects                          | True   |
| KINCUT | Use a kinematic cut-off on the decay               | True   |

Table 1: Default parameters used in the CHARYBDIS generator.

121 samples studied, enabling investigation of the many theoretical uncertainties modelled by generator pa-  
 122 rameter switches (see Table 2).

| $n$ | $m_{\text{BH}}$ (TeV) | $\sigma$ (pb) | Note      |
|-----|-----------------------|---------------|-----------|
| 2   | 5-14                  | 40.7          |           |
| 2   | 8-14                  | 0.34          |           |
| 4   | 5-14                  | 24.3          |           |
| 7   | 5-14                  | 22.3          |           |
| 2   | 5-14                  | 6.4           | MPLNCK=2  |
| 3   | 5-14                  | 28.5          |           |
| 5   | 5-14                  | 22.7          |           |
| 2   | 5-14                  | 40.7          | KINCUT=0  |
| 7   | 5-14                  | 22.3          | KINCUT=0  |
| 2   | 5-14                  | 40.7          | TIMEVAR=0 |
| 7   | 5-14                  | 22.3          | TIMEVAR=0 |
| 2   | 5-14                  | 40.7          | NBODY=4   |
| 7   | 5-14                  | 22.3          | NBODY=4   |

Table 2: Monte Carlo datasets and their respective cross-sections used in this analysis. The first four samples were simulated using both full and fast simulations; the lower nine samples were simulated using the fast simulation ATLFast. The final column shows the CHARYBDIS parameter that was changed with respect to the reference set shown in Table 1.

123 Black holes decay democratically to all particles of the Standard Model, so few Standard Model  
 124 processes should produce the same particle spectrum. Black hole decays are characterised by a number  
 125 of high energy and transverse momentum objects, so the primary Standard Model backgrounds are states  
 126 with high multiplicity or high energy jets. The predominant backgrounds to our signal are described  
 127 below and their datasets and cross-sections are listed in Table 3. Sizeable samples are required due to  
 128 their large cross-sections at the LHC.

- 129 •  $t\bar{t}$  leptonic and hadronic decay modes. This process yields the largest contribution to the back-  
 130 ground due to its large cross-section at the LHC and the large branching ratio to hadronic final  
 131 states. The matrix element calculation is done with MC@NLO [37] and HERWIG is used to



| Process                                  | $\sigma$ (pb)       |
|--|---------------------|
| Semi/Fully Leptonic $t\bar{t}$           | 463                 |
| Hadronic $t\bar{t}$                      | 370                 |
| QCD dijets                               | $12.84 \times 10^3$ |
| $W \rightarrow e\nu_e + \text{jets}$     | 281                 |
| $W \rightarrow \mu\nu_\mu + \text{jets}$ | 279                 |
| $Z \rightarrow ee + \text{jets}$         | 25.8                |
| $Z \rightarrow \mu\mu + \text{jets}$     | 26.0                |
| $\gamma + \text{jets}$                   | $5.00 \times 10^3$  |
| $\gamma\gamma + \text{jets}$             | 67.6                |

Table 3: Background Monte Carlo datasets and their respective branching ratio times cross-sections.

perform the parton shower evolution, parton decay and their hadronisation.

- QCD dijet production. The requirements placed on the hadronic part of the signal events reduces the contribution from low- $p_T$  QCD jets. This background is generated using PYTHIA 6.4 [38]. Note that the complete QCD inclusive jet production is not fully modelled by the PYTHIA dijet simulation due to the lack of higher-order QCD contributions. Very low-statistics samples of multijet samples generated by ALPGEN [39] were also used.
- $W \rightarrow \ell\nu + \text{jets}$  production. These backgrounds, though coming from the hard process, have cross-sections that rapidly become small compared to the signal as more jets are added. Vector boson plus jets samples were generated using ALPGEN.
- $Z \rightarrow \ell\ell + \text{jets}$  production.
- $\gamma(\gamma) + \text{jets}$  production.

### 3.2 Detector Simulation

The detector simulation and reconstruction of both signal and background Monte Carlo events were performed within the ATLAS offline framework.

Fast simulation (ATLFAST) was used to widen the range of signal samples studied. The primary advantage of this is one of processing rate: since no detector interactions are modelled it requires less than one second per event. In contrast, full simulation requires approximately 15 minutes for typical Standard Model events, and over 30 minutes per black hole event. Despite this advantage, there are drawbacks: the fast simulation does not include a complete treatment of lepton isolation and misidentification nor of photon conversion.

The same generator signal samples were passed through the full and fast simulations in order to understand the differences in black hole events. Variables ranging from simple multiplicities to event shapes were compared. Sample distributions of particle multiplicity and  $\cancel{E}_T$  are shown in Figure 1. The multiplicity difference is due to differing default jet algorithms; we use a cone algorithm with radius  $\Delta R = 0.4$  in the full simulation, whereas ATLFAST uses a  $k_\perp$  algorithm. Using the same algorithm for both samples gives very close agreement, nonetheless this discrepancy will have an effect in analyses dependent purely upon multiplicity information. All other variables investigated showed concordant results.

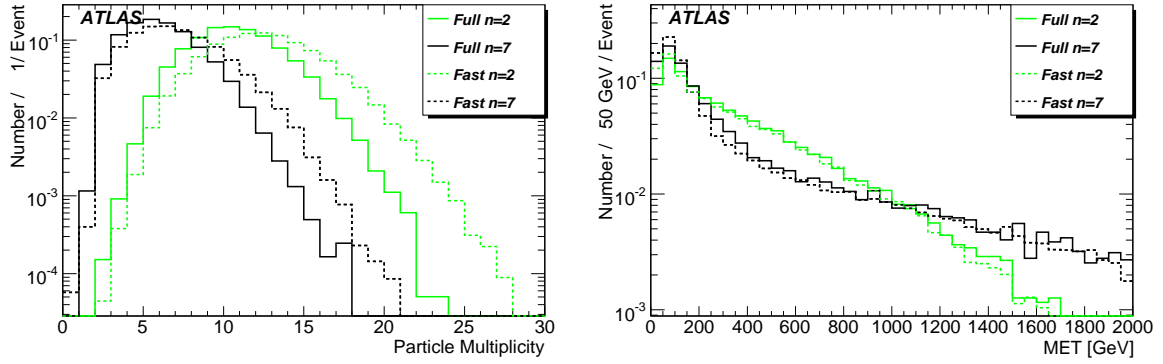


Figure 1: Total particle multiplicity and missing transverse energy distributions for signal samples from fast and full simulation.

## 4 Event Properties

The high mass scale, and the thermal nature of the decay process, result in black hole events being characterised by a large number of high- $p_T$  final state particles, including all the Standard Model fields. Graviton emission is also expected, but is not simulated in CHARYBDIS. Of the final state particles, the detector can measure jets, electrons, muons and photons well, and will be able to reconstruct some of the  $Z$  and  $W$  bosons. The missing transverse energy, produced mainly by neutrino and graviton emission, can also be measured. In this section, the data sample with two extra dimensions and black hole masses above 5 TeV is used as the reference signal sample.

A key feature of the black hole decays is that the Hawking temperature is higher for larger  $n$ , for a given black hole mass. Higher temperature produces higher energy emissions, with the consequence that the energy is shared between fewer particles. This has a significant effect on the multiplicity and event shape distributions. Similarly, the samples with a higher black hole low-mass cutoff produce more high energy final state particles.

### 4.1 Particle Types and Multiplicities

Figure 2 shows the types of particles produced directly by black hole decay. The vertical axis shows the average number of particles per black hole decay. From this figure, we see that a heavier black hole has more decay products. The particle-antiparticle balance is broken by the initial state of two protons colliding. Moreover, due to conservation of energy and momentum, colour connection etc., a perfect democratic decay cannot be achieved, e.g., the number of top quarks is smaller than that of lighter quarks. The possibility of identifying fermions and bosons and determining their branching ratios in black hole decays was studied in [40].

Figure 3 shows  $p_T$  and pseudorapidity ( $\eta$ ) distributions of particles produced directly from black hole decays. As expected, the shape depends little on particle type. Figure 4 shows the reconstructed multiplicity of final-state jets, leptons and photons. Four signal samples are shown for  $n = 2, 4$  and  $7$  with a minimum black hole mass of 5 TeV, and for  $n = 2$  with a minimum black hole mass of 8 TeV. The figure also compares the reference signal to the backgrounds. The multiplicity in the signal falls as  $n$  rises, because the black holes decay at a higher temperature.

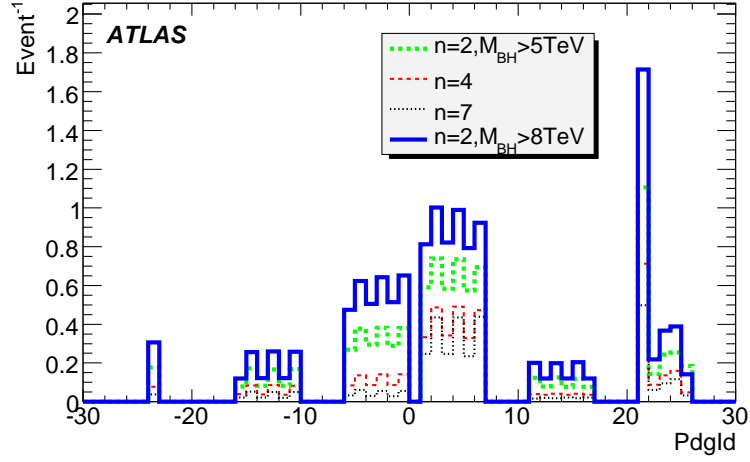


Figure 2: PDG code of particles emitted from black hole decay for a minimum black hole mass of 5 TeV and  $n = 2, 4$  and  $7$  and for a minimum black hole mass of 8 TeV and  $n = 2$ . The vertical axis shows multiplicity per black hole decay.

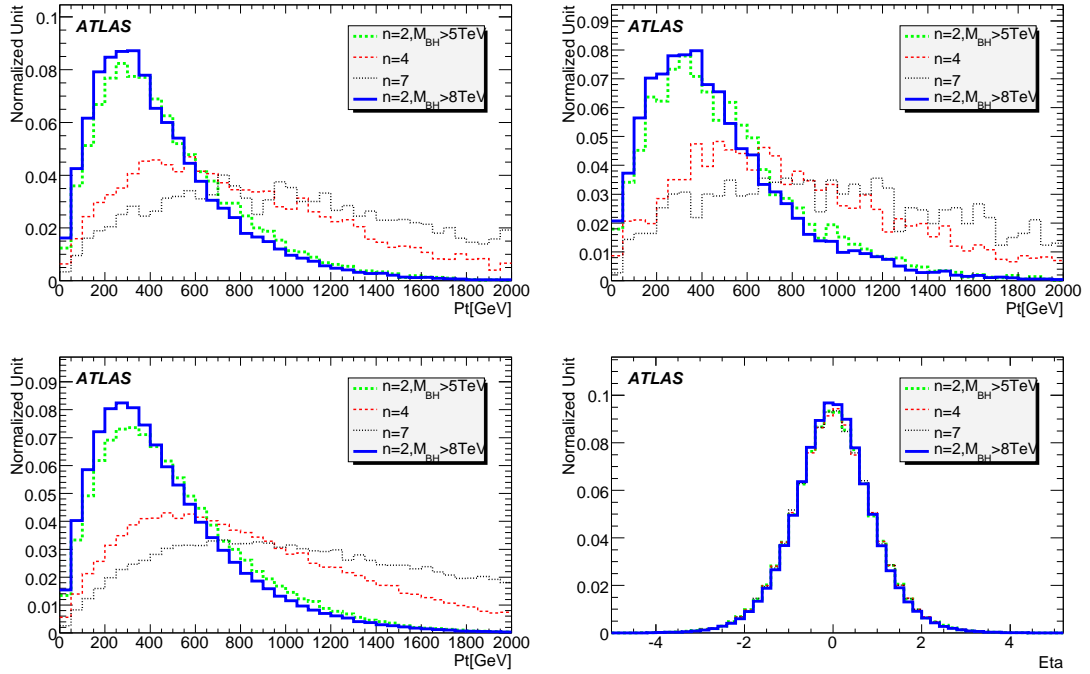


Figure 3: Generator  $p_T$  distributions (top row): leptons (left) and Z bosons (right) emitted from the black hole. The bottom row shows  $p_T$  and  $\eta$  spectra for all particles emitted from the black hole.

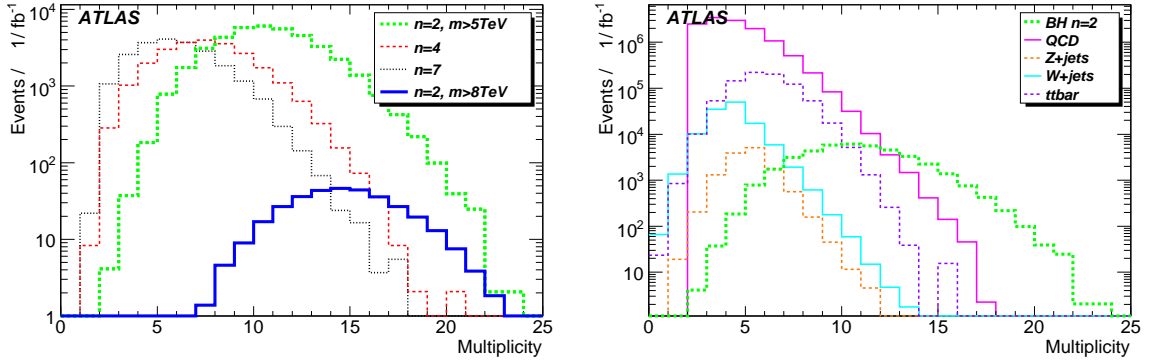


Figure 4: Multiplicities of reconstructed objects for (left) black hole samples and (right) backgrounds. They are normalised to the integrated luminosity of  $1 \text{ fb}^{-1}$ .

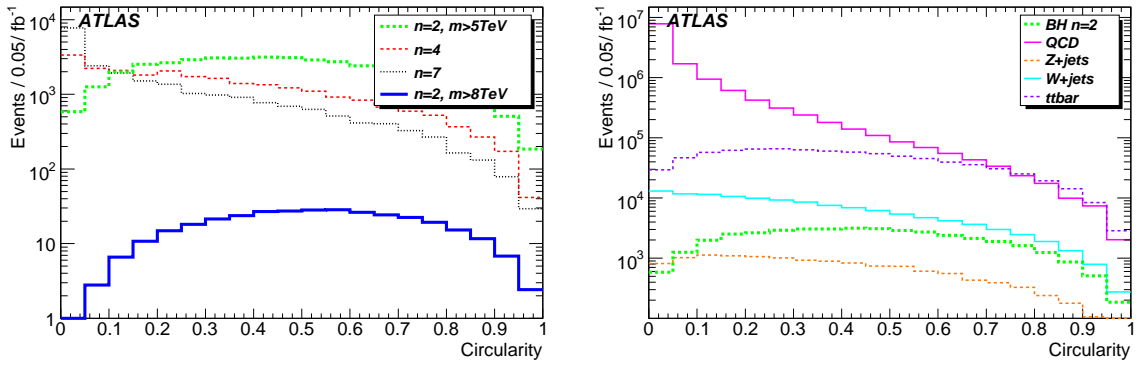


Figure 5: Circularity calculated from reconstructed objects for (left) black hole samples and (right) backgrounds.

## 4.2 Event Shape

At first sight, one would expect black hole events to be very different from the background in event shape variables [38,41,42] such as sphericity, because of the high multiplicity thermal decay. However, the event shape of the black hole events varies considerably with  $n$ , making such variables less useful than could be hoped. Though the background distributions show less variation, when these are scaled by their large cross sections, there is a large degree of overlap, disfavouring their use as a cut variable. Additionally, our ignorance of the decay modes of the final black hole remnant introduces a significant systematic effect. In our version of CHARYBDIS, once the mass of the black hole has dropped below the Planck scale, the remnant decays to either 2 or 4 bodies. We have selected the two-body option for our standard samples. This means that at high  $n$ , where events can reach this stage after few emissions, the circularity of the events is reduced, and the thrust increased.

The distinguishing power between signal and backgrounds of a selection of event shape variables was studied; Figure 5 shows the circularity distribution for the same samples as Figure 4; similarly Figs. 6 and 7 show their thrust distributions, sphericity and aplanarity. The expected bias towards more “jet-like” events is clearly seen at high  $n$ . For this reason, we choose not to use event shape variables as a discriminant in this analysis.

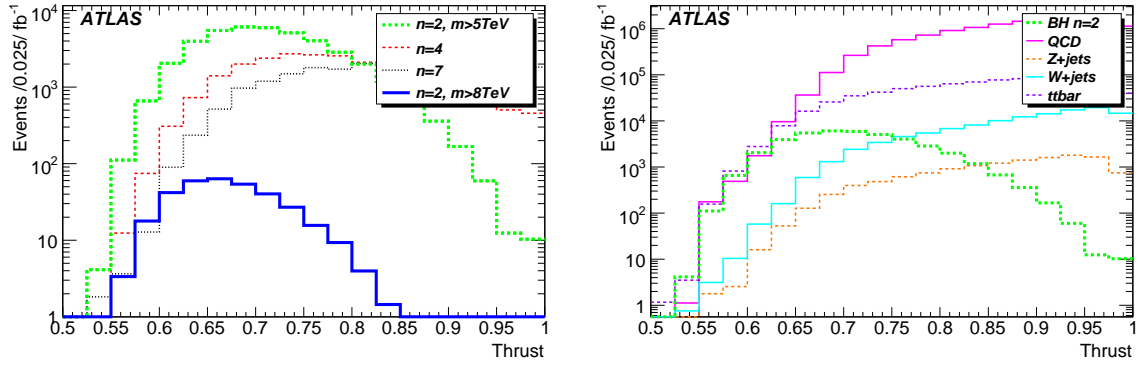
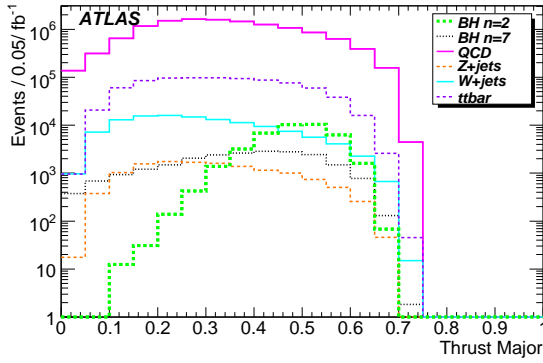
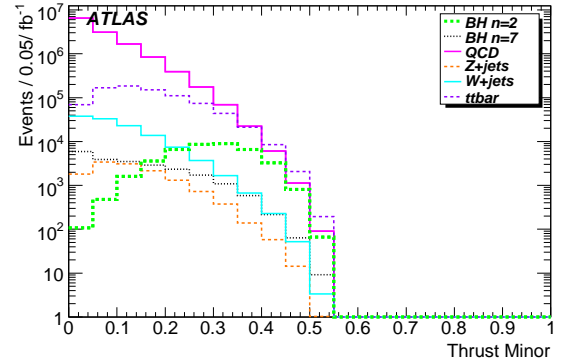


Figure 6: Thrust calculated from reconstructed objects for (left) black hole samples and (right) QCD dijet and  $t\bar{t}$  backgrounds.

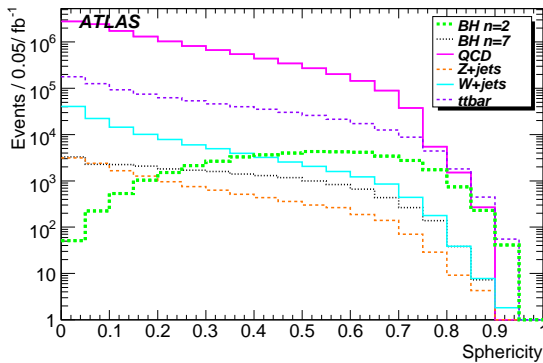
(a) Thrust major



(b) Thrust minor



(c) Sphericity



(d) Aplanarity

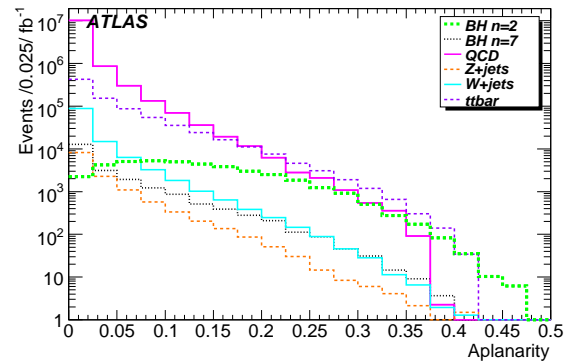


Figure 7: Different event shape variables for black hole samples and backgrounds. They are normalised to the integrated luminosity of 1 fb<sup>-1</sup>.

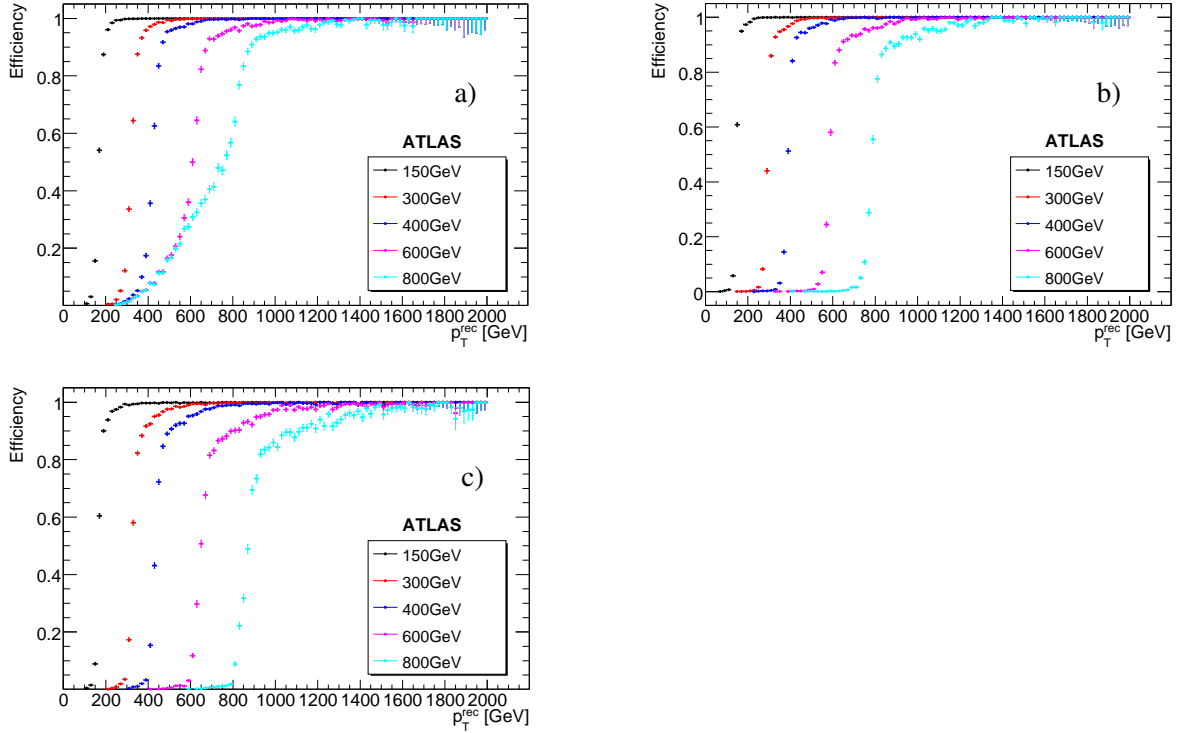


Figure 8: Simulated jet trigger efficiencies as functions of the offline reconstructed jet  $p_T$  for a) L1, b) L2 and c) EF. The efficiencies are determined for different  $p_T$ -thresholds: 150 GeV (black), 300 GeV (red), 400 GeV (blue), 600 GeV (magenta) and 800 GeV (cyan).

## 5 Trigger

The ATLAS trigger and data-acquisition system consists of three levels (L1, L2, EF) of online event selection [43]. Each subsequent trigger level refines the decisions made at the previous level and may apply additional selection criteria. The ATLAS trigger is described in detail in ref. [44].

### 5.1 Triggering on Black Holes

Each black hole produces multiple decay products, including hadronic jets, leptons and photons, as described in Section 4. The jets typically carry a dominant fraction of the visible decay energy and hence provide the best option for triggering black hole events.

The response of the jet trigger, as simulated in the current version of the ATLAS detector simulation, is demonstrated in Figure 8. The plots show the trigger efficiencies for various  $p_T$ -thresholds as functions of the jet  $p_T$  reconstructed offline. For these plots, a match between the jet reconstructed offline and at the respective trigger level is required. The matching consists of searching for the closest offline jet in  $\Delta R = \sqrt{(\Delta\eta)^2 + (\Delta\phi)^2}$ , where  $\Delta\eta$  and  $\Delta\phi$  are the distances between the reconstructed jet and the trigger jet in pseudorapidity  $\eta$  and azimuth  $\phi$ , respectively. To avoid incorrect matching for L1 jets, a modified criterion is applied: the L1 jet closest in energy to the reconstructed jet is chosen among the jets found within the  $\Delta R = 0.5$  distance around the reconstructed jet. The shape of the L1 efficiency distribution for the 800 GeV threshold is due to the saturation of the L1 trigger tower energies at 255 GeV. Events in which the transverse energy in one trigger tower exceeds 255 GeV are automatically accepted, as larger values fill up the memory of the L1 trigger analog-to-digital converters.

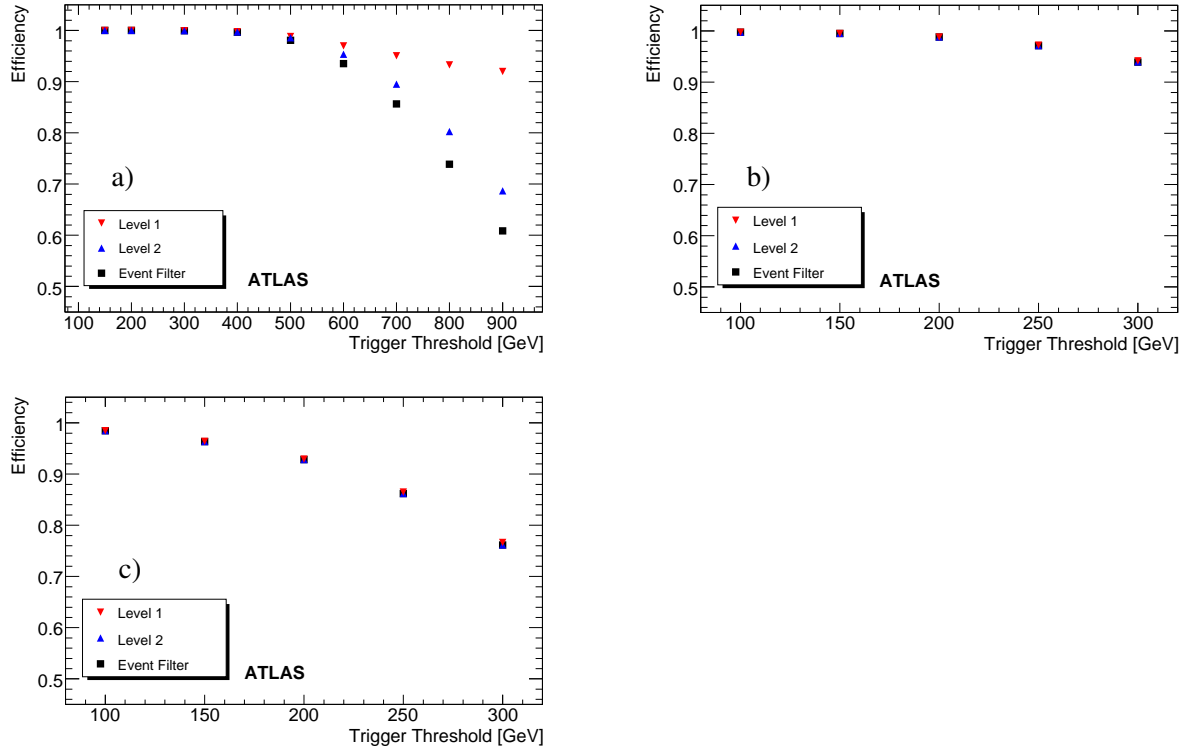


Figure 9: Simulated jet trigger efficiencies for black hole events from the signal sample with  $n = 2$  and  $m > 5$  TeV as functions of the jet  $p_T$  threshold for a) single-jet trigger, b) 3-jet trigger and c) 4-jet trigger. The efficiencies are determined for L1 (black), L2 (red) and EF (blue).

The efficiency at each trigger level is determined independently of the decisions at the other levels. Were the trigger chain to have the same threshold on all levels, the total efficiency would be the convolution of the respective functions. The L2 algorithms are based on regions of interest provided by L1, hence it is not possible to determine their efficiency completely independently of the L1 decisions. The L2 algorithms were run on all L1 jet RoI starting from the lowest L1 jet  $p_T$  threshold of 35 GeV. This is much lower than the thresholds studied, making the L2 decision (shown in Figure 8b) virtually independent of the L1 efficiency.

The total trigger efficiencies are listed in Table 4 for three signal samples and demonstrated in Figure 9 for the signal sample with  $n = 2$  and  $m > 5$  TeV. The highest efficiency is provided by the single-jet trigger, which we consider to be the master trigger for the black hole events. The presence of multiple high- $p_T$  jets per event, each of which is likely to pass the trigger, results in very high total efficiencies. Setting this trigger threshold at 400 GeV will provide greater than 99% efficiency at all trigger levels. The Standard Model process rate at this threshold is expected to be less than 0.1 Hz at an instantaneous luminosity of  $10^{31} \text{ cm}^{-2} \text{ s}^{-1}$ , which should allow this trigger to run at this threshold without prescaling for the first few years of LHC data taking. The rate of black hole events is expected to be less than 5 mHz at the  $10^{31} \text{ cm}^{-2} \text{ s}^{-1}$  luminosity. For the start-up running at the luminosity of  $10^{31} \text{ cm}^{-2} \text{ s}^{-1}$ , it is planned to set the highest threshold for the single-jet trigger at 120 GeV, guaranteeing an efficiency of almost 100% for black hole events.

Alternatively, a trigger based on the scalar sum of transverse energies of all recorded decay products (“sum- $E_T$  trigger”) can be used. No simulation of this trigger is available in the samples used in this study. Looking at this sum in the offline reconstruction suggests that this trigger would collect nearly

a) CHARYBDIS:  $n = 2, m > 5$  TeV

| Trigger | L1    | L2    | EF    |
|---------|-------|-------|-------|
| j100    | 1     | 1     | 1     |
| j400    | 0.997 | 0.997 | 0.997 |
| 3j100   | 0.998 | 0.998 | 0.998 |
| 3j250   | 0.972 | 0.971 | 0.971 |
| 4j100   | 0.985 | 0.985 | 0.985 |
| 4j250   | 0.865 | 0.862 | 0.862 |

b) CHARYBDIS:  $n = 4, m > 5$  TeV

| Trigger | L1    | L2    | EF    |
|---------|-------|-------|-------|
| j100    | 1     | 1     | 1     |
| j400    | 0.997 | 0.997 | 0.996 |
| 3j100   | 0.952 | 0.952 | 0.952 |
| 3j250   | 0.886 | 0.885 | 0.885 |
| 4j100   | 0.807 | 0.806 | 0.806 |
| 4j250   | 0.612 | 0.607 | 0.607 |

c) CHARYBDIS:  $n = 7, m > 5$  TeV

| Trigger | L1    | L2    | EF    |
|---------|-------|-------|-------|
| j100    | 1     | 1     | 1     |
| j400    | 0.990 | 0.987 | 0.985 |
| 3j100   | 0.807 | 0.806 | 0.805 |
| 3j250   | 0.710 | 0.704 | 0.704 |
| 4j100   | 0.525 | 0.522 | 0.522 |
| 4j250   | 0.343 | 0.341 | 0.341 |

Table 4: Simulated jet trigger efficiencies for black hole events as functions of the jet- $p_T$  threshold for different simulation samples.

100% of black hole events for Planck scales above 1 TeV. It is foreseen to run this trigger in the start-up data taking, unrescaled at the threshold of 650 GeV.

Based on experience from previous collider experiments, one may expect detector hardware problems at the beginning of data taking. In particular, noisy channels in the calorimeter or trigger electronics may cause high trigger rates for the single-jet trigger and for the sum- $E_T$  trigger, such that even the highest threshold triggers have to be prescaled. In such cases, a multijet (3- or 4-jet) trigger is considered for use until the detector problems are resolved. The efficiencies of such triggers are listed in Table 4.

In the present study, the minimum mass of a black hole is set at 5 TeV or more in order to be safely above the Planck scale. At lower masses one may expect an increased rate of dijet events described by a contact interaction. The single-jet trigger or the sum- $E_T$  trigger at the thresholds considered above are well suited for detecting such signatures. Such events may not, however, be selected by multijet triggers.

The trigger efficiencies, studied here in the simulation, have to be determined from data. An unbiased determination requires an “orthogonal” trigger, e.g. a trigger based on fully independent information from that used by the master trigger. A muon trigger which is based solely on signals in the muon detector should be well suited for such studies.

## 6 Signal Selection and Background Rejection

### 6.1 Event Selection

Since all types of Standard Model particles are produced from black hole decay, we make full use of particle identification information (PID) from our detectors. First we select muons, electrons, photons and jets, which are called *objects* in this section. Table 5 shows the details of their selection criteria.

The identification of objects is sometimes ambiguous: e.g., an electron could be simultaneously reconstructed as a jet. To resolve this, we apply PID to each object, selecting muons, electrons, photons and jets in that order of priority. Once an object passes the PID criteria in a given category, any remaining



266 ambiguous assignments are removed if they match the chosen object within a  $\Delta R$  of less than 0.1.

Next we select black hole events using these objects as described below. Then we reconstruct a black hole from all the selected objects for the selected event. The mass of the black hole in an event is calculated from the four-momenta of the reconstructed final state objects and missing  $E_T$ , which is included in the calculation to improve the reconstructed mass resolution:

$$p_{\text{BH}} = \sum_{i=\text{objects}} p_i + (\cancel{E}_T, \cancel{E}_{Tx}, \cancel{E}_{Ty}, 0), \quad (2)$$

$$m_{\text{BH}} = \sqrt{p_{\text{BH}}^2}. \quad (3)$$

267 We present two methods to select black hole events. One is based on the scalar summation of  $p_T$   
 268 and the other on the multiplicity of high- $p_T$  objects. Both make use of the characteristic of a black hole  
 269 having large mass. After that, we require a high- $p_T$  lepton to reject backgrounds further.

270 Figure 10 shows the scalar summation of the  $p_T$  of each object,  $\sum |p_T|$ , which demonstrates good  
 271 background discrimination and high signal efficiency for all black hole samples. We require  $\sum |p_T|$  to be  
 272 larger than 2.5 TeV to reject backgrounds. This requirement is relatively unaffected by changes in the  
 273 model, in particular by changes to the number of extra dimensions  $n$ . Figure 11 shows  $m_{\text{BH}}$  distributions  
 274 after this requirement. The QCD dijet background is already well suppressed, but we also investigated  
 275 the effect of a further selection, requiring a lepton with a  $p_T > 50$  GeV. This resulted in the QCD dijet  
 276 background being rejected by a factor greater than  $10^6$  as shown in Table 6, which summarises the event  
 277 numbers for an integrated luminosity of  $1 \text{ fb}^{-1}$ . Though the high statistics QCD samples used were  
 278 generated with PYTHIA, a leading order generator, there were also  $p_T$ -sliced small ALPGEN multijet  
 279 samples available. When investigated using the  $\sum |p_T|$  and lepton cut method, a very similar, marginally  
 280 lower number of background events was predicted according to the very limited statistics available.  
 281 Larger scale studies would be needed to conclude anything more concrete. Poisson confidence limits are  
 282 used for samples where fewer than 20 events passed the requirements. Signal cross-section errors are  
 283 statistical only, the theoretical uncertainties are large as discussed in Section 2. <sup>5)</sup>

284 An alternative selection procedure was also used. Figure 12 shows the  $p_T$  distributions of the leading,  
 285 2nd-, 3rd- and 4th-leading objects out of all the selected objects. The 4th-leading object still has larger  $p_T$   
 286 in the signal events than in the background events. We require the number of objects with  $p_T > 200$  GeV  
 287 to be equal to or greater than four. Figure 14 (left) shows  $m_{\text{BH}}$  distributions after this requirement. Since  
 288 QCD processes still remain large, a lepton requirement is again used to decrease it. Figure 13 shows the

<sup>5)</sup>In the case of two hadronic subsamples ( $t\bar{t}$  and dijets) where very few events passed the  $\sum |p_T|$  requirement, the lepton requirement rejection factor was applied to the  $\sum |p_T|$  requirement's Poisson bound to estimate the background distribution error.

(a) muon

$|\eta| < 2.5, p_T > 15 \text{ GeV}$   
 Central track match ( $0 \leq \chi^2 < 100$ )  
 Isolation  $E_{T,\text{cone } 0.2} < \min(100, 0.2p_T + 20) \text{ GeV}$

(b) electron

$|\eta| < 2.5$  except for  $1.00 < |\eta| < 1.15, 1.37 < |\eta| < 1.52$   
 $p_T > 15 \text{ GeV}$   
*medium* selection [45]

(c) photon

$|\eta| < 2.5, p_T > 15 \text{ GeV}$   
*tight* selection [45]  
 Isolation  $E_{T,\text{cone } 0.2} < 0.2p_T + 20 \text{ GeV}$

(d) jet

Cone algorithm ( $R = 0.4$ ) based on calorimeter towers  
 $|\eta| < 2.5, p_T > 20 \text{ GeV}$

Table 5: Particle selection

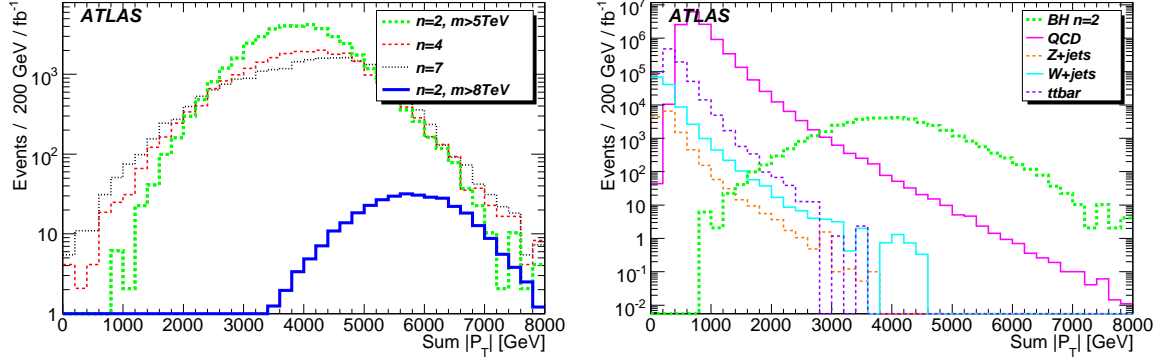


Figure 10:  $\sum |p_T|$  distributions for (left) black hole samples and (right) backgrounds (QCD dijet,  $t\bar{t}$  and vector boson plus jets). They are normalised to an integrated luminosity of  $1 \text{ fb}^{-1}$ .

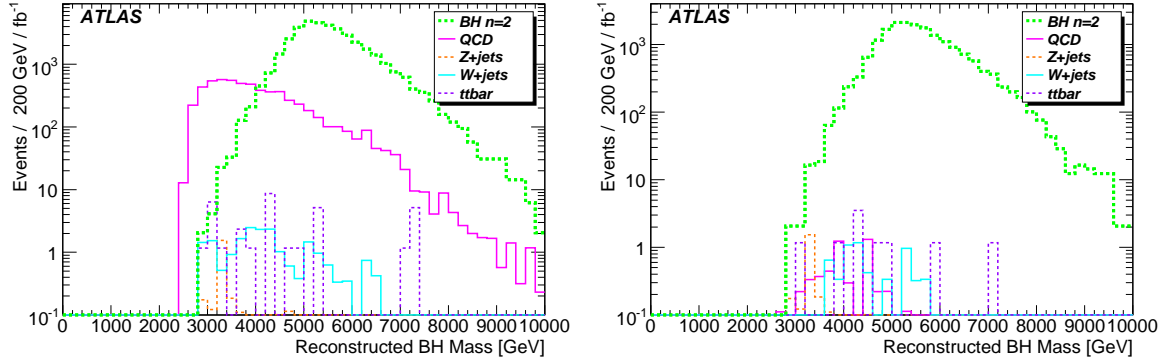


Figure 11: Black hole mass distribution with a requirement  $\sum |p_T| > 2.5 \text{ TeV}$  (left), and black hole mass distribution with an additional requirement on the lepton- $p_T$  of  $p_T > 50 \text{ GeV}$  (right). The signal sample with  $n = 2$  and  $m > 5 \text{ TeV}$  and backgrounds are shown.

| Dataset                              | Before selection<br>(fb)   | $\sum  p_T  > 2.5 \text{ TeV}$<br>(fb) | After requiring a lepton<br>(fb) | acceptance           |
|--------------------------------------|----------------------------|--|----------------------------------|----------------------|
| $n = 2, m > 5 \text{ TeV}$           | $40.7 \pm 0.1 \times 10^3$ | $39.2 \pm 0.3 \times 10^3$             | $18.6 \pm 0.2 \times 10^3$       | 0.46                 |
| $n = 4, m > 5 \text{ TeV}$           | $24.3 \pm 0.1 \times 10^3$ | $22.6 \pm 0.2 \times 10^3$             | $6668 \pm 83$                    | 0.27                 |
| $n = 7, m > 5 \text{ TeV}$           | $22.3 \pm 0.1 \times 10^3$ | $20.1 \pm 0.2 \times 10^3$             | $3574 \pm 60$                    | 0.17                 |
| $n = 2, m > 8 \text{ TeV}$           | $338.2 \pm 1$              | $338.1 \pm 2.5$                        | $212 \pm 16$                     | 0.63                 |
| $t\bar{t}$                           | $833 \pm 100 \times 10^3$  | $23.6^{+12.2}_{-6.7}$                  | $8.2^{+2.43}_{-2.43}$            | $9.8 \times 10^{-6}$ |
| QCD dijets                           | $12.8 \pm 3.7 \times 10^6$ | $5899^{+1773}_{-1771}$                 | $5.37^{+3.25}_{-2.02}$           | $4.3 \times 10^{-7}$ |
| $W_{\ell\nu} + \geq 2 \text{ jets}$  | $1.9 \pm 0.04 \times 10^6$ | $12.3^{+9.0}_{-1.8}$                   | $4.67^{+8.75}_{-0.93}$           | $2.4 \times 10^{-6}$ |
| $Z_{\ell\ell} + \geq 3 \text{ jets}$ | $51.8 \pm 1 \times 10^3$   | $2.75^{+2.02}_{-2.01}$                 | $2.57^{+0.95}_{-0.64}$           | $5.0 \times 10^{-5}$ |

Table 6: Acceptance for each signal and background dataset in fb after requiring  $\sum |p_T| > 2.5 \text{ TeV}$ , and a lepton with  $p_T > 50 \text{ GeV}$ .

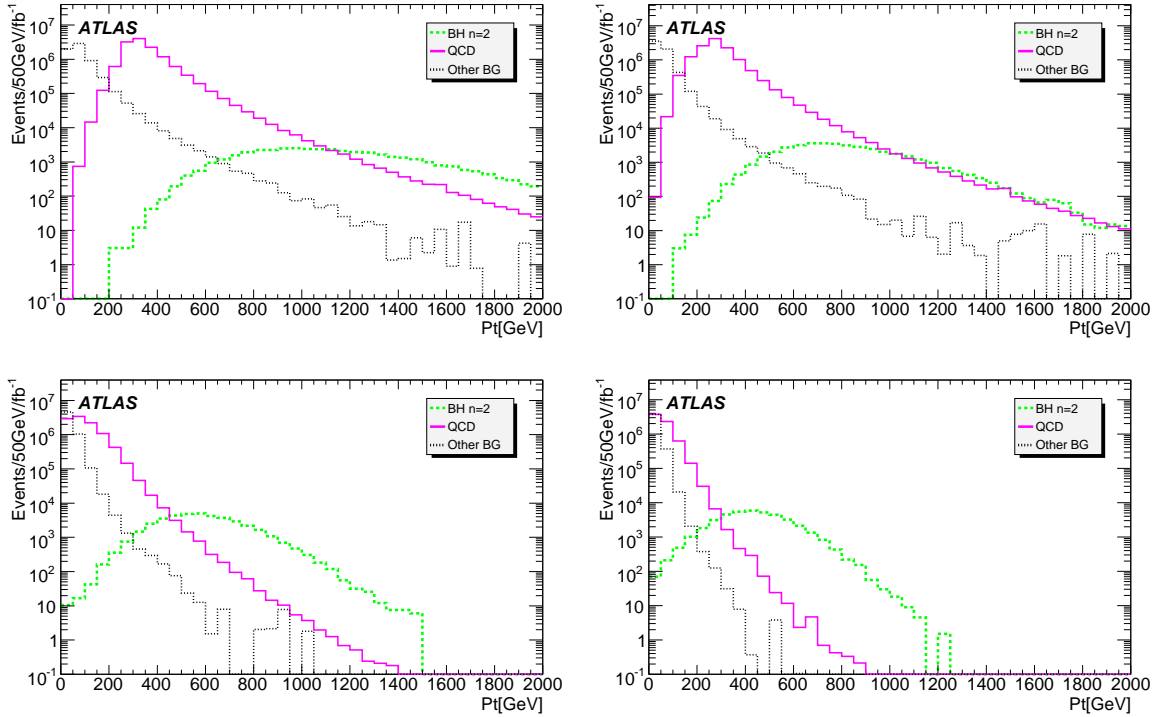


Figure 12:  $p_T$  distributions of leading (top left), 2nd- (top right), 3rd- (bottom left) and 4th-leading (bottom right) objects out of all the selected objects for the signal sample with  $n = 2$  and  $m > 5$  TeV and backgrounds (see Table 7).

distribution of the highest  $p_T$  lepton (muon or electron). As expected, the number of leptons from QCD processes is small. Requiring the number of leptons (muons or electrons) with  $p_T > 200$  GeV to be equal to or greater than one results in the  $m_{BH}$  distributions shown in Figure 14(right).

The shape of the background in the region of high  $m_{BH}$  was fitted with a gaussian plus an asymmetric gaussian (Figure 15) and that function is used to estimate the number of background events.

CHARYBDIS does not include graviton emission. In practice this, and the energy lost in gravitational interactions during the balding phase, would be another source of  $\cancel{E}_T$ . Consequently we expect CHARYBDIS to underestimate this for black hole events. Nonetheless, each of the black hole samples studied in this analysis often have very wide distributions of  $\cancel{E}_T$ , with tails extending out to several TeV. This property of models with black holes is most unusual and hard to reproduce in other new physics scenarios, and should make it possible to distinguish between Black Holes and the majority of SUSY models for example.

A requirement on  $\cancel{E}_T$  above  $\sim 500 - 600$  GeV was studied as an alternative to a lepton requirement for black hole signal selection. Figure 16 shows the potential of this method, and contrasts these models with three common supersymmetric models of different cross-section and mass scale. Despite the early evidence for the presence of black holes, there are disadvantages to relying on such a selection. Firstly, our ability to reconstruct the black hole's mass is aided by limiting  $\cancel{E}_T$  to be under 100 GeV (Figure 22). Such a signal from high  $\cancel{E}_T$  events would be dominated by those events reconstructed most poorly, limiting their use for cross-section measurement and discovery. The theoretical uncertainties are large and difficult to quantify, and finally there are experimental difficulties in calibrating and accurately measuring this variable across a wide energy range.

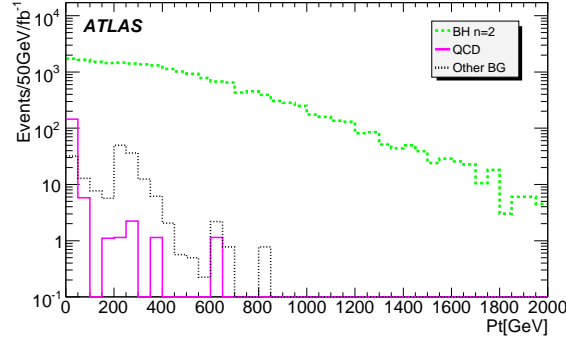


Figure 13:  $p_T$  distributions of the leading lepton (electron or muon) after requiring the number of objects (electron, muon, photon or jet) with  $p_T > 200$  GeV to be larger than 3 for the signal sample with  $n = 2$  and  $m > 5$  TeV and backgrounds (see Table 7).

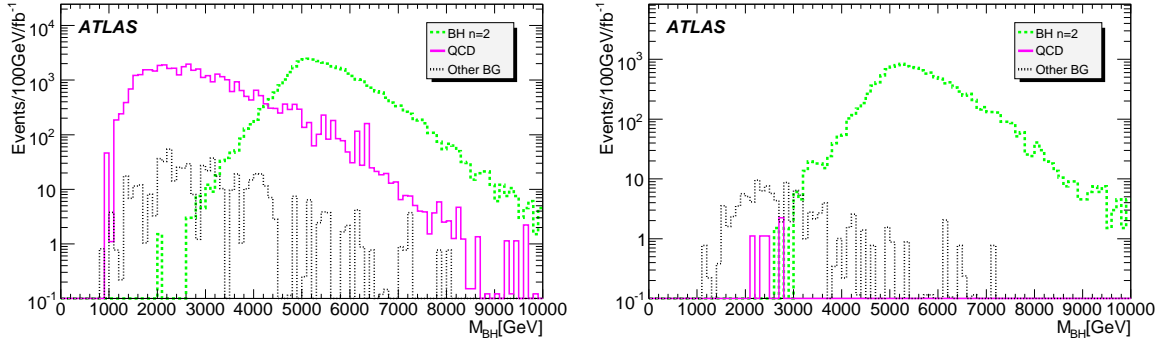


Figure 14: Black hole mass distribution for the signal sample with  $n = 2$  and  $m > 5$  TeV and backgrounds (see Table 7) after multiplicity requirement of at least 4 objects with  $p_T > 200$  GeV (left plot) and an additional requirement of a lepton (electron or muon) with  $p_T > 200$  GeV (right plot).

| Dataset                | Before selection<br>(fb) | After multi-object<br>requirement (fb) | After lepton requirement<br>(fb) | Acceptance           |
|------------------------|--------------------------|--|----------------------------------|----------------------|
| $n = 2, m > 5$ TeV     | $40.7 \times 10^3$       | $38.9 \pm 0.4 \times 10^3$             | $14.0 \pm 0.2 \times 10^3$       | 0.34                 |
| $n = 4, m > 5$ TeV     | $24.3 \times 10^3$       | $17.9 \pm 0.3 \times 10^3$             | $4521 \pm 126$                   | 0.19                 |
| $n = 7, m > 5$ TeV     | $22.3 \times 10^3$       | $9953 \pm 185$                         | $1956 \pm 82$                    | 0.087                |
| $n = 2, m > 8$ TeV     | 338                      | $338 \pm 4$                            | $164 \pm 3$                      | 0.49                 |
| $t\bar{t}$             | $833 \times 10^3$        | $129 \pm 27$                           | $36^{+12}_{-9}$                  | $4.3 \times 10^{-5}$ |
| QCD dijets             | $12.8 \times 10^6$       | $38.9 \pm 1.9 \times 10^3$             | $6^{+107}_{-3}$                  | $5.6 \times 10^{-7}$ |
| W+jets                 | $560 \times 10^3$        | $99^{+28}_{-22}$                       | $56^{+24}_{-13}$                 | $1 \times 10^{-3}$   |
| Z+jets                 | $51.8 \times 10^3$       | $29^{+90}_{-4}$                        | $19^{+90}_{-3}$                  | $4 \times 10^{-4}$   |
| $\gamma(\gamma)$ +jets | $5.1 \times 10^6$        | $285^{+87}_{-76}$                      | $0^{+40}_{-0}$                   | $< 10^{-5}$          |

Table 7: Acceptance of the 4-object requirements for each dataset in fb. 90% confidence limits are used when no events passed the requirements.

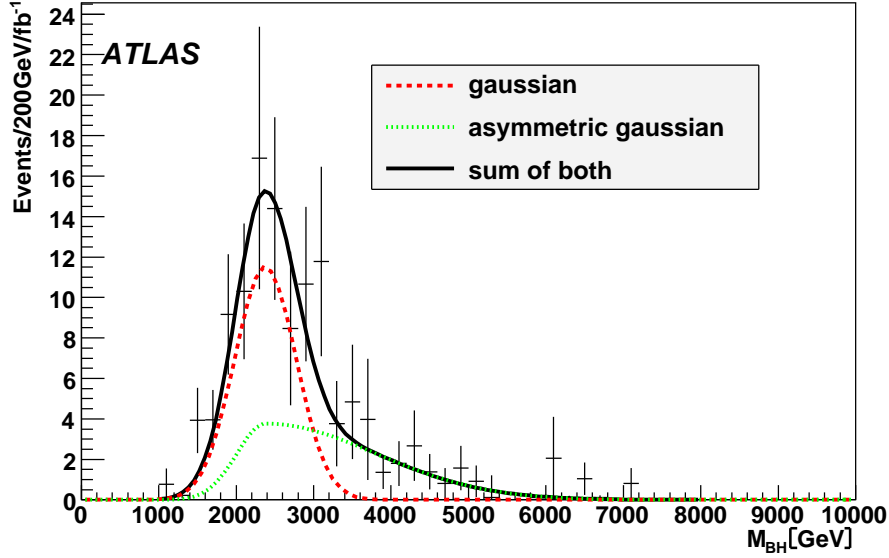


Figure 15: The background shape after the 4-object and lepton requirements is shown (data points). The points were fitted by the sum (black line) of a gaussian (red line) and an asymmetric gaussian (green line).

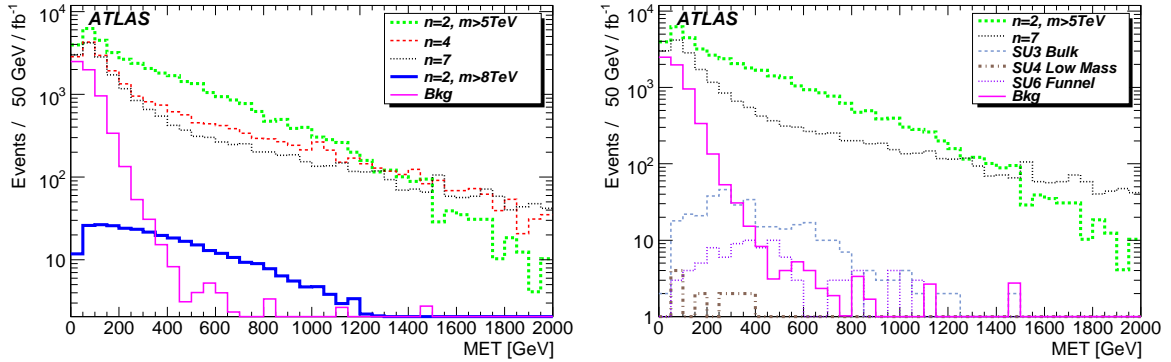


Figure 16: The left hand plot shows the missing transverse energy distributions after a  $\sum |p_T| > 2.5$  TeV requirement. A requirement of  $\cancel{E}_T > 500$  GeV would leave negligible background and a large number of signal events for all samples. The right hand plot compares two black hole samples with three supersymmetric models with a range of mass scales; the two classes of models can easily be distinguished by their differing cross-sections and the extent of the  $\cancel{E}_T$  tail.

## 6.2 Discovery Reach

Producing a robust discovery potential for black hole events is difficult, because the semi classical assumptions used to model them are only valid well above the Planck scale. Close to the Planck scale, events may occur due to gravitational effects with lower multiplicities, but without the signatures anticipated by our event selections. As the energy rises above the threshold needed for black hole creation, our requirements should become more efficient. Lack of theoretical understanding makes it impossible to model this threshold region.

To account for this, we impose a lower requirement on the true mass of black holes created in our simulated samples,  $BH_{thresh}$ , normally set at 5 TeV, and we do not attempt to account for any additional signal from lower masses. In order to estimate the discovery potential, two methods have been considered:

1. we keep our signal selection requirements constant, and increase the value of  $BH_{thresh}$ . Since the analysis requirements are unchanged, the background remains constant, while the signal drops as the production of events occurs at higher mass. We then evaluate the luminosity required to detect a minimum of 10 signal events, with  $S/\sqrt{B} > 5$ , assuming the production cross-section is as high as predicted. Such a study is shown in Figure 17, using the  $\Sigma|p_T|$  and lepton requirements. This method produces conservative limits, taking some account of the uncertainty in the production cross-section near the threshold.
2. We keep the production model unchanged with  $BH_{thresh} = 5$  TeV, but apply an additional requirement on the reconstructed black hole mass. This requirement reduces substantially background events, while allowing the higher mass signal to pass unchanged. This is less conservative, since it allows black hole signal events to be produced at low mass, but to migrate above the reconstructed mass requirement because of the detector mass resolution, hence increasing the signal. As before, we use the nominal value of the production cross-section, and evaluate the luminosity needed to meet our discovery criteria, this time as a function of reconstructed mass. A study using this method is shown in Figure 18 using the 4-object and lepton requirements.

The two approaches are complementary and illustrate the uncertainties in different ways. We observe that the search reach is limited eventually at high mass by the falling production cross-section, reflecting the falling parton luminosity and the limited energy of the LHC. We conclude that, if the semi classical cross-section estimates are valid, black holes can be discovered above a 5 TeV threshold with a few  $\text{pb}^{-1}$  of data, while  $1 \text{ fb}^{-1}$  would allow a discovery to be made even if the production threshold was at 8 TeV.

## 7 Systematic Uncertainties

### 7.1 Signal uncertainties

We have investigated the systematic uncertainties using fast simulation runs, having checked that the full and fast simulations agree well for this purpose.

There are a number of theoretical parameters associated with CHARYBDIS which can generate systematic errors in the estimates of the acceptance for signal events. These are:

- The kinematic cutoff. This parameter is normally true, and causes the generator to end thermal emission if an unphysical emission is randomly selected. The generator moves immediately to the final remnant decay phase. This approximation deteriorates at high numbers of extra dimensions because of the high temperature and emitted particle energies. We have investigated the alternative, where a new emission is selected until a physical one is chosen. In this case, thermal emission will continue until the black hole mass falls below  $M_{DL}$ .

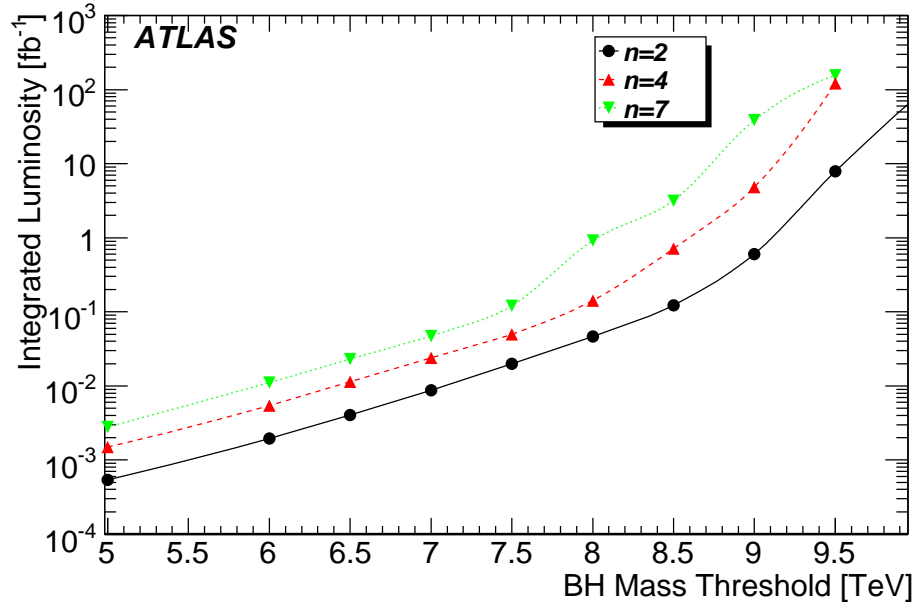


Figure 17: Discovery potential using  $\sum |p_T|$  and lepton selections: required luminosity as a function of black hole mass threshold.

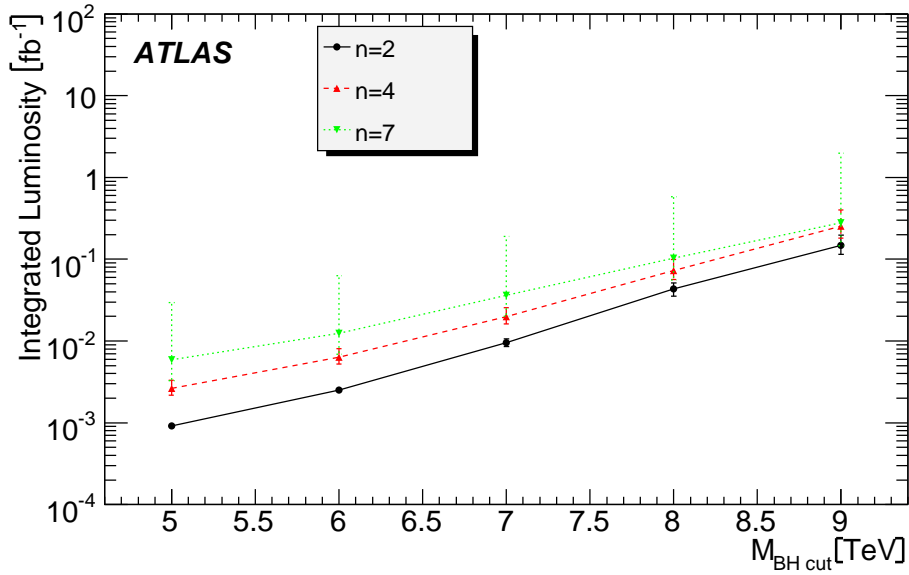


Figure 18: Discovery potential for black holes with the 4-objects and lepton requirements with systematic uncertainties: required luminosity as a function of a requirement on the reconstructed black hole mass.

- Temperature variation. The Hawking temperature of the black hole is normally allowed to increase as its mass decreases, as expected if the black hole has time to equilibrate between decays. We have investigated the alternative of keeping the temperature fixed at the initial value, as would be the case if the black hole decayed very quickly or “suddenly” (see Table 8).
- Number of extra dimensions. In addition to our full simulation samples with  $n = 2, 4$  and  $7$ , we have simulated  $n = 3$  and  $5$  with the fast simulation. As noted above, the events become more jet-like at high  $n$  and the particle multiplicity drops (see Figure 20), due to the increased Hawking temperature. Our signal selection remains robust, as shown in Table 8.
- Planck scale. We have investigated changing the Planck scale from its default value of  $M_{\text{DL}} = 1$  TeV to 2 TeV. We note that, since the model is only valid for black hole masses much larger than the Planck scale, this scenario is not well modelled in the range of masses accessible at the LHC.
- Remnant decay. We have investigated changing the remnant decay model from a two-body to a four-body mode (see Figure 20).

Figure 19 shows the effect of changing the kinematic cutoff on the particle multiplicity and  $\sum |p_T|$  distributions. Since the black hole is forced to decay thermally until it falls below  $M_{\text{DL}}$ , the multiplicity is higher, and the events have lower energy emissions. The total energy remains constant, however so the  $\sum |p_T|$  distribution is relatively stable.

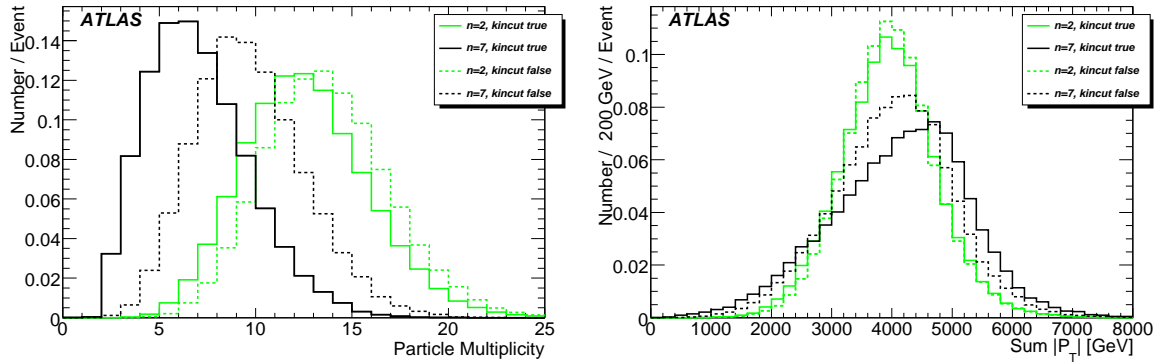


Figure 19: Particle multiplicity and  $\sum |p_T|$  distributions, showing the variation when the kinematic cut-off parameter is changed.

The acceptance of the signal for various parameter choices are shown in Table 8. Compared to the standard full simulation, the largest effect is observed for high  $n$ , when the kinematic cut-off parameter is changed. This is as expected, since this parameter has a large effect on the evolution of the black hole during its decay. Similarly changing the remnant decay from 2 to 4 bodies has a large effect at high  $n$ ; the effect of this, and of changing number of extra dimensions is shown in Figure 20.

## 7.2 Uncertainties on detector performance

Two kinds of systematic uncertainties on detector performance were studied. One is an uncertainty on lepton identification efficiency. To estimate this effect, we loosened and tightened particle identification selections, by changing the hadronic leakage for electrons and the isolation cut for muons. The changes in signal efficiencies are around 2%.

The effect of a 5% error in the jet energy scale (JES) was also considered. The effect of these uncertainties on the discovery potential is shown in Figure 18.



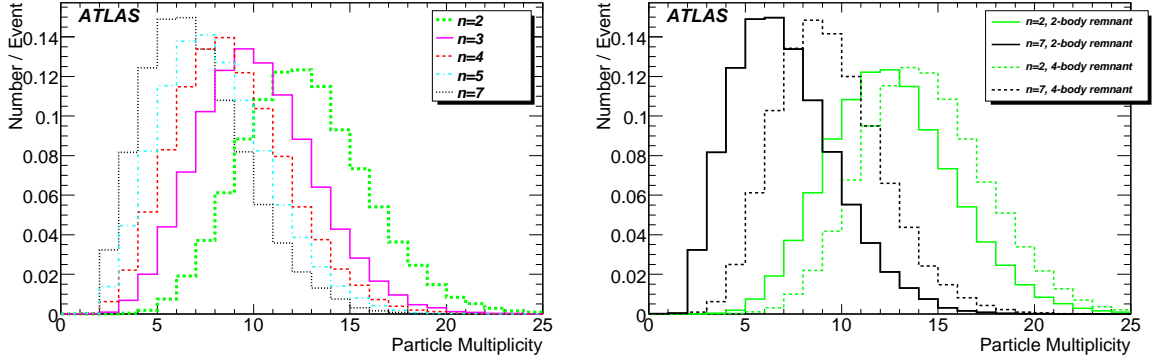


Figure 20: Particle multiplicity distributions, showing the variation produced by a change in the number of extra dimensions, or the number of particles produced by remnant decay.

| $n$ | Full Sim | Fast Sim | Kin. Cut off | $T_H$ -variation off | 4-body remnant |
|-----|----------|----------|--------------|----------------------|----------------|
| 2   | 45.8     | 42.9     | 47.2         | 48.7                 | 47.9           |
| 3   | -        | 33.2     | -            | -                    | -              |
| 4   | 27.4     | 26.6     | -            | -                    | -              |
| 5   | -        | 21.7     | -            | -                    | -              |
| 7   | 16.1     | 15.9     | 29.2         | 16.6                 | 27.4           |

Table 8: Signal acceptance (%) for different model assumptions.

## 8 Results

### 8.1 Search Reach for Black Hole Production at the LHC

The studies presented show that the ATLAS detector is capable of discovering the production of black holes up to the kinematic limit of the LHC, assuming that the signal is correctly modelled. This conclusion is largely based on the predicted huge production cross-section, and the small background from QCD dijets at very high- $p_T$ , especially when the presence of a high energy lepton is required. However, both of these assumptions are suspect. The high production cross-section is subject to considerable discussion in the literature, as discussed in Section 2. Moreover, until the LHC has measured the QCD cross-section at 14 TeV, we cannot be certain of the tails of the QCD distributions. The Monte Carlo simulations of these tails are working at the limit of their validity, given the high energies and large multiplicities involved.

For these reasons, we prefer not to place too much weight on the detailed search reach limits. Instead, we confine ourselves to the statement that, with current understanding, the black hole signature considered should be clearly visible if it exists.

### 8.2 Determination of Model Parameters

We have considered the possibility of extracting model parameters from the data, should a signal be observed. There are two key parameters: the Planck scale  $M_D$  (or  $M_{DL}$  depending on the convention) and the number of extra dimensions  $n$ . In Ref. [46, 47] a method was proposed to extract  $M_D$  from the cross-section data, which fixes the Planck scale (within the model assumptions), and from events with high energy emissions.

The Hawking temperature  $T_H$  of the black hole depends on  $n$ . If we detect events with emissions near  $m_{\text{BH}}/2$ , the energy of those emissions is a measure of the initial  $T_H$ . Hence, over the sample of black holes, the probability of such emissions is a measure of the characteristic temperature, and can be used to extract  $n$ . This method was first put forward in Ref. [46], and here is made compatible with the need for background rejection requirements. The requirements described in Section 6 are not appropriate: the lepton requirement biases the selected events in favour of final states with many particles, and hence against those events with a single high energy emission. A suitable requirement was found to be  $\sum |p_T| > 3.5$  TeV; this removes the background without biasing the signal events selected.

Figure 21 shows the probability of a hard emission for two samples, compared to the predictions. The method requires accurate mass resolution, and so an additional requirement on  $\cancel{E}_T < 100$  GeV is applied. The addition of this requirement lowers the efficiency noticeably, but does improve the black hole mass reconstruction; details of the resolution and efficiency can be found in Figure 22. The data are consistent with the expected value of  $n$ , but due to this reduction in signal efficiency, more data would be required to make a definitive measurement. It should be noted that this measurement requires the Planck scale to be known. If this cannot be determined from the production cross-section, it is likely that the threshold behaviour near the Planck scale would provide an indication of its value. At present, no theoretical model exists to allow us to make predictions in this region.

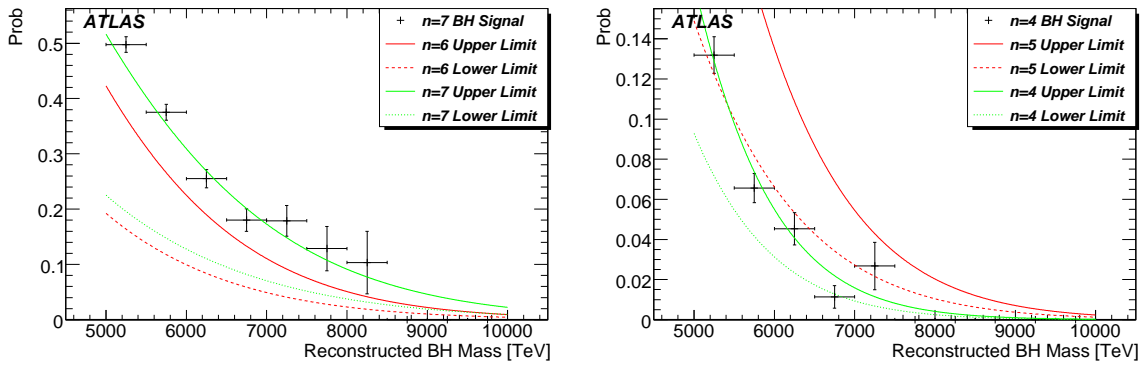


Figure 21: The probability of a hard emission near  $m_{\text{BH}}/2$  for  $n = 7$  and  $n = 4$ . The bands show the expected range for  $n = 7$  and  $n = 6$ , and for  $n = 5$  and  $n = 4$ , respectively, for a luminosity of approximately  $0.75 \text{ fb}^{-1}$ .

## 9 Summary

The search for black holes in the first  $100 \text{ pb}^{-1}$  of LHC data with the ATLAS detector and software framework was simulated.

We summarised the current experimental limits on black hole production and studied with the help of the black hole event generator CHARYBDIS and Standard Model Monte Carlo data sets the basic event properties, trigger and selection efficiencies, theoretical and experimental uncertainties of black hole production at the LHC for a flat ADD extra dimension scenario with the Planck scale  $M_{\text{DL}} = 1$  TeV. We have explored the uncertainties inherent in the theoretical modelling and our understanding of the detector. We conclude that, if the semi-classical cross section estimates are valid, black holes above a 5 TeV threshold can be discovered with a few  $\text{pb}^{-1}$  of data, while  $1 \text{ fb}^{-1}$  would allow a discovery to be made even if the production threshold was 8 TeV.

|                                       |        | Normalisation | Mean (GeV)   | Resolution (GeV) |
|---------------------------------------|--------|---------------|--------------|------------------|
| Without<br>$\cancel{E}_T$ requirement | Narrow | $1018 \pm 26$ | $-217 \pm 5$ | $276 \pm 9$      |
|                                       | Wide   | $276 \pm 30$  | $-148 \pm 9$ | $722 \pm 13$     |
| With<br>$\cancel{E}_T$ requirement    | Narrow | $318 \pm 12$  | $-116 \pm 8$ | $215 \pm 9$      |
|                                       | Wide   | $108 \pm 7$   | $118 \pm 18$ | $635 \pm 16$     |

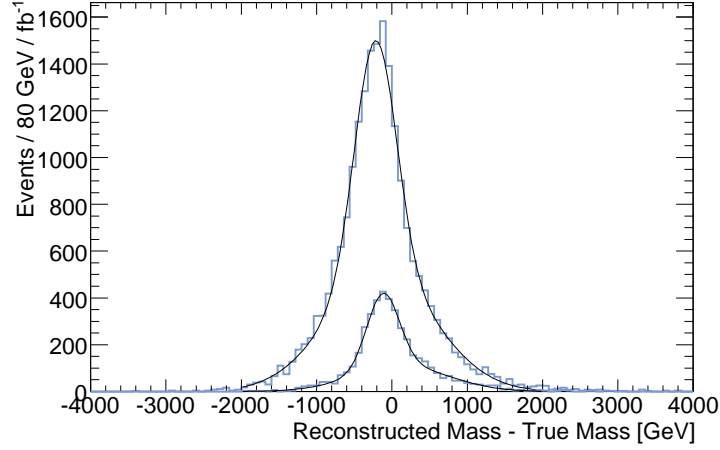


Figure 22: Black hole mass resolution distributions and their fits to double Gaussian functions, using a  $\Sigma |p_T|$  and lepton requirement ( $1 \text{ fb}^{-1}$ ). The upper curve is without a  $\cancel{E}_T$  cut. The lower curve has an additional requirement on  $\cancel{E}_T < 100 \text{ GeV}$ .

## References

- [1] N. Arkani-Hamed, S. Dimopoulos, and G. R. Dvali, *Phys. Lett.* **B429** (1998) 263–272, arXiv:hep-ph/9803315.
- [2] I. Antoniadis, N. Arkani-Hamed, S. Dimopoulos, and G. R. Dvali, *Phys. Lett.* **B436** (1998) 257–263, arXiv:hep-ph/9804398.
- [3] N. Arkani-Hamed, S. Dimopoulos, and G. R. Dvali, *Phys. Rev.* **D59** (1999) 086004, arXiv:hep-ph/9807344.
- [4] L. Randall and R. Sundrum, *Phys. Rev. Lett.* **83** (1999) 3370–3373, arXiv:hep-ph/9905221.
- [5] L. Randall and R. Sundrum, *Phys. Rev. Lett.* **83** (1999) 4690–4693, arXiv:hep-th/9906064.
- [6] G. F. Giudice, R. Rattazzi, and J. D. Wells, *Nucl. Phys.* **B544** (1999) 3–38, arXiv:hep-ph/9811291.
- [7] **Particle Data Group** Collaboration, W. M. Yao *et al.*, *J. Phys.* **G33** (2006) 1–1232.
- [8] S. Dimopoulos and G. L. Landsberg, *Phys. Rev. Lett.* **87** (2001) 161602, arXiv:hep-ph/0106295.
- [9] S. Hossenfelder, arXiv:hep-ph/0412265.
- [10] P. Kanti, *Int. J. Mod. Phys.* **A19** (2004) 4899–4951, arXiv:hep-ph/0402168.
- [11] X. Calmet and S. D. H. Hsu, arXiv:0711.2306 [hep-ph].

- 447 [12] E. G. Adelberger, B. R. Heckel, and A. E. Nelson, *Ann. Rev. Nucl. Part. Sci.* **53** (2003) 77–121,  
448 arXiv:hep-ph/0307284.
- 449 [13] P. Shukla and A. K. Mohanty, *Pramana* **60** (2002) 1117–1120, arXiv:hep-ph/0201029.
- 450 [14] **CDF** Collaboration, A. Abulencia *et al.*, *Phys. Rev. Lett.* **97** (2006) 171802,  
451 arXiv:hep-ex/0605101.
- 452 [15] **ALEPH** Collaboration, arXiv:hep-ex/0212036.
- 453 [16] S. Mele and E. Sanchez, *Phys. Rev.* **D61** (2000) 117901, arXiv:hep-ph/9909294.
- 454 [17] **D0** Collaboration, *D0 Note* **4336** (2004) .
- 455 [18] S. Hannestad and G. G. Raffelt, *Phys. Rev.* **D67** (2003) 125008, arXiv:hep-ph/0304029.
- 456 [19] M. Casse, J. Paul, G. Bertone, and G. Sigl, *Phys. Rev. Lett.* **92** (2004) 111102,  
457 arXiv:hep-ph/0309173.
- 458 [20] M. Fairbairn, *Phys. Lett.* **B508** (2001) 335–339, arXiv:hep-ph/0101131.
- 459 [21] M. Fairbairn and L. M. Griffiths, *JHEP* **02** (2002) 024, arXiv:hep-ph/0111435.
- 460 [22] N. Kaloper, J. March-Russell, G. D. Starkman, and M. Trodden, *Phys. Rev. Lett.* **85** (2000)  
461 928–931, arXiv:hep-ph/0002001.
- 462 [23] K. R. Dienes, *Phys. Rev. Lett.* **88** (2002) 011601, arXiv:hep-ph/0108115.
- 463 [24] G. F. Giudice, T. Plehn, and A. Strumia, *Nucl. Phys.* **B706** (2005) 455–483,  
464 arXiv:hep-ph/0408320.
- 465 [25] L. A. Anchordoqui, J. L. Feng, H. Goldberg, and A. D. Shapere, *Phys. Rev.* **D68** (2003) 104025,  
466 arXiv:hep-ph/0307228.
- 467 [26] L. A. Anchordoqui, J. L. Feng, H. Goldberg, and A. D. Shapere, *Phys. Rev.* **D65** (2002) 124027,  
468 arXiv:hep-ph/0112247.
- 469 [27] R. C. Myers and M. J. Perry, *Ann. Phys.* **172** (1986) 304.
- 470 [28] J. Pumplin *et al.*, *JHEP* **07** (2002) 012, arXiv:hep-ph/0201195.
- 471 [29] M. R. Whalley, D. Bourilkov, and R. C. Group, arXiv:hep-ph/0508110.
- 472 [30] C. M. Harris and P. Kanti, *JHEP* **10** (2003) 014, arXiv:hep-ph/0309054.
- 473 [31] D. M. Gingrich, *JHEP* **11** (2007) 064, arXiv:0706.0623 [hep-ph].
- 474 [32] C. M. Harris, P. Richardson, and B. R. Webber, *JHEP* **08** (2003) 033, arXiv:hep-ph/0307305.
- 475 [33] D. M. Gingrich, arXiv:hep-ph/0610219.
- 476 [34] G. Marchesini *et al.*, *Comput. Phys. Commun.* **67** (1992) 465–508.
- 477 [35] G. Corcella *et al.*, *JHEP* **01** (2001) 010, arXiv:hep-ph/0011363.
- 478 [36] D. F. E. Richter-Was and L. Poggioli, *ATLAS Physics Note* **ATL-Phys-98-131** .

- 479 [37] J. Collins, *Phys. Rev.* **D65** (2002) 094016, arXiv:hep-ph/0110113.
- 480 [38] T. Sjostrand, S. Mrenna, and P. Skands, *JHEP* **05** (2006) 026, arXiv:hep-ph/0603175.
- 481 [39] M. L. Mangano, M. Moretti, F. Piccinini, R. Pittau, and A. D. Polosa, *JHEP* **07** (2003) 001,  
482 arXiv:hep-ph/0206293.
- 483 [40] J. P. Ottersbach, *Diploma Thesis, Bergische Universitaet Wuppertal* **WU D 07-10** (2007) .
- 484 [41] G. C. Fox and S. Wolfram, *Nucl. Phys.* **B149** (1979) 413.
- 485 [42] S. Brandt and H. D. Dahmen, *Zeit. Phys.* **C1** (1979) 61.
- 486 [43] **ATLAS** Collaboration, *CERN/LHCC* **98-15** (1998) .
- 487 [44] **ATLAS** Collaboration, “The ATLAS Trigger for early running.” This volume.
- 488 [45] **ATLAS** Collaboration, “Reconstruction and identification of electrons in ATLAS.” This volume.
- 489 [46] C. M. Harris *et al.*, *JHEP* **05** (2005) 053, arXiv:hep-ph/0411022.
- 490 [47] J. Tanaka, T. Yamamura, S. Asai, and J. Kanzaki, *Eur. Phys. J.* **C41** (2005) 19–33,  
491 arXiv:hep-ph/0411095.

